Integrated Recovery of Elevation and Photometric Reflectance Properties from Hyperspectral Data

Von der Fakultät
Elektrotechnik und Informationstechnik
der Technischen Universität Dortmund
genehmigte

Dissertation

zur Erlangung des akademischen Grades
Doktor der Ingenieurwissenschaften
eingereicht von

Arne Grumpe

Dortmund, 2015

Tag der mündlichen Prüfung:	17.04.2015
Hauptreferent:	Prof. Dr. Christian Wöhler
Korreferent:	Prof. Dr. Josef Pauli

Abstract

Optical measurements have become standard tools in modern applications, e.g. remote sensing, industrial quality control and robotics. The applications range from object detection within images and the recovery of the object's shape from one or multiple images to the determination of physical object properties depending on its spectral reflectance. The former group of techniques relies on the spatial distribution of the object's reflectance and the illumination and viewing geometry and the local topography. The latter group, in contrast, analyses the reflectance properties of one single image element, i.e. one pixel, representing the object along the spectral/colour direction.

Photogrammetry, e.g. stereo image analysis or bundle adjustment, uses the viewing geometry. The object topography is recovered by intersecting rays from multiple viewing points/orientations and thus applying a pure geometric reasoning. It is well known, that the same object area may appear extremely different if the illumination and/or viewing geometry changes and thus one of the main problems of photogrammetry is the establishment of corresponding object points within multiple images. Consequently, the lateral resolution of photogrammetric surface model is typically lower than the lateral resolution of the images.

The dependence of the object's appearance on the illumination and observation geometry, i.e. the incidence angle and the emittance angle, is used by photometric methods, i.e. photoclinometry or shape from shading. The orientation of the object's surface model that best matches the observed brightness is computed. In a second step, the surface is recovered from the orientations, i.e. the surface gradient field. The photometric methods thus yield surface models at image resolution. They are, however, prone to systematic errors that originate from the integration of small systematic errors of the gradient estimation step.

The spectral analysis is commonly based on diagnostic spectral features, i.e. spectral absorption bands which are related to resonance frequencies in the object's molecules. Commonly, the spectral absorption bands are characterised by colour ratio images or more sophisticated parameters, e.g. the wavelength of the absorption minimum and the relative absorption depth in relation to a material without absorption. Since the object's appearance, i.e. the measured reflectance, is influence by the illumination and viewing geometry, the measurements need to be normalised. Often, the phase angle, i.e. the angle between the illumination direction and the viewing direction, is corrected while the local topography, i.e. the local incidence angle and the local emittance angle, are not included in the normalisation. The phase angle correction is commonly applied on a global scale, i.e. the spatial distribution of different reflectance properties is neglected. Furthermore, independently derived topographic models, e.g. photogrammetry or laser altimeters, require a co-registration procedure and, often, are of lower lateral resolution.

The aforementioned methods may be subdivided into methods with respect to the spatial reflectance distribution and methods with respect to the spectral reflectance dis-

tribution. Current research focuses on one of the groups. Hyperspectral imagery, however, provides simultaneous knowledge on the local surface topography, i.e. shading, and the spectral reflectance.

The earth's moon has been of scientific interest for a long time and thus a wealth of measurements exists and is publicly available. The available measurements include high resolution topography models derived from stereo image analysis and laser altimeter measurements, hyperspectral reflectance measurements and elemental abundances measured by gamma ray spectrometers. This wealth of data is rarely met in industrial applications and thus the lunar surface is an ideal object for the method development. Additionally, the distance to the earth's moon does not allow for in-situ measurements and thus many remote sensing techniques have been developed within the past years. Thus, this thesis is based on lunar hyperspectral imagery acquired by the Moon Mineralogy Mapper onboard the Indian Chandrayaan-1 mission. The methods and techniques developed in this thesis, however, are not limited to the lunar surface and may be applied to any spectral analysis scenario.

The goal of this thesis is to bridge the gap between spatial and spectral analysis of reflectance measurements, i.e. to extract and combine the spatial and the spectral information from hyperspectral images. This is achieved by an integrated framework for the recovery of local surface topography and the normalisation of spectral data.

The spectral reflectance measurements are normalised with respect to a local topography model using a physically motivated reflectance model, often termed reflectance function. The parameters of the reflectance model are explicitly assumed to be spatially varying. The resolution of the parameter maps is adapted to the spatial resolution of the underlying topography model. Since the radiance spectrum emitted from one surface element is composed of a reflected illumination spectrum and a thermal emission spectrum, a method to estimate the local surface temperature based on the measured radiance and the superposition of a black body emission spectrum and a reflectance model is developed.

The local surface topography is refined to image resolution using single-image or multiple-image photometric techniques, i.e. the local surface orientation is extracted from the spectral imagery. In order to suppress the systematic reconstruction errors, the shape from shading techniques are extended applying a relative depth constraint and an absolute depth constraint. The extension developed in this thesis requires an initial surface topography model of lower lateral resolution, e.g. a surface model computed by stereo analysis or laser altimeter measurements. The relative depth constraint influences the surface gradient estimation step and aims at the suppression of errors before the integration step, i.e. the accumulation of systematic errors. It is, however, not possible to cover all causes of systematic errors, e.g. imperfect radiance calibrations. Thus, an absolute depth constraint is added to the surface gradient integration step.

The developed techniques are applied to derive a near-global Moon Mineralogy Mapper mosaic. Based on this mosaic, a regression method is applied to map parameters of the spectral absorption bands onto elemental abundances measured by the Lunar Prospector

Gamma-Ray Spectrometer. To obtain co-registered images, an illumination independent image registration method is developed based on the recovered elevation models, which, by definition, are co-registered to the original image. Finally, the photometric surface refinement methods are applied to Lunar Orbiter Narrow Angle Camera images to derive to elevation models of the highest possible resolution.

The results show that the influence of the local topography is nearly eliminated from the normalised reflectance maps. A qualitative analysis of the obtained parameters of the reflectance model, e.g. the single-scattering albedo, is in good agreement with known bright and dark areas, e.g. bright volcanic domes or dark ash deposits. An analysis of the temperature estimation shows, that accurate estimates of temperatures above 300 K are possible. Comparing the results of the refined topographic models to single high accuracy laser altimeter measurements show that the depth error is comparable to stereo analysis while the lateral resolution is greatly increased. The presented image registration technique based on the topography models achieves sub-pixel accuracy.

Acknowledgements

First and foremost I would like to thank my advisor Prof. Christian Wöhler for providing helpful knowledge and experience, valuable discussions and the freedom to develop and pursue new ideas. Furthermore, I would like to thank my second advisor Prof. Josef Pauli for his the effort of providing his expertise.

Moreover, I would like to thank my colleagues Steffen Herbort and Malte Lenoch for countless discussions, providing different view times and the great time working together.

Parts of the evaluations of the proposed methods were performed on the LiDO HPC cluster at TU Dortmund. I would like to thank the LiDO team for their support.

During the course of this thesis I was fortunate to supervise the students Fethi Belkhir and Vladimir Zirin, who contributed through their thesis, discussions, and a pleasant working atmosphere.

Finally, I would like to thank my friends and my family for encouragement and greatly appreciated distraction throughout the whole time.

List of related Publications

This thesis is based on the following publications of the author. The publications are listed in descending chronological order.

Peer-reviewed journal articles and book chapters

(Grumpe et al., 2014a) A. Grumpe, F. Belkhir, and C. Wöhler. Construction of lunar DEMs based on reflectance modelling. *Advances in Space Research*, 53(12): 1735–1767, 2014a. doi: 10.1016/j.asr.2013.09.036.

(Grumpe and Wöhler, 2014) A. Grumpe and C. Wöhler. Recovery of elevation from estimated gradient fields constrained by digital elevation maps of lower lateral resolution. *ISPRS Journal of Photogrammetry and Remote Sensing*, 94:37–54, 2014. doi: 10.1016/j.isprsjprs.2014.04.011.

(Wöhler et al., 2014) C. Wöhler, A. Grumpe, A. Berezhnoy, M. U. Bhatt, and U. Mall. Integrated topographic and spectral analysis of the lunar surface: Application to impact melt flows and ponds. *Icarus*, 235:86–122, 2014. doi: 10.1016/j.icarus.2014.03.010.

(Wöhler and Grumpe, 2013) C. Wöhler and A. Grumpe. Integrated DEM Construction and Calibration of Hyperspectral Imagery: A Remote Sensing Perspective. In Michael Breuß, Alfred Bruckstein, and Petros Maragos, editors, *Innovations for Shape Analysis: Models and Algorithms*, Mathematics and Visualization, pages 467–492, Berlin Heidelberg, 2013. Springer-Verlag.

Conference contributions

(Grumpe et al., 2014b) A. Grumpe, V. Zirin, and C. Wöhler. Phase Angle Based Correction of the Moon Mineralogy Mapper Radiance Measurements. In *Lunar and Planetary Science Conference*, volume 45 of *Lunar and Planetary Inst. Technical Report*, page #2562, 2014b.

(Grumpe and Wöhler, 2012) A. Grumpe and C. Wöhler. Image-Based Construction of Lunar Digital Elevation Models of very High Lateral Resolution. In *Lunar and Planetary Science Conference*, volume 43 of *Lunar and Planetary Inst. Technical Report*, page #2597, 2012.

(Grumpe et al., 2012a) A. Grumpe, F. Belkhir, V. Zirin, and C. Wöhler. Normalisation of hyperspectral data with respect to illumination and local topography. *Geophysical Research Abstracts*, 14:EGU2012–11034, 2012a.

(Grumpe et al., 2012b) A. Grumpe, C. Wöhler, and A. Berezhnoy. Full Topographic Correction of M3 Data for Lunar Elemental Abundance Estimation. In *Proc. 3th Moscow Solar System Symposium*, volume 3, Moscow, Russia, 2012b.

(Grumpe et al., 2012c) A. Grumpe, V. Zirin, F. Belkhir, and C. Wöhler. Normalisation of Continuum-removed Lunar Spectra. In *Proc. 1st European Lunar Symposium*, Berlin, Germany, 2012c.

(Wöhler and Grumpe, 2012) C. Wöhler and A. Grumpe. Correction of Chandrayaan-1 M^3 Lunar Hyperspectral Image Data with Respect to Local Topography. In *Lunar and Planetary Science Conference*, volume 43 of *Lunar and Planetary Inst. Technical Report*, page #1906, 2012.

(Herbort et al., 2011) S. Herbort, A. Grumpe, and C. Wöhler. Reconstruction of non-Lambertian surfaces by fusion of Shape from Shading and active range scanning. In *Proc. 18th International Conference on Image Processing (ICIP), Invited contribution*, pages 17–20, Brussels, Belgium, 2011. IEEE. doi: 10.1109/ICIP.2011.6115812.

(Grumpe et al., 2011a) A. Grumpe, F. Brinkmeier, and C. Wöhler. Analysis of Topographic Effects Observed in Spectral Features Extracted from Chandrayaan-1 M3 Imagery. In *Lunar and Planetary Science Conference*, volume 42 of *Lunar and Planetary Inst. Technical Report*, page #1484, 2011a.

(Grumpe et al., 2011b) A. Grumpe, S. Herbort, and C. Wöhler. 3D Reconstruction of Non-Lambertian Surfaces with Non-Uniform Reflectance Parameters by Fusion of Photometrically Estimated Surface Normal Data with Active Range Scanner Data. In T. Luhman and C. Müller, editors, *Photogrammetrie - Laserscanning - Optische 3D-Messtechnik. Beiträge der Oldenburger 3D-Tage*, pages 54–61. Wichmann, 2011b.

(Grumpe and Wöhler, 2011a) A. Grumpe and C. Wöhler. DEM construction and calibration of hyperspectral image data using pairs of radiance images. In *7th International Symposium on Image and Signal Processing and Analysis (ISPA)*, pages 609–614. IEEE, 2011a.

(Grumpe and Wöhler, 2011b) A. Grumpe and C. Wöhler. A Photometric Approach to the Construction of Lunar Digital Elevation Maps Using Chandrayaan-1 M3 Imagery in Combination with Laser Altimetry Data. In *Lunar and Planetary Science Conference*, volume 42 of *Lunar and Planetary Inst. Technical Report*, page #1478, 2011b.

Contents

Contents **xi**

1 Introduction **1**
1.1 Lunar hyperspectral imagery 1
1.2 Motivation 3
1.3 Contribution 3

2 Related work: Normalisation of (hyper-)spectral data **5**
2.1 Instruments and datasets 5
2.1.1 (Hyper-)spectral instruments 6
2.1.2 Digital elevation models (DEM) 9
2.2 Sensor calibration 11
2.2.1 Radiometric calibration 12
2.2.2 Photometric normalisation 12
2.3 Reflectance modelling 15
2.3.1 Terminology and definitions 15
2.3.2 Commonly used models 17
2.3.3 The Hapke model 18
2.4 Thermal emission 19
2.4.1 Simulation based approaches 20
2.4.2 Published M^3 temperature estimation (Clark et al., 2011) 21

3 Related work: Photometric surface reconstruction **23**
3.1 Intensity based surface reconstruction 23
3.2 Fusion with depth data 25

3.3 Reference methods 28
3.3.1 DEM from gradient estimates according to Horn (1990) 28
3.3.2 Shape from shading (SfS) according to Horn (1990) 29
3.3.3 Additional DEM constraint according to Shao et al. (1991) 31

4 Contribution: Normalisation of (hyper-)spectral data 33
4.1 Thermal emission 34
4.1.1 Surface temperature estimation 34
4.1.2 Results 37
4.2 Reflectance parameter estimation 38
4.2.1 General problem formulation 38
4.2.2 Hapke based normalisation 40
4.2.3 Results 45
4.3 Phase angle/Sensor temperature based effects 53
4.3.1 Dataset and data processing 54
4.3.2 CR based correction method 58
4.3.3 Radiance based correction method 58
4.3.4 Results 66

5 Contribution: Photometric surface reconstruction 73
5.1 Terminology 73
5.2 Relative depth constraint 74
5.2.1 Relative depth error term 75
5.2.2 Extended photoclinometry method (PHCL) 77
5.2.3 Extended shape from shading method (SfS) 79
5.2.4 Reconstruction method 82
5.3 Absolute depth constraint 83
5.3.1 Absolute depth error term 83
5.3.2 Depth from gradient field 85
5.3.3 Stopping criteria 90
5.3.4 Further extended SfS method 91
5.4 The reconstruction algorithm 93
5.5 Results 94
5.5.1 Relative depth constraint 94
5.5.2 Absolute depth constraint 105

6 Application scenarios 129
6.1 Photometrically corrected near-global mosaic 129
6.2 Mapping elemental abundances 133

6.2.1 Spectral parameters . . . 133
6.2.2 Construction of elemental abundance maps . . . 135
6.2.3 Construction of petrographic maps . . . 140
6.3 Illumination independent image registration . . . 143
6.3.1 Overview . . . 144
6.3.2 Alignment measures . . . 145
6.3.3 Transformations . . . 148
6.3.4 Evaluation . . . 148
6.4 Narrow-Angle Camera (NAC) derived DEM of highest resolution . . . 153

7 Outlook **161**

8 Summary and conclusion **163**

Bibliography **167**

List of Figures **185**

List of Tables **189**

List of Symbols **191**

A Levenberg-Marquardt Optimisation **I**

B Calculus of Variations **V**

1

Introduction

Optical devices have become widely used sensors, and optical measurements have become standard tools for non-invasive object analysis in industrial and scientific applications, remote sensing, industrial quality control and robotics. They are applicable of the object under study is not to be modified or simply inaccessible. Additionally, image based methods provide a vast amount of information over the whole image area and thus may replace an impractical amount of probing. There are two important common applications. The former analysis the object's shape based on the spatial reflectance distribution, while the latter analysis the spectral reflectance properties of the object, i.e. the objects colour, to derive information on physical object properties, e.g. quality assessment of butter cookies (Andresen et al., 2013) or the mineralogical composition of lunar rocks (Schmidt et al., 2014). Commonly, work focuses on either extracting the shape of the object or analysing the spectral reflectance distribution, while spectral imagery may contain both and the object's shape as a matter of fact influences both. Consequently, this thesis aims at an integrated analysis of the spatial and the spectral reflectance distribution recovering the object's shape from the spatial reflectance and normalising the spectral reflectance with respect to the object's shape.

1.1 Lunar hyperspectral imagery

The earth's moon has been of scientific interest for a long time and thus a wealth of measurements, especially orbital measurements covering nearly the global lunar surface, exists and is publicly available. These measurements include (but are not limited to) high resolution topographic models derived from stereo analysis and laser altimetry, (hyperspectral) reflectance measurements and elemental abundances measured by gamma ray spectrometers. Furthermore, there are physically motivated models describing the reflectance properties of the lunar surface (Shkuratov et al., 1999a,b; Hapke, 1981, 1984, 1986, 2002). The lunar surface is thus an ideal target for the development of methods.

According to Shkuratov et al. (2011), optical measurements of the lunar surface can be sub-divided into three categories: Phase photometry, Spectrophotometry and Polarimetry.

Polarimetry aims at the derivation of physical objects properties based on the polarisation properties of the reflected light. Since it is of no importance to this thesis, the dedicated reader may refer to Shkuratov et al. (2011) for information on polarimetry.

Phase photometry deals with reflectance measurements at the same wavelength range but different illumination conditions, i.e. different incidence, emission and phase angles. Consequently, the reflectance behaviour, i.e. the observed reflectance under different illumination conditions, of the lunar surface has been studied and models were developed. The most prominent models are those by (Hapke, 1981) and Shkuratov et al. (1999a). Since the incidence and emission angles change with the local topography of the lunar surface, the change in reflectance, i.e. the shading, provides clues on the local topography. Consequently, it is possible to recover the shape of the lunar surface from the shading observed in reflectance images as proposed by van Diggelen (1951), Wildey (1975), Horn (1975) and Kirk (1987).

Spectrophotometry analysis the spectral reflectance to derive the mineralogical and/or elemental composition of the lunar surface. The main minerals of the lunar surface are plagioclase feldspars, pyroxenes, olivine and ilmenite (Heiken et al., 1991). The bright highland material is predominated by the plagioclase feldspars, which were mainly identified based on their brightness (Shkuratov et al., 2011). The other minerals compose the dark maria regions. Due to transitions of the element iron, Fe^{2+} to be precise, these minerals exhibit crystal field absorption bands at characteristic wavelengths (Burns, 1993). Cloutis and Gaffey (1993) present laboratory spectra of lunar analogue minerals in the range 300 nm to 2600 nm of plagioclase (absorption band near 1300 nm), ilmenite (no band visible), pyroxenes (bands near 930 nm and near 1950 nm) and olivine (triple band resulting in a broad absorption band near 1050 nm). Similarly, McCord et al. (1972) present telescope-based measurements of lunar mare, highland, and bright crater areas. Burns et al. (1972) and Adams (1974) show that different pyroxenes may be distinguished by the position of the absorption bands. These spectral absorptions have been used to identify minerals in telescope-based reflectance spectra and later orbiter-based reflectance measurements. The identified components include impact melt (e.g. Smrekar and Pieters, 1985), spinel (e.g. Cloutis et al., 2004) and hydroxyl (e.g. Pieters et al., 2009b). Charette et al. (1974) quantified the absorptions using ratios of images at characteristic wavelengths, and showed that the wavelength ratio images are correlated to the titanium dioxide content. Mapping the titanium content has been continued by Melendrez et al. (1994) using telescope data and Lucey et al. (1998) using the Clementine orbiter multispectral imagery. In addition to titanium dioxide, Lucey et al. (1995); Lucey et al. (1998, 2000) estimate the iron oxide content based on wavelength ratios. Later Shkuratov et al. (2005a) and Wöhler et al. (2011) proposed different approaches to map the spectral reflectance onto elemental abundance values measured by a gamma ray spectrometer.

1.2 Motivation

It is well known, that the topography has an influence on the observed reflectance spectra. This influence is not compensated by ratios, i.e. the effect is wavelength dependent. It was noted by Robinson and Jolliff (2002) that the shaded walls of lunar craters contained anomalously high percent of weight (wt%) elemental Iron (Fe) abundance estimates. The effect increased towards the lunar poles, where the northern or southern crater wall is always shaded. Robinson and Jolliff (2002) quantified that the Iron oxide (FeO) and Titanium dioxide (TiO_2) abundance maps derived from Clementine data showed an absolute difference of as much as 5 wt% (FeO) and 4 wt% (TiO_2) on 30 ° slopes. The strength of the effect varies over shaded and sun-facing areas. It is, however, stronger on shaded areas.

Additionally, the assumption of global parameters of the reflectance model leads to the selection problem as mentioned by Hillier et al. (1999). Due to the typical nadir-view of orbiter cameras, the phase angle equals the incidence angle and thus measurements acquired at higher phase angles typically correspond to surface areas of higher selenographic latitude. Consequently, different measurements along the range of phase angles most likely represent surface materials of different mineralogical composition.

To compensate the aforementioned effects, a topographic model, preferably of better lateral resolution than the image data, and methods to estimate spatially varying parameters of the reflectance model are required. The estimation of local reflectance properties and high resolution topographic models is the target of photometric methods, e.g. photoclinometry (Kirk et al., 2003a) and shape from shading (Horn, 1990). Using the shading variations along the lateral coordinate axes, the inclination of the surface and thus its gradient field may be retrieved from reflectance measurements.

This thesis aims at the combination of photometric shading and spectral information, i.e. the information along the lateral coordinate axes and the information along the spectral direction, by using photometric methods to extract the topography and the reflectance model that is necessary for the normalisation of the spectral data. The coupled estimation of topography and reflectance parameters obtains a self-consistent solution with spatially varying reflectance model parameters.

1.3 Contribution

Within this thesis, an integrated approach to the photometric surface refinement and the photometric normalisation is presented.

The normalisation procedure estimates the surface temperature, compensates the thermal emission component and applies a photometric normalisation to the measured radiance data. Topographic effects are corrected using the co-registered high resolution digital elevation models computed using the shading clues from the optical image and the devel-

oped extensions to the classic shape from shading problem. The normalisation procedure explicitly deals with spatially varying reflectance parameters by estimating maps of the reflectance model parameters that are co-registered to the images.

The developed surface refinement methods combine classic shape from shading methods with measured depth data of lower lateral resolution introducing a relative depth constraint and an absolute depth constraint to the optimisation problem. The relative depth constraint influences the surface gradient estimation step and aims at the suppression of errors before the integration step, i.e. the accumulation of systematic errors. It is, however, not possible to cover all causes of systematic errors, e.g. imperfect radiance calibrations. Thus, an absolute depth constraint is added to the surface gradient integration step which forces the refined to add only high frequent details and keep the low frequent information.

The developed techniques are applied to derive a near-global Moon Mineralogy Mapper mosaic. Based on this mosaic, a regression method is applied to map parameters of the spectral absorption bands onto elemental abundances measured by the Lunar Prospector Gamma-Ray Spectrometer. To obtain co-registered images, an illumination independent image registration method is developed based on the recovered elevation models, which, by definition, are co-registered to the original image. Finally, the photometric surface refinement methods are applied to Lunar Orbiter Narrow Angle Camera images to derive to elevation models of the highest possible resolution.

2

Related work: Normalisation of (hyper-)spectral data

In general, spectral sensors measure a value, the so-called sensor counts, which is a possibly non-linear function of the radiance reflected from a target object into the sensor. To derive the reflectance, the sensor values require a conversion, the so-called radiance calibration. The reflectance, however, highly depends on the observation geometry, i.e. the orientation of the local topography of the object's surface, the position of the light source and the viewing direction of the observer. A normalised reflectance is thus computed by the so-called photometric normalisation or photometric correction.

At first, an overview on the recent instruments measuring the lunar reflectance and the lunar topography is given in Section 2.1. The calibration and normalisation of the datasets are then described in Section 2.2. Section 2.3 details common reflectance models for the photometric normalisation. The measured radiance is composed of the radiance reflected by the object and, especially at higher wavelengths ($> 2800\,\mathrm{nm}$), the thermal irradiation of the object. Consequently, methods estimating the thermal component of the radiance are given in Section 2.4.

This chapter has been adapted and/or adopted from: (Grumpe et al., 2014a; Wöhler and Grumpe, 2013)

2.1 Instruments and datasets

This section provides an overview over available datasets. Each spectral sensor/instrument has its unique wavelength range and spectral resolution. The available spectral data is reviewed in Section 2.1.1. In order to normalise the spectral data with respect to local surface topography, digital elevation models (DEM) are required. The corresponding instruments are introduced in Section 2.1.2.

2.1.1 (Hyper-)spectral instruments

An extensive overview of the recent (hyper-)spectral measurements of the lunar surface is provided by Pieters et al. (2013), Besse et al. (2013b) and Ohtake et al. (2013). In general, there are two distinct groups of spectral sensors. The first group measures only one footprint at a time and creates a spectral profile along the track. They are thus referred to as "profile based instruments". The second group acquires complete images at distinct wavelength ranges and are referred to as "image based instruments". The former commonly feature a very high spectral resolution while the latter yield a better lateral resolution at the cost of spectral resolution. For completeness, a brief introduction of all recent spectral instruments is given. The normalisation of spectral data, however, requires the knowledge of the local surface topography (cf. Section 2.2), while the methods for the recovery of the local surface topography developed in this thesis require images (cf. Chapter 5). Consequently, this thesis is based on an image based instrument, namely the Moon Mineralogy Mapper, which is described in detail at the end of this section. Notably, all methods may be applied to profile based sensors after co-registration on image based sensors (e.g. Grumpe et al., 2013) which, however, increases the complexity of the problem and is thus not regarded in this thesis.

Profile based instruments

The SIR-2 instrument (Mall et al., 2009), a near-infrared grating spectrometer, was part of the payload of the Indian spacecraft Chandrayaan-1. The spectrometer measured the spectral radiance in 256 bands within the interval 940 nm–2400 nm using a single detector. The spectral sampling distance between adjacent bands was about 6 nm. The field of view was 0.127 ° which corresponds to a footprint size of about 220 m at the nominal 100 km orbit. Due to its active cooling system and control, the SIR-2 instrument had an extremely stable detector temperature.

The Spectral Profiler (SP) is a grating spectrometer carried by the Japanese spacecraft SELENE (Yamamoto et al., 2011). It consists of two gratings and three detectors for the visible (VIS: 500 nm–1000 nm) and the near-infrared (NIR1: 900 nm–1700 nm, NIR2: 1700 nm–2600 nm) wavelength ranges. Consequently, it covers the wavelength range 500 nm–2600 nm spread over 162 bands at a spectral sampling distance of 6 nm–8 nm. The field of view is 0.23 ° which corresponds to a footprint size of about 500 m.

Image based instruments

The Clementine Mission (e.g. Nozette et al., 1994; Eliason et al., 1998) acquired a global multispectral dataset of the lunar surface. In contrast to Earth based measurements, the spectral resolution was quite low while the lateral resolution was greatly increased and, more importantly, the orbital measurements enabled the mapping of the lunar far side. The acquired multispectral dataset consisted of 11 bands spread over two different

cameras. The first camera acquired data in the ultraviolet-visible (UVVIS) wavelength range, i.e. five bands centred at 415 nm, 750 nm, 900 nm, 950 nm and 1000 nm, while the second camera acquired data in the near-infrared (NIR) wavelength range, i.e. six bands centred at 1100 nm, 1250 nm, 1500 nm, 2000 nm, 2600 nm, and 2780 nm. The lateral resolution of the measurements was 100 m–300 m per pixel. Due to the low spectral resolution, the Clementine dataset is almost outdated with the release of more recent datasets. It is, however, the first global multispectral dataset of the lunar surface.

The Multiband Imager (MI) is a high resolution multiband push broom camera onboard SELENE (Ohtake et al., 2008, 2010). It consists of two detector arrays with a total of nine spectral bands. The visible wavelength range is covered by five channels (VIS: 415 nm, 750 nm, 900 nm, 950 nm, 1000 nm) and the near infrared wavelength range is covered by four channels (NIR: 1000 nm, 1050 nm, 1250 nm, 1550 nm). The corresponding spatial resolution is 20 m per pixel for the VIS detector and 62 m per pixel for the NIR detector.

The Robotic Lunar Observatory (ROLO) is designed for and dedicated to radiometric measurements of the Earth's moon (Kieffer and Stone, 2005). The idea behind the ROLO program is the use of the Moon's reflectance in in-flight calibrations of instruments. Due to the Moon rotating around its axis at the same rate as it travels around the Earth, only the Near Side of the Moon's surface is visible. The telescope measurements, however, are taken at well defined environment, e.g. stable and continuous sensor temperatures ensured by liquid nitrogen cooling, which are not met in orbital measurements. The wavelength range 350 nm–2500 nm is covered by two different detectors for the Visible–Near Infrared (VNIR) and the Shortwave Infrared (SWIR), respectively. The 32 measured bands are divided into 23 VNIR bands and nine SWIR bands limited by interference filters of different widths. The spatial resolution is about 7.1 km per pixel in the VNIR and 14.3 km per pixel in the SWIR (Besse et al., 2013b), respectively.

The Lunar Reconnaissance Orbiter Camera (LROC) (Robinson et al., 2010) consists of two different imaging devices. The Wide Angle Camera (WAC) is a push broom camera with seven colour channels (315 nm, 360 nm, 415 nm, 566 nm, 604 nm, 643 nm, 689 nm). All colour channels are projected onto a single CCD sensor. It has a 90 ° field of view in monochrome mode and a 60 ° field of view in colour mode. The WAC images are acquired at a resolution of 100 m per pixel from the nominal 50 km orbit. The Narrow Angle Camera (NAC) consists of two cameras, namely the left and the right NAC, that provide images at a resolution of 0.5 m–2.0 m per pixel. Each NAC has a field of view of 2.86 ° and its own line scan CCD sensor. Both NAC are combined to create a 5.7 ° field of view which corresponds to an image width of 5 km from the nominal 50 km orbit.

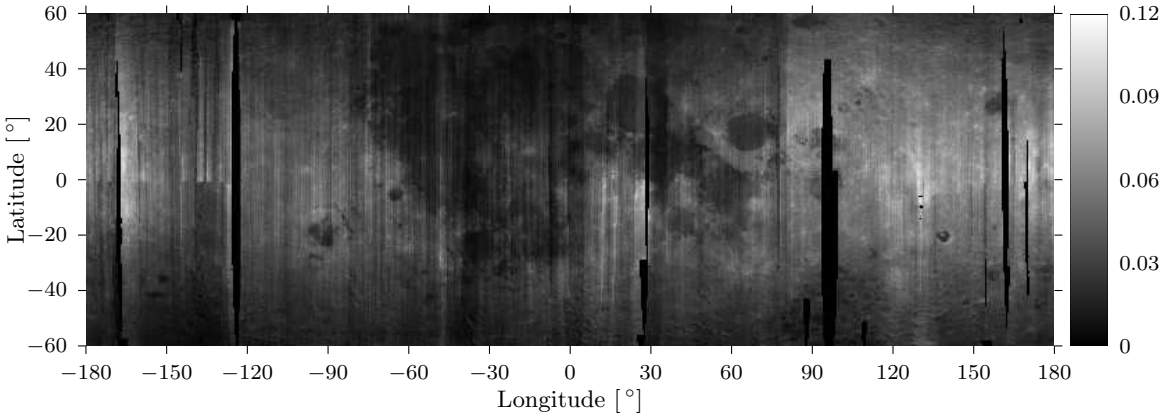

(a) Mean M^3 reflectance.

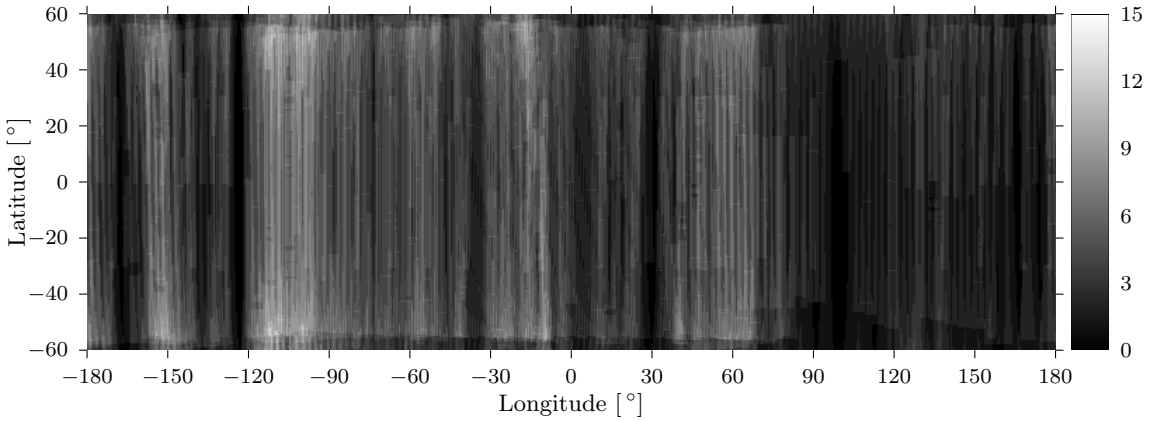

(b) Amount of overlapping images.

Figure 2.1: Global M^3 mosaic at 2 pixels per degree resolution. The mosaic is limited to ±60 °. (a) Mean reflectance at 1579 nm. (b) Number of available images for each region.

The Moon Mineralogy Mapper

A recently released hyper-spectral data set of the Moon has been obtained by the Moon Mineralogy Mapper (M^3) instrument[1] carried by the Indian spacecraft Chandrayaan-1. According to Pieters et al. (2009a), the M^3 sensor is a push broom camera which scans lines with a ground pixel size of about 140 m. In the so called "global mode", it provides 85 channels measuring the spectral radiance in the range between 450 nm and 3000 nm. The filter width of each channel is about 10 nm. There is also a so-called "target mode" of higher spectral resolution. However, its coverage is limited to a few

[1]Available at http://moonmineralogymapper.jpl.nasa.gov/

regions of interest. Thus, this thesis is restricted to the global mode measurements. The M^3 radiance data are accompanied by the spectral solar irradiance, the coordinates of each pixel in selenographic longitude and latitude, and, pixel-wise, the solar distance, the solar zenith and azimuth angles with respect to a spherical body, as well as the direction toward the spacecraft. These angles and derived vectors allow the computation of all necessary angles with respect to an arbitrary surface normal.

The M^3 images are published as measured by the push broom sensor, i.e. as a concatenation of scan-lines. The spatial distance between two subsequent scan-lines is not constant. Furthermore, the DEM construction methods (cf. Chapter 5) are based on a cylindrical projection of the spherical body which spans a rectangular grid, i.e. the selenographic longitude is the first unit vector and the selenographic latitude is the second unit vector. The data is thus remapped to the selenographic coordinate system using a fixed grid with 300 pixels per degree latitude and longitude, respectively. This corresponds to about 100 m per pixel and avoids sub-sampling effects. Interpolation is performed using the natural neighbour method (Sibson, 1981).

Fig. 2.1(a) shows a near-global mosaic of the reflectance averaged over all M^3 images at 1579 nm at a resolution of 2 pixels per degree longitude and latitude. In all images, north is on top unless indicated otherwise. The near-global mosaic extends to a latitude of $\pm 60\,^\circ$. The brightness variations are due to different illumination conditions and missing spectral normalisation. The corresponding number of co-registered images, i.e. the amount of different observations of the same surface, from different orbits is shown in Fig. 2.1(b). Notably, there are regions where only one observation is available. The full spatial resolution is illustrated by Fig. 2.2(a) showing a remapped M^3 image of the crater Aristarchus (longitude 312 °E–314 °E, latitude 22 °N–26 °N).

2.1.2 Digital elevation models (DEM)

Two global topographic datasets have recently been published, namely the Lunar Orbiter Laser Altimeter (LOLA) DEM[2] (Smith et al., 2010; Zuber et al., 2010) and the "near-global lunar 100 m raster DEM"[3] (GLD100) (Scholten et al., 2012).

The Lunar Orbiter Laser Altimeter (LOLA) carried by the Lunar Reconnaissance Orbiter (LRO) spacecraft provides time-of-flight range measurements. Based on ground truth measurements, the standard deviation of the one-way laser ranging is 0.1 m (Riris et al., 2009). This precision is significantly higher than the capability to track the spacecraft's orbit (Zuber et al., 2010). According to Zuber et al. (2010), the precision of ± 0.1 m is achieved only for the polar topography measurements while the global depth error is higher than ± 1 m at a lateral resolution of 50 m along the measured track. A gridded global DEM has been derived by binning the point measurements and interpolating empty

[2]Available at http://lunar.gsfc.nasa.gov/lola/

[3]Available at http://wms.lroc.asu.edu/lroc/global_product/100_mpp_DEM

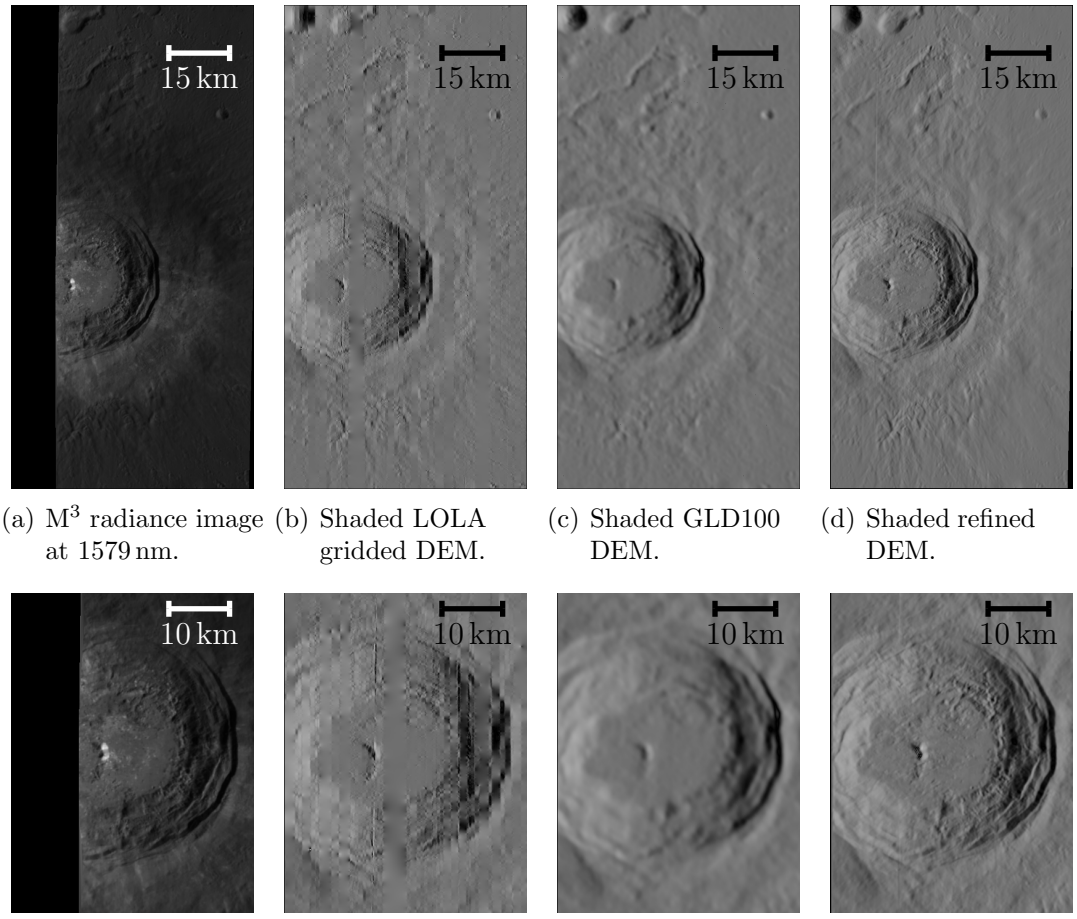

(a) M^3 radiance image at 1579 nm. (b) Shaded LOLA gridded DEM. (c) Shaded GLD100 DEM. (d) Shaded refined DEM.

(e) M^3 radiance image at 1579 nm. (f) Shaded LOLA gridded DEM. (g) Shaded GLD100 DEM. (h) Shaded refined DEM.

Figure 2.2: Comparison of datasets. The DEM are rendered using the Hapke IMSA model with a constant single-scattering albedo of $w = 0.4$. The incidence angle corresponds to 60 °. (a)–(d) Region around the crater Aristarchus (longitude 312 °E–314 °E, latitude 22 °N–26 °N, diameter: 41 km). (e)–(h) Close-up view of the crater. M^3 Image credit: NASA/JPL-Caltech

bins, which shows interpolation artefacts between different tracks (Neumann, 2010). The global DEM published at a lateral resolution of 512 pixels per degree, which corresponds to about 60 m per pixel near the lunar equator, is used for the DEM refinement (cf. Chapter 5). The regions of interest are cropped from the original map and resized to the 300 pixels per degree resolution of the remapped M^3 data. The shaded LOLA DEM of the crater Aristarchus is shown in Fig. 2.2(b) and clearly reveals interpolation artefacts. Hence, the effective lateral resolution is lower than the 100 m of the grid. Due to the very

high accuracy, the single-point measurements are used as ground truth and the refined DEM are compared to these (cf. Section 5.5).

Similar to LOLA, a laser altimeter (LALT) carried by the Japanese spacecraft SELENE measured the topography of the lunar surface (Araki et al., 2009). The footprint size was about 40 m and thus the resolution is somewhat lower than the resolution of LOLA. Furthermore, the instrument precision of ± 0.55 m results in a total accuracy of ± 4.1 m after considering the positioning errors (Araki et al., 2009). LALT thus does not match the precision of LOLA. Consequently, the LALT dataset is not further considered in this thesis.

The Global Lunar DEM 100 m topographic model (GLD100) is a nearly global DEM obtained by stereo analysis of images taken by the Wide Angle Camera (WAC) carried by LRO. The nominal resolution of the GLD100 is 100 m per pixel (Scholten et al., 2012). The regions of interest are extracted from the global GLD100 data and remapped to the M^3 grid. Fig. 2.2(c) shows the shaded GLD100 for the crater Aristarchus. Due to the area-based correspondence matching approach inherent to the employed stereo analysis method, small-scale features with an extent of less than 1.5 km are likely to be not or inaccurately represented within the GLD100 data (Scholten et al., 2012), such that the effective lateral resolution of the GLD100 is significantly lower than the resolution of the M^3 hyper-spectral data. Recently, a technique to increase the lateral resolution and the absolute accuracy by using the angular distance between different colour channels, i.e. using every colour channel as an independent image at a different viewing direction, has been presented by Korokhin et al. (2014). Their data, however, is not available on a global scale.

In summary, all available global lunar DEM do not share the lateral resolution of the M^3 hyper-spectral data. Therefore, photometric methods that aim to increase the lateral DEM resolution to the resolution of the M^3 data are required (cf. Chapter 5). The result for the crater Aristarchus is presented in Fig. 2.2(d).

2.2 Sensor calibration

In order to interpret the measured values of the spectral instruments, the sensor counts need to be converted to physically meaningful values. The so-called radiometric calibration thus depends highly on the corresponding hardware. The common steps of the radiometric calibration are given in Section 2.2.1. The result, typically a radiance value, then needs to be converted to reflectance and, in order to be comparable to different measurements, needs to be normalised with respect to the illumination geometry. The normalisation procedure is described in Section 2.2.2

2.2.1 Radiometric calibration

Typically, optical sensors are built up of a telescope or a different optic element to capture the light reflected from the surface spot of interest. The captured light is then split into different wavelength intervals, e.g. using a grating, a prism or different filters. Finally, the desired fraction of the incident light falls onto a photo-detector and the resulting current is measured and digitised using electronic components. Notably, there may be different photo-detectors for different wavelengths resulting in a complex cross-calibration problem. The measured digits, i.e. the sensor counts, depend on the incident light, however, all parts in the chain may influence the sensor reading. The calibration is thus highly sensor specific and out of the scope of this thesis.

In general, the detector elements, i.e. the semiconductors, have a dark current and possibly varying sensitivity. The calibration steps thus include dark frame and flat field corrections, i.e. the dark signal is subtracted and the sensitivity/gain is corrected by a factor. Furthermore, the quantity of light reaching the detector is influenced by the exposure time, i.e. the time interval where the photo detector is exposed to the incident light. Other steps are the conversion from measured quantities to physical quantities, commonly radiance values, and the correction of possibly non-linear effects of the sensor elements.

Details about the corresponding sensor calibrations are given in:

SIR-2	(Mall et al., 2009)
Spectral Profiler	(Yamamoto et al., 2011)
Clementine UVVIS	(McEwen et al., 1998)
Moon Mineralogy Mapper	(Green et al., 2011)
Multiband Imager	(Kodama et al., 2010)
ROLO	(Kieffer and Stone, 2005)
LROC	(Robinson et al., 2010)

2.2.2 Photometric normalisation

The radiometric calibration yields radiance values. In order to interpret the surface properties, the surface's reflectance needs to be recovered from the measured radiance. This is commonly achieved by division by the incident light flux, i.e. the solar irradiance, normalised to the target distance from the sun. The resulting apparent reflectance still depends on the illumination geometry, i.e. the sun position, the viewing direction and the local surface topography. The compensation of this geometric effect is the goal of the photometric normalisation.

In order to normalise the Clementine data, McEwen et al. (1998) applied a modified model of McEwen (1991, 1996), i.e. a product of a phase angle dependent function and the Lommel-Seeliger law. In order to approximate multiple scattering, a Lambertian reflectance term weighted by one minus the phase angle dependent function was added.

The phase angle dependent function was set to be a third order polynomial with global coefficients. The local surface topography was neglected and a perfect sphere of the lunar radius was used to compute the geometric angles. The normalised reflectance values resulting from this official calibration method with respect to a Halon standard were distributed on the internet, however, they were found to be systematically increased. Later, Hillier et al. (1999) recalibrated the Clementine dataset with respect to the Apollo landing sites and provided fits of the Hapke model (Hapke, 1981, 1984, 1986). The Hapke model, however, was extended to cover the coherent back scatter opposition effect which was not included before the later improvement by Hapke (2002).

This pioneering work influenced all the later instrument normalisations. Yokota et al. (2011) applied the model of McEwen (1991) to the SP data. The coefficients of the phase angle dependent polynomial were determined for the dark Mare regions and the bright Highland regions, separately. For each region, two sets of coefficients, i.e. for small and for large phase angles, were determined, respectively. Again, the local topography was neglected and a spherical model of the lunar surface was applied.

Analogously, Ohtake et al. (2008) normalised the MI data using the photometric model of McEwen (1991). Unlike the SP normalisation, the photometric MI normalisation is implemented with multiple options. One option is the assumption of a spherical lunar model without local topography. The option chosen by Ohtake et al. (2010), in contrast, uses image matching within the the different MI bands to derive a local topography model, i.e. applying stereo analysis using the maximum angular distance between the MI bands of about 11 ° while the minimum angular distance is 3 °–4 °. A similar photogrammetric technique is applied to the WAC data by Korokhin et al. (2014).

The ROLO measurements were distorted by the Earth's atmosphere, e.g. light diffusely scattered by the atmosphere. Thus, Kieffer and Stone (2005) applied a statistical correction for the influence of the atmosphere. Additionally, Kieffer and Stone (2005) found the physically based models inappropriate, i.e. the residual was considerably larger than the observational noise. The residual of the model by Shkuratov et al. (1999b) was 4% and the dependence on the parameters was quite complex. Thus, Kieffer and Stone (2005) did not attempt to make the non-linear unknowns a function of the so-called libration, i.e. small oscillating movements of the Moon with respect to the point of observation were neglected. The integral phase functions as modelled by Hapke (1993) were not investigated. Consequently, Kieffer and Stone (2005) developed their own empirical model consisting of four polynomials describing the dependence on the phase angle neglecting opposition effects, the distribution of dark maria and bright highlands, the face of the Moon that is seen and a strictly empirical polynomial, respectively.

To normalise the SIR-2 data, Mall et al. (2010) use the physically motivated model by Shkuratov et al. (1999b). The normalised reflectance is obtained by multiplying the measured reflectance by the ratio of the photometric model evaluated at target illumination and viewing geometry to the photometric model evaluated at the actual illumination and viewing geometry. The photometric model is composed of a product of the so-called

disk function, describing the Earth-based brightness distribution over the lunar disk, and a phase angle dependent function. The disk function is adopted from Akimov (1988) and Akimov et al. (2000). The phase dependency is computed using the so-called equigonal albedo model adopted from Korokhin et al. (2007) and Velikodsky et al. (2010). Mall et al. (2010) do not mention the topography model used to derive the incidence and emittance angles.

In case of the M^3, the normalisation is somewhat more complicated. Due to the loss of its star sensors, the position and orientation of Chandrayaan–1 was not accurately known. In order to co-register the images, Boardman et al. (2011) used a shaded version of the gridded LOLA DEM and overlapping M^3 images to create a consistent positioning in the LRO coordinate system. The reflectance was then normalised by Hicks et al. (2011). Following the reasoning of McEwen (1991), a product of the Lommel-Seeliger law and a phase angle dependent function was applied. The Lambertian term approximating the multiple scattering was omitted. The phase angle dependent function, again, was modelled by a polynomial. One set of coefficients of the sixth-order polynomial was computed for the Mare and the Highland regions, respectively. To compensate topographic artefacts, the local incidence and emittance angles were computed based on the gridded LOLA DEM. Later, it became known that the sensor temperature had a large influence on the measured reflectance (Pieters et al., 2013; Besse et al., 2013a). The empirical correction approach is described in the technical note describing the software interface of the M^3 data (Lundeen et al., 2011). M^3 measurement ratios of the same area contained radiance artefacts if the sensor temperature during data acquisition was different. Lundeen et al. (2011) showed that these artefacts do not appear in images obtained at similar sensor temperature and that these artefacts are similar all over the lunar surface and thus not dependent on the observed surface properties. To compensate the sensor temperature, six co-registered images at different sensor temperatures in the range 147 K–168 K spanning almost the whole range of sensor temperatures during operation are selected. Based on the selected images, a correction factor was computed for each sensor temperature and each sensor channel, respectively. A linear model was fit to the correction factors to obtain a correction function with respect to the sensor temperature. In order to compensate the thermal emission of the surface (cf. Section 2.4), the magnitude of the correction was smoothly reduced from 2100 nm to longer wavelengths. Finally, Besse et al. (2013a) recomputed the model by Hicks et al. (2011) after applying the empirical correction. The order of the polynomial, however, was reduced to fourth-order and the coefficients were fit globally, i.e. there are no different sets for Mare and Highland regions. Due to the interpolation artefacts within the gridded LOLA DEM, Besse et al. (2013a) note that the amount of topography related artefacts increases towards the equatorial region. Simultaneously, Clark et al. (2011) developed a method to estimate the thermal emission of the surface. The method is described in detail in Section 2.4.2.

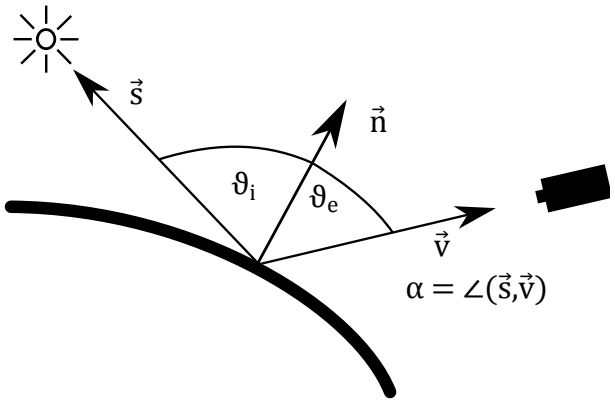

Figure 2.3: Illustration of the illumination and observation geometry.

2.3 Reflectance modelling

The observed reflectance of a surface changes with the light source position, the viewer position and/or orientation and the orientation of the surface normal, i.e. the viewing geometry. Since these effects are wavelength dependent and highly influence the interpretation of spectra, the normalisation of spectral data requires a model describing the dependence of the observed reflectance on the viewing geometry.

Section 2.3.1 summarises the terminology and definitions used in the later descriptions of the reflectance models. Common reflectance models are then summarised in Section 2.3.2 and the main model applied in this thesis is detailed in Section 2.3.3.

2.3.1 Terminology and definitions

The bidirectional reflectance R is the proportion of light emitted by a light source in the direction given by **s** incident on a surface with the surface normal **n** that is reflected into a camera in the direction **v**. The geometry is illustrated in Fig. 2.3, showing that the surface reflectance depends on the surface orientation, and knowledge of the reflectance behaviour of the surface allows thus the estimation of the surface orientation from reflectance measurements. The latter fact is important for the photometric methods reviewed in Chapter 3 and presented in Chapter 5. This section will review the physical quantities involved in the 3D surface reconstruction process.

The power per unit area incident on a surface illuminated by a light source is termed irradiance E. The corresponding physical unit is $\mathrm{W\,m^{-2}}$. According to the reflectance behaviour of the surface, a specific fraction of the light is reflected into the camera. This light fraction that is emitted by the surface and falls into the camera is called radiance L and is measured in $\mathrm{W\,m^{-2}\,sr^{-1}}$. If E or L are measured for a single wavelength λ, they are called spectral irradiance and spectral radiance, respectively (Hapke, 1981; Kieffer and

Stone, 2005). The mathematical relationship is

$$L = R\left(\mathbf{s}, \mathbf{v}, \mathbf{n}, \mathbf{\Psi}\right) \cdot E \tag{2.1}$$

where R is the bidirectional reflectance and $\mathbf{\Psi}$ is a vector containing surface properties, i.e. its colour or light scattering behaviour. In order to obtain the reflectance R, the observed spectral radiance needs to be divided by the irradiance. Often, the power per unit area E_{norm} emitted by the light source is known in some reference distance r_{ref}. As its decrease is proportional to the squared distance from the light source, Eq. (2.1) has to be modified to

$$L = R\left(\mathbf{s}, \mathbf{v}, \mathbf{n}, \mathbf{\Psi}\right) \cdot \frac{E_{\text{norm}}}{\left(\frac{r_s}{r_{\text{ref}}}\right)^2} \tag{2.2}$$

where r_s is the distance between the light source and the observed surface. While in general r_s depends on the shape of the surface, here it is assumed that the distance between surface and light source is much larger than the depth variations across the surface. The value of R depends on the orientation of the surface and thus contains information about the shape of the surface. In order to extract this information from the measured reflectance, a mathematical description in terms of a reflectance model is necessary.

The so-called "reflectance function" R of a surface (sometimes also termed "photometric function") is given by the ratio between the observed surface radiance L and the irradiance E. In general, the amount of light reflected from the surface depends on the the surface normal $\mathbf{n}$, the direction $\mathbf{s}$ to the light source, the direction $\mathbf{v}$ to the camera, and inherent surface properties (Horn, 1986). For planetary surfaces, where the intensity of the light reflected from the surface is independent of the azimuth angle of the light source, the reflectance function usually depends on the angle ϑ_i between the surface normal $\mathbf{n}$ and the direction $\mathbf{s}$ to the light source, the emission angle ϑ_e between $\mathbf{n}$ and the direction $\mathbf{v}$ to the camera, and on the phase angle α between the vectors $\mathbf{s}$ and $\mathbf{v}$ (Hapke, 1981). An illustration of these vectors and angles is provided by Fig. 2.3. The modelling of the reflectance is described in detail in Section 2.3.2 and Section 2.3.3. The following sections assume the existence of a reflectance model and focus on the reconstruction of the surface shape.

Another important term is the continuum-removed (CR) reflectance. The reflectance of a surface carries information on the mineral decomposition of the surface, e.g. different materials cause higher absorption at distinct wavelength. These absorption troughs are more or less shaped like a Gaussian (Farr et al., 1980). The depth of the absorptions troughs, however, is of the order of a few percent of the absolute reflectance. To produce a spectrum emphasising the absorption, the so-called continuum, i.e. a reflectance spectrum without any absorption, is computed and used as a reference. A typical approximation to the continuum is the convex hull of the reflectance spectrum (Fu et al., 2007). The CR spectrum is then obtained by dividing the reflectance spectrum by the convex hull.

2.3.2 Commonly used models

There are two distinct groups of models, namely empirical and analytical models. The empirical models, which are commonly used in photoclinometry and normalisation of spectral data, are reviewed by McEwen (1991). McEwen (1991) suggests a product of a functional depending on the phase angle and a Lommel-Seeliger law or a Minnaert function. The functional depending on the phase angle is set to be a wavelength dependent polynomial, as in the case of McEwen et al. (1998), Hicks et al. (2011) and Besse et al. (2013a).

The latter group consists of physically motivated, analytical functions. In case of the lunar surface the prominent models are Hapke (2002) and Shkuratov et al. (1999a). Both models are based on the reflection of one particle which is modelled as a slab. The overall reflectance is then estimated by adding first or higher order scattering between multiple particles in a layer of regolith. The difference between Hapke (1981) and Shkuratov et al. (1999a) is the modelling of the single-particle scattering function which is also termed "phase function" (Poulet et al., 2002). While Shkuratov et al. (1999a) predicts the functional, Hapke (1981) considers it a free parameter of the model. This also holds for Hapke (2002) which is an extension of higher order scattering to the original model. Additionally, Hapke (1984) proposed an extension to take into account the surface roughness unresolved by the detector. The proposed extension is valid for arbitrary reflectance models.

All methods rely on the knowledge of the surface topography. Thus, the method of choice needs to be applicable to the photometric methods given in Chapter 5. According to Bertsatos and Makris (2010), small-scale albedo changes dominate the photometric error and thus a simultaneous estimation of the reflectance parameters is necessary. Due to the typically large number of parameters, empirical modelling is not suitable for a simultaneous surface reconstruction and reflectance parameter estimation. Although it is possible to limit the parameters of the empirical models, e.g. by decreasing the order of the polynomial, the accuracy of the model decreases as well. Furthermore, the estimated parameters of the phase function are often global or semi-global estimates, such as in McEwen et al. (1998), Hicks et al. (2011) and Besse et al. (2013a), which contradicts the necessity for parameter estimation on small spatial scales. Furthermore, McEwen (1991) states that the Hapke model provides accurate fits to planetary surfaces and relates all regarded photometric functions to the model by Hapke (1981, 1984, 1986). The reason for using the Minnaert and Lommel-Seeliger laws is given by their low computational complexity. Efford (1991) shows that the empirical models do not cover the effect of macroscopic roughness and thus lead to biased topography profiles. In principle it is possible to apply the extension proposed by Hapke (1984) to the empirical models but the computational complexity is greatly increased. Hence, this thesis is based on the Hapke model which is detailed in the following section.

2.3.3 The Hapke model

A reflectance model commonly used for modelling the reflectance properties of planetary surfaces is the Hapke model R_{AMSA} (Hapke, 1981, 1984, 1986, 2002), which in its most advanced form proposed by Hapke (2002) is given by

$$R_{\mathrm{AMSA}}(\mu_0, \mu, \alpha) = \frac{w}{4\pi} \frac{\mu_0}{\mu_0 + \mu} \left[f_{\mathrm{phase}}(\alpha) B_{\mathrm{SH}}(\alpha) + M(\mu_0, \mu) \right] B_{\mathrm{CB}}(\alpha) \tag{2.3}$$

with $\mu_0 = \cos \vartheta_i$ and $\mu = \cos \vartheta_e$. The parameter w denotes the intrinsic reflectivity of a single surface particle and is therefore termed "single-scattering albedo" (Hapke, 1981). The term $M(\mu_0, \mu)$ in Eq. (2.3) is governed by the incidence angle and the emission angle but also depends non-linearly on the single-scattering albedo w. It models the multiple scattering component of the light reflected from the surface. The so-called "single-particle scattering function" $f_{\mathrm{phase}}(\alpha)$ describes the scattering behaviour of an individual particle. The "isotropic multiple scattering approximation" (IMSA) is regarded by Hapke (1981, 1986), while Hapke (2002) suggests the usage of the single particle scattering function $f_{\mathrm{phase}}(\alpha)$ to model the anisotropic scattering behaviour for a better multiple scattering approximation, resulting the "anisotropic multiple scattering approximation" (AMSA). Hapke (1984) introduces an approach that takes into account the macroscopic surface roughness, given by the average inclination angle $\bar{\theta}$ on spatial scales not resolved by the imaging device, for an arbitrary reflectance function.

For planetary surfaces consisting of porous regolith, the reflectance function displays a sharp peak around $\alpha = 0°$. This phenomenon is termed "opposition effect". It is partially due to shadow hiding, as holes in the porous regolith are filled by shadows for large phase angles which disappear for small phase angles (Hapke, 1986), and partially due to coherent backscattering as a consequence of constructive interference of multiply scattered light waves at small phase angles (Hapke, 2002). According to Hapke (2002), the function $B_{\mathrm{SH}}(\alpha)$ is given by

$$B_{\mathrm{SH}}(\alpha) = 1 + \frac{B_{\mathrm{SH}_0}}{1 + (1/h_{\mathrm{SH}}) \tan(\alpha/2)}. \tag{2.4}$$

The parameters B_{SH_0} and h_{SH} denote the strength and width of the shadow-hiding opposition effect, where $B_{\mathrm{SH}_0} \leq 1$. The more complex formulation of $B_{\mathrm{CB}}(\alpha)$ by Hapke (2002) includes two parameters B_{CB_0} and h_{CB}. However, unless very small phase angles below about 1° are covered by the observations, it is commonly impossible to separate the two components of the opposition effect from each other. In this case, the overall opposition effect is taken into account by neglecting the function $B_{\mathrm{CB}}(\alpha)$ in Eq. (2.4) and in turn allowing for values of B_{SH_0} beyond 1 (Warell, 2004).

In order to reduce the computational complexity, the less accurate R_{IMSA} proposed by Hapke (1986)

$$R_{\mathrm{IMSA}}(\mu_0, \mu, \alpha) = \frac{w}{4\pi} \frac{\mu_0}{\mu_0 + \mu} \left[f_{\mathrm{phase}}(\alpha) B_{\mathrm{SH}}(\alpha) + H(\mu_0) H(\mu) - 1 \right] \tag{2.5}$$

may be used for the photometric surface reconstruction. The effects are discussed in Section 5.5. Following the above reasoning, the opposition effects have been summarised in $B_{\mathrm{SH}}(\alpha)$. The function $H(x) = (1 + 2x)/(1 + 2\sqrt{1 - wx})$ is a first order approximation to the Chandrasekhar H-function (Chandrasekhar, 1960, pp. 105ff).

The single-particle scattering function $f_{\mathrm{phase}}(\alpha)$ is the most important parameter of the Hapke model as it governs the proportion of the incident light that is directly scattered into the imaging device and, more importantly, is part of the multiple scattering approximation within the Hapke AMSA model. A common choice of $f_{\mathrm{phase}}(\alpha)$ is the two-parameter Double Henyey-Greenstein (DHG) function

$$f_{\mathrm{DHG}}(\alpha) = \frac{1+c}{2}\frac{1-b^2}{(1+2b\cos\alpha+b^2)^{3/2}} + \frac{1-c}{2}\frac{1-b^2}{(1-2b\cos\alpha+b^2)^{3/2}} \tag{2.6}$$

(McGuire and Hapke, 1995; Hapke, 2002; Warell, 2004). However, the DHG only converges towards Rayleigh scattering for small particles if the forward and backward scattering lobes are equal (Cornette and Shanks, 1992). Hence, Cornette and Shanks (1992) developed the formulation of $f_{\mathrm{phase}}(\alpha)$ according to

$$f_{\mathrm{CS}}(\alpha) = \frac{3}{2}\frac{1-\xi^2}{2+\xi^2}\frac{1+\cos^2\alpha}{(1+\xi^2-2\xi\cos\alpha)^{3/2}}. \tag{2.7}$$

This model is convenient as the expression has the advantage of a physically reasonable convergence towards Rayleigh scattering for small particle sizes and the dependence on only a single parameter ξ. The latter is important if the scattering parameter is desired to be estimated from data. It reduces the number of model degrees of freedom and thus the amount of data necessary for parameter estimation.

2.4 Thermal emission

Since the reflectance is derived from radiance measurements and thus not measured directly, the measurements are influenced by all radiance components. Unfortunately, every surface emits thermal radiation which is added to the reflected irradiance of the sun. The temperature of the lunar surface ranges from about 40 K to 400 K. The latter produces thermal radiation in the measured wavelength range, i.e. at wavelengths of 2600 nm and above. The thermal radiation thus influences the estimation of the 2000 nm pyroxene absorption feature and needs to be removed from the measured radiance data. A general approach simulating the surface temperature based on thermal equilibrium is described in Section 2.4.1. The simulation, however, requires knowledge of the local surface topography. Additionally the computations are more complex the simple model of Clark et al. (2011). This data driven approach is described in 2.4.2.

2.4.1 Simulation based approaches

The radiation absorbed by a surface induces an increase of the surface energy, i.e. surface temperature. If the emitted energy equals the absorbed energy, i.e. thermal equilibrium is reached, the temperature does not change. Thus, neglecting head conductance, the power of the emitted thermal radiance of the surface equals the power of the absorbed solar irradiance.

The apparent brightness, i.e. the apparent radiance, of the surface amounts to

$$L_{\text{app}}(\mathbf{s}, \mathbf{v}, \mathbf{n}, \lambda, T) = E_{\text{sun}}(\lambda) R(\mathbf{s}, \mathbf{v}, \mathbf{n}, \lambda) + \beta(\mathbf{v}, \mathbf{n}, \lambda) B(\lambda, T) \tag{2.8}$$

where $\mathbf{s}$, $\mathbf{v}$ and $\mathbf{n}$ denote the direction towards the light source, the direction towards the observer and the surface normal, respectively. All elements may depend on the wavelength λ. $B(\lambda, T)$ is the emission spectrum of a black body of temperature T and $\beta(\mathbf{v}, \mathbf{n}, \lambda)$ is the directional emissivity. The component $\beta(\mathbf{v}, \mathbf{n}, \lambda) B(\lambda, T)$ thus models the thermal radiation emitted by the surface itself. In contrast, $E_{\text{sun}}(\lambda) R(\mathbf{s}, \mathbf{v}, \mathbf{n}, \lambda)$ describes the fraction of the solar irradiance $E_{\text{sun}}(\lambda)$ that is reflected into the observer. $R(\mathbf{s}, \mathbf{v}, \mathbf{n}, \lambda)$ is the bidirectional reflectance of the surface.

Assuming that no heat conductance within the lunar surface exists, the temperature T may be estimated using the Stefan-Boltzmann law (Shkuratov et al., 2011):

$$T = T_0 \sqrt[4]{(1 - A_{\text{dh}}) \cos \vartheta_i}. \tag{2.9}$$

$T_0 = \sqrt[4]{C_{\text{sun}} / \sigma_{\text{b}}}$ is the temperature of a surface area where $\beta = 1$ and the solar irradiance falls normally. $C_{\text{sun}} = 1367 \left[\frac{\text{W}}{\text{m}^2}\right]$ is the solar constant and $\sigma_{\text{b}} = 5.67 \cdot 10^{-8} \left[\frac{\text{W}}{\text{m}^2\text{K}^4}\right]$ is the Stefan-Boltzmann coefficient.

The directional-hemispherical albedo A_{dh} amounts to (Shkuratov et al., 2011):

$$A_{\text{dh}} = \frac{1}{C_{\text{sun}}} \int_{\lambda=0}^{\infty} E_{\text{sun}}(\lambda) R_{\text{dh}}(\vartheta_i, \lambda) d\lambda \tag{2.10}$$

where

$$R_{\text{dh}}(\vartheta_i, \lambda) = \frac{1}{\cos \vartheta_i} \int_{\Delta_{\text{azi}}=0}^{2\pi} \int_{\vartheta_e=0}^{\frac{\pi}{2}} R(\mathbf{s}, \mathbf{v}, \mathbf{n}, \lambda) \cos \vartheta_e \sin \vartheta_e d\vartheta_e d\Delta_{\text{azi}} \tag{2.11}$$

describes the fraction of the solar irradiance that is reflected into the whole upper hemisphere, i.e. the fraction of the solar irradiance that is not absorbed. The azimuth difference Δ_{azi} is the angle between the planes of incidence and scattering.

A more complex approach has been presented by Berezhnoy et al. (2012) who additionally consider the heat flux from the interior of the Moon, the solar radiation reflected from other parts of the surface and the thermal radiation of neighbouring surface areas.

Both methods, however, require a high resolution topographic map of the area of interest to accurately determine the components. According to Boardman et al. (2011), sufficiently high resolution topographic maps matching the lateral resolution of the M^3 data do not exist globally.

2.4.2 Published M^3 temperature estimation (Clark et al., 2011)

In order to normalise the whole M^3 data set, millions or billions of spectra need to be processed. Furthermore, the local lunar topography, the local albedo, the local directional emissivity and the thermal conductance are not known at spatial scales required for simulations, e.g. ray tracing. Thus, Clark et al. (2011) propose a fast method that is purely data based.

The model by Clark et al. (2011) operates on the observed reflectance $R_{\text{obs}}(\mathbf{s}, \mathbf{v}, \mathbf{n}, \lambda)$, i.e.

$$R_{\text{obs}}(\mathbf{s}, \mathbf{v}, \mathbf{n}, \lambda) = R(\mathbf{s}, \mathbf{v}, \mathbf{n}, \lambda) + \beta(\mathbf{v}, \mathbf{n}, \lambda) \cdot \frac{B(\lambda, T)}{E_{\text{sun}}(\lambda)} \tag{2.12}$$

where $R(\mathbf{s}, \mathbf{v}, \mathbf{n}, \lambda)$ is the undistorted reflectance of the surface, $\beta(\mathbf{v}, \mathbf{n}, \lambda)$ is the directional emissivity, $B(\lambda, T)$ is the emission spectrum of a black body of temperature T and $E_{\text{sun}}(\lambda)$ is the solar irradiance.

Since the observed reflectance depends on the temperature and the local topography, i.e. the photometric normalisation function, all unknowns need to be estimated from the data. According to Clark et al. (2011), the space weathering results in an approximately linear functional dependence of the reflectance on the wavelength in the wavelength range 2600 nm–3000 nm and thus a linear projection from the shorter wavelengths towards the high wavelengths is computed. The linear model is used to predict the reflectance at the higher wavelength and estimate the temperature. The steps given by Clark et al. (2011) are as follows:

1. Compute a linear model $R_{\text{lin}}(\mathbf{s}, \mathbf{v}, \mathbf{n}, \lambda)$ of $R_{\text{obs}}(\mathbf{s}, \mathbf{v}, \mathbf{n}, \lambda)$ based on the channels centred at 1550 nm and 2350 nm and evaluate the model at 2700 nm.

2. Subtract the linear projection from the observed reflectance and assume the remainder to be the thermal component.

3. If the result is negative, the temperature is not derived. Otherwise, the temperature T_1 is estimated by adapting the black body emission spectrum to match the estimated thermal component. The directional emissivity is assumed to be independent of the wavelength and set to $\beta(\mathbf{v}, \mathbf{n}, \lambda) = 1 - R_{\text{obs}}(\mathbf{s}, \mathbf{v}, \mathbf{n}, 1550\,\text{nm})$.

4. Estimate the undistorted reflectance according to $R(\mathbf{s}, \mathbf{v}, \mathbf{n}, \lambda) = R_{\text{obs}}(\mathbf{s}, \mathbf{v}, \mathbf{n}, \lambda) - \beta(\mathbf{v}, \mathbf{n}, \lambda)\frac{B(\lambda, T_1)}{E_{\text{sun}}(\lambda)}$.

5. Compute the photometrically normalised reflectance $R_{\text{norm}}(\lambda)$ using a photometric normalisation method and estimate a wavelength dependent directional emissivity $\beta(\mathbf{v}, \mathbf{n}, \lambda) = 1 - R_{\text{norm}}(\lambda)$. The photometric normalisation is omitted by Clark et al. (2011) due to the phase angle correction being not available, yet.

6. Compute a new linear model $R_{\text{normlin}}(\lambda)$ of $R_{\text{norm}}(\lambda)$ based on the channels centred at 2280 nm and 2590 nm and evaluate the model at 2700 nm.

7. Estimate the temperature T_2 by repeating 2–3 using the emissivity from 5.

8. If the temperature difference $|T_1 - T_2| < 2\,\text{K}$ the solution is complete. Otherwise determine a new estimation of $R(\mathbf{s}, \mathbf{v}, \mathbf{n}, \lambda)$ based on T_2 by repeating 4–7.

The algorithm terminates after two or three temperature estimates. Clark et al. (2011) note that additional iterations did not produce better results. In contrast, thermal emission is added back to reflectance spectra displaying 2000 nm pyroxene absorption bands after three iterations are exceeded. The latter might be a consequence of the chosen wavelengths for interpolation. The 2000 nm pyroxene absorption is rather broad, starts at about 1500 nm and ends at about 2000 nm (e.g. Adams and McCord, 1971). Thus, the second set of interpolation nodes reside within the absorption trough. Additionally, the temperature is estimated based on a single channel neglecting the information of the remaining channels.

3

Related work: Photometric surface reconstruction

The apparent/measured reflectance of a surface depends on the angle of incidence and the angle of emittance and thus on the inclination of a surface (cf. Section 2.3). The reflectance thus may be used to recover surface gradient estimates. The surface, however, is a three dimensional object and the gradient field thus consists of two partial derivatives. Therefore, estimating both components of the gradient field from a single reflectance measurement requires additional constraints, so-called regularisations. To recover the surface from the possibly erroneous gradient field, which is subject to noise and model inaccuracies, an often neglected integration step is required. The literature regarding these problems is reviewed in Section 3.1.

Lately, the availability of high resolution stereo images and laser range scanners enables the direct measurement of the surface. These, however, are subject to high-frequent noise and yield a lateral resolution that is lower than the resolution of available high-resolution images. The measured surfaces may be used to constrain the photometric surface estimation problem. Section 3.2 provides an overview over the corresponding literature.

Finally, Section 3.3 details the standard methods that are used as a reference for the methods proposed in this thesis.

This chapter has been adapted and/or adopted from: (Grumpe and Wöhler, 2014; Grumpe et al., 2014a; Wöhler and Grumpe, 2013)

3.1 Intensity based surface reconstruction

In contrast to common photogrammetric surface construction techniques, e.g. bundle adjustment and stereo image processing (McGlone et al., 2004), which generally yield DEM at lateral resolutions one order of magnitude lower than the image resolution (Kirk et al., 2003a; Schenk, 2008; Scholten et al., 2012), photometric or intensity-based methods

regard the imaging device as a sensor measuring brightness that gives clues about the surface inclination. Hence, photometric methods estimate a surface which is co-registered with the original image. Furthermore, photometric methods, e.g. shape from shading, are able to construct DEM based on single images.

Early work on the estimation of slopes and heights from photometric data was based on image profiles (van Diggelen, 1951; Davis and Soderblom, 1984). Pioneering methods for area-based 3D surface reconstruction based on image intensity information were introduced by Horn (1970, 1975). Similar approaches to the estimation of topographic data from photometric image information, sometimes referred to as 2D-photoclinometry, were developed by Wildey (1975) and Kirk (1987).

Horn (1990) provides an extensive survey of the development of photometric methods. Most of them focus on the estimation of gradients from shading information since the proportion of light reflected from a surface depends on the surface slope rather than the absolute height. Furthermore, Horn (1990) presents a coupled scheme for simultaneous estimation of surface height and gradients. This method is referred to as "Shape from Shading" (SfS). Since the proposed methods (cf. Chapter 5) extend the SfS method by Horn (1990), this method is reviewed in detail in Section 3.3.

Most photometric methods estimate the surface gradient field. Thus, the integrability of estimated surface gradients and the estimation of the surface height have been of large interest to the community. Solutions are presented by Frankot and Chellappa (1988), Horn (1990) and Agrawal et al. (2006).

An early variant is the iterative relaxation scheme by Horn (1990). Often, the photometrically estimated surface gradients contain local inaccuracies and the integrability is thus not assured. The method by Horn (1990) ensures integrability by finding the surface that minimizes the so-called integrability error. The integrability error is the squared difference between the estimated surface gradients and the gradients of the estimated surface. Hence, a surface whose gradients fit the photometric gradient estimates in a least mean square sense is obtained. Using the calculus of variations Horn (1990) derived a corresponding Poisson equation. An iterative relaxation scheme is obtained by applying the finite difference methods to the corresponding equations. This method is thus referred to as "Poisson solver". It is one of the reference methods detailed in Section 3.3.

Frankot and Chellappa (1988) enforce the integrability by spectral decomposition of the surface and solve a linearised system of equations in the Fourier domain. The integration of the estimated surface gradients takes place in the frequency domain. In contrast to the iterative relaxation method, this method does not involve any iterative procedure and thus does not depend on an initial choice of the surface. In a similar manner, Simchony et al. (1990) derive an integration method by applying the sine transform which, in the continuous case, corresponds to the method by Frankot and Chellappa (1988).

A generalised equation comprising the Poisson solver by Horn (1990), the method of Frankot and Chellappa (1988) and more special cases is presented by Agrawal et al. (2006). The generalised equation results in a continuum of solutions which ranges from

the Poisson solver to Diffusion. The former uses spatially invariant weights while the latter allows a scaling and linear combination of the coordinate axes. Agrawal et al. (2006) present four cases of solutions. These are the RANSAC algorithm, the so-called α-surfaces using anisotropic binary weights, M-estimators using anisotropic continuous weights and Diffusion tensors.

3.2 Fusion with depth data

While an extensive body of literature exists on shape from shading and shape recovery from photometric measurements, the fusion of photometric information and absolute depth measurements, such as laser range scanning or geometrical methods like stereo analysis or bundle adjustment, has been developed within the last decade.

Soderblom et al. (2002) propose a method to identify the parameters of the reflectance model such that the height profile obtained from Mars Orbiter Narrow Angle Camera images matches a track of laser range scanning single point measurements of the Mars Orbiter Laser Altimeter in a least squares sense. The resolution of the resulting profile is one to two orders of magnitude larger than the resolution of the laser profile. An extension towards an area-based method that uses gridded and interpolated Mars Orbiter Laser Altimeter measurements has been presented by Soderblom and Kirk (2003). The images are registered onto a shaded depth map and the parameters of the reflectance model are then estimated until the estimated height matches the depth map in a least-squares sense. The resolution of the depth map increases by a factor of about 200 (Soderblom and Kirk, 2003). Both methods restrict variations of the reflectance parameters to the lateral resolution of the laser range scanning data, i.e. use area-wise constant parameters. This method has been applied to candidate landings sites for Mars Exploration Rovers by Kirk et al. (2003b). Furthermore, Kirk et al. (2003a) included this method into the ISIS software framework. By performing a fixed number of iterations, the photometric estimate yields an interpolation of an existing DEM (Kirk et al., 2003a). This approach, however, does not constrain the solution of the photoclinometry towards the DEM. Although the lateral resolution of the DEM is captured by a smooth interpolation and mapping onto the image grid it is not further regarded during the optimisation. The least squares matching between the estimated surface and the a-priori DEM during the computation of the parameters of the reflectance model implicitly assumes that the mean depth of both DEM is equal. Assuming that the resolution of the image is several times higher than the resolution of the a-priori DEM, the estimated surface will contain small scale features, e.g. craters and rocks, that are not contained in the a-priori DEM. These are likely to change the mean depth of the estimated surface. If these small scale features are not taken into account before the comparison it may influence the estimation of the photometric model.

In the context of synthetic aperture radar image analysis, Frankot and Chellappa (1990) propose a method to incorporate elevation data of low resolution into a shape

from shading framework. A combination of stereo image analysis and photometric surface estimation techniques has been proposed by Shao et al. (1991). Among other methods, Shao et al. (1991) propose the fusion of the integration of surface gradients inferred from reflectance data with measured absolute depth data by minimizing a weighted sum of the integrability error and the difference between the estimated and the measured depth data where measurements are available. It extends the method proposed by Horn (1990). The method introduced in this work can be seen as a generalization of the approach by Shao et al. (1991). This reference method is reviewed in further detail in Section 3.3.

Fassold et al. (2004) developed an algorithm for the fusion of photometric depth estimation with a stereo DEM. However, their method is restricted to Lambertian reflectance and applies a smoothness regularisation. Unfortunately, planetary surfaces like that of the Moon do not show a Lambertian reflectance behaviour, and the smoothness regularisation tends to produce overly smooth DEM and, even worse, drives the obtained DEM away from the photometric optimum (Horn, 1990).

A method to combine depth from gradient fields and sparse depth data, e.g. known depth points, has been proposed by Horovitz and Kiryati (2004). The depth points are integrated into the optimisation using weighted least squares to limit the influence of single depth points. Horovitz and Kiryati (2004) present different weighting functions. However, the choice of the weighting function affects the smoothness of the surface and thus limits the usability of the approach. A second method introduced by Horovitz and Kiryati (2004) is the correction of a previously estimated photometrically obtained DEM, which is achieved by interpolating the depth difference between the absolute depth data and the photometrically obtained DEM based on the thin plate equation. The thin plate equation yields a smooth interpolation behaviour and thus can be interpreted as the extraction of the low spatial frequency error which is inherent to photometric methods: Small errors of the gradient estimates accumulate during the integration step and tend to introduce a bias of the resulting surface at low spatial frequencies. The final DEM is then computed as the superposition of the photometrically obtained DEM and the interpolation function.

At the same time, Dorrer et al. (2004) proposed the de- and re-shading method for dense depth data of "sufficient quality", regarding the example of the Mars Orbiter Wide Angle Camera. The existing DEM is added to the photometric optimisation problem as a soft constraint, i.e. a weighted error term describing the squared difference between the optimised and the existing topography model is added to the overall error functional. The approach is restricted to Lambertian reflectance and uniform albedos. Similar to Soderblom and Kirk (2003), the different resolutions of the data sets are not taken into account. This approach has been demonstrated by Albertz et al. (2005) and Kirk et al. (2006), considering data of the High Resolution Stereo Camera of the Mars Express spacecraft.

The inaccuracy of measured depth data is explicitly considered by Nehab et al. (2005). Their range scanner depth data provides reliable low-frequency components while the

high-frequency components tend to be noisy. The opposite is true for intensity-based gradient estimates where the small high-frequency component errors build up to large low-frequency component errors, the bias. In order to fuse both data sources, Nehab et al. (2005) propose a two step algorithm. First, the photometrically estimated gradient field is rotated such that the low-frequency components of both gradient fields match. Second, a linearised error functional is optimised by minimising the violation of an orthogonality constraint between the normals and the tangents of the estimated surface as well as minimising the Euclidean distance between the estimated DEM and the measured absolute depth data.

The method presented by Gaskell et al. (2008) uses a different way to constrain the photometric surface estimation. First, the average albedo and the background intensity are derived for each image. Then a mixture of the Lambert and the Lommel-Seeliger reflectance functions is applied to derive a relative albedo and the surface gradients at a randomly chosen pixel and its four nearest neighbours. The depth of the chosen pixel is then estimated by integrating the average gradient of the chosen and each of the four neighbouring pixels, respectively. The four results and a weighted constraining depth value are averaged to obtain the final depth value for the chosen pixel. This procedure is repeated until convergence is achieved (Gaskell et al., 2008).

Schenk (2002) has developed a method that independently computes stereo analysis and photoclinometry for the estimation of icy shells. The stereo DEM is used to control the long-wavelength component of the photoclinometry DEM. This is achieved by merging the low-frequency component of the stereo DEM with the high-frequency component of the photoclinometry result. Later, Schenk (2008) applied these techniques to icy satellites and used the combination of stereo analysis and photoclinometry whenever possible.

Ng et al. (2010) propose a new method to recover a surface from an estimated gradient field that does not enforce discrete integrability. The surface is represented by a non-linear continuous function that is expanded into kernel functions. The kernel functions have a linear representation in a higher dimensional space and thus the integrability constraint is computed in a higher dimensional space. Additionally, existing depth data may be included as additional constraints. The drawback, however, is the very large system of equations arising from the constraints and the necessity of a regularization term that originates from the high dimensionality of the problem. Furthermore, the estimated surface gradients and the measured depth data are considered accurate. The non-linear function matches the possibly noisy gradient field and measured depth. To eliminate the noise, a smoothness constraint is added.

The more recent method for the refinement of existing DEM by Barron and Malik (2011) estimates the surface shape on small spatial scales simultaneously with the pixel-wise albedo based on a single image, assuming a Lambertian reflectance model. To separate the effects of the surface gradients and the albedo on the observed image intensities from each other, the statistical properties of "typical" albedo maps and surfaces are learned from examples. The approach allows for an integration of independently obtained

depth information obtained e.g. by stereo image analysis or active range scanning into the estimated small-scale surface data. The method is extended by Barron and Malik (2012) towards an additional estimation of the illumination conditions.

A different development is the inclusion of the photometric information into the stereo process. Lohse et al. (2006) optimise the surface in the object space. The surface is rendered using the photometric information and projected into the stereo cameras. The photometric error functional is then computed between the measured and the projected images. This method is most stable for oblique views. Since most spectral datasets are recorded using a nadir view, an additional sensor would be necessary. Additionally, Lohse et al. (2006) state that their method is sensitive to the reflectance model. Similarly, Gehrke (2006) includes photometric cues and the derivation of reflectance parameters into the facets stereo algorithm by Weisensee (1992). The algorithm, however, still requires oblique views.

3.3 Reference methods

Within this thesis, there are three important reference methods. Section 3.3.1 describes the method by Horn (1990) which recovers a depth map from a possibly non-integrable field of estimated gradients and gives an extension towards non-uniformly spaced grids. The coupled method of estimating surface gradients from reflectance images and the corresponding surface, i.e. shape from shading, is then detailed in Section 3.3.2. Finally, Section 3.3.3 summarises an extension to the shape from shading method by Shao et al. (1991) who introduced an absolute depth constraint.

3.3.1 DEM from gradient estimates according to Horn (1990)

A technique that estimates the surface inclination based on the physical reflectance is photoclinometry (Wilhelms, 1964). An overview of photoclinometry methods is provided by Horn (1990). Due to the nature of the shading information being based on the surface inclination, these approaches estimate surface gradients rather than the surface itself. Therefore, a method to obtain the surface shape from the gradients is necessary. This section reviews the integration method introduced by Horn (1990) and adds an extension to non-uniform pixel grids.

In general, the surface gradient estimates p and q are influenced by noise and model uncertainties and thus are not integrable. In contrast, a physically reasonable surface is differentiable and the problem can be reformulated to determine the surface z whose gradients $\frac{\partial z}{\partial x}$ and $\frac{\partial z}{\partial y}$ are closest to the estimates p and q by minimising the integrability error term

$$E_{\text{int}} = \int_{\mathbf{x}} \int_{\mathbf{y}} \frac{1}{2} \left(\frac{\partial z}{\partial x} - p \right)^2 + \frac{1}{2} \left(\frac{\partial z}{\partial y} - q \right)^2 dxdy \tag{3.1}$$

where $\mathbf{x}$ and $\mathbf{y}$ define the region of interest. Since the derivatives of z appear inside the integral, the equation has to be solved using the calculus of variations (cf. Appendix B). The resulting Euler equation is

$$\Delta z = \frac{\partial p}{\partial x} + \frac{\partial q}{\partial y} \tag{3.2}$$

and the corresponding natural boundary condition is

$$\mathbf{n}_\Omega^T \cdot \begin{bmatrix} \frac{\partial z}{\partial x} \\ \frac{\partial z}{\partial y} \end{bmatrix} = \mathbf{n}_\Omega^T \cdot \begin{bmatrix} p \\ q \end{bmatrix}, \tag{3.3}$$

where $\mathbf{n}_\Omega$ is the vector orthogonal to the surface boundary Ω.

Horn (1990) uses a discrete approximation of the Laplace operator and assumes a square pixel grid to obtain the update equation

$$z_{u,v}^{(n_\text{iter}+1)} = \bar{z}^{(n_\text{iter})} - \frac{\varepsilon_\text{px}^2}{\kappa} \left(\left.\frac{\partial p}{\partial x}\right|_{u,v} + \left.\frac{\partial q}{\partial y}\right|_{u,v} \right) \tag{3.4}$$

where $z_{u,v}^{(n_\text{iter}+1)}$ is the z value of pixel (u, v) at iteration $n + 1$, $\bar{z}^{(n)}$ is the mean over the adjacent pixels at iteration n_iter, κ is the number of non-zero entries in the discrete Laplacian filter minus one, and ε_px is the edge length of a pixel. In order to apply this approach to a non-uniform grid, the discrete Laplacian is approximated by

$$\Delta z \approx \frac{z_{u,v+1} - 2z_{u,v} + z_{u,v-1}}{h_x^2} + \frac{z_{u+1,v} - 2z_{u,v} + z_{u-1,v}}{h_y^2} \tag{3.5}$$

where h_x and h_y are the edge lengths in x and y direction, respectively, of pixel (u, v). The explicit dependence of the edge length on the pixel coordinates will be omitted for readability. However, the edge length in either direction may vary across the image. Inserting Eq. (3.5) into Eq. (3.2) and solving for $z_{u,v}$ yields the update equation

$$z_{u,v}^{(n_\text{iter}+1)} = \frac{h_x^2 \left(z_{u+1,v}^{(n_\text{iter})} + z_{u-1,v}^{(n_\text{iter})} \right) + h_y^2 \left(z_{u,v+1}^{(n_\text{iter})} + z_{u,v-1}^{(n_\text{iter})} \right) - h_x^2 h_y^2 \left(\left.\frac{\partial p}{\partial x}\right|_{u,v} + \left.\frac{\partial q}{\partial y}\right|_{u,v} \right)}{2\left(h_x^2 + h_y^2\right)}. \tag{3.6}$$

3.3.2 Shape from shading (SfS) according to Horn (1990)

Horn (1990) describes a method for the simultaneous recovery of surface gradients and depth from the measured reflectance. In contrast to photoclinometry methods which are mostly profile-based (Horn, 1990), the described method is area-based. The surface orientation may be represented by the surface normal $\mathbf{n}$ of the surface gradients p and q, where

$$\mathbf{n} = \frac{1}{\sqrt{p^2 + q^2 + 1}} \begin{bmatrix} -p \\ -q \\ 1 \end{bmatrix}. \tag{3.7}$$

Therefore, the surface orientation may be obtained by minimising

$$E_{\mathrm{I}} = \frac{1}{2}\left(R\left(\mathbf{s},\mathbf{v},\mathbf{n}(p,q)\right) - I\right)^2 \tag{3.8}$$

where R is the modelled reflectance and I is the measured intensity/reflectance value. However, if inter-pixel scattering is excluded such that the reflectance of a surface pixel only depends on its gradients, there is only one measured intensity value but two unknowns p and q per pixel. In order to solve this under-determined system of equations, a further regularisation term is needed. At this point, Horn (1990) suggests to minimise

$$E_{\mathrm{Horn}} = E_{\mathrm{I}} + \gamma E_{\mathrm{int}} \tag{3.9}$$

to enforce integrability of the surface gradient field and simultaneously reconstruct the surface z and the gradient estimates p and q. In Eq. (3.9), γ is a weighting factor which will be examined later on.

Horn (1990) treats p, q and z as independent variables and proposes an alternating update scheme. Since there are no derivatives of p and q in the equation, it is an ordinary calculus problem. Deriving with respect to p and q and setting the resulting equations to zero yields

$$p = \frac{\partial z}{\partial x} - \frac{1}{\gamma}\left(R - I\right)\frac{\partial R}{\partial p}, \tag{3.10}$$

$$q = \frac{\partial z}{\partial y} - \frac{1}{\gamma}\left(R - I\right)\frac{\partial R}{\partial q}. \tag{3.11}$$

Since derivatives of z appear within Eq. (3.9), a solution is obtained using the calculus of variations. However, E_{I} does not depend on z, and the problem reduces to minimising the integrability error E_{int} (cf. Section 3.3.1). This leads to the coupled system of equations

$$p_{u,v}^{(n_{\mathrm{iter}}+1)} = \left.\frac{\partial z}{\partial x}\right|_{u,v}^{(n_{\mathrm{iter}})} - \frac{1}{\gamma}\left(R\big|_{\frac{\partial z}{\partial x}^{(n_{\mathrm{iter}})}} - I\right)\left.\frac{\partial R}{\partial p}\right|_{\frac{\partial z}{\partial x}^{(n_{\mathrm{iter}})}}, \tag{3.12}$$

$$q_{u,v}^{(n_{\mathrm{iter}}+1)} = \left.\frac{\partial z}{\partial y}\right|_{u,v}^{(n_{\mathrm{iter}})} - \frac{1}{\gamma}\left(R\big|_{\frac{\partial z}{\partial y}^{(n_{\mathrm{iter}})}} - I\right)\left.\frac{\partial R}{\partial q}\right|_{\frac{\partial z}{\partial y}^{(n_{\mathrm{iter}})}}, \tag{3.13}$$

$$\begin{aligned} z_{u,v}^{(n_{\mathrm{iter}}+1)} = {} & \frac{h_x^2\left(z_{u+1,j}^{(n_{\mathrm{iter}})} + z_{v-1,j}^{(n_{\mathrm{iter}})}\right) + h_y^2\left(z_{u,v+1}^{(n_{\mathrm{iter}})} + z_{u,v-1}^{(n_{\mathrm{iter}})}\right)}{2\left(h_x^2 + h_y^2\right)} \\ & - \frac{h_x^2 h_y^2\left(\left.\frac{\partial p}{\partial x}\right|_{u,v}^{(n_{\mathrm{iter}}+1)} + \left.\frac{\partial q}{\partial y}\right|_{u,v}^{(n_{\mathrm{iter}}+1)}\right)}{2\left(h_x^2 + h_y^2\right)}, \end{aligned} \tag{3.14}$$

which is solved sequentially by updating p and q prior to updating z. Horn (1990) notes that the convergence is improved if the error function is evaluated at the partial derivatives

of the obtained surface rather than inserting p and q. The estimates of p and q are always close to the solution, since they originate from an ordinary calculus problem. In contrast z_x and z_y represent the surface at the current iteration. The reflectance model and its derivatives thus are evaluated using the partial derivatives of the surface of the current iteration. Notably, γ is anti-proportional to the change in z_x and z_y. Thus, the weighting factor γ can be interpreted as a step size parameter. The update equation for z differs from the previous section by the changing values of p and q, which are taken from the current iteration and are no longer constant.

Since the convergence radius of this method is rather small, Horn (1990) proposes an additional smoothness constraint. This artificial constraint influences the solution and prevents the algorithm from converging to the solution of the aforementioned algorithm. However, the smoothness constraint is not necessary for the remainder of this thesis and is thus omitted here.

3.3.3 Additional DEM constraint according to Shao et al. (1991)

The recovery of depth from surface normals has been solved by Horn (1990) by minimising the integrability error (cf. Section 3.3.1). In addition, Shao et al. (1991) minimise the difference to an a-priori known DEM by minimising the weighted sum

$$E_{\text{Shao}} = E_{\text{int}} + \int_{\mathbf{x}} \int_{\mathbf{y}} \tau(x,y) \frac{1}{2} \left(z - z_{\text{DEM}}\right)^2 dxdy \tag{3.15}$$

where the weight τ depends on the lateral coordinates x and y. It is zero-valued if no measurement for the corresponding pixel is available and constant elsewhere. Thus, it is a special case of the method proposed in Section 5.3.2 for dense DEM z_{DEM} whose lateral resolution matches the lateral resolution of the image.

The update equation given by Shao et al. (1991) is

$$\begin{aligned} z_{u,v}^{(n_{\text{iter}}+1)} =& \frac{1}{2\alpha_{\text{ext}}^2(u,v) + \alpha_{\text{ext}}(u,v)\hat{\tau}(u,v) + 2} \left(- \left(\left.\frac{\partial p}{\partial x}\right|_{u,v} + \left.\frac{\partial q}{\partial y}\right|_{u,v} \right) h_y^2(u,v) + \right. \\ & \left. \alpha_{\text{ext}}(u,v)\hat{\tau}(u,v) z_{\text{DEM}}(u,v) + \alpha_{\text{ext}}^2(u,v) z_{\text{h}}^{(n_{\text{iter}})}(u,v) + z_{\text{v}}^{(n_{\text{iter}})}(u,v) \right) \end{aligned} \tag{3.16}$$

where ${\alpha_{\text{ext}}}^2(u,v) = \left(\frac{h_y(u,v)}{h_x(u,v)}\right)^2$ denotes the ratio of the vertical and the horizontal pixel extents and $z_{\text{h}}(u,v)$ and ${z_{\text{v}}}^{(n_{\text{iter}})}(u,v)$ denote the sum over the two pixels adjacent in horizontal and vertical direction, respectively. The update equation uses a normalised weight $\hat{\tau}$ which corresponds to a normalisation of τ by setting

$$\hat{\tau}(u,v) = h_x(u,v) h_y(u,v) \tau(u,v) \tag{3.17}$$

as shown in the following derivation. In order to keep the weight parameter τ comparable to the method presented in Section 5.3, a different update equation is derived by applying the calculus of variations (cf. Appendix B) to Eq. (3.15). This yields the Euler equation

$$\tau z - \Delta(z) = \tau z_{\mathrm{DEM}} - \left(\frac{\partial p}{\partial x} + \frac{\partial q}{\partial y} \right). \tag{3.18}$$

By using the central differences operators the update equation

$$\begin{aligned} z_{u,v}^{(n_{\mathrm{iter}}+1)} = & \frac{1}{2\alpha_{\mathrm{ext}}^2(u,v) + h_y^2(u,v)\tau(u,v) + 2} \left(- \left(\left. \frac{\partial p}{\partial x} \right|_{u,v} + \left. \frac{\partial q}{\partial y} \right|_{u,v} \right) h_y^2(u,v) + \right. \\ & \left. h_y^2(u,v)\tau(u,v) z_{\mathrm{DEM}}(u,v) + \alpha_{\mathrm{ext}}^2(u,v) z_{\mathrm{h}}^{(n_{\mathrm{iter}})}(u,v) + z_{\mathrm{v}}^{(n_{\mathrm{iter}})}(u,v) \right). \end{aligned} \tag{3.19}$$

is readily obtained. A comparison of the coefficients of $\tau(u,v)$ and $\hat{\tau}(u,v)$ in Eq. (3.16) and Eq. (3.19) proves Eq. (3.17).

4

Contribution: Normalisation of (hyper-)spectral data

The normalisation of spectral reflectance data with respect to standard geometry involves different steps. At first, the measured sensor counts have to be converted to radiance measurements. This step is highly specific to the sensor of choice and will not be considered during this thesis. It will be assumed that the available sensor data is converted to radiance measurements.

Due to thermal emission, the measured radiance can be subdivided into two categories: heat rays irradiated by the surface and incident light reflected by the surface. The former depends on the temperature of the surface and the latter depends on the incident light intensity and the surface reflectance properties. In remote sensing, only the reflected component is of interest. Hence, the thermal emission has to be identified and removed from the measured radiance. The proposed method is described in Section 4.1.

Afterwards, the measured radiance is converted to reflectance dividing the measured radiance by the portion of light incident on the surface area. To compensate differences in the illumination and viewing geometry, the reflectance is normalised to standard geometry using the Hapke AMSA model. This is achieved by estimating the model parameters based on the available measurements and evaluating the model at standard geometry inserting the estimated parameters. The details of the method are given in Section 4.2.

Additionally, a method to compensate observed phase angle dependent effects is given in Section 4.3. Later, it was published that the sensor temperature was not compensated in the original data set. Thus, it is possible that the observed effects may also be caused by the sensor temperature. The correction may be applied at either end of the normalisation chain by modifying the normalised reflectance or modifying the radiance at the beginning of the processing chain.

This chapter has been adapted and/or adopted from: (Grumpe et al., 2014a,b; Wöhler and Grumpe, 2013; Grumpe et al., 2012a,c; Grumpe and Wöhler, 2011a,b; Grumpe et al., 2011a)

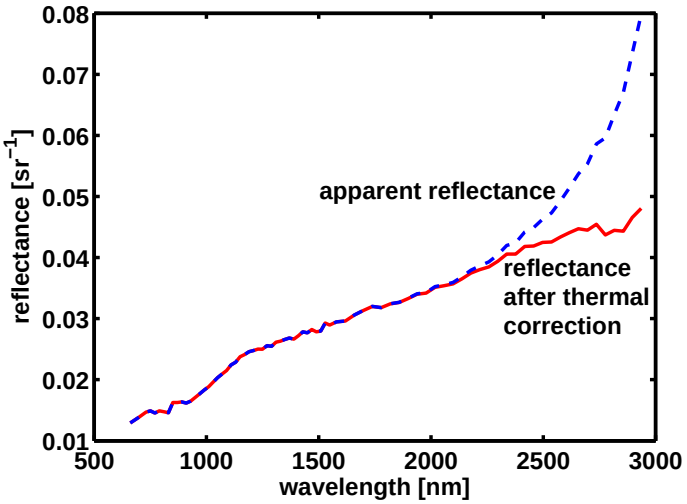

Figure 4.1: Comparison of apparent and thermally corrected reflectance. The corrected spectrum (red line) and the apparent reflectance spectrum (blue dashed line) for temperature of $T = 368\,\mathrm{K}$ are shown. The spectrum beyond 2200 nm is severely influenced.

4.1 Thermal emission

The method by Clark et al. (2011) (cf. Section 2.4.2) uses a linear reflectance projection based on points influenced by the 2 micron pyroxene absorption. In addition, the temperature is estimated based on only one instrument channel.

To avoid these problems and increase the robustness of the temperature estimation, a method using multiple instrument channels and laboratory measurements of a reference lunar sample is described in Section 4.1.1. Section 4.1.2 presents the results on a global scale and a comparison to Clark et al. (2011) on a local scale.

4.1.1 Surface temperature estimation

The measured radiance value is composed of the solar irradiance reflected by a surface area and the thermal radiation of the surface area. This thermal component severely distorts the apparent reflectance, i.e. the measured radiance divided by the solar irradiance. Fig. 4.1 shows the inferred reflectance spectrum with correction (red line) and without correction (blue dashed line) at a temperature of $T = 368\,\mathrm{K}$ which is a reasonable temperature during the lunar day. The thermal component influences the reflectance spectrum above 2200 nm and thus the interpretation of the absorption near 2000 nm.

The estimation of the surface temperature is based on the assumption that the observed radiance spectrum $L_{\mathrm{app}}(\mathbf{s}, \mathbf{v}, \mathbf{n}, \lambda, T)$ can be modelled as the superposition of the portion of the solar irradiance spectrum $E_{\mathrm{sun}}(\lambda)$ reflected into the sensor and the emission

spectrum $\beta(\mathbf{v}, \mathbf{n}, \lambda)B(\lambda, T)$ of a black body (Schowengerdt, 2006, pp. 63ff.) of temperature T. The emissivity $\beta(\mathbf{v}, \mathbf{n}, \lambda)$ is approximately wavelength independent. Thus,

$$L_{\text{app}}(\mathbf{s}, \mathbf{v}, \mathbf{n}, \lambda) = c_{\text{refl}} E_{\text{sun}}(\lambda) R_{\text{ref}}(\lambda) + \beta(\mathbf{v}, \mathbf{n}) B(\lambda, T) \tag{4.1}$$

where R_{ref} is a reference reflectance spectrum and c_{refl} is a wavelength-independent factor that absorbs the photometric normalisation factor and a possible scaling, i.e. different brightness of the surface. The directional emissivity $\beta(\mathbf{v}, \mathbf{n}, \lambda)$ is assumed to be constant and set to 0.95 (Berezhnoy et al., 2012; Greenhagen and Paige, 2006).

A linear extrapolation of the returned lunar sample no. 62231[1] (Pieters, 1999) is selected to be the reference reflectance spectrum. The linear model R_{62231} is determined y minimising the squared difference between the model and the reflectance spectrum of lunar sample no. 62231 in the wavelength range 2400 nm–2600 nm which yields

$$R_{\text{ref}}(\lambda) = R_{62231}(\lambda) = 0.081151 \cdot 10^{-3}\lambda + 0.1423. \tag{4.2}$$

The values of c_{refl} and T are obtained by minimising

$$E_{\text{temp}} = \frac{1}{2} \sum_{k=1}^{N_{\text{temp}}} \left(L_{\text{meas}}(\mathbf{s}, \mathbf{v}, \mathbf{n}, \lambda_k) - L_{\text{app}}(\mathbf{s}, \mathbf{v}, \mathbf{n}, \lambda_k)\right)^2 \tag{4.3}$$

where N_{temp} is the number of instrument channels in the wavelength range 2377 nm – 2936 nm and λ_k is the corresponding centre wavelength of the kth channel. Notably, due to the limited wavelength coverage of the M^3 sensor, it is not possible to estimate temperature values below about 300 K.

To minimise E_{temp}, the Levenberg-Marquardt optimisation without implicit bounds (cf. Appendix A) is applied. The corresponding partial derivatives are

$$\frac{\partial E_{\text{temp}}}{\partial T} = \sum_{k=1}^{N_{\text{temp}}} \left(L_{\text{app}}(\mathbf{s}, \mathbf{v}, \mathbf{n}, \lambda_k) - L_{\text{meas}}(\mathbf{s}, \mathbf{v}, \mathbf{n}, \lambda_k)\right) \beta(\mathbf{v}, \mathbf{n}, \lambda_k) \frac{\partial B(\lambda_k, T)}{\partial T} \text{ and} \tag{4.4}$$

$$\frac{\partial E_{\text{temp}}}{\partial c_{\text{refl}}} = \sum_{k=1}^{N_{\text{temp}}} \left(L_{\text{app}}(\mathbf{s}, \mathbf{v}, \mathbf{n}, \lambda_k) - L_{\text{meas}}(\mathbf{s}, \mathbf{v}, \mathbf{n}, \lambda_k)\right) E_{\text{sun}}(\lambda_k) R_{62231}(\lambda_k). \tag{4.5}$$

Finally, the thermally corrected radiance spectrum $L_{\text{corr}}(\lambda)$ is obtained according to

$$L_{\text{corr}}(\mathbf{s}, \mathbf{v}, \mathbf{n}, \lambda) = L_{\text{app}}(\mathbf{s}, \mathbf{v}, \mathbf{n}, \lambda) - \beta(\mathbf{v}, \mathbf{n}, \lambda) B(\lambda, T). \tag{4.6}$$

[1] Available at http://www.planetary.brown.edu/pds/AP62231.html

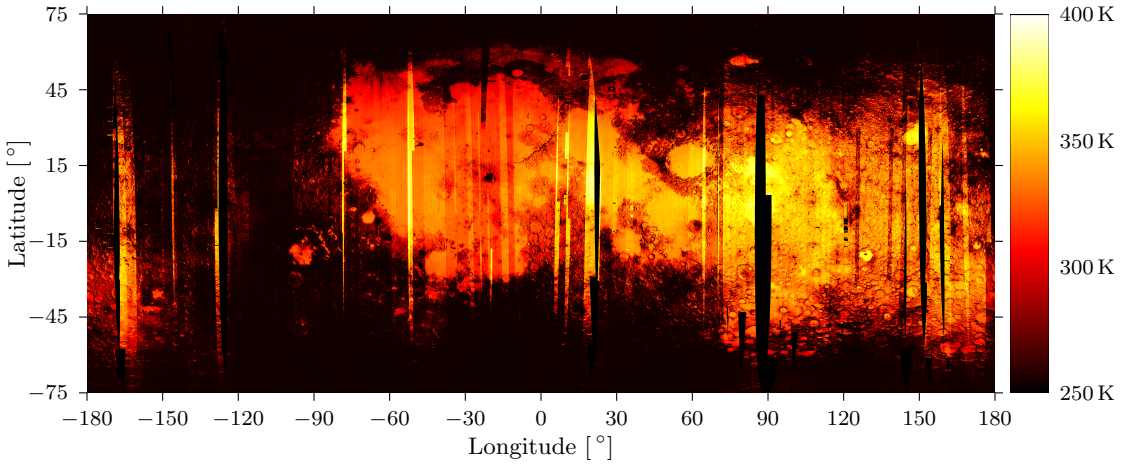

(a) Minimal estimated temperature.

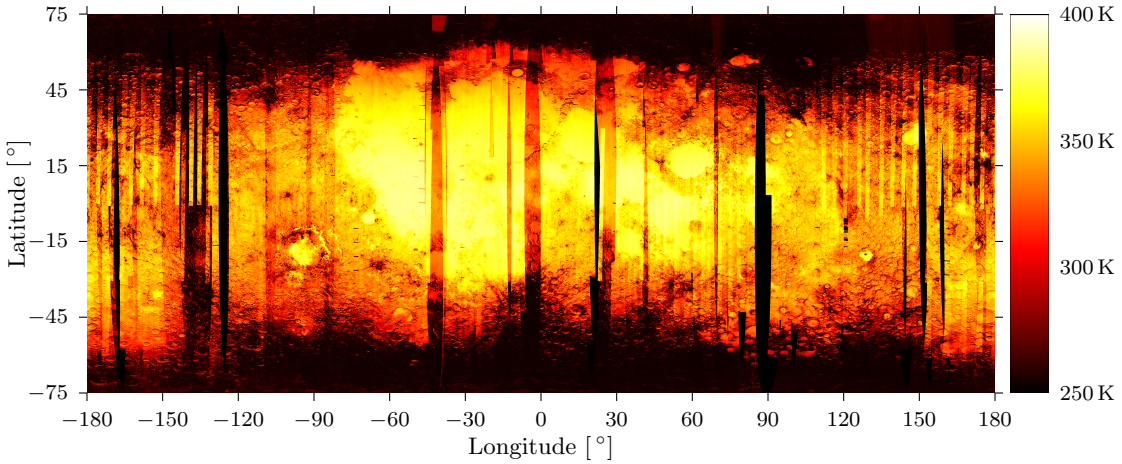

(b) Maximal estimated temperature.

Figure 4.2: Global surface temperature estimates. (a) Minimal temperature estimated from all M^3 images. (b) Maximal temperature estimated from all M^3 images.

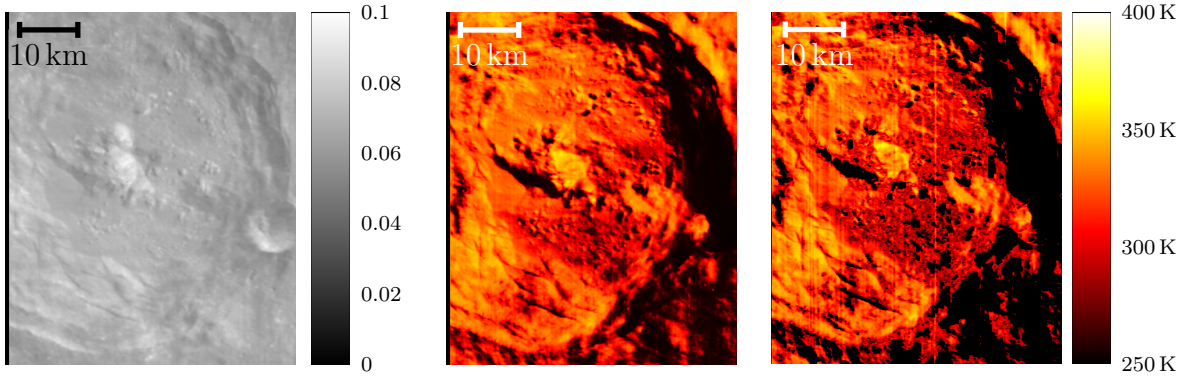

(a) M^3 reflectance image. (b) Proposed method. (c) (Clark et al., 2011).

Figure 4.3: Local surface temperature estimates. (a) M^3 images at 1579 nm. The phase angle is 31.6 °. Image Credit: NASA/JPL-Caltech. (b) Estimated surface temperature using the proposed method. (c) Estimated temperatures by Clark et al. (2011). The lateral offset between the different temperature maps resembles the different co-registration procedures.

4.1.2 Results

A mosaic of the inferred minimal and maximal temperature, respectively, is shown in Fig. 4.2. The estimated temperatures are below 400 K which may be considered the maximum temperature of the lunar surface. Furthermore, the estimated temperatures are either above 260 K or way below 250 K. This is caused by the limited wavelength range that does not allow for an accurate estimation of temperatures below 300 K. From the observations it seems possible to derive temperatures down to 260 K. The estimated temperatures, however, should be interpreted cautiously since they are based on very little information contained in the bands near 3000 nm which may show hydroxyl based absorption features and thus violate the assumption of a linear model. In general, the estimated temperature profiles match the structure of the lunar surface. The estimated temperatures decrease towards the lunar poles. This effect is caused by the increasing incidence angle of the solar flux. Each strip from south to north or vice versa is acquired within less than two hours while a lunar day lasts about 27 days and 7.75 hours. One single strip thus represents an instant of approximately the same illumination and the increased temperature of the Mare regions is considered to be due to higher absorption. This corresponds to the darker appearance of the Mare regions.

Fig. 4.3 shows the local temperature estimates for the lunar crater Lowell (103.4 °W, 13.0 °S). The estimates are based on the M^3 image M3G20090713T192732. For compari-

son, the temperatures estimated by Clark et al. (2011)[2] are shown as well. Both methods are in good agreement for temperatures above 300 K. The local topography is more apparent in the proposed method which indicates that the temperature differences caused by shading are covered while the method by Clark et al. (2011) is missing large fractions of the temperatures in shaded regions.

4.2 Reflectance parameter estimation

In general, the parameters of the reflectance model may change from one pixel to the next. The estimation of these parameters depends on the knowledge of the local topography. A general approach to the estimation of reflectance parameters is described in Section 4.2.1. The Hapke based normalisation procedure is then given in in Section 4.2.2.

4.2.1 General problem formulation

The thermally corrected radiance L_{corr} (cf. Section 4.1) is converted to measured reflectance R_{meas} by dividing by the solar irradiance E_{sun}, i.e.

$$R_{\text{meas}} = \frac{L_{\text{corr}} r_{\text{sun}}^2}{E_{\text{sun}}} \tag{4.7}$$

where r_{sun} is the distance from the sun to the observed lunar surface. Since the r_{sun} is several orders of magnitude larger than the local topography, the local topography is ignored during this step.

R_{meas} is then normalised to standard viewing geometry, i.e $\vartheta_i = 30\,^\circ$ incidence angle, $\vartheta_e = 0\,^\circ$ emission angle and $\alpha = 30\,^\circ$ phase angle, by computing the parameters of the reflectance model with respect to the viewing geometry during observation and evaluating the reflectance model at standard viewing geometry. Thus, the normalisation procedure highly depends on the local topography.

To allow for sharp boundaries of different surface materials, the parameters of the reflectance model need to change pixel-wise, i.e. the parameters are spatially variable. Available DEM, however, do not match the resolution of the M^3 spectral data (Boardman et al., 2011). Techniques for the refinement of DEM are presented in Chapter 5, but all techniques require the estimation of surface reflectance parameters. Hence, the parameter estimation procedure needs to fuse datasets of different lateral resolutions.

Assuming that the lateral resolution of the DEM is lower than the lateral resolution of the spectral data, there is a region Ω_{refl} around each image position (u, v) that represents the cell spacing of the native resolution of the DEM, i.e. the spatial extent of Ω_{refl} is one pixel if the resolutions of the DEM and the spectral data match and it is larger than one

[2]Available at http://pds-imaging.jpl.nasa.gov/volumes/m3.html (Level 2 data)

pixel otherwise. Since the reflectance model depends on the local topography, the DEM resolution restricts the resolution of the locally varying reflectance parameters and the reflectance model is assumed to be constant within this region, i.e the same parameters should match all observed intensities within Ω_{refl}. Notably, the measured reflectance and the viewing geometry depend on the spatial coordinates x and y.

The parameters are then obtained by minimising

$$E_{\text{refl}} = \frac{1}{2}\sum_{i=1}^{N_{\text{im}}} \left(w_{\text{refl}}(x,y) * R_{\text{meas},i}\left(\mathbf{s}_i(x,y), \mathbf{v}_i(x,y), \mathbf{n}(x,y), \lambda\right)\right. \\ \left. - R_{\text{model}}\left(\tilde{\mathbf{s}}_i(x,y), \tilde{\mathbf{v}}_i(x,y), \tilde{\mathbf{n}}(x,y), \boldsymbol{\Psi}\left(\lambda\right)\right)\right)^2 \tag{4.8}$$

where $\boldsymbol{\Psi}\left(\lambda\right)$ is a vector containing all, possibly wavelength dependent parameters of the reflectance model $R_{\text{model}}\left(\tilde{\mathbf{s}}_i(x,y), \tilde{\mathbf{v}}_i(x,y), \tilde{\mathbf{n}}(x,y), \boldsymbol{\Psi}\left(\lambda\right)\right)$. The number of available co-registered images is denoted by N_{im}, $R_{\text{meas},i}\left(\mathbf{s}_i(x,y), \mathbf{v}_i(x,y), \mathbf{n}(x,y), \lambda\right)$ is the measured reflectance of the ith image and $\tilde{\mathbf{s}}_i$, $\tilde{\mathbf{v}}_i$ are the corresponding average vectors pointing to the light source position and the viewer position, respectively. The average surface normal $\tilde{\mathbf{n}}$ does not depend on the time of image acquisition. All directions are averaged over the region Ω_{refl} using the averaging filter function $w_{\text{refl}}(x,y)$, i.e.

$$\tilde{\mathbf{n}} = \begin{pmatrix} w_{\text{refl}}(x,y) * n_x(x,y) \\ w_{\text{refl}}(x,y) * n_y(x,y) \\ w_{\text{refl}}(x,y) * n_z(x,y) \end{pmatrix} \tag{4.9}$$

where $*$ denotes the convolution and $n_x(x,y)$, $n_y(x,y)$ and $n_z(x,y)$ denote the components of the surface normal $\mathbf{n}(x,y)$ in x, y and z direction, respectively. The equations for $\tilde{\mathbf{s}}_i$ and $\tilde{\mathbf{v}}_i$ are formed accordingly.

Possible choices for w_{refl} are the local average, a disk filter or any other averaging operation as long as $w_{\text{refl}} * 1 = 1$. Within this work, the two filters of choice are the identity using the Dirac delta function and a Gaussian $w_{\text{refl}} = g_{\sigma_{\text{refl}}}(x,y)$ of width σ_{refl} with

$$g_{\sigma_{\text{refl}}}(x,y) = \frac{1}{\sqrt{2\pi\sigma_{\text{refl}}^2}} e^{-\frac{x^2+y^2}{2\sigma_{\text{refl}}^2}}. \tag{4.10}$$

The former corresponds to the case of matching lateral resolutions and one set of reflectance parameters is computed for each image pixel while the latter is used to map the reflectance parameters at the DEM resolution. The parameter σ_{refl} is proportional to the ratio of the true lateral resolutions of the spectral data and the DEM. Since the Dirac delta function can be interpreted as

$$\lim_{\sigma_{\text{refl}} \to 0} g_{\sigma_{\text{refl}}}(x,y), \tag{4.11}$$

only the Gaussian formulation will be used for clarity and the case of the Dirac delta function will be denoted by $\sigma_{\text{refl}} = 0$. Notably, for $\sigma_{\text{refl}} > 0$ the algorithm still computes

one parameter value per pixel of the original image. Due to the Gaussian low-pass, however, the resulting map does not resemble the full image resolution.

Since $R_{\text{model}}\left(\tilde{\mathbf{s}}_i(x,y), \tilde{\mathbf{v}}_i(x,y), \tilde{\mathbf{n}}(x,y), \boldsymbol{\Psi}\left(\lambda\right)\right)$ is constant over the region Ω_{refl} Eq. (4.8) is minimised efficiently using the Levenberg-Marquardt method (cf. Appendix A). For brevity, the dependence on the wavelength λ and the spatial coordinates x and y is omitted. Expanding Eq. (4.8) and using $w_{\text{refl}} * 1 = 1$ yields

$$\begin{aligned} E_{\text{refl}} = \frac{1}{2} \sum_{i=1}^{N_{\text{im}}} & w_{\text{refl}} * R_{\text{meas},i}^2 \\ & -2R_{\text{model}}\left(\tilde{\mathbf{s}}_i, \tilde{\mathbf{v}}_i, \tilde{\mathbf{n}}, \boldsymbol{\Psi}\right)\left(w_{\text{refl}} * R_{\text{meas},i}\right) \\ & +R_{\text{model}}^2\left(\tilde{\mathbf{s}}_i, \tilde{\mathbf{v}}_i, \tilde{\mathbf{n}}, \boldsymbol{\Psi}\right). \end{aligned} \tag{4.12}$$

Consequently, the element (i,l) of the Jacobian $\mathbf{J}_{\text{refl}}$ of E_{refl}, i.e. the partial derivative of the residual corresponding to the ith image with respect to the lth parameter Ψ_l is

$$\begin{aligned} \mathbf{J}_{\text{refl}i,l} = & -\left(w_{\text{refl}} * R_{\text{meas},i}\right) \frac{\partial R_{\text{model}}\left(\tilde{\mathbf{s}}_i, \tilde{\mathbf{v}}_i, \tilde{\mathbf{n}}, \boldsymbol{\Psi}\right)}{\partial \theta_l} \\ & + R_{\text{model}}\left(\tilde{\mathbf{s}}_i, \tilde{\mathbf{v}}_i, \tilde{\mathbf{n}}, \boldsymbol{\Psi}\right) \frac{\partial R_{\text{model}}\left(\tilde{\mathbf{s}}_i, \tilde{\mathbf{v}}_i, \tilde{\mathbf{n}}, \boldsymbol{\Psi}\right)}{\partial \theta_l} \end{aligned} \tag{4.13}$$

From Eq. (4.9), Eq. (4.12) and Eq. (4.13) follows, that it is sufficient to apply the convolution to the directions, the measured reflectance and the squared measured reflectance before the optimisation procedure. The pre-filtering of the data leads to pixel-wise independent optimisation problems that may be solved in parallel.

The wavelength dependence of the reflectance and the parameters of the reflectance model leads to one optimisation problem per sensor channel, i.e. a different set of parameters is estimated for each channel of the instrument.

4.2.2 Hapke based normalisation

Due to the non-linear influence of the shading, i.e. the viewing geometry, on the reflectance spectrum, the Hapke AMSA model is chosen for the normalisation procedure. Other common models, e.g. the Lunar-Lambert model or the Minnaert model (cf. Section 2.3.2), consist of a product of wavelength dependent parameters and a phase angle dependent term. During the normalisation procedure, the wavelength dependent component cancels out and the model is not able to compensate wavelength dependent distortions of the spectrum due to shading.

Regardless of the multiple scattering approximation, the parameters of the Hapke model (cf. Section 2.3.3) may be categorised as the single-particle scattering albedo w, the phase function $f_{\text{phase}}(\alpha)$, parameters describing the opposition effect B_{SH_0}, h_{SH}, B_{CB_0}, h_{CB} and the unresolved surface roughness $\bar{\theta}$.

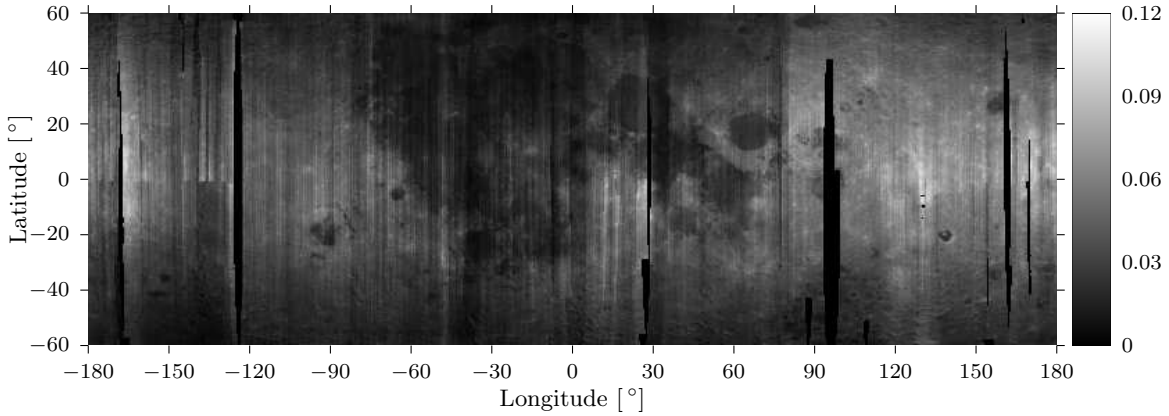

(a) Global average reflectance at 1579 nm.

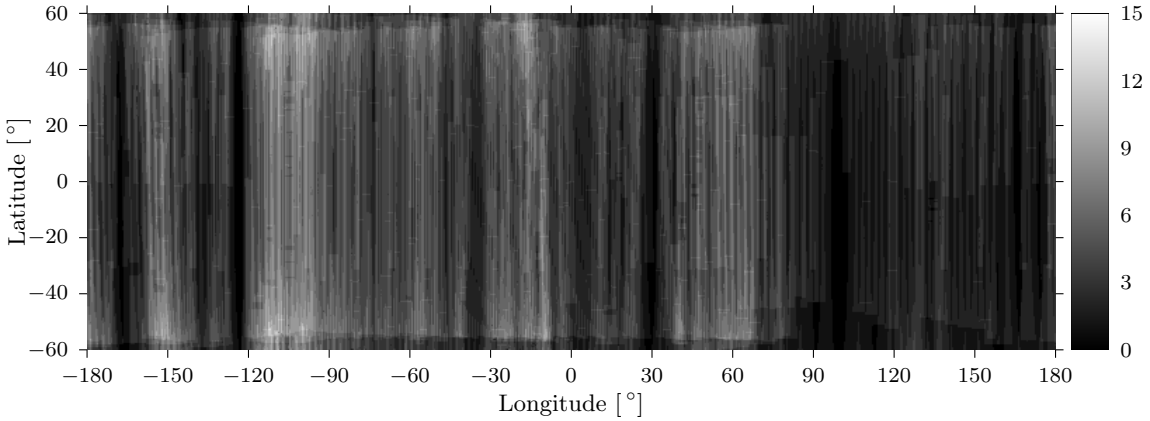

(b) No. of M^3 images.

Figure 4.4: Global coverage of the M^3 dataset. (a) The reflectance at 1579 nm averaged over all co-registered M^3 images, respectively. (b) Amount of co-registered images (c) Minimal incidence angle extracted from all M^3 images. (d) Maximal incidence angle extracted from all M^3 images.

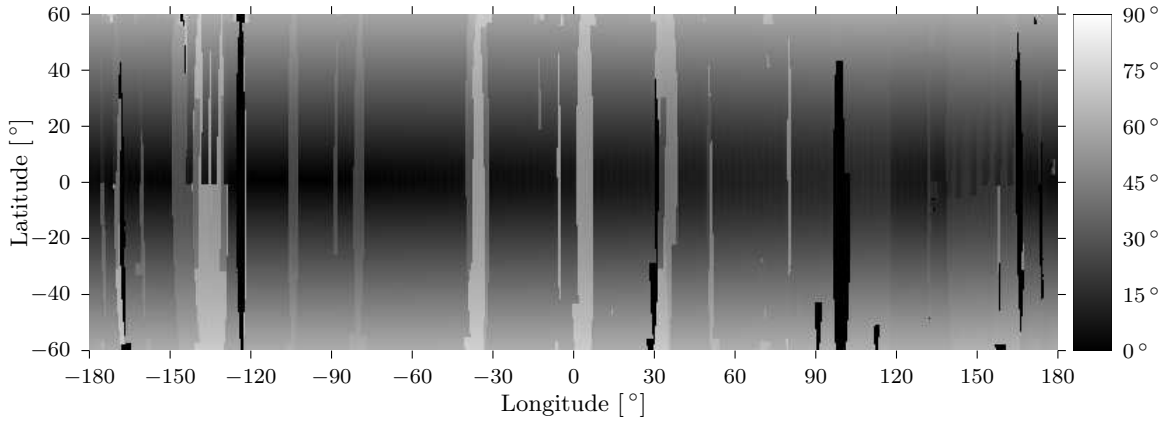

(c) Minimal incidence angle.

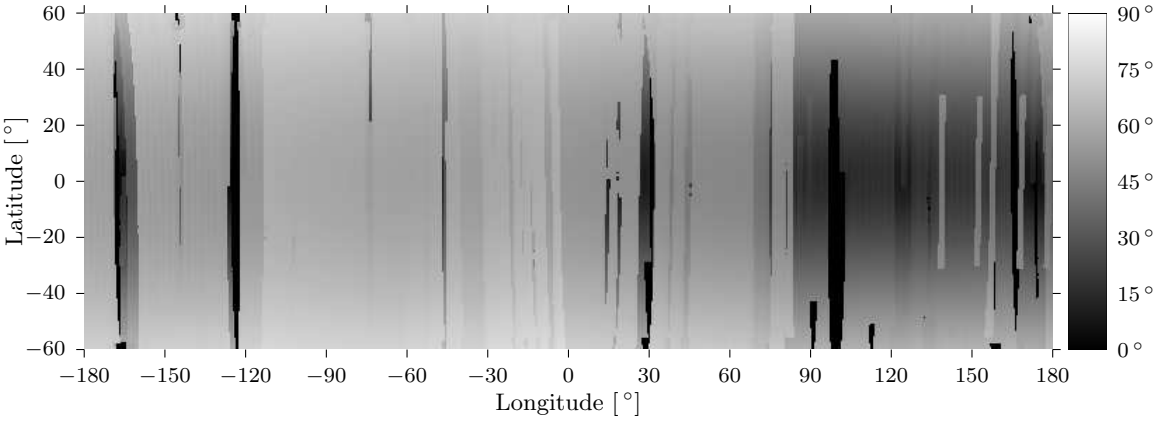

(d) Maximal incidence angle.

Figure 4.4: (continued)

Fig. 4.4(a) shows a global mosaic of the reflectance averaged over all M^3 images at 1579 nm at a resolution of 2 pixels per degree longitude and latitude. It extends to a latitude of ±60 °. The brightness variations are due to different illumination conditions and missing spectral normalisation re-emphasising the necessity for photometric normalisation. The corresponding number of co-registered images from different orbits is shown in Fig. 4.4(b). Fig. 4.4(c) and Fig. 4.4(d) show the minimum and maximum incidence angles, respectively. Due to the nadir orientation of the instrument, the emission angles are always close to zero. The maximum interval of the incidence angle for a specific region is about 60 ° while it is usually below 40 °. This small interval of incidence and thus also phase angles does not allow for an estimation of all surface parameters, since phase angles larger than 90 ° are completely missing. Furthermore, the limited number of observations

per region (cf. Fig. 4.4(b)) shows that the available range of phase angles is spread over a few images only. The areas with a high number of observations, however, show a very narrow range of phase angles. Thus, it is impossible to determine all parameters of the full Hapke model and the amount of estimated parameters has to be narrowed down significantly.

The most important parameter of the Hapke model in terms of the overall accuracy is the single-particle scattering function $f_{\text{phase}}(\alpha)$ as it governs the proportion of the incident light that is directly scattered into the imaging device and, more importantly, is part of the multiple scattering approximation within the Hapke AMSA model. The geologic interpretation of spectral data, however, aims at the determination of the mineralogical composition of the surface and a mixture of different surface materials leads to a mixture of single-scattering albedos (Mustard and Pieters, 1989; Mustard et al., 1998). Furthermore, Bertsatos and Makris (2010) state that the phase function of the lunar-Lambert model can be assumed to be constant if the range of different phase angles while the small-scale albedo variations are assumed to dominate the reconstruction error of photoclinometry. This is important to the photometric methods presented in Chapter 5. Since all M^3 observations where acquired at phase angles in the range $20\,^\circ$–$90\,^\circ$, the opposition effect is neglected and according to Shkuratov et al. (2005b) the effect of the unresolved surface roughness may be compensated by an albedo variation for small phase angle ranges.

In consequence, the estimation of parameters is restricted to the single-particle scattering albedo w and, in case of multiple observations covering a phase angle range of at least $10\,^\circ$, the single-particle scattering function $f_{\text{phase}}(\alpha)$. More correct, the range of available phase angles is rather narrow and, consequently, the estimated $f_{\text{phase}}(\alpha)$ resembles the scattering behaviour in the phase angle range and a physical interpretation of $f_{\text{phase}}(\alpha)$ should be treated with caution. The remaining parameters are adopted from Warell (2004) and the effect of both opposition effects is combined in one opposition effect term accordingly. Warell (2004) use a Double Henyey-Greenstein phase function $f_{\text{DHG}}(\alpha)$ which does not have a physically plausible limit (cf. Cornette and Shanks (1992)) and requires the estimation of two parameters. Due to the available range of phase angles, however, the second lobe is impossible to determine. The phase function proposed by Cornette and Shanks (1992) $f_{\text{CS}}(\alpha)$, in contrast, is determined by a single asymmetry parameter ξ. Thus, $f_{\text{CS}}(\alpha)$ is applied if the phase function is estimated from the available data to reduce the complexity of the optimisation problem.

The values of w and ξ are determined using the Levenberg-Marquard algorithm with implicit bounds (cf. Appendix A) and the limits for the parameters are set to be $w \in [0, 1]$ and $\xi \in [-1, 1]$.

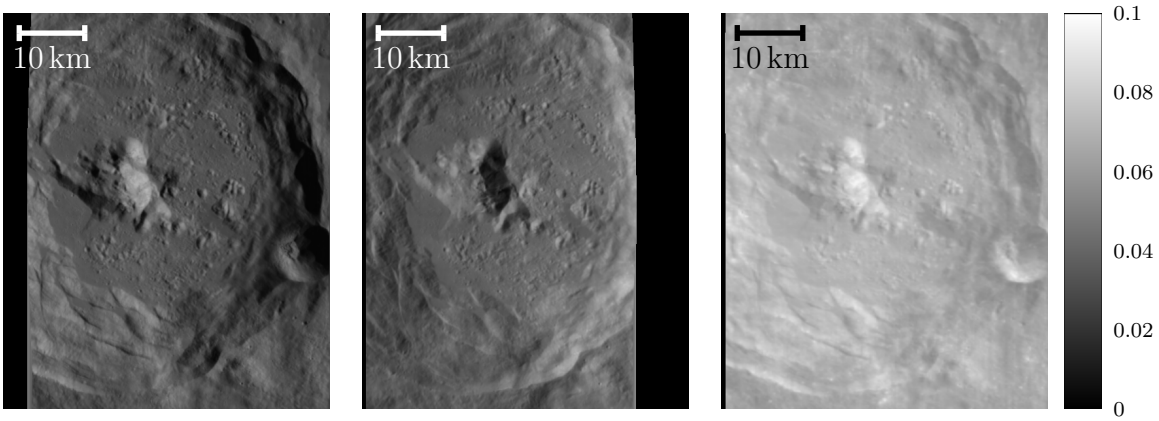

(a) M3G20090213T115953. (b) M3G20090422T193000. (c) M3G20090422T193000.

Figure 4.5: M^3 reflectance images of the lunar crater Lowell (103.4 °W, 13.0 °S). (a)–(c) M^3 refelctance images at 1579 nm. The corresponding phase angles are 59.9 °, 54.3 ° and 31.6 °, respectively. Image Credit: NASA/JPL-Caltech

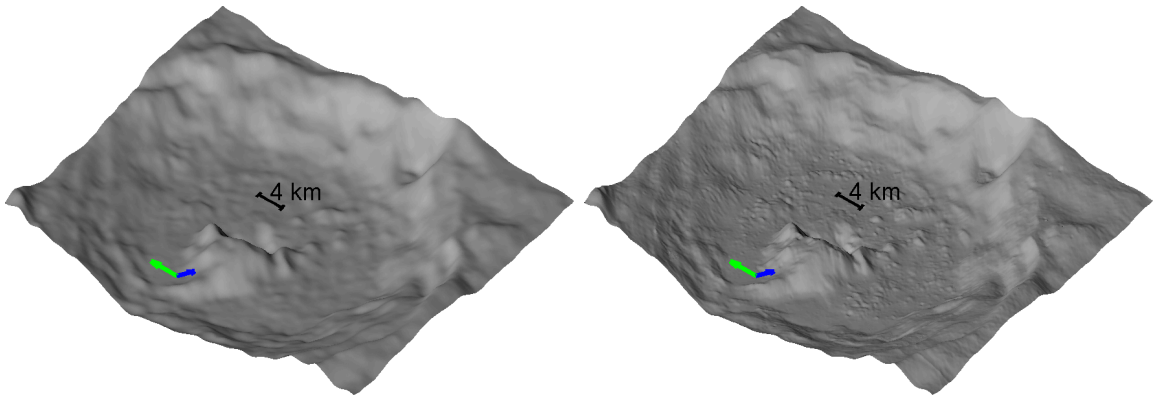

(a) GLD100. (b) Refined DEM.

Figure 4.6: Topographic models of the lunar crater Lowell (103.4 °W, 13.0 °S). (a) GLD100 by Scholten et al. (2012). (b) Refined DEM computed using the further extended shape from shading method described in Section 5.3.4. The lighting direction is indicated by the blue arrow and the green arrow points towards the north. All heights are three times exaggerated.

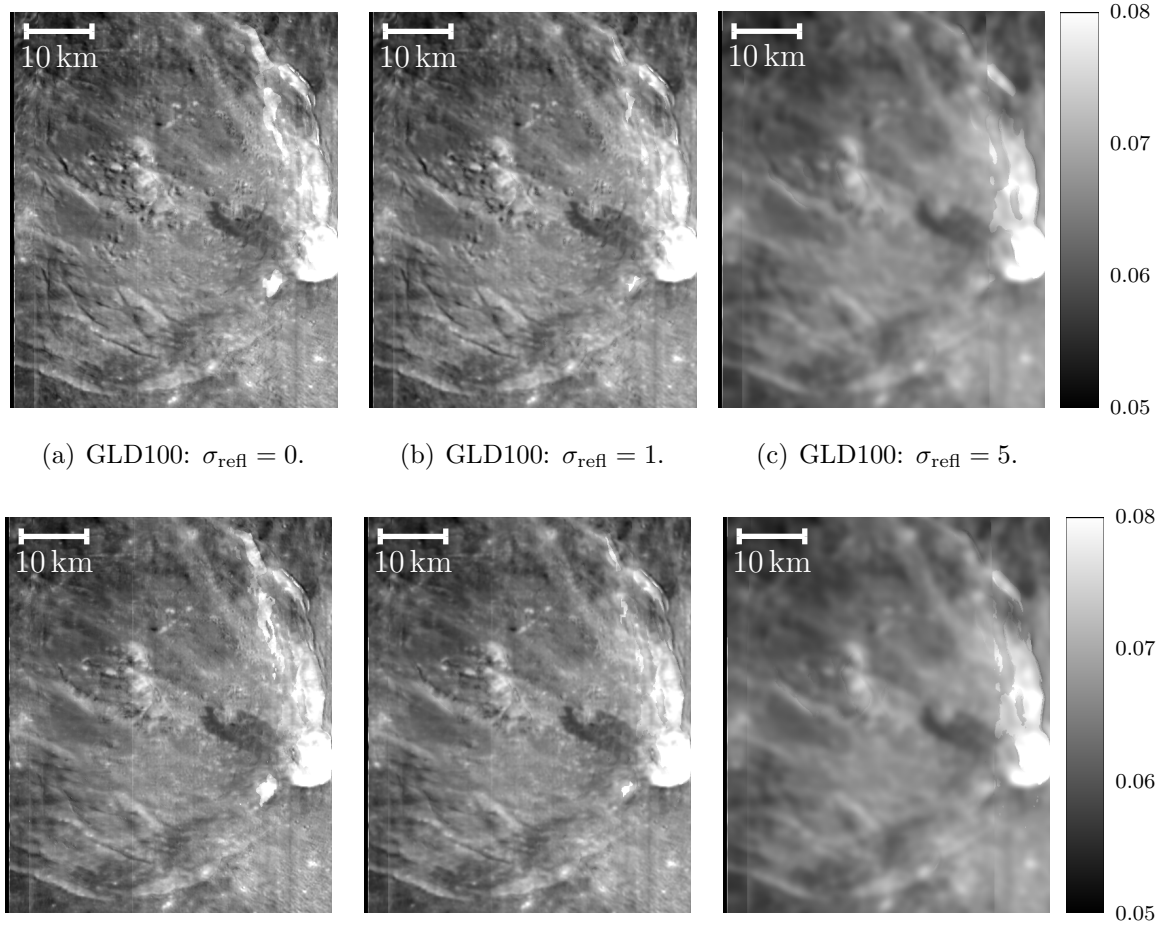

(a) GLD100: $\sigma_{\text{refl}} = 0$. (b) GLD100: $\sigma_{\text{refl}} = 1$. (c) GLD100: $\sigma_{\text{refl}} = 5$.

(d) Refined DEM: $\sigma_{\text{refl}} = 0$. (e) Refined DEM: $\sigma_{\text{refl}} = 1$. (f) Refined DEM: $\sigma_{\text{refl}} = 5$.

Figure 4.7: Influence of the parameter σ_{refl}. (a)–(c) Normalised reflectance at 1579 nm for various values of σ_{refl}. The topography was corrected using the GLD100. (d)–(f) Normalised reflectance at 1579 nm for various values of σ_{refl}. The topography was corrected using the refined DEM.

4.2.3 Results

The influence of the parameter σ_{refl} and a comparison to the official normalised M^3 data published on the internet[3] is presented for the lunar crater Lowell (103.4 °W, 13.0 °S). It is captured in the three M^3 images M3G20090213T115953, M3G20090422T193000 and M3G20090713T192732. The corresponding phase angles are 59.9 °, 54.3 ° and 31.6 °, respectively. The corresponding images at 1579 nm are shown in Fig. 4.5.

[3]Available at http://pds-imaging.jpl.nasa.gov/volumes/m3.html (Level 2 data)

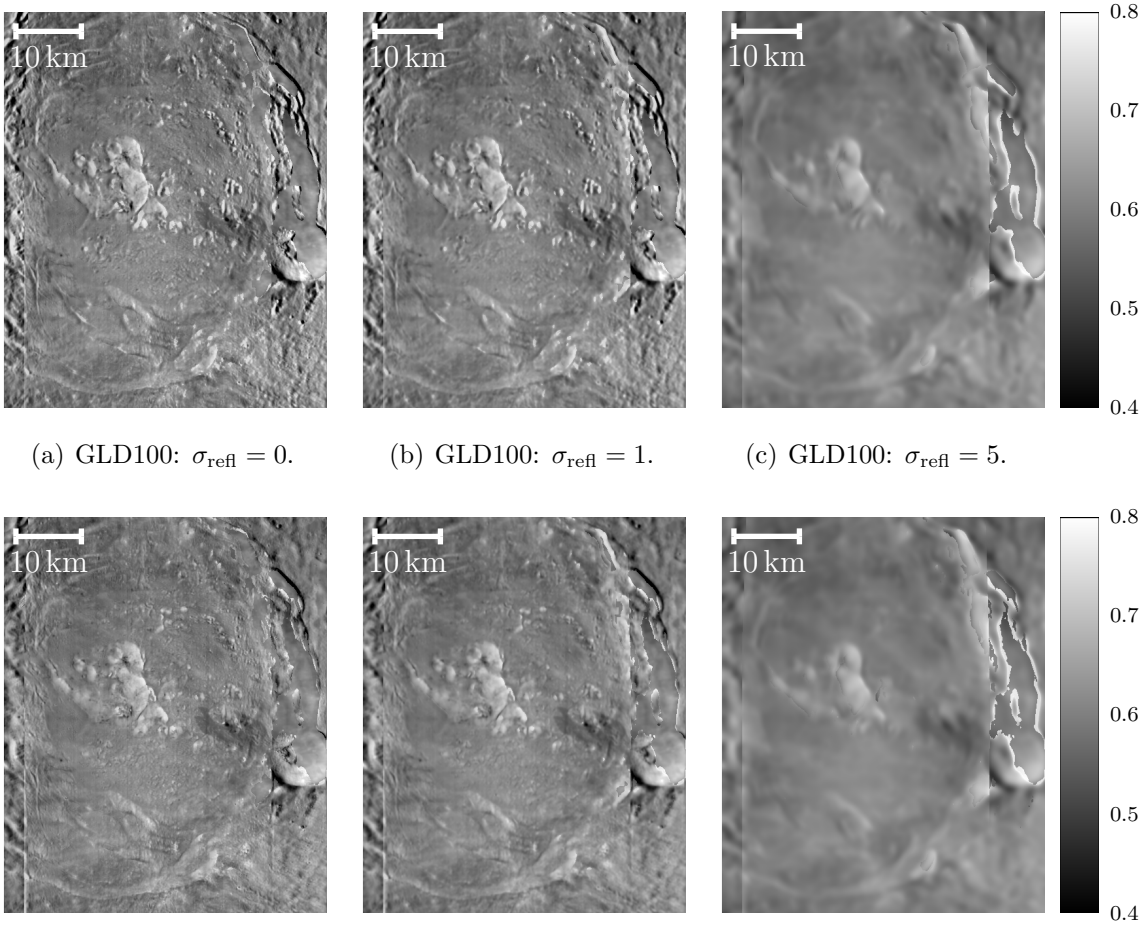

(a) GLD100: $\sigma_{\text{refl}} = 0$. (b) GLD100: $\sigma_{\text{refl}} = 1$. (c) GLD100: $\sigma_{\text{refl}} = 5$.

(d) Refined DEM: $\sigma_{\text{refl}} = 0$. (e) Refined DEM: $\sigma_{\text{refl}} = 1$. (f) Refined DEM: $\sigma_{\text{refl}} = 5$.

Figure 4.8: Influence of the parameter σ_{refl}. (a)–(c) Estimated single-scattering albedo w at 1579 nm for various values of σ_{refl}. The topography was corrected using the GLD100. (d)–(f) Estimated single-scattering albedo w at 1579 nm for various values of σ_{refl}. The topography was corrected using the refined DEM.

The GLD100 DEM and the refined DEM computed using the further extended shape from shading method (cf. Section 5.3.4) are shown in Fig. 4.6. For both DEM, the influence of the parameter σ_{refl} on the resulting reflectance is shown in Fig. 4.7. While there are differences apparent for $\sigma_{\text{refl}} = 0$ and $\sigma_{\text{refl}} = 1$, e.g. near the central peak and in the southern half of the crater, the shading caused by the local topography is visible in the GLD100 based normalisation. The normalised reflectance for larger values of σ_{refl} appears to be identical.

The estimated single-scattering albedo w (cf. Fig. 4.8) shows the same behaviour. The

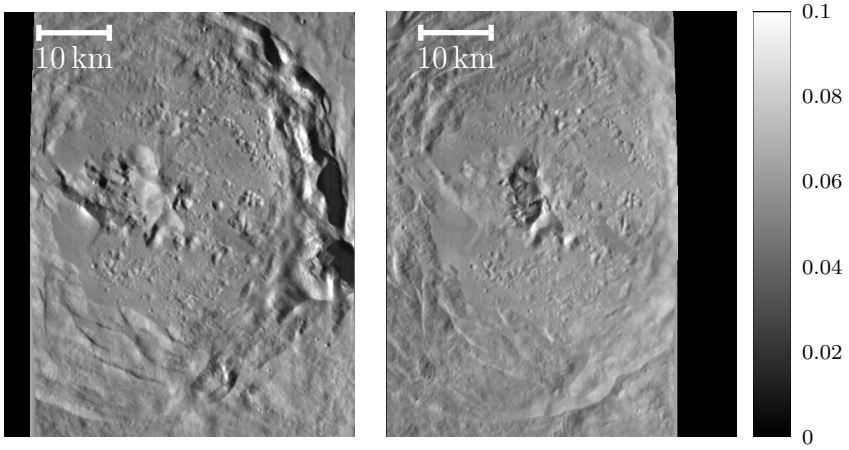

(a) M3G20090213T115953. (b) M3G20090422T193000.

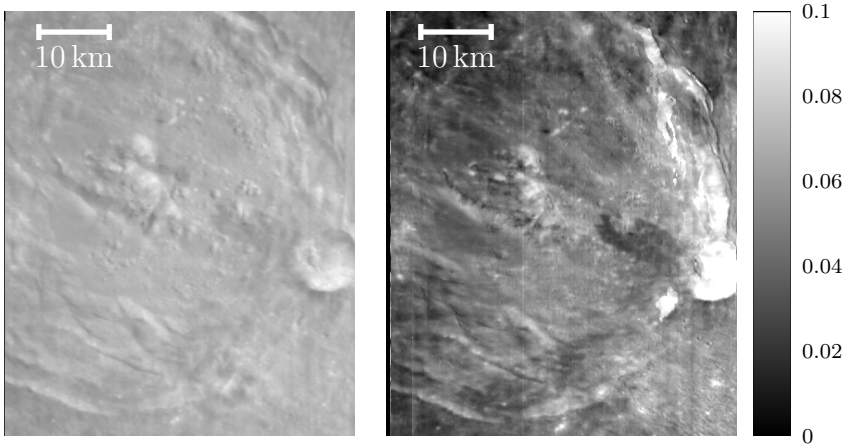

(c) M3G20090713T192732. (d) Proposed normalisation method.

Figure 4.9: Comparison to the official M^3 reflectance. (a)–(c) M^3 images at 1579 nm normalised using the global polynomial approach by Besse et al. (2013a). (d) M^3 reflectance at 1579 nm normalised using the proposed method. The reflectance parameters are estimated pixel-wise and the information of all available images is included.

introduced low-pass filtering thus effectively reduces the lateral resolution of the obtained parameter maps leading to identical results. Consequently, the reflectance parameter estimation may be applied at a different resolution than the spatial resolution of the image. This is important for the DEM refinement procedures detailed in Chapter 5 that assumes an a-priori known DEM of lower lateral resolution. The reflectance parameters are initially estimated using high values of σ_{refl} and the DEM may be iteratively refined

by reducing σ_{refl} after a new refined DEM has been computed.

Fig. 4.9 shows the officially distributed normalised M^3 reflectance maps at 1579 nm and the result of the proposed normalisation procedure. It is evident that the global polynomial approach by Besse et al. (2013a) does not completely remove the influence of the local topography. Furthermore, the global coefficients of the polynomial do not match the surface properties of the targeted area well, i.e. the image acquired close to 30 ° phase angle is systematically brighter than the images acquired at large phase angles. The integrated refinement of the DEM and normalisation of the spectral data (cf. Fig. 4.9(d)), in contrast, does not show significant artefacts related to the local topography. The average brightness obtained by the proposed method is close to the average brightness of the normalised reflectance image acquired at 30 ° phase angle, but some regions on the crater floor show significantly lower reflectance values.

Due to the lack of ground truth data for the single-scattering albedo w and the asymmetry parameter ξ and the dependence on the DEM, the evaluation is purely qualitative. An evaluation based on synthetic images is discussed in the evaluation of the surface refinement methods (cf. Section 5.5.1).There are, however, some noteworthy findings which are discussed in detail and examined according to plausibility and relation to geologic effects. The images, the derived reflectance parameters and the DEM are shown in Fig. 4.10. The refined DEM was computed using the photometric methods described in Section 5.2

The single-scattering albedo w and the asymmetry parameter ξ of $p_{\text{CS}}(\alpha)$ were estimated based on the refined DEM of the region around the Mairan highland domes termed Mairan T, Mairan "middle", and Mairan "south" by Wilson and Head (2003) (cf. Fig. 4.10(d) and Fig. 4.10(e)). These volcanic edifices are discussed in detail e.g. by Head and McCord (1978) and Wilson and Head (2003). To remove the effect of thermal radiation on the reflectance data, the thermal component is subtracted from the image radiances according to the method described in Section 4.1.

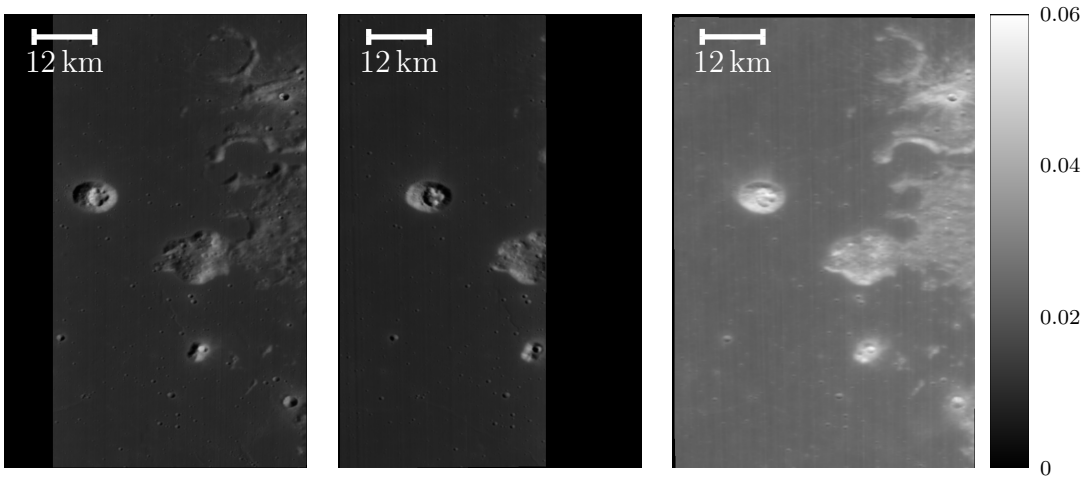

(a) M^3 reflectance image 1. (b) M^3 reflectance image 2. (c) M^3 reflectance image 3.

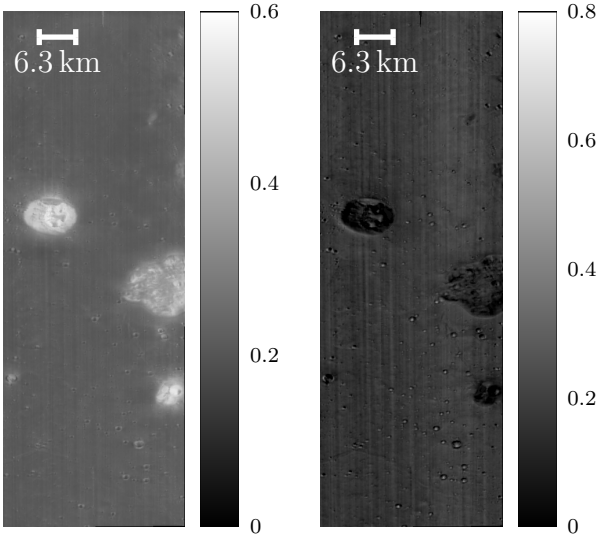

(d) Single scattering albedo w.

(e) Asymmetry parameter ξ.

Figure 4.10: Surface refinement of the Mairan region (longitude 311 °E–313 °E, latitude 40 °N–43 °N). The westernmost dome Mairan T is of nearly circular shape with a diameter of about 6.5 km (a)–(c) M^3 reflectance images at 1579 nm. Image credit: NASA/JPL-Caltech. (d) Estimated single-scattering albedo w at 1579 nm. (e) Estimated single-particle scattering function parameter ξ at 1579 nm. (f) GLD100. (g) Result of the shape from shading algorithm. The elevation axis of both DEM is scaled by a factor of three. The lighting direction is indicated by the blue arrow and the green arrow points towards the north.

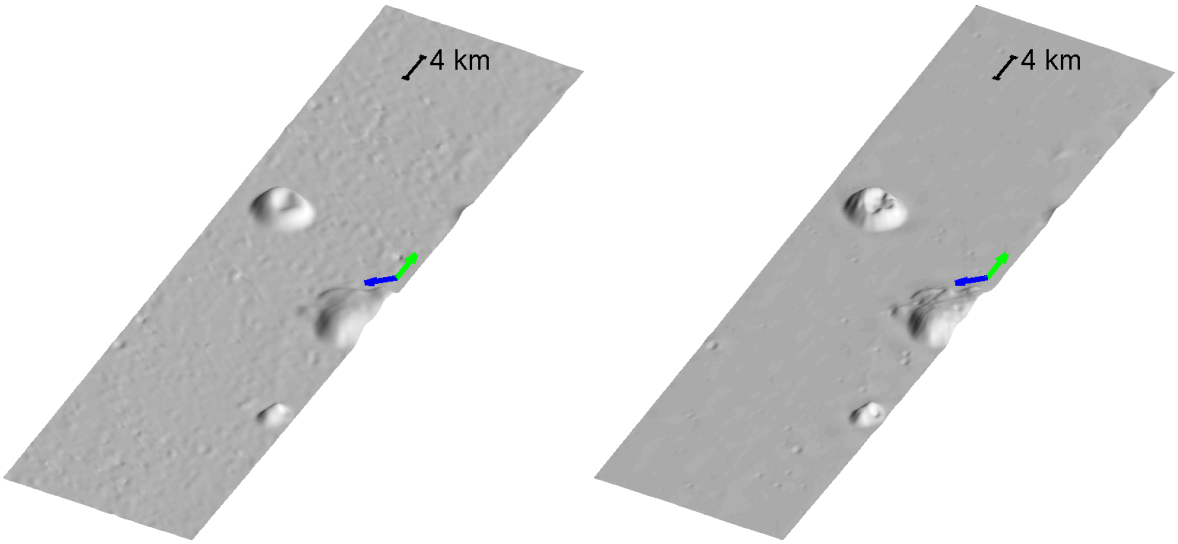

(f) GLD100 DEM. (g) Refined DEM.

Figure 4.10: (continued)

The wavelength dependence of the single-scattering albedo w and the single-particle scattering function parameter ξ is shown in Fig. 4.11(b) and Fig. 4.11(c), respectively. The lateral distribution, i.e. the parameters maps at 1579 nm for the volcanoes is shown in Fig. 4.12. The two spectra represent the wavelength-dependent reflectance parameters of the undisturbed mare surface and the volcano Mairan T, indicating systematic differences in the reflectance properties between the different units. All three domes are considerably brighter than the surrounding mare. This change in brightness might be due to a different grain size, a different optical maturity or a different mineral composition of the surface. The Mairan domes, however, are widely considered to be of a mineral composition which is strongly different from that of mare and typical highland surfaces, as discussed, among others, by Head and McCord (1978) and Glotch et al. (2011). The volcanic domes Mairan T and Mairan "south" are characterised by significantly lower ξ values than the surrounding mare surface, corresponding to a lower slope of the single-particle scattering function in the regarded range of phase angles. This supports the interpretation of different surface materials. In contrast, the ξ values associated with the dome Mairan "middle" are more similar to those of the surrounding mare.

Furthermore, as a general rule small fresh craters are characterised by increased ξ values on the crater floors and lowered ξ values on their inner walls and outer rims, i.e. the inner walls and outer rims have less steep single-particle scattering functions in the regarded phase angle range than the crater floors (cf. Fig. 4.12(h)). The craters shown have a diameter of up to 2 km which corresponds to 20 pixels. These craters are supposed to be within the resolution limit and typically show a depth-to-diameter ratio of 0.2 when

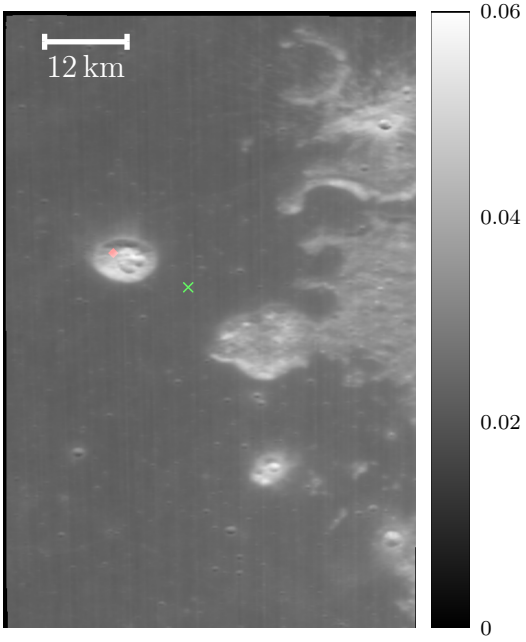

(a) M^3 reflectance image.

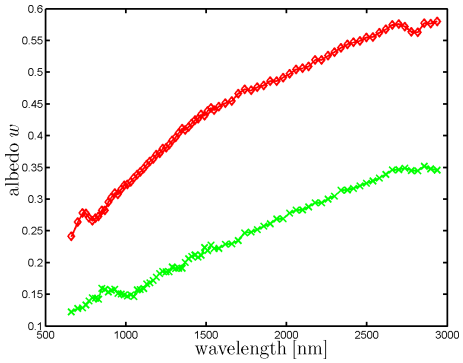

(b) Spectrum of the single-scattering albedo w at 1579 nm.

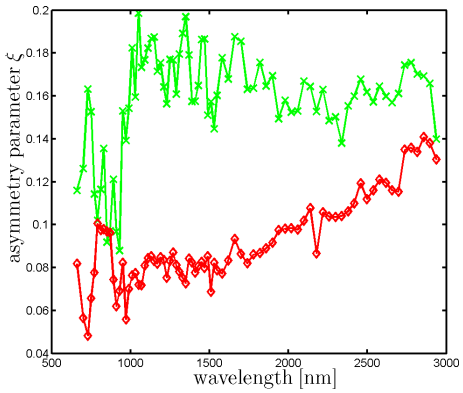

(c) Spectrum of the asymmetry parameter ξ at 1579 nm.

Figure 4.11: Spectral reflectance parameters of the Mairan region (longitude 311 °E–313 °E, latitude 40 °N–43 °N). The westernmost dome Mairan T is of nearly circular shape with a diameter of about 6.5 km. (a) M^3 reflectance images. Image credit: NASA/JPL-Caltech. (b) Albedo spectrum for the pixels marked in (a) as green and red square. (c) Asymmetry parameter spectrum for the pixels marked in (a) as green and red square.

having a fresh appearance, as it is known from lunar crater catalogue data (Wood and Andersson, 1978). Since the smaller craters show the same characteristic lowered ξ value on the crater rim, it is assumed that the lowered ξ values on the inner crater walls and outer rims are not a depth-related artefact. However, the high ξ values on the crater floors may be due to the cast shadows that occur for larger phase angles, pretending an excessively strong decrease in radiance with increasing phase angle. According to Poulet et al. (2002), the size of the regolith particles is a major factor governing the single-particle scattering function. In addition to that, it is pointed out by Dollfus (1998) that the particle size shows a clear inverse correlation with soil maturity (the period of time the

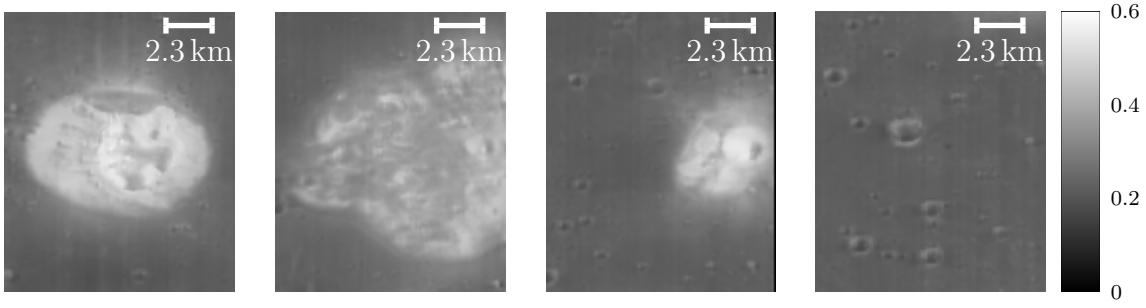

(a) Mairan T: w. (b) Mairan "middle": w. (c) Mairan "south": w. (d) Cluster of craters: w.

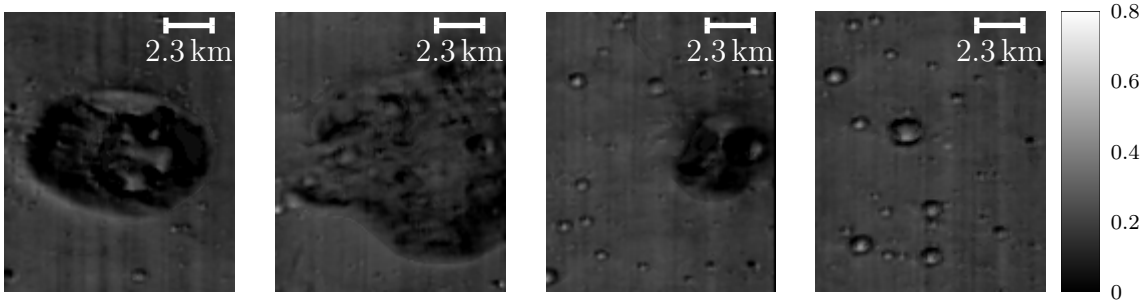

(e) Mairan T: ξ. (f) Mairan "middle": ξ. (g) Mairan "south": ξ. (h) Cluster of craters: ξ.

Figure 4.12: Reflectance parameters map of the Mairan region (longitude 311 °E–313 °E, latitude 40 °N–43 °N). (a)–(d) Single-scattering albedo w at 1579 nm for the Mairan domes and a cluster of small craters. (e)–(h) Asymmetry parameter ξ at 1579 nm for the Mairan domes and a cluster of small craters. In comparison to the surrounding mare surface, Mairan T and Mairan "south" show an increased albedo and a decreased asymmetry parameter, while in contrast Mairan "middle" shows a slightly increased albedo but only a small change of the asymmetry parameter. Interestingly, the inner walls and outer rims of small, fresh craters also show increased single-scattering albedos and decreased asymmetry parameters.

surface material has been exposed to space weathering), i.e. particle size decreases with increasing soil maturity. Hence, assuming that the observed variations of ξ across small fresh craters may indicate systematic differences between the particle sizes associated with the crater floors and the inclined inner walls and outer rims, respectively. A possible explanation is a continuous exposure of immature material (i.e. material not yet altered by space weathering effects) on the inner crater walls and outer rims, as here the uppermost regolith layer may tend to slide down the steep slopes and uncover the material beneath. This, however, is just a hypothesis due to the mentioned possibly shadowing effect.

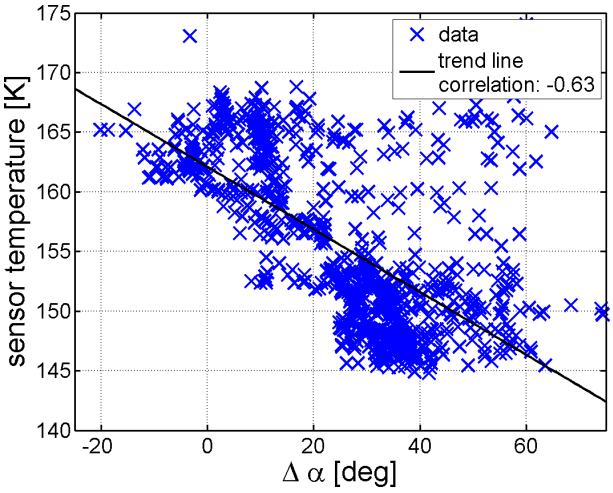

Figure 4.13: Phase angle dependence of the sensor temperature. The M^3 sensor temperature is scattered over the corresponding phase angle change. The correlation coefficient amounts to -0.63 and the reference phase angle is 30 °.

4.3 Phase angle/Sensor temperature based effects

It is well known that the radiance measured by the M^3 sensor has been severely distorted by the sensor temperature (Pieters et al., 2013; Lundeen et al., 2011; Besse et al., 2013a). A correction based on an area observed under six different sensor temperature conditions has been presented by Lundeen et al. (2011) and applied to the published v3 version of the M^3 dataset. Simultaneously, Grumpe and Wöhler (2011a) discovered systematic deviations between normalised reflectance values derived from co-registered images acquired at different phase angles based on the original version of the M^3 dataset, which was published in two parts, i.e the v1 version and the v2 version of the M^3 dataset. For brevity, the v1 dataset and the v2 dataset are both denoted v1 in this thesis. Due to the correlation between the change of the phase angle and the sensor temperature (cf. Fig. 4.13), it is not possible to distinguish between these effects. This section deals with the correction of the phase angle effect described by Grumpe and Wöhler (2011a) due to the development history of the framework. Notably, the effect will be termed sensor temperature effect due to the widely accepted influence of the sensor temperature as described by Lundeen et al. (2011). All methods may be applied based on the sensor temperature by exchanging phase angle and sensor temperature.

The two distinct methods are based on the same dataset given in Section 4.3.1. Since the continuum-removed (CR) reflectance is commonly used in geologic interpretations, both methods aim at the compensation of the influence of the phase angle differences on the CR spectrum. The CR spectrum, however, is obtained at the end of the very complex and highly non-linear process chain. Hence, Section 4.3.2 describes a method to remove

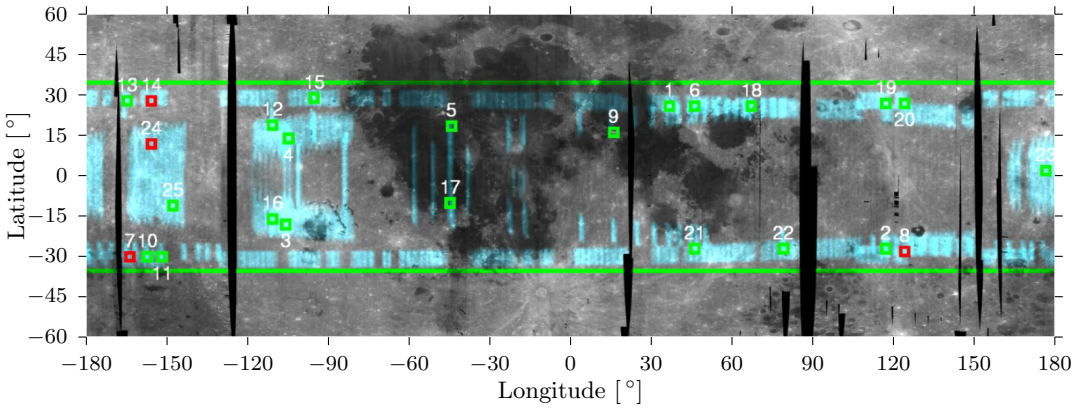

Figure 4.14: Dataset for the correction of the sensor temperature effect: All regions that contain measurements at $\alpha_0 \pm 5\,^\circ$ are emphasised by a light bluish shade. The numbered rectangles mark the 25 selected regions. A red rectangle indicates that the available data in the selected region did not contain a sufficiently large phase angle range. Due to geometric reasons, the search was limited to $\pm 35\,^\circ$. The limits are marked by the horizontal green lines.

the effects from the already normalised CR reflectance. In contrast, Section 4.3.3 gives a method to modify the radiance at the beginning of the processing chain which requires simplifications of the process chain. In contrast to the method by Lundeen et al. (2011), the presented methods do not require all involved images to be co-registered. The only requirement is that one co-registered image at a reference phase angle is available with other images may be required at arbitrary but different phase angles.

4.3.1 Dataset and data processing

The reference phase angle is set according to the standard geometry, i.e. $\alpha_0 = 30\,^\circ$ (Pieters, 1999). At a scale of 20 pixel per degree, 25 regions containing measurements at $\alpha_0 \pm 5\,^\circ$ and measurements at arbitrary phase angles are selected all over the lunar surface. The selected regions are shown in Fig. 4.14 and are spread as uniformly distributed as possible. Images that cover only a small fraction of the region are removed from the dataset. Accordingly, some regions no longer contain measurements within the range $\alpha_0 \pm 5\,^\circ$, and are discarded. These regions are marked by red rectangles while the remaining regions are marked by green rectangles. The detailed locations, M^3 image names and mean phase angles per image are given in Table 4.1.

At first, the thermal emission component is estimated and compensated (cf. Section 4.1). To ensure co-registered M^3 images, the techniques described in Section 6.3 are applied. The photometric methods detailed in Chapter 5 are then applied to derive high

Table 4.1: Detailed information on the selected regions. The table summarises the selected regions, the corresponding location on the lunar surface in selenographic latitude and longitude, the name of the M^3 images that contain the selected regions and the corresponding mean phase angles, respectively.

Location		Dataset	
Name	Selenographic coordinates	M^3 images	Mean phase angles [°]
Region 1	35.5 °E–37.5 °E 25.0 °N–27.0 °N	M3G20090106T152345	33.8
		M3G20090605T212253	25.2
		M3G20090730T122229	50.0
Region 2	116.0 °E–118.0 °E 26.0 °S–28.0 °S	M3G20090530T201123	36.0
		M3G20090627T031213	20.9
Region 3	105.0 °W–107.0 °W 17.0 °S–19.0 °S	M3G20090213T155552	56.9
		M3G20090213T180532	61.7
		M3G20090423T012445	53.2
		M3G20090713T233042	28.5
Region 4	104.0 °W–106.0 °W 13.0 °N–15.0 °N	M3G20090213T140913	55.2
		M3G20090213T155552	60.3
		M3G20090422T213930	56.3
		M3G20090422T235626	52.0
		M3G20090616T115723	16.8
		M3G20090713T233042	33.3
Region 5	44.0 °W–45.0 °W 18.0 °N–19.0 °N	M3G20081119T021733	28.7
		M3G20090112T165924	28.0
		M3G20090209T014431	59.2
Region 6	45.0 °E–47.0 °E 25.0 °N–27.0 °N	M3G20090105T194305	30.8
		M3G20090202T042831	52.2
		M3G20090605T040250	24.1
		M3G20090729T185951	47.6
Region 7	163.0 °W–165.0 °W 29.0 °S–31.0 °S	M3G20090621T065503	37.9
		M3G20090718T101402	37.3
Region 9	15.0 °E–16.6 °E 15.6 °N–17.0 °N	M3G20090108T044645	28.0
		M3G20090204T113444	48.7
		M3G20090204T134332	56.5

Table 4.1: (continued)

Location		Dataset	
Name	Selenographic coordinates	M^3 images	Mean phase angles [°]
Region 10	156.0 °W–158.0 °W 29.0 °S–31.0 °S	M3G20090121T033745	43.6
		M3G20090426T235045	57.8
		M3G20090620T134543	31.1
		M3G20090620T181042	34.5
		M3G20090717T211502	37.8
		M3G20090718T014252	48.0
		M3G20090814T061444	53.3
Region 11	151.0 °W–153.0 °W 29.0 °S–31.0 °S	M3G20090426T141200	58.3
		M3G20090620T051312	31.5
		M3G20090717T124352	38.1
		M3G20090717T171142	48.5
		M3G20090813T213525	56.5
Region 12	110.0 °W–112.0 °W 18.0 °N–20.0 °N	M3G20081124T023528	29.6
		M3G20090214T020800	59.8
		M3G20090214T034413	65.2
		M3G20090423T093030	54.0
		M3G20090617T005342	24.9
		M3G20090714T080142	27.3
Region 13	164.0 °W–166.0 °W 27.0 °N–29.0 °N	M3G20081225T133906	31.6
		M3G20090621T025007	24.0
		M3G20090621T065503	26.3
		M3G20090718T101402	36.4
Region 15	94.5 °W–96.5 °W 18.0 °N–20.0 °N	M3G20090212T222453	59.9
		M3G20090615T185632	20.9
		M3G20090615T232402	19.8
		M3G20090713T064052	35.6
Region 16	110.0 °W–112.0 °W 15.0 °S–17.0 °S	M3G20081124T023528	27.8
		M3G20090214T020800	60.5
		M3G20090214T034413	65.2
		M3G20090423T093030	54.7
		M3G20090714T080142	27.0

Table 4.1: (continued)

Location		Dataset	
Name	Selenographic coordinates	M^3 images	Mean phase angles [°]
Region 17	44.0 °W–46.0 °W 9.0 °S–11.0 °S	M3G20081119T021733	28.2
		M3G20090112T165924	26.2
		M3G20090209T014431	54.9
Region 18	66.0 °E–68.0 °E 25.0 °N–27.0 °N	M3G20090131T130631	51.7
		M3G20090131T151551	56.5
		M3G20090603T134223	30.6
Region 19	116.0 °E–118.0 °E 26.0 °N–28.0 °N	M3G20081231T113333	32.8
		M3G20090530T160828	30.0
		M3G20090530T201123	21.4
		M3G20090627T031213	39.3
Region 20	123.0 °E–125.0 °E 26.0 °N–28.0 °N	M3G20090530T030925	30.4
		M3G20090530T073724	21.8
		M3G20090626T142653	38.0
Region 21	45.0 °E–47.0 °E 26.0 °S–28.0 °S	M3G20090105T194305	32.1
		M3G20090202T024131	49.0
		M3G20090202T042831	54.0
		M3G20090605T040250	32.5
		M3G20090729T185951	43.6
Region 22	78.0 °E–80.0 °E 26.0 °S–28.0 °S	M3G20090103T084105	32.0
		M3G20090602T163012	42.6
Region 23	175.5 °E–177.5 °E 1.0 °N–3.0 °N	M3G20090123T064545	38.1
		M3G20090719T203200	26.3
		M3G20090720T003411	40.0
Region 25	147.0 °W–149.0 °W 10.0 °S–12.0 °S	M3G20090426T061945	52.2
		M3G20090717T041548	25.9
		M3G20090717T084032	38.9
		M3G20090813T125543	51.7

resolution DEM of all regions. Based on the derived DEM, areas with no surface slopes, i.e. slopes less than 2 °, are segmented. All correction methods are based on these datasets without surface slopes to distinguish between effects caused by the local topography and the target effects.

4.3.2 CR based correction method

The geologic interpretation is commonly based on characteristic parameters of the ferrous absorption troughs near 1000 nm and near 2000 nm (cf. Section 6.2.1 for computation details). These parameters, e.g. the position of the reflectance minima and the depth of the absorption troughs, show a clear phase angle dependence as shown in Fig. 4.15. Since the effect is supposed to be corrected in the v3 dataset, this method is developed based on the v1 dataset.

These parameters are extracted from the CR reflectance R_{CR} and thus, an empirical correction of the CR reflectance is computed:

$$\hat{R}_{\mathrm{CR}}(\lambda) = a_{\mathrm{CR}}(\lambda, \alpha) R_{\mathrm{CR}}(\lambda) + b_{\mathrm{CR}}(\lambda, \alpha) \tag{4.14}$$

where a different set of coefficients $a_{\mathrm{CR}} = a_{\mathrm{CR},1}\Delta\alpha + a_{\mathrm{CR},0}$ and $b_{\mathrm{CR}} = b_{\mathrm{CR},1}\Delta\alpha + b_{\mathrm{CR},0}$ is computed for each sensor channel, respectively. The coefficients are based on the phase angle change $\Delta\alpha = \alpha - \alpha_0$ where $\alpha_0 = 30\,^\circ$ denotes the phase angle at standard geometry. By minimising the sum of squared differences between the CR reflectance of all images acquired at a phase angle α and the image acquired at the reference phase angle $\alpha_{\mathrm{ref}} = 30\,^\circ \pm 2\,^\circ$, the values of the coefficients are determined. Notably, the reflectance obtained at α_{ref} is not corrected.

4.3.3 Radiance based correction method

If the effect is sensor temperature related, the origin resides at the beginning of the process chain. Thus, a second approach directly modifying the measured radiance is developed. Since the sensor is based on HgCdTe semiconductors, a multiplicative (gain) and an additive (offset) component are assumed (Feng et al., 2011):

$$L_{\mathrm{corr}}(\alpha, \lambda) = g_{\mathrm{temp}}(\Delta\alpha, \lambda) L_{\mathrm{sensor}}(\lambda) + c_{\mathrm{temp}}(\Delta\alpha, \lambda). \tag{4.15}$$

The corrected and the distorted radiances are denoted by $L_{\mathrm{corr}}(\alpha, \lambda)$ and $L_{\mathrm{sensor}}(\lambda)$, respectively. The functions $g_{\mathrm{temp}}(\Delta\alpha, \lambda)$ and $c_{\mathrm{temp}}(\Delta\alpha, \lambda)$ represent a temperature/phase angle dependent gain compensation and a temperature/phase angle dependent dark current compensation. Both components are assumed to be a polynomial of degree d_{gain} and

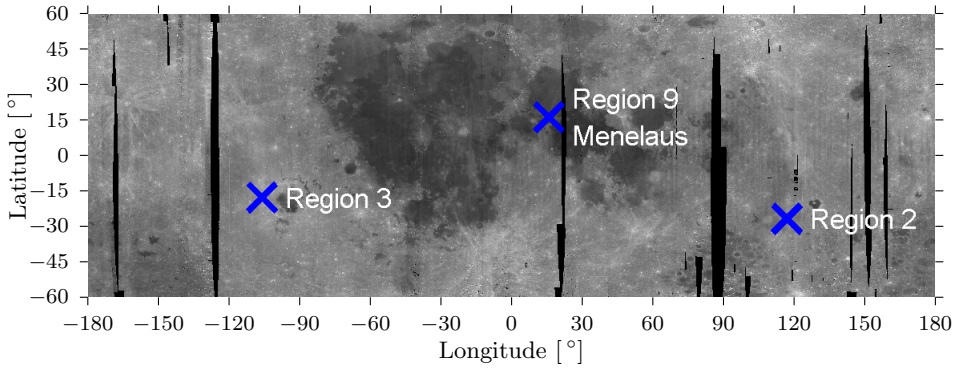

(a) Example regions.

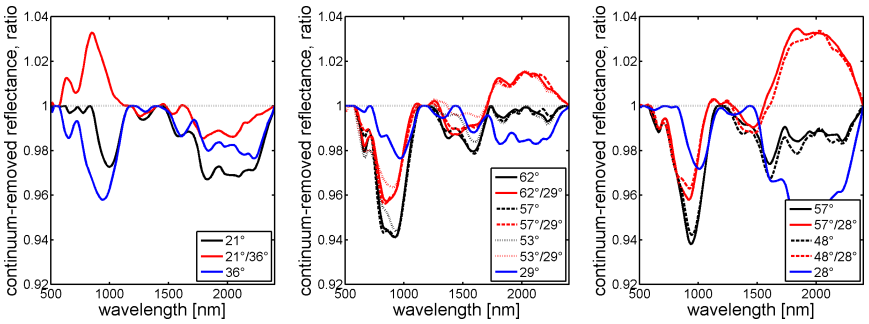

(b) Average CR spectra.

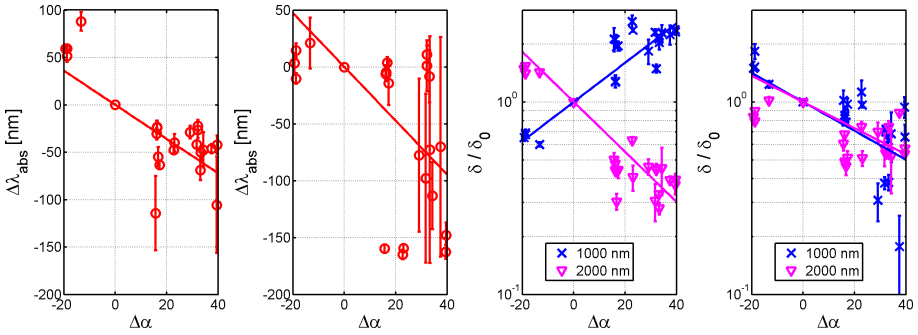

(c) Spectral parameters.

Figure 4.15: CR spectra dependence on the phase angle. (a) Location of three selected regions containing images at multiple phase angles. (b) The black and blue lines correspond to the CR spectra of the normalised reflectance averaged over the non-inclined areas within each image, respectively. The red lines display the ratio with respect to the reference image. (c) The change of the reflectance minimum's position and the depth of the absorption trough at 1000 nm are shown over the change in the phase angle with respect to the reference image. For comparison, the normalisation described in Section 4.2 and the data by Hicks et al. (2011) are presented. All figures are based on the v1 dataset.

d_{offset} in the phase angle change $\Delta\alpha = \alpha - \alpha_0$, i.e.

$$g_{\text{temp}}(\Delta\alpha, \lambda) = \sum_{d=0}^{d_{\text{gain}}} g_d(\lambda)\Delta\alpha^d \text{ and} \tag{4.16}$$

$$c_{\text{temp}}(\Delta\alpha, \lambda) = \sum_{d=0}^{d_{\text{offset}}} c_d(\lambda)\Delta\alpha^d \tag{4.17}$$

with a total $N_{\text{coeff}} = d_{\text{gain}} + d_{\text{offset}} + 2$ coefficients denoted by $g_d(\lambda)$ and $c_d(\lambda)$ for the gain polynomial and the offset polynomial, respectively. Notably, Feng et al. (2011) show that the temperature dependent gain is linear in $1/T_{\text{sensor}}$ in the corresponding sensor temperature range $T_{\text{sensor}} \in [145\,\text{K}, 170\,\text{K}]$. Thus, the temperature based correction should use the formulation

$$\Delta\alpha \leftarrow \frac{1}{T_{\text{sensor}}} - \frac{1}{T_{\text{sensor}_0}}. \tag{4.18}$$

The reference sensor temperature is $T_{\text{sensor}_0} = 156\,\text{K}$ (Lundeen et al., 2011; Green et al., 2011). Here, the real and the reference phase angle are denoted by α and α_0, respectively. The reference phase angle is set to $\alpha_0 = 30\,^\circ$ according to the standard geometry of spectral data (Pieters, 1999). Due to the wavelength dependence, each sensor channel is corrected by a different set of coefficients, respectively.

The coefficients are determined minimising the error function comprised of three different error terms

$$E_{\text{sensor}} = E_{\text{CR}} + \mu_{\text{ident}} E_{\text{ident}} + \mu_{\text{ref}} E_{\text{ref}} \tag{4.19}$$

with two weighting factors μ_{ident} and μ_{ref}.

The first component E_{CR} measures the deviation of the CR reflectance derived from the jth spectrum acquired at any phase angle α from the CR reflectance derived from the corresponding reference spectrum denoted by j_{ref} acquired at α_{ref} and thus emphasises the absorption features:

$$E_{\text{CR}} = \sum_{j=1}^{N_{\text{spec}}} \sum_{k=1}^{N_{\text{chan}}} \left(f_{\text{CR}}\left(f_{\text{norm}}\left(L_{\text{corr},j}(\alpha_j, \lambda_k)\right)\right) - f_{\text{CR}}\left(f_{\text{norm}}\left(L_{\text{corr},j_{\text{ref}}}(\alpha_{j_{\text{ref}}}, \lambda_k)\right)\right)\right)^2. \tag{4.20}$$

The squared error is summed over all N_{spec} spectra and all N_{chan} sensor channels. The corresponding centre wavelength of the kth channel is denoted by λ_k. At first, the radiance L_{corr} converted to reflectance and photometrically normalised using $f_{\text{norm}}(L_{\text{corr}})$ and then the CR spectrum is computed from the reflectance R by $f_{\text{CR}}(R)$. Since the ideal value of α_0 is rarely matched, a deviation of $\pm 5\,^\circ$ is tolerated and the reference phase angle is thus denoted by α_{ref} and the reference phase angle of the jth spectrum is denoted by $\alpha_{j_{\text{ref}}}$, respectively.

Notably, the radiance measured at $\alpha_{j_{\text{ref}}}$ is subject to correction due to the small deviations from α_0. Consequently, the reference characteristic is lost and the second

component E_{ident} of the fitness function constrains the solution to identity for small phase angle deviations, i.e. if the phase angle is close to the reference phase angle, the normalised reflectance is expected to be as similar as possible to the normalised reflectance reflectance derived from the sensor reading $L_{\text{sensor},j}(\lambda_k)$:

$$E_{\text{ident}} = \sum_{j=1}^{N_{\text{spec}}} \sum_{k=1}^{N_{\text{chan}}} \left(f_{\text{norm}} \left(L_{\text{corr},j}(\alpha_0, \lambda_k) \right) - f_{\text{norm}} \left(L_{\text{sensor},j}(\lambda_k) \right) \right)^2 . \tag{4.21}$$

This component, however, only affects the constants of the polynomial since the higher order coefficients cancel out for $\alpha_j = \alpha_0$.

The first component does not cover the absolute reflectance due to the CR spectra and the second component implies an identity for small phase angle deviations but does not take into account the absolute reflectance of the reference measurements. Hence, a third component

$$E_{\text{ref}} = \sum_{j=1}^{N_{\text{spec}}} \sum_{k=1}^{N_{\text{chan}}} \left(f_{\text{norm}} \left(L_{\text{corr},j}(\alpha_j, \lambda_k) \right) - f_{\text{norm}} \left(L_{\text{sensor},j_{\text{ref}}}(\lambda_k) \right) \right)^2 . \tag{4.22}$$

is included that constrains all normalised reflectance values to be close to the normalised reflectance derived from of the corresponding reference spectrum $L_{\text{sensor},j_{\text{ref}}}(\lambda_k)$.

To normalise the spectral data, the full Hapke model (Hapke, 2002) R_{Hapke} is applied, i.e. the measured radiance is divided by the solar irradiance and the single-scattering albedo w of the Hapke model is estimated for each spectrum and each channel (cf. Section 4.2, $\sigma_{\text{refl}} = 0$), respectively. The remaining parameters are adopted from Warell (2004). Thus, the fitness function is highly non-linear and w depends on the correction parameters $g_1(\lambda)$, $g_0(\lambda)$, $c_1(\lambda)$ and $c_0(\lambda)$. Furthermore, the standard continuum removal approach, i.e. division by the convex hull (Fu et al., 2007), introduces another non-linearity. Hence, the resulting optimisation problem is very complex.

The error function, however, may be linearised using an iterative optimisation and a few simplifications. Then, the coefficients are updated. This sequential normalisation and coefficient update is repeated until either the fitness function or the coefficients do not change any more. Consequently, the normalisation function $f_{\text{norm}}(L(\lambda)) = c_{\text{norm}}(\lambda)L(\lambda)$ is represented by a wavelength dependent factor

$$c_{\text{norm},j}(\lambda) = \frac{R_{\text{Hapke}}(L_{\text{corr},j}(\lambda))}{L_{\text{corr},j}(\lambda)}. \tag{4.23}$$

Additionally, the highly non-linear continuum-removal is replaced by a linear but similar technique. Instead of dividing by the convex hull, a second order polynomial that is fit to the reflectance data is subtracted. Similar to the division by the convex hull, this approach eliminates the absolute reflectance and emphasises the deviations from the

parabola, i.e. the absorption bands. Consequently, the error function is linear in the channel coefficients and the unique set of current iterations coefficients can be determined using linear least squares techniques.

The resulting over determined system of equations is linear in the model coefficients and contains millions of spectra and is thus extremely large. To update the parameters, however, only the moment matrices of the pseudo inverse are necessary. Hence, an update is possible by handling relatively small matrices. There are $3N_{\text{chan}}$ equations per spectrum corresponding to each of the three components of the error function.

At first, all N_{chan} values are grouped in vectors, i.e.

$$\begin{aligned}
\mathbf{g}_d &= \left[g_d(\lambda_1), \cdots, g_d(\lambda_{N_{\text{chan}}})\right]^{\mathrm{T}}, \\
\mathbf{c}_d &= \left[c_d(\lambda_1), \cdots, c_d(\lambda_{N_{\text{chan}}})\right]^{\mathrm{T}}, \\
\mathbf{c}_{\text{norm},j} &= \left[c_{\text{norm},j}(\lambda_1), \cdots, c_{\text{norm},j}(\lambda_{N_{\text{chan}}})\right]^{\mathrm{T}} \text{ and} \\
\mathbf{L}_{\text{sensor},j} &= \left[L_{\text{sensor},j}(\lambda_1), \cdots, L_{\text{sensor},j}(\lambda_{N_{\text{chan}}})\right]^{\mathrm{T}}.
\end{aligned} \tag{4.24}$$

Using the diagonal matrix operator

$$\operatorname{diag}(\mathbf{g}_d) = \begin{bmatrix} g_1 & 0 & 0 \\ 0 & \ddots & 0 \\ 0 & 0 & g_{N_{\text{chan}}} \end{bmatrix} \tag{4.25}$$

and the definition

$$\mathbf{D}_{d,j} = \begin{cases} \Delta\alpha^d \operatorname{diag}(\mathbf{L}_{\text{sensor},j}) & \text{if } d \in [0, d_{\text{gain}}] \\ \Delta\alpha^{d-(d_{\text{gain}}+1)} \operatorname{diag}(\mathbf{1}_{N_{\text{chan}}}) & \text{if } d \in [d_{\text{gain}}+1, N_{\text{coeff}}-1] \end{cases} \tag{4.26}$$

where $\mathbf{1}_{N_{\text{chan}}}$ is a vector with N_{chan} elements filled with ones, Eq. (4.15) is rewritten in matrix form:

$$\begin{aligned}
\mathbf{L}_{\text{corr},j} &= \begin{bmatrix} \mathbf{D}_{0,i} & \cdots & \mathbf{D}_{d_{\text{gain}}+d_{\text{offset}}+1,j} \end{bmatrix} \begin{bmatrix} \mathbf{g}_0 \\ \vdots \\ \mathbf{g}_{d_{\text{gain}}} \\ \mathbf{c}_0 \\ \vdots \\ \mathbf{c}_{d_{\text{offset}}} \end{bmatrix} \\
&= \mathbf{X}_{\text{sensor},j} \boldsymbol{\theta}_{\text{sensor}}.
\end{aligned} \tag{4.27}$$

$\mathbf{X}_{\text{sensor},j}$ combines the radiance and phase angle values of the jth spectrum and $\boldsymbol{\theta}_{\text{sensor}}$ contains the model coefficients. Accordingly, the normalised reflectance is given by

$$\begin{aligned}
\mathbf{R}_{\text{norm},j} &= \operatorname{diag}(\mathbf{c}_{\text{norm},j})\, \mathbf{L}_{\text{corr},j} \\
&= \operatorname{diag}(\mathbf{c}_{\text{norm},j})\, \mathbf{X}_{\text{sensor},j} \boldsymbol{\theta}_{\text{sensor}} \\
&= \mathbf{X}_{\text{norm},j} \boldsymbol{\theta}_{\text{sensor}}
\end{aligned} \tag{4.28}$$

where $\mathbf{X}_{\text{norm},j} = \text{diag}\left(\mathbf{c}_{\text{norm},j}\right)\mathbf{X}_{\text{sensor},j}$ absorbs the normalisation factor and the sensor measurements. It is well known, that a second order polynomial fit to the reflectance using linear least squares may be written as

$$\mathbf{R}_{\text{poly},j} = \mathbf{X}_{\text{poly}}\mathbf{R}_{\text{norm},j} \qquad \text{where} \tag{4.29}$$

$$\mathbf{X}_{\text{poly}} = \mathbf{X}_{\lambda}^{\text{T}}\left(\mathbf{X}_{\lambda}^{\text{T}}\mathbf{X}_{\lambda}\right)^{-1}\mathbf{X}_{\lambda}^{\text{T}} \qquad \text{and} \tag{4.30}$$

$$\mathbf{X}_{\lambda} = \begin{bmatrix} \lambda_1^2 & \lambda_1 & 1 \\ \vdots & \vdots & \vdots \\ \lambda_{N_{\text{chan}}}^2 & \lambda_{N_{\text{chan}}} & 1 \end{bmatrix}. \tag{4.31}$$

Combining Eq. (4.24) to Eq. (4.31) provides a fully linear description of the CR spectrum $\mathbf{R}_{\text{CR},j}$:

$$\begin{aligned} \mathbf{R}_{\text{CR},j} &= \mathbf{R}_{\text{norm},j} - \mathbf{R}_{\text{poly},j} \\ &= \left(\mathbf{I} - \mathbf{X}_{\text{poly}}\right)\mathbf{R}_{\text{norm},j} \\ &= \tilde{\mathbf{X}}_{\text{poly}}\mathbf{X}_{\text{norm},j}\boldsymbol{\theta}_{\text{sensor}} \end{aligned} \tag{4.32}$$

with $\tilde{\mathbf{X}}_{\text{poly}} = \left(\mathbf{I} - \mathbf{X}_{\text{poly}}\right)$ where $\mathbf{I}$ denotes the identity matrix. Notably, only $\mathbf{X}_{\text{norm},j}$ depends on α_j. From Eq. (4.32) follow the N_{chan} linear equations derived from E_{CR} for the jth spectrum:

$$\begin{aligned} 0 =& \tilde{\mathbf{X}}_{\text{poly}}\mathbf{X}_{\text{norm},j}\boldsymbol{\theta}_{\text{sensor}} \\ & - \tilde{\mathbf{X}}_{\text{poly}}\mathbf{X}_{\text{norm},j_{\text{ref}}}\boldsymbol{\theta}_{\text{sensor}} \Leftrightarrow \\ 0 =& \tilde{\mathbf{X}}_{\text{poly}}\left(\mathbf{X}_{\text{norm},j} - \mathbf{X}_{\text{norm},j_{\text{ref}}}\right)\boldsymbol{\theta}_{\text{sensor}} \\ =& \tilde{\mathbf{X}}_{\text{poly}}\Delta\mathbf{X}_{\text{norm},j}\boldsymbol{\theta}_{\text{sensor}} \end{aligned} \tag{4.33}$$

where $\mathbf{X}_{\text{norm},j}$ combines the normalisation coefficient and the radiance values of the jth radiance spectrum and $\mathbf{X}_{\text{norm},j_{\text{ref}}}$ combines the normalisation coefficient and the radiance values of the corresponding reference spectrum, respectively. Consequently, the matrix $\Delta\mathbf{X}_{\text{norm},j} = \left(\mathbf{X}_{\text{norm},j} - \mathbf{X}_{\text{norm},j_{\text{ref}}}\right)$ describes the difference between the normalised reflectance of the jth radiance spectrum and its corresponding reference spectrum.

Similarly, Eq. (4.21) yields

$$\mu_{\text{ident}}\,\mathbf{X}_{\text{norm},j}\big|_{\alpha_0}\,\boldsymbol{\theta}_{\text{sensor}} = \mu_{\text{ident}}\text{diag}\left(\mathbf{c}_{\text{norm},j}\right)\mathbf{L}_{\text{sensor},j} \tag{4.34}$$

where $\mathbf{c}_{\text{norm},j}$ and $\mathbf{L}_{\text{sensor},j}$ are the normalisation factor of and the radiance measured by the sensor of jth measurement, respectively. Here, the matrix $\mathbf{X}_{\text{norm},j}$ is evaluated at α_0. Notably, the weight μ_{ident} may not be cancelled out since the equation is part of a linear system of equations.

The last component E_{ident} (cf. Eq. (4.22)) is written as

$$\mu_{\text{ref}}\mathbf{X}_{\text{norm},j}\boldsymbol{\theta}_{\text{sensor}} = \mu_{\text{ref}}\text{diag}\left(\mathbf{c}_{\text{norm},j_{\text{ref}}}\right)\mathbf{L}_{\text{sensor},j_{\text{ref}}}. \tag{4.35}$$

Thus the radiance of the jth measurement is corrected according to its phase angle α_j, converted to reflectance, normalised and then compared to the normalised reflectance derived from the uncorrected reference radiance spectrum $\mathbf{L}_{\text{sensor},j_{\text{ref}}}$.

Finally, the whole system of equations is set up combining the equations of all measurements:

$$\mathbf{A}_{\text{sensor}}\boldsymbol{\theta}_{\text{sensor}} = \mathbf{b}_{\text{sensor}} \qquad \text{with} \tag{4.36}$$

$$\mathbf{A}_{\text{sensor}} = \begin{bmatrix} \tilde{\mathbf{X}}_{\text{poly}}\Delta\mathbf{X}_{\text{norm},1} \\ \vdots \\ \tilde{\mathbf{X}}_{\text{poly}}\Delta\mathbf{X}_{\text{norm},N_{\text{spec}}} \\ \mu_{\text{ident}}\ \mathbf{X}_{\text{norm},1}\big|_{\alpha_0} \\ \vdots \\ \mu_{\text{ident}}\ \mathbf{X}_{\text{norm},N_{\text{spec}}}\big|_{\alpha_{N_{\text{spec}}}} \\ \mu_{\text{ref}}\mathbf{X}_{\text{norm},1} \\ \vdots \\ \mu_{\text{ref}}\mathbf{X}_{\text{norm},N_{\text{spec}}} \end{bmatrix} \qquad \text{and} \tag{4.37}$$

$$\mathbf{b}_{\text{sensor}} = \begin{bmatrix} \mathbf{0}_{N_{\text{chan}}} \\ \vdots \\ \mathbf{0}_{N_{\text{chan}}} \\ \mu_{\text{ident}}\text{diag}\left(\mathbf{c}_{\text{norm},1}\right)\mathbf{L}_{\text{sensor},1} \\ \vdots \\ \mu_{\text{ident}}\text{diag}\left(\mathbf{c}_{\text{norm},N_{\text{spec}}}\right)\mathbf{L}_{\text{sensor},N_{\text{spec}}} \\ \mu_{\text{ref}}\text{diag}\left(\mathbf{c}_{\text{norm},1_{\text{ref}}}\right)\mathbf{L}_{\text{sensor},1_{\text{ref}}} \\ \vdots \\ \mu_{\text{ref}}\text{diag}\left(\mathbf{c}_{\text{norm},N_{\text{spec}_{\text{ref}}}}\right)\mathbf{L}_{\text{sensor},N_{\text{spec}_{\text{ref}}}} \end{bmatrix} \tag{4.38}$$

where $\mathbf{0}_{N_{\text{chan}}}$ is a vector containing N_{chan} zero valued elements. It is well known that the sum of squared residuals of this system of equations is minimised by the pseudo-inverse $\mathbf{A}^{+}_{\text{sensor}}$ of $\mathbf{A}_{\text{sensor}}$:

$$\begin{aligned} \mathbf{A}^{\text{T}}_{\text{sensor}}\mathbf{A}_{\text{sensor}}\boldsymbol{\theta}_{\text{sensor}} &= \mathbf{A}^{\text{T}}_{\text{sensor}}\mathbf{b}_{\text{sensor}} \Leftrightarrow \\ \boldsymbol{\theta}_{\text{sensor}} &= \left(\mathbf{A}^{\text{T}}_{\text{sensor}}\mathbf{A}_{\text{sensor}}\right)^{-1}\mathbf{A}^{\text{T}}_{\text{sensor}}\mathbf{b}_{\text{sensor}} \\ &= \mathbf{A}^{+}_{\text{sensor}}\mathbf{b}_{\text{sensor}}. \end{aligned} \tag{4.39}$$

Hence, instead of creating a linear system of millions of equations it is sufficient to compute the matrix $\mathbf{A}_{\text{reduced}} = \mathbf{A}^{\text{T}}_{\text{sensor}}\mathbf{A}_{\text{sensor}}$ containing $N_{\text{coeff}}N_{\text{chan}}$ by $N_{\text{coeff}}N_{\text{chan}}$ elements

and the vector $\mathbf{b}_{\text{reduced}} = \mathbf{A}_{\text{sensor}}^{\text{T}}\mathbf{b}_{\text{sensor}}$ containing $N_{\text{coeff}}N_{\text{chan}}$ elements largely reducing computational resources, e.g. memory.

From Eq. (4.37) and Eq. (4.38) follows the block symmetric matrix

$$\mathbf{A}_{\text{reduced}} = \begin{bmatrix} \mathbf{A}_{0,0} & \cdots & \mathbf{A}_{0,m} & \cdots & \mathbf{A}_{0,N_{\text{coeff}}-1} \\ \vdots & \ddots & & & \vdots \\ \mathbf{A}_{n,0} & & \mathbf{A}_{n,m} & & \mathbf{A}_{n,N_{\text{coeff}}-1} \\ \vdots & & & \ddots & \vdots \\ \mathbf{A}_{N_{\text{coeff}}-1,0} & \cdots & \mathbf{A}_{N_{\text{coeff}}-1,m} & \cdots & \mathbf{A}_{N_{\text{coeff}}-1,N_{\text{coeff}}-1} \end{bmatrix} \text{ where}$$

$$\mathbf{A}_{n,m} = \begin{cases} \sum_{j=1}^{N_{\text{spec}}} \Delta\tilde{\mathbf{D}}_{n,j}^{\text{T}}\tilde{\mathbf{X}}_{\text{poly}}^{\text{T}}\tilde{\mathbf{X}}_{\text{poly}}\Delta\tilde{\mathbf{D}}_{m,j} \\ \qquad +\mu_{\text{ident}}^2\tilde{\mathbf{D}}_{n,j}^{\text{T}}\tilde{\mathbf{D}}_{m,j} \\ \qquad +\mu_{\text{ref}}^2\tilde{\mathbf{D}}_{n,j}^{\text{T}}\tilde{\mathbf{D}}_{m,j} & \text{if} \quad \begin{array}{lll} n=0 & \wedge & m=0 \\ \vee\ n=0 & \wedge & m=d_{\text{gain}}+1 \\ \vee\ n=d_{\text{gain}}+1 & \wedge & m=0 \\ \vee\ n=d_{\text{gain}}+1 & \wedge & m=d_{\text{gain}}+1 \end{array} \\ \sum_{j=1}^{N_{\text{spec}}} \Delta\tilde{\mathbf{D}}_{n,j}^{\text{T}}\tilde{\mathbf{X}}_{\text{poly}}^{\text{T}}\tilde{\mathbf{X}}_{\text{poly}}\Delta\tilde{\mathbf{D}}_{m,j} \\ \qquad +\mu_{\text{ref}}^2\tilde{\mathbf{D}}_{n,j}^{\text{T}}\tilde{\mathbf{D}}_{m,j} & \text{else} \end{cases} \tag{4.40}$$

on the left hand side. The two diagonal matrices $\tilde{\mathbf{D}}_{n,j} = \text{diag}\left(\mathbf{c}_{\text{norm},j}\right)\mathbf{D}_{n,j}$ and $\Delta\tilde{\mathbf{D}}_{n,j} = \text{diag}\left(\mathbf{c}_{\text{norm},j}\right)\mathbf{D}_{n,j} - \text{diag}\left(\mathbf{c}_{\text{norm},j_{\text{ref}}}\right)\mathbf{D}_{n,j_{\text{ref}}}$ are the diagonal matrices from Eq. (4.26) weighted with the normalisation factors. The first case of $\mathbf{A}_{n,m}$ corresponds to the constant coefficients of the gain and offset polynomials and thus contains terms corresponding to E_{ident}. The other case is determined only by E_{CR} and E_{ref}. Accordingly, the vector $\mathbf{b}_{\text{reduced}}$ on the right hand side of the equation is given by

$$\mathbf{b}_{\text{reduced}} = \begin{bmatrix} \mathbf{b}_0 \\ \vdots \\ \mathbf{b}_n \\ \vdots \\ \mathbf{b}_{N_{\text{coeff}}-1} \end{bmatrix} \text{ where}$$

$$\mathbf{b}_n = \begin{cases} \sum_{j=1}^{N_{\text{spec}}} \mu_{\text{ident}}^2\tilde{\mathbf{D}}_{n,j}^{\text{T}}\text{diag}\left(c_{\text{norm,j}}\right)\mathbf{L}_{\text{sensor,j}} \\ \qquad +\mu_{\text{ref}}^2\tilde{\mathbf{D}}_{n,j}^{\text{T}}\text{diag}\left(c_{\text{norm,j}}\right)\mathbf{L}_{\text{sensor,j}_{\text{ref}}} & \text{if} \quad \begin{array}{r} d=0 \\ \vee = d_{\text{gain}}+1 \end{array} \\ \sum_{j=1}^{N_{\text{spec}}} \mu_{\text{ref}}^2\tilde{\mathbf{D}}_{n,j}^{\text{T}}\text{diag}\left(c_{\text{norm,j}}\right)\mathbf{L}_{\text{sensor,j}_{\text{ref}}} & \text{else.} \end{cases} \tag{4.41}$$

Since there is no interdependence between different spectra in the sum, it is possible to determine $\mathbf{A}_{\text{reduced}}$ and $\mathbf{b}_{\text{reduced}}$ for each spectrum, e.g. in parallel, and sum the results.

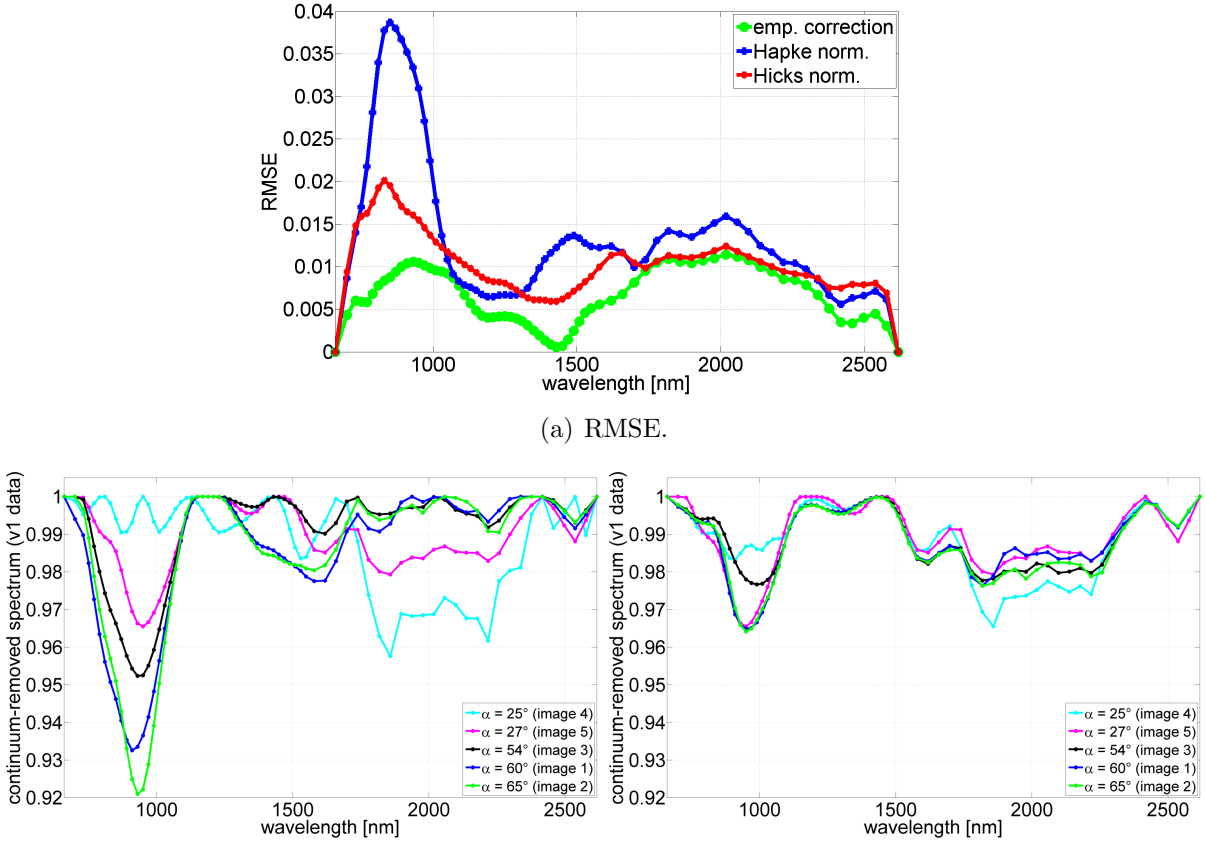

(a) RMSE.

(b) Uncorrected CR spectra.

(c) Corrected CR spectra.

Figure 4.16: Result of the CR based correction based on the v1 dataset. (a) The overall root mean squared error for each M^3 channel. (b) The uncorrected reflectance spectra of an exemplary pixel. (c) The corrected reflectance spectra of an exemplary pixel.

4.3.4 Results

All results shown in this section are derived by adapting the parameters of the methods to the non-inclined surface areas.

The results of the CR based approach are presented in Fig. 4.16. The spectral root mean squared error (RMSE) over the whole dataset (cf. Fig. 4.16(a)) clearly shows an improvement compared to the spectra normalised using the Hapke model or the polynomial proposed by Hicks et al. (2011). The improvement is especially strong in the diagnostic wavelength range around 1000 nm. From the uncorrected CR reflectance (cf. Fig. 4.16(b)) and the corrected CR reflectance (cf. Fig. 4.16(c)) follows that not only the depth but also the position of the minimum shifts. The position is important diagnostic parameter for the interpretation of mineral spectra, e.g. the calcium content (Matsunaga

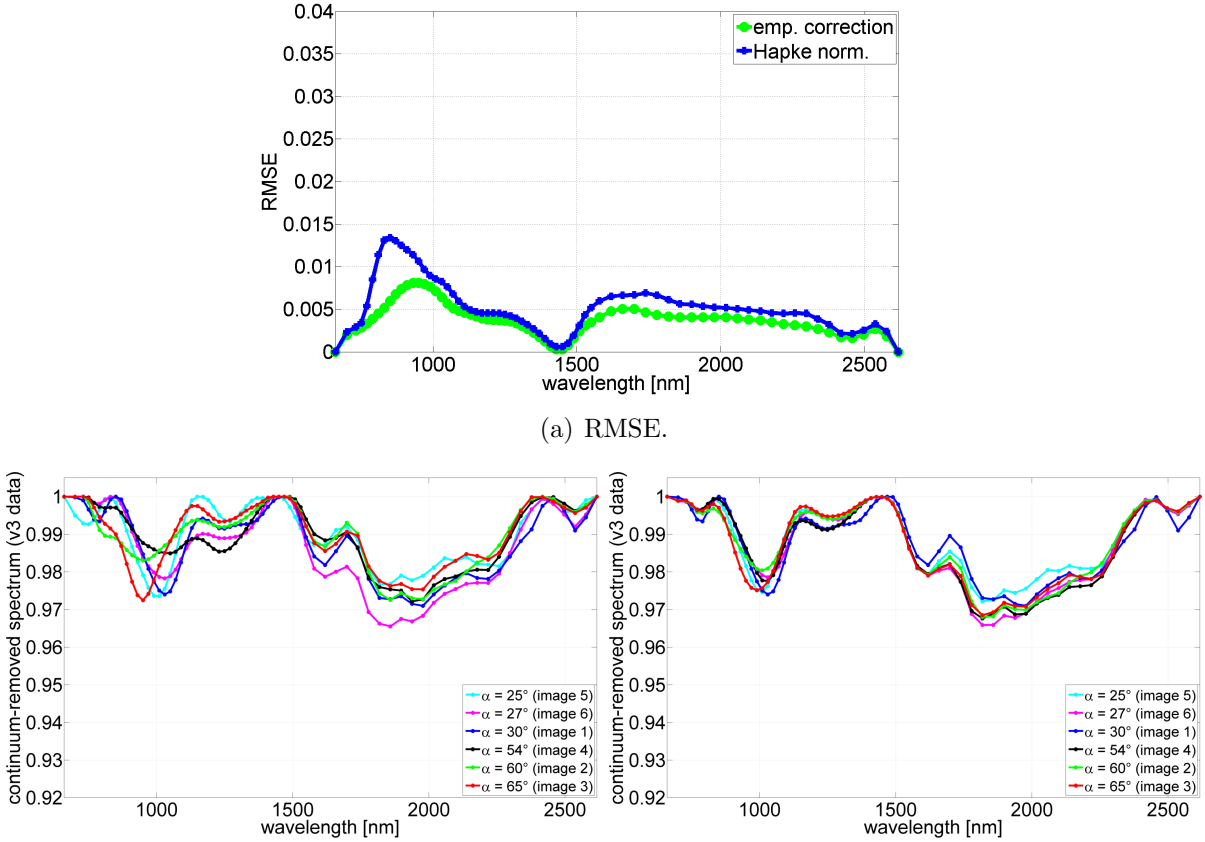

(a) RMSE.

(b) Uncorrected CR spectra.

(c) Corrected CR spectra.

Figure 4.17: Result of the CR based correction based on the v3 dataset. (a) The overall root mean squared error for each M^3 channel. (b) The uncorrected reflectance spectra of an exemplary pixel. (c) The corrected reflectance spectra of an exemplary pixel.

et al., 2008). The better results of the polynomial by Hicks et al. (2011) compared to the pure Hapke based normalisation may be caused by the empirical coefficient that are "trained" to remove the observed phase angle/sensor temperature based effects while this effect is not included in the Hapke model. This hypothesis is confirmed if the method is applied to the v3 data where the effect of the sensor temperature is supposed to be removed (cf. Fig. 4.17). Comparing Fig. 4.16(a) and Fig. 4.17(a) shows that the RMSE of the Hapke based normalisation is greatly reduced by the compensation of the sensor temperature. The empirical correction, however, still yields better results, i.e. a decreased RMSE and more homogenous reflectance values (cf. Fig. 4.17(b) and Fig. 4.17(c)), which hints to an imperfect compensation of the sensor temperature or a residual phase angle based effect. The normalisation of Hicks et al. (2011) is calibrated to the v1 dataset and

Table 4.2: Residual errors of the radiance based approach. The residual error greatly decreases if the two weighting factors μ_{ident} and μ_{ref} tend towards zero. For comparison, the residual error without modification of the radiance data is $7.6 \cdot 10^{-3}$.

μ_{ident} \ μ_{ref}	1.00	0.50	0.10	0.05	0.01
1.00	$6.4 \cdot 10^{-3}$	$6.4 \cdot 10^{-3}$	$14.0 \cdot 10^{-3}$	$19.8 \cdot 10^{-3}$	$10.1 \cdot 10^{-3}$
0.50	$6.3 \cdot 10^{-3}$	$6.4 \cdot 10^{-3}$	$13.9 \cdot 10^{-3}$	$19.8 \cdot 10^{-3}$	$9.8 \cdot 10^{-3}$
0.10	$6.0 \cdot 10^{-3}$	$6.0 \cdot 10^{-3}$	$15.6 \cdot 10^{-3}$	$23.0 \cdot 10^{-3}$	$7.9 \cdot 10^{-3}$
0.05	$5.9 \cdot 10^{-3}$	$5.9 \cdot 10^{-3}$	$16.4 \cdot 10^{-3}$	$25.9 \cdot 10^{-3}$	$8.1 \cdot 10^{-3}$
0.01	$5.9 \cdot 10^{-3}$	$5.9 \cdot 10^{-3}$	$14.4 \cdot 10^{-3}$	$21.9 \cdot 10^{-3}$	$2.6 \cdot 10^{-3}$
0	$5.9 \cdot 10^{-3}$	$5.8 \cdot 10^{-3}$	$14.1 \cdot 10^{-3}$	$19.2 \cdot 10^{-3}$	$0.5 \cdot 10^{-3}$

thus yields worse results on the v3 dataset. It is thus excluded from the evaluation. This, again, points towards the sensor temperature being absorbed in the coefficients of the polynomial.

Notably, the correction factors applied to the v3 dataset are absorbed by the multiplicative factor of the radiance based method. Thus, the radiance based method is applied directly to the v3 dataset. The error term to be minimised is comprised of three parts which are combined using two weighting factors. Thus, the algorithm is evaluated for various combinations. The residual error is defined as the error of the CR based approach, i.e. the root mean squared difference between the CR spectrum at phase angle α and the CR spectrum at phase angle α_{ref}. Notably, the convex hull approach is adopted from the CR based approach for this evaluation. The residual errors for the combinations are shown in Table 4.2. For large and small values of μ_{ref}, all residual errors are less than reference value of $7.6 \cdot 10^{-3}$ in case of no correction. The effect of μ_{ident} seems to be of minor influence. In fact, the identity constraint seems to prevent the algorithm from finding the absolute minimum. In most cases, decreasing μ_{ident} results in a decreased residual error.

The residual error is largely reduced if the weighting factors tend towards zero. In contrast to the CR based approach, the radiance based approach does modify the spectrum obtained at α_{ref} and thus the decreased residual error is caused by an artificial "flattening" of the spectra eliminating the absorptions. Fig. 4.18 shows the relative band depth of the 1000 nm absorption trough of Region 6 for the combination with the lowest residual error. Compared to the relative band depth of the unmodified reference spectra (cf. Fig. 4.18(a)), the relative band depth of both the spectra at the reference phase angle $\alpha_{\text{ref}} = 30.8\,^\circ$ and the spectra at $\alpha_1 = 52.2$ and $\alpha_2 = 24.1$ is greatly decreased. The residual error thus decreases if the constraints are softened by decreasing the weighting factors. The observation of the increasing identity constraint preventing the algorithm from finding the optimal value may be explained by this behaviour.

To avoid this behaviour, the error function of the CR based approach is adopted, i.e. the root mean squared difference to the unmodified spectrum at reference phase angle

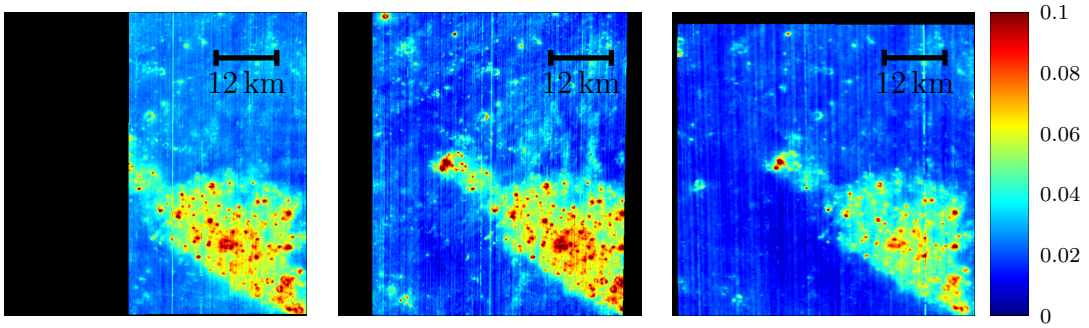

(a) $\alpha_{\text{ref}} = 30.8\,°$: no correction (b) $\alpha_1 = 52.2\,°$: no correction (c) $\alpha_2 = 24.1\,°$: no correction

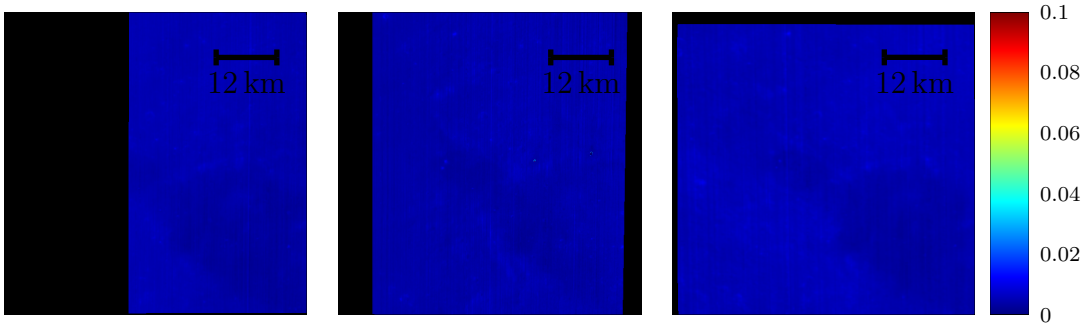

(d) $\alpha_{\text{ref}} = 30.8\,°$: corrected (e) $\alpha_1 = 52.2\,°$: corrected (f) $\alpha_2 = 24.1\,°$: corrected

Figure 4.18: Relative band depth for $\mu_{\text{ident}} = 0$ and $\mu_{\text{ref}} = 0.01$. (a)–(c) The relative band depth of Region 6. The band depth is extracted from the reflectance without application of the correction. The band depth of the spectrum at α_{ref} shown in (a) is the expected result. (d)–(f) After application of the correction, the relative band depth values are decreased leading to almost non-existent absorptions. The low values of the weighting factors disable the constraint of the optimisation problem and the reflectance spectra are flattened to produce a low residual error. This eliminates the absorption features.

Table 4.3: Reference errors of the radiance based approach. The reference errors are computed with respect to an uncorrected image acquired at the reference phase angle.

μ_{ident} \ μ_{ref}	1.00	0.50	0.10	0.05	0.01
1.00	$6.1 \cdot 10^{-3}$	$6.2 \cdot 10^{-3}$	$14.2 \cdot 10^{-3}$	$20.3 \cdot 10^{-3}$	$10.0 \cdot 10^{-3}$
0.50	$6.0 \cdot 10^{-3}$	$6.1 \cdot 10^{-3}$	$14.1 \cdot 10^{-3}$	$20.3 \cdot 10^{-3}$	$10.2 \cdot 10^{-3}$
0.10	$5.9 \cdot 10^{-3}$	$6.2 \cdot 10^{-3}$	$16.3 \cdot 10^{-3}$	$23.7 \cdot 10^{-3}$	$13.7 \cdot 10^{-3}$
0.05	$5.9 \cdot 10^{-3}$	$6.2 \cdot 10^{-3}$	$18.2 \cdot 10^{-3}$	$27.3 \cdot 10^{-3}$	$16.6 \cdot 10^{-3}$
0.01	$5.9 \cdot 10^{-3}$	$6.2 \cdot 10^{-3}$	$20.1 \cdot 10^{-3}$	$28.0 \cdot 10^{-3}$	$21.0 \cdot 10^{-3}$
0	$5.9 \cdot 10^{-3}$	$6.2 \cdot 10^{-3}$	$20.2 \cdot 10^{-3}$	$26.5 \cdot 10^{-3}$	$22.6 \cdot 10^{-3}$

is computed. This error is referred to as reference error. The reference errors for all combinations are given in Table 4.3. The reference errors are largely increased if the weight factors tend towards zero. Furthermore, the trend of decreasing errors for decreased values of μ_{ident} is no longer apparent. The identity error does not show a large influence on the reference errors if the weight μ_{ref} is sufficiently large. The minimal reference error is obtained for $\mu_{\text{ident}} = 0.1$ and $\mu_{\text{ref}} = 1$. Fig. 4.19 shows the relative band depth of the 1000 nm absorption trough of Region 6 for the combination with the lowest reference error. The produced result shows an improved band depth image. Especially the image acquired at $\alpha_1 = 52.2\,^\circ$ shows a large improvement. The overestimated band depth in the south-eastern part of the image is successfully reduced to the band depth values observed at α_{ref} and the north-eastern area is more homogeneous. Thus, the choice of μ_{ref} and μ_{ident} is crucial for the success of the correction. From Table 4.3, however, follows that any choice with $\mu_{\text{ref}} \geq 0.5$ may produce reasonable results.

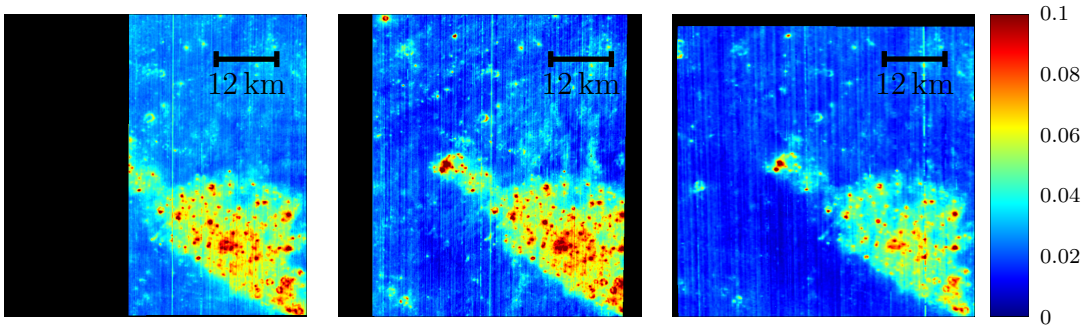

(a) $\alpha_{\text{ref}} = 30.8\,°$: no correction (b) $\alpha_1 = 52.2\,°$: no correction (c) $\alpha_2 = 24.1\,°$: no correction

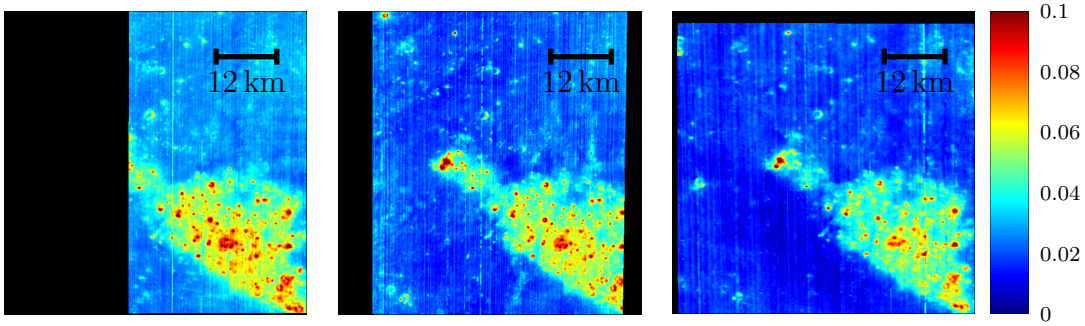

(d) $\alpha_{\text{ref}} = 30.8\,°$: corrected (e) $\alpha_1 = 52.2\,°$: corrected (f) $\alpha_2 = 24.1\,°$: corrected

Figure 4.19: Relative band depth for $\mu_{\text{ident}} = 0.1$ and $\mu_{\text{ref}} = 1.0$. (a)–(c) The band depth of Region 6 is extracted from the reflectance without application of the correction. The band depth of the spectrum at α_{ref} shown in (a) is the expected result. (d)–(f) The relative band depth of Region 6 after applying the proposed correction method. The corrected band depth at α_1 is more similar to the expected result. The other band depth images are barely modified due to the small deviation from $\alpha_0 = 30\,°$

5

Contribution: Photometric surface reconstruction

The photometric surface estimation requires two different steps. First, the surface normal, i.e. the surface gradients, are estimated from the shading information and second, the surface is obtained from the possibly non-integrable gradient field. The a-priori known DEM data provides constraints in both steps. This chapter describes the integration of the a-priori known DEM data into the photometric surface reconstruction methods. Additionally, the DEM data is explicitly assumed to be of lower lateral resolution than the reflectance data.

At first, the terms frequently used in this chapter are defined in Section 5.1. Including the relative depth data, i.e. the gradients of the a-priori known DEM, into the photometric estimation of the surface gradient field targets the reduction of errors in the estimation due to inaccurate reflectance data and/or reflectance models. These techniques, which are described in Section 5.2, are mathematically less complex then including the absolute depth data into the reconstruction. The absolute depth data, i.e. the a-priori known DEM itself, allows to constraint the problem of estimating a surface from a photometrically estimated gradient field. Thus, it helps to suppress the accumulation of small systematic errors in the estimated gradient field. The corresponding techniques are detailed in Section 5.3.

This chapter has been adapted and/or adopted from: (Grumpe and Wöhler, 2014; Grumpe et al., 2014a; Wöhler and Grumpe, 2013; Grumpe and Wöhler, 2012; Grumpe et al., 2011b; Grumpe and Wöhler, 2011a,b)

5.1 Terminology

In this chapter, the terms “photoclinometry” (PHCL) and “shape from shading” (SfS) are used frequently. Both terms are often considered as synonyms, denoting the recovery of topography from intensity or shading information, e.g. reflectance, in images. Historically, the term photoclinometry originates from planetary science while shape from shading was

developed in the machine vision community. There are, however, a couple of differences within both methods. Here, the reasoning of Horn (1990) is followed. However, it is no longer possible to distinguish between profile and area-based techniques due to the more recent development of area-based inclination estimation approaches. The main differences that are used to distinguish between both methods are as follows:

- The term photoclinometry originates from the photometric estimation of inclinations, i.e. surface slopes (van Diggelen, 1951; Davis and Soderblom, 1984). A subsequent, often neglected step is the integration of the estimated surface slopes which yields an estimate of the surface.

- Shape from shading aims at an integrated approach to determine surface inclination and height.

The area-based reconstruction schemes solve directly for the elevations but are still labelled "photoclinometry" by most planetary scientists. Nevertheless, the complementary algorithms presented in this chapter can be divided into one algorithm that directly estimates the elevations while the other one estimates the surface slopes and computes the DEM in a subsequent step. Therefore, it is regarded as useful to distinguish between both methods by referring to the determination of gradients as photoclinometry and the direct determination of elevations as shape from shading.

Furthermore, the a-priori known DEM is used to restrict the solutions using so-called soft constraints. The result is influenced by adding a deviation from the constraint to the error functional instead of enforcing a hard constraint. Consequently, the word constraint is used in the meaning of a soft constraint unless indicated otherwise.

5.2 Relative depth constraint

The original SfS method by Horn (1990) (cf. Section 3.3) does not include partial derivatives of the photometric gradient estimates p and q. Imposing a direct constraint on these gradients, thus, results in an ordinary calculus problem. Section 5.2.1 describes the error term, i.e. the constraint, and its important properties. This error term explicitly takes into account that the known DEM is of lower lateral resolution than the reflectance image. Since this error term is sufficient to estimate a complete gradient field, Section 5.2.2 provides a method to recover the surface's gradient field from a reflectance image and an a-priori known DEM. Section 5.2.3 then describes an extension to the original SfS problem including the a-priori known DEM. Both methods yield complementary results (cf. Section 5.5.1). The combination of both methods is describes in Section 5.2.4.

5.2.1 Relative depth error term

The problem of estimating surface gradients from a measured reflectance image relies on the shading of the reflectance image, i.e. the surface gradient estimates p and q are determined such that the squared difference between a reflectance model and the measured reflectance is minimised. Instead of estimating surface gradients solely based on the pixel intensities, the pair of gradients which is "closest" to the existing DEM is searched. The "closeness" obviously cannot be computed on the full image resolution level because the lateral resolution of the existing DEM is assumed to be lower than the lateral resolution of the reflectance image. To deal with these different resolution levels, the DEM error term

$$E_{\text{grad}} = \int_{\mathbf{x}} \int_{\mathbf{y}} \frac{1}{2} \left(f_{\text{lp}}(p) - f_{\text{lp}} \left(\frac{\partial z_{\text{DEM}}}{\partial x} \right) \right)^2 + \frac{1}{2} \left(f_{\text{lp}}(q) - f_{\text{lp}} \left(\frac{\partial z_{\text{DEM}}}{\partial y} \right) \right)^2 dxdy \tag{5.1}$$

is introduced where $\mathbf{x}$ and $\mathbf{y}$ define the region of interest, z_{DEM} is the DEM and $f_{\text{lp}}(\cdot)$ is an arbitrary low-pass function. This can be interpreted as the Euclidean distance in a space that is spanned by the low-pass transformation $f_{\text{lp}}(\cdot)$. An intuitive choice of $f_{\text{lp}}(\cdot)$ which is used within this work is the correlation with a Gaussian kernel according to

$$\begin{aligned} E_{\text{grad}} \leftarrow \int_{\mathbf{x}} \int_{\mathbf{y}} & \frac{1}{2} \left(g_{\sigma_{\text{grad}}} \circ p - g_{\sigma_{\text{grad}}} \circ \frac{\partial z_{\text{DEM}}}{\partial x} \right)^2 \\ & + \frac{1}{2} \left(g_{\sigma_{\text{grad}}} \circ q - g_{\sigma_{\text{grad}}} \circ \frac{\partial z_{\text{DEM}}}{\partial y} \right)^2 dxdy, \end{aligned} \tag{5.2}$$

where $g_{\sigma_{\text{grad}}}$ is a Gaussian filter of width σ_{grad} and $\circ$ is the correlation operator.

Before the optimisation algorithm is presented in detail, a few desirable properties of E_{grad} are subject to discussion. In most numerical optimisation algorithms the image pixels are treated as variables and the image is vectorised. However, Eq. (5.5) contains the derivative of E_{grad} with respect to p and q, which can be computed for each pixel by two subsequent filter operations. To prove this, the chain rule is applied:

$$\frac{\partial E_{\text{grad}}}{\partial p} = \int_{\mathbf{x}} \int_{\mathbf{y}} \left(g_{\sigma_{\text{grad}}} \circ \left(p - \frac{\partial z_{\text{DEM}}}{\partial x} \right) \right) \cdot \frac{\partial}{\partial p} \left(g_{\sigma_{\text{grad}}} \circ p \right) dxdy. \tag{5.3}$$

Now, the correlation integral in the second part is formulated and the derivative with respect to p at the coordinates $(\hat{x}, \hat{y})$ is computed. The correlation integral amounts to

$$g_{\sigma_{\text{grad}}} \circ p = \int_{-\infty}^{\infty} \int_{-\infty}^{\infty} g_{\sigma_{\text{grad}}}(\psi, \zeta) \cdot p(x + \psi, y + \zeta) d\psi d\zeta. \tag{5.4}$$

Since the derivative describes the change in the correlation integral if a small change in p at the coordinate $(\hat{x}, \hat{y})$ occurs, the derivative is of non-zero value only if $\psi = -x + \hat{x}$ and $\zeta = -y + \hat{y}$. Inserting these dependencies into Eq. (5.3) yields

$$\begin{aligned}
\left.\frac{\partial E_{\text{grad}}}{\partial p}\right|_{\hat{x},\hat{y}} &= \int_{\mathbf{x}} \int_{\mathbf{y}} \left(g_{\sigma_{\text{grad}}} \circ \left(p - \frac{\partial z_{\text{DEM}}}{\partial x} \right) \right) \cdot g_{\sigma_{\text{grad}}}(\hat{x} - x, \hat{y} - y) dx dy \\
&= \left(g_{\sigma_{\text{grad}}} \circ \left(p - \frac{\partial z_{\text{DEM}}}{\partial x} \right) \right) * g_{\sigma_{\text{grad}}} \qquad (5.5) \\
\left.\frac{\partial E_{\text{grad}}}{\partial q}\right|_{\hat{x},\hat{y}} &= \left(g_{\sigma_{\text{grad}}} \circ \left(q - \frac{\partial z_{\text{DEM}}}{\partial y} \right) \right) * g_{\sigma_{\text{grad}}} \qquad (5.6)
\end{aligned}$$

where $*$ is the convolution operator. Therefore, the derivative of E_{grad} with respect to p can be computed by a correlation followed by a convolution using the same filter kernel. The derivative with respect to q can be proved in an analogous manner.

A second important property is shown by computing the second derivatives of E_{grad} with respect to p and q. The Hessian

$$\mathbf{H}_{\text{grad}} = \begin{bmatrix} h_{\text{grad}} & 0 \\ 0 & h_{\text{grad}} \end{bmatrix} \qquad (5.7)$$

is a diagonal matrix with positive diagonal elements h_{grad} and thus is positive definite. Therefore, the error term E_{grad} is convex and always "pulls" towards the only solution $p = \frac{\partial z_{\text{DEM}}}{\partial x}$ and $q = \frac{\partial z_{\text{DEM}}}{\partial y}$ and thus can be seen as an "added pull" towards the original DEM. This can be verified by computing h_{grad}.

The second derivative of E_{grad} with respect to p only is given, since the derivative of E_{grad} with respect to q follows the same reasoning and E_{grad} is the superposition of two functions depending either on p or q alone. Consequently, the mixed terms are zero. Furthermore, E_{grad} is quadratic and the second derivative has to be constant. The term $g_{\sigma_{\text{grad}}} * \left(g_{\sigma_{\text{grad}}} \circ \frac{\partial z_{\text{DEM}}}{\partial x} \right)$ does not depend on p and does not influence the second derivative. Therefore, the equation

$$\begin{aligned}
h_{\text{grad}}|_{\hat{x},\hat{y}} = \Bigg[\frac{\partial}{\partial p} \int_{\mathbf{x}} \int_{\mathbf{y}} & g_{\sigma_{\text{grad}}}(x - \hat{x}, y - \hat{y}) \\
& \int_{-\infty}^{\infty} \int_{-\infty}^{\infty} g_{\sigma_{\text{grad}}}(\psi, \zeta) \cdot p(x + \psi, y + \zeta) d\psi d\zeta dx dy \Bigg]_{\hat{x},\hat{y}} \qquad (5.8)
\end{aligned}$$

is obtained. Again, the inner integral only provides a contribution if $\psi = -x + \hat{x}$ and $\psi = -y + \hat{y}$. Inserting this relation and using the rotational invariance of the Gaussian

yields

$$\begin{aligned} h_{\text{grad}}|_{\hat{x},\hat{y}} &= \int_{\mathbf{x}} \int_{\mathbf{y}} g_{\sigma_{\text{grad}}}(x-\hat{x}, y-\hat{y}) \cdot g_{\sigma_{\text{grad}}}(-x+\hat{x}, -y+\hat{y}) dxdy \\ &= \int_{\mathbf{x}} \int_{\mathbf{y}} g^2_{\sigma_{\text{grad}}}(x-\hat{x}, y-\hat{y}) dxdy \end{aligned} \tag{5.9}$$

which is a definite integral over a quadratic function and thus a positive value.

5.2.2 Extended photoclinometry method (PHCL)

Existing photoclinometry methods are mostly profile-based and often require additional constraints on the recovery of the two surface gradients from a single measured radiance. A comparably simple extension is the usage of multiple images by modifying the intensity error E_{I} according to

$$E_{\text{I}} \leftarrow \frac{1}{N_{\text{im}}} \sum_{i=1}^{N_{\text{im}}} \frac{1}{2} \int_{\mathbf{x}} \int_{\mathbf{y}} \left(R\left(\mathbf{s}_i, \mathbf{v}_i, \mathbf{n}(p,q)\right) - I_i \right)^2 dxdy, \tag{5.10}$$

where $\mathbf{s}_i$ and $\mathbf{v}_i$ are the light source and viewing positions for the i-th image, respectively, I_i is the measured reflectance, and N_{im} is the number of images. Due to multiple overflights during different orbits, the dataset contains multiple images observed under different illumination conditions. In order to use as much of the available data as possible, this new formulation of E_{I} is used.

Additionally, the a-priori known DEM is included in the surface gradient estimation. The surface gradients are determined by minimising a weighted sum of both the intensity and the DEM error E_{grad} (cf. Section 5.2.1). This yields gradient estimates that best reproduce the observed image while being close to the existing DEM in the low-pass domain. The overall error functional E_{phcl} then amounts to

$$E_{\text{PHCL}} = E_{\text{I}} + \delta \cdot E_{\text{grad}} \tag{5.11}$$

with δ as an arbitrary weighting factor.

The optimisation is performed using a modified version of the unconstrained Levenberg-Marquardt algorithm (cf. Appendix A). The Levenberg-Marquardt algorithm minimises the residuals of E_{PHCL}, which correspond to

$$r_i = R(\mathbf{s}_i, \mathbf{v}_i, \mathbf{n}(p,q)) - I_i;\ i \in [1, N_{\text{im}}], \tag{5.12}$$

$$r_{N_{\text{im}}+1} = f_{\text{lp}}(p) - f_{\text{lp}}(\frac{\partial z_{\text{DEM}}}{\partial x}), \tag{5.13}$$

$$r_{N_{\text{im}}+2} = f_{\text{lp}}(q) - f_{\text{lp}}(\frac{\partial z_{\text{DEM}}}{\partial y}) \tag{5.14}$$

with $R(\mathbf{s}_i, \mathbf{v}_i, \mathbf{n}(p,q))$ as the modelled reflectance using the light source direction ($\mathbf{s}_i$) and viewer direction ($\mathbf{v}_i$) of the ith image I_i. The error gradient is computed for the oth pixel according to

$$\nabla E_{\mathrm{PHCL}}|_{x(o),y(o)} = \begin{bmatrix} \frac{\partial E_{\mathrm{I}}}{\partial p}\Big|_{x(o),y(o)} + \delta \left.\frac{\partial E_{\mathrm{grad}}}{\partial p}\right|_{x(o),y(o)} \\ \frac{\partial E_{\mathrm{I}}}{\partial q}\Big|_{x(o),y(o)} + \delta \left.\frac{\partial E_{\mathrm{grad}}}{\partial q}\right|_{x(o),y(o)} \end{bmatrix} \tag{5.15}$$

where $x(o)$ and $y(o)$ are the spatial coordinates of the oth pixel. The derivative of E_{grad} has been previously discussed, and the derivative of E_{I} is estimated using finite differences. The computation of the Jacobian matrix is more complex and the fact that only $\mathbf{M} = {\mathbf{J}_{\mathrm{phcl}}}^T \mathbf{J}_{\mathrm{phcl}}$ needs to be computed is used. $\mathbf{M}$ is a block symmetric matrix given by

$$\mathbf{M} = \begin{bmatrix} \mathbf{A}_1 & & & \mathbf{B}_{n,m} \\ & \ddots & & \\ & & \mathbf{A}_n & \\ & & & \ddots \\ \mathbf{B}_{m,n} = \mathbf{B}_{n,m} & & & \mathbf{A}_{N_{\mathrm{px}}} \end{bmatrix} \tag{5.16}$$

The block diagonal elements $\mathbf{A}_n$ are of the form

$$\mathbf{A}_n = \begin{bmatrix} \delta g^2_{\sigma_{\mathrm{grad}}}(0) + \sum_{k=1}^{N_{\mathrm{im}}} [R_p]^2_{x(n),y(n)} & \sum_{k=1}^{N_{\mathrm{im}}} R_p|_{x(n),y(n)} \cdot R_q|_{x(n),y(n)} \\ \sum_{k=1}^{N_{\mathrm{im}}} R_p|_{x(n),y(n)} \cdot R_q|_{x(n),y(n)} & \delta g^2_{\sigma_{\mathrm{grad}}}(0) + \sum_{k=1}^{N_{\mathrm{im}}} [R_q]^2_{x(n),y(n)} \end{bmatrix} \tag{5.17}$$

where $g_{\sigma_{\mathrm{grad}}}(0)$ is the maximum of the Gaussian filter and $R_p = \frac{\partial R(\mathbf{s}_i, \mathbf{v}_i, \mathbf{n}(p,q))}{\partial p}$ and $R_q = \frac{\partial R(\mathbf{s}_i, \mathbf{v}_i, \mathbf{n}(p,q))}{\partial q}$ are the partial derivatives of R with respect to p and q, respectively. Because of the assumption that there are no interreflections between different pixels, the radiance terms vanish within the off-diagonal block matrices, and the non-zero off-diagonal elements reduce to

$$\mathbf{B}_{n,m} = \begin{bmatrix} \delta g^2_{\sigma_{\mathrm{grad}}}(d_{\mathrm{px}}(n,m)) & 0 \\ 0 & \delta g^2_{\sigma_{\mathrm{grad}}}(d_{\mathrm{px}}(n,m)) \end{bmatrix} \tag{5.18}$$

with $d_{\mathrm{px}}(n,m) = \sqrt{(x(n) - x(m))^2 + (y(n) - y(m))^2}$.

Notably, the value of the Gaussian decreases with increasing distance to the pixel corresponding to the main diagonal. In addition, δ is chosen as small as possible and thus yields elements of $\mathbf{B}_{n,m}$ which are several orders of magnitude smaller than the intensity error. Therefore, the off-diagonal elements of $\mathbf{M}$ are set to zero and obtain an in-a-block diagonal matrix. The inverse of a block-diagonal matrix is another block-diagonal matrix in which the blocks are inverted. In this case, this means that the blocks $\mathbf{A}_n$ which

belong to p and q of the same pixel need to be inverted. Thus the image structure may be retained and the inverse of a 2×2 matrix may be computed for each of the N_{px} pixels instead of computing the inverse of a $2N_{\text{px}} \times 2N_{\text{px}}$ matrix. Notably, this simplification only applies to the matrix $\mathbf{J}_{\text{phcl}}^T \mathbf{J}_{\text{phcl}}$ while the gradient on the right-hand side of the Levenberg-Marquard update equation (cf. Appendix A) is computed using the true values. Thus, for large values of the Levenberg-Marquard parameter the optimisation approaches a gradient descent using the true gradient.

The optimisation iterates until $((E_{\text{PHCL}}^{(n-1)} - E_{\text{PHCL}}^{(n)})/E_{\text{PHCL}}^{(n-1)} > 1e-6) \wedge (n < N_{\text{MaxPHCL}})$ or 50 subsequent updates are rejected.

The corresponding surface is retrieved from p and q using the method proposed by Horn (1990) which is described in Section 3.3. There are two parameters for the PHCL optimisation process, namely σ_{grad} and δ. There is an intuitive way to choose the former while the latter needs to be chosen empirically. The Gaussian kernel width σ_{grad} represents a transformation between the different lateral resolutions of the DEM and the image. If the DEM consists of sparse data which has been interpolated to the image grid then σ_{grad} needs be be large enough to bridge the interpolation gaps. This is evident in the case of the LOLA gridded DEM where the gaps between adjacent tracks have been interpolated. The GLD100 is a dense stereo DEM and shows no large interpolation artefacts but suffers from high-frequency noise. This again needs to be attenuated by σ_{grad}. Finally, there are small-scale surface details visible within the image that are missing in the DEM. Since the main goal of the algorithm is the recovery of the small-scale details, these details should not influence the comparison in the low-pass domain. Therefore, σ_{grad} also needs to be large enough to "hide" the small-scale details that are apparent within the image.

The choice of δ is somewhat more difficult. If δ is large then the recovered surface gradients are very close to the DEM and the gain in lateral resolution is negligible. In contrast, if δ approaches zero divergence of the algorithm tends to occur. Therefore, δ is set as small as possible based on the convergence of the algorithm. A suitable choice is $\delta = 2.0 \cdot 10^{-4}$ but it can be decreased or increased as necessary

5.2.3 Extended shape from shading method (SfS)

Similar to Horn (1990) the next step is the simultaneous recovery of height and gradients from shading and the existing DEM. This is achieved by the addition of E_{grad} to the original error term to obtain

$$E_{\text{SfS}} = E_{\text{I}} + \gamma \cdot E_{\text{int}} + \delta \cdot E_{\text{grad}}. \tag{5.19}$$

The computation of the update equations is straightforward and follows the same reasoning as Horn (1990). If the photometric gradient estimates p, q and the surface z are considered independent, then the optimal surface z has to be computed as described in Section 3.3. The newly added error term does not depend on z and therefore the update

equation for z can be taken from Section 3.3. In terms of p and q, the minimisation is an ordinary calculus problem. Computing the derivatives with respect to p and q and setting to zero yields

$$(R - I)\,\frac{\partial R}{\partial p} - \gamma \cdot \left(\frac{\partial z}{\partial x} - p\right) + \delta \cdot \frac{\partial}{\partial p} E_{\text{grad}} = 0, \tag{5.20}$$

$$(R - I)\,\frac{\partial R}{\partial q} - \gamma \cdot \left(\frac{\partial z}{\partial y} - q\right) + \delta \cdot \frac{\partial}{\partial q} E_{\text{grad}} = 0. \tag{5.21}$$

The partial derivatives of E_{grad} are computed as described in Section 5.2.1 and the partial derivatives of the reflectance model R are estimated using finite differences. Horn (1990) proposes to evaluate the error functions at $\frac{\partial z}{\partial x}$ and $\frac{\partial z}{\partial y}$ (cf. Section 3.3). This strategy is adopted. From Eq. (5.20), Eq. (5.21), and Eq. (3.6) then follow the update equations of the pixel (u, v) at iteration n:

$$\begin{aligned} p_{u,v}^{(n_{\text{iter}}+1)} = {} & \left.\frac{\partial z}{\partial x}\right|_{u,v}^{(n_{\text{iter}})} - \frac{1}{\gamma}\left(R|_{\left.\frac{\partial z}{\partial x}\right|_{u,v}^{(n_{\text{iter}})}} - I_{u,v}\right) \left.\frac{\partial R}{\partial p}\right|_{\left.\frac{\partial z}{\partial x}\right|_{u,v}^{(n_{\text{iter}})}} \\ & + \frac{\delta}{\gamma}\left(g_{\sigma_{\text{grad}}} \circ \left(g_{\sigma_{\text{grad}}} * \left(\frac{\partial z}{\partial x} - \frac{\partial z_{\text{DEM}}}{\partial x}\right)\right)\right)\Bigg|_{u,v}^{(n_{\text{iter}})}, \end{aligned} \tag{5.22}$$

$$\begin{aligned} q_{u,v}^{(n_{\text{iter}}+1)} = {} & \left.\frac{\partial z}{\partial y}\right|_{u,v}^{(n_{\text{iter}})} - \frac{1}{\gamma}\left(R|_{\left.\frac{\partial z}{\partial y}\right|_{u,v}^{(n_{\text{iter}})}} - I_{u,v}\right) \left.\frac{\partial R}{\partial q}\right|_{\left.\frac{\partial z}{\partial y}\right|_{u,v}^{(n_{\text{iter}})}} \\ & + \frac{\delta}{\gamma}\left(g_{\sigma_{\text{grad}}} \circ \left(g_{\sigma_{\text{grad}}} * \left(\frac{\partial z}{\partial y} - \frac{\partial z_{\text{DEM}}}{\partial y}\right)\right)\right)\Bigg|_{u,v}^{(n_{\text{iter}})}, \end{aligned} \tag{5.23}$$

$$\begin{aligned} z_{u,v}^{(n_{\text{iter}}+1)} = {} & \frac{h_x^2\left(z_{u+1,v}^{(n_{\text{iter}})} + z_{u-1,v}^{(n_{\text{iter}})}\right) + h_y^2\left(z_{u,v+1}^{(n_{\text{iter}})} + z_{u,v-1}^{(n_{\text{iter}})}\right)}{2\left(h_x^2 + h_y^2\right)} \\ & - \frac{h_x^2 h_y^2\left(\left.\frac{\partial p}{\partial x}\right|_{u,v}^{(n_{\text{iter}}+1)} + \left.\frac{\partial q}{\partial y}\right|_{u,v}^{(n_{\text{iter}}+1)}\right)}{2\left(h_x^2 + h_y^2\right)}. \end{aligned} \tag{5.24}$$

The optimisation continues until the value of the overall error term increases or a specified number of iterations is exceeded. The maximum number of iterations is set to $N_{\text{MaxSfS}} = 500$ which is rarely reached. The parameters are chosen similarly to the extended photoclinometry scheme presented in Section 5.2.2. The Gaussian kernel width σ_{grad} is chosen such that interpolation gaps like those appearing inside the gridded LOLA DEM disappear and small details that appear in the image but are missing in the DEM are not apparent after filtering. The weight δ, again, should be chosen as small as possible but as large as needed for convergence. Commonly, a suitable choice is $\delta = 2.0 \cdot 10^{-4}$ but

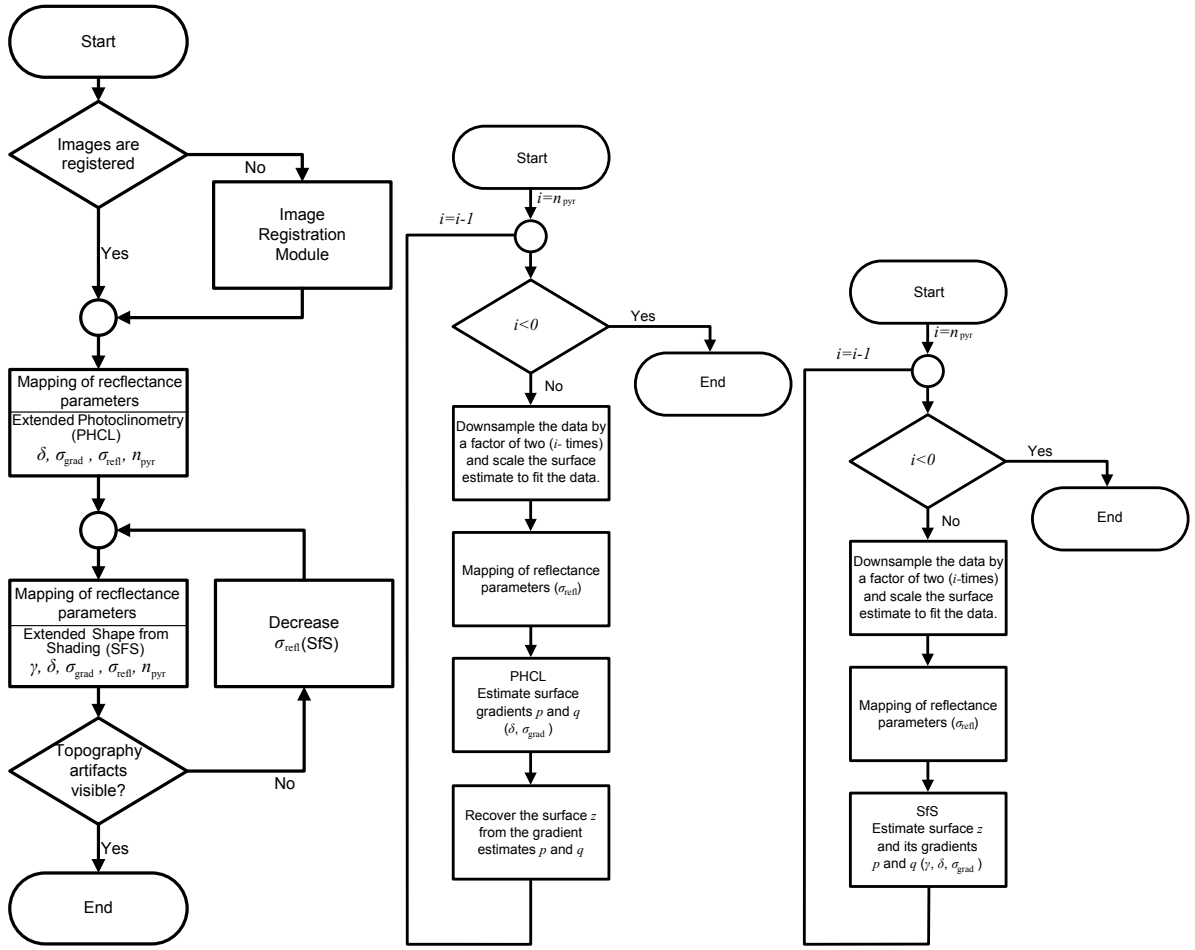

(a) Overview (b) PHCL scheme (c) SfS scheme

Figure 5.1: Flow charts of the proposed algorithm. (a) Extended overview of the complete system. All parameters have been included in the corresponding blocks. A different set of parameters is used for the PHCL and the SfS algorithm, respectively. The parameters with the same name, however, have the same meaning within the algorithms. (b) Detailed overview of the PHCL algorithm. (c) Detailed overview of the SfS algorithm.

it can be decreased or increased as necessary. The weight γ can be interpreted as a step size and is largely problem dependent. As initial value $\gamma = 2.5 \cdot 10^{-4}$ is chosen and it is increased if the algorithm diverges or decreased if the algorithm converges very slowly, i.e. exceeds N_{MaxSfS}.

5.2.4 Reconstruction method

Fig. 5.1 summarises the complete reconstruction process and the parameters of the single algorithms. The PHCL and the SfS algorithms are illustrated in Fig. 5.1(b) and Fig. 5.1(c), respectively. If necessary, the radiance images are registered using the illumination-independent image registration algorithm (cf. Section 6.3). The co-registered radiance images are then used as an input to the PHCL algorithm (cf. Section 5.2.2) which first estimates the parameters of the reflectance model based on the initial surface and then computes the surface gradients based on the estimated reflectance model. The integration of the determined surface gradients using the variational approach as proposed by Horn (1990) is considered a part of the PHCL algorithm and not mentioned explicitly. Finally, the resulting surface is forwarded to the SfS algorithm (cf. Section 5.2.3). Again, the SfS algorithm consists of a reflectance parameter estimation prior to the surface reconstruction. This order of PHCL and SfS is motivated by the evaluation, which shows that the PHCL provides a good initial surface for the SfS algorithm (cf. Section 5.5.1). A comparison between the results of the PHCL algorithm and the SfS algorithm shows that the DEM obtained using the PHCL tends to exhibit steeper slopes. This may be due to the subsequent integration step, which adapts the DEM to the gradient field which might suffer from small errors. The SfS algorithm, in contrast, adapts the DEM and the surface gradients within each iteration, which results in lower slopes. Although there is no direct evidence for this, using the possibly overestimated slopes from the PHCL algorithm as initial input to the SfS algorithm, which flattens the slopes, might lead to the increased accuracy.

To process DEM and reflectance images at largely different resolutions and to decrease the computational load, both algorithms may be applied to different pyramid levels N_{pyr}, where each level corresponds to a down-sampling by a factor of two. Notably, the estimation during PHCL and SfS minimises different functions and thus the parameters may differ. The notation is as follows:

- δ_{PHCL}, $\sigma_{\text{grad}_{\text{PHCL}}}$, $\sigma_{\text{refl}_{\text{PHCL}}}$ and $N_{\text{pyr}_{\text{PHCL}}}$ are the parameters of the PHCL algorithm denoting the weight and the width of the low-pass filter for the relative depth DEM constraint, while $\sigma_{\text{refl}_{\text{PHCL}}}$ denotes the range of influence of pixels during the parameter estimation and $N_{\text{pyr}_{\text{PHCL}}}$ denotes the number of pyramid levels.

- δ_{SfS}, $\sigma_{\text{grad}_{\text{SfS}}}$, $\sigma_{\text{refl}_{\text{SfS}}}$ and $N_{\text{pyr}_{\text{SfS}}}$ are the SfS parameters analogous to the PHCL algorithm. The parameter γ_{SfS} denotes the weight of the integrability error term.

After convergence of the SfS algorithm, the surface has the same lateral resolution as the radiance image. However, due to the low-pass filtering step during the reflectance parameter estimation there is some bias in the estimation of the surface gradients. Analogous to the strategy by Horn (1990) of solving a system of coupled equations, a new set of reflectance parameters is estimated using the result of the SfS algorithm and the SfS

algorithm is recomputed. This corresponds to an estimation of two unknowns, namely the surface and the reflectance parameters, by updating one at a time while the other is considered constant. To account for the increase in lateral resolution, $\sigma_{\text{refl}_{\text{SfS}}}$ is decreased during each computation. The notation is $\sigma_{\text{refl}_{\text{SfS}}} = \{\sigma_{\text{refl}_1}, \cdots, \sigma_{\text{refl}_n}\}$, where σ_{refl_n} is the value of $\sigma_{\text{refl}_{\text{SfS}}}$ during the nth iteration of the SfS algorithm, i.e. the nth subsequent execution of the SfS algorithm using a possibly different σ_{refl_n}.

5.3 Absolute depth constraint

The second step of the photometric surface reconstruction is the integration of the estimated gradient field. This aims at the reduction and/or suppression of accumulated small systematic errors during the gradient estimation step. Including the absolute depth of the a-priori known DEM into the gradient integration step involves a modification of the original calculus of variations (cf. Section 3.3). At first, the Euler equation and boundary conditions of the modified problem are derived in Section 5.3.1. An iterative solver of the Euler equation is then detailed in Section 5.3.2 and Section 5.3.3 deals with stopping criteria. Section 5.3.4 finally described how to include the modified gradient estimation problem into the shape from shading algorithm.

5.3.1 Absolute depth error term

Horn (1990) searches for a surface z whose gradients $\frac{\partial z}{\partial x} = z_x$ and $\frac{\partial z}{\partial y} = z_y$ are close to the photometric surface gradient estimates p and q, respectively. This is achieved by minimising the so-called integrability error

$$E_{\text{int}} = \int_{\mathbf{x}} \int_{\mathbf{y}} \frac{1}{2} (z_x - p)^2 + \frac{1}{2} (z_y - q)^2 \, dxdy \tag{5.25}$$

within a region defined by Ω, here denoted by the vectors $\mathbf{x}$ and $\mathbf{y}$ specifying the integration path along the boundary of Ω. This notation is convenient for rectangular regions, i.e. images. However, it applies to any region shape. Since this equation contains z and its partial derivatives, this is no ordinary calculus problem. Using the calculus of variations, Horn (1990) derives the corresponding Euler equation

$$\Delta z = p_x + q_y \tag{5.26}$$

where $p_x = \frac{\partial p}{\partial x}$ and $q_y = \frac{\partial q}{\partial y}$ and the boundary conditions

$$\mathbf{n}_\Omega^T \cdot \begin{bmatrix} \frac{\partial z}{\partial x} \\ \frac{\partial z}{\partial y} \end{bmatrix} = \mathbf{n}_\Omega^T \cdot \begin{bmatrix} p \\ q \end{bmatrix} \tag{5.27}$$

where $\mathbf{n}_\Omega$ is the vector normal to the region boundary Ω.

To include the absolute depth information of the a-priori known surface z_{DEM} to the surface estimation problem,

$$\begin{aligned} E_{\mathrm{absDepth}} &= E_{\mathrm{int}} + \tau \cdot \underbrace{\int_{\mathbf{x}} \int_{\mathbf{y}} \frac{1}{2} \left(f_{\mathrm{lp}}(z) - f_{\mathrm{lp}}(z_{\mathrm{DEM}}) \right)^2 dxdy}_{E_{\mathrm{depth}}} \\ &= E_{\mathrm{int}} + \tau \cdot \int_{\mathbf{x}} \int_{\mathbf{y}} \frac{1}{2} \left(g_{\sigma_{\mathrm{absDepth}}} * z - g_{\sigma_{\mathrm{absDepth}}} * z_{\mathrm{DEM}} \right)^2 dxdy \qquad (5.28) \\ &= \int_{\mathbf{x}} \int_{\mathbf{y}} F\left(z, z_x, z_y\right) dxdy. \qquad (5.29) \end{aligned}$$

is minimised. The Gaussian low-pass filter $g_{\sigma_{\mathrm{absDepth}}}$ of width $\sigma_{\mathrm{absDepth}}$ is applied using a convolution ($*$). The new term may be interpreted as the least squared distance between the surface z and the known depth data z_{DEM} in a space where the high-frequency components are ignored and only the low-frequency component is relevant. The resulting error functional is thus a generalisation of the reference algorithm by Shao et al. (1991) (cf. Section 3.3). It contains z as well as its first-order partial derivatives z_x and z_y. Hence, the optimal solution $\hat{z}$ is found using the calculus of variations (cf. Appendix B). The surface is composed of the optimal surface and a variation η such that $z = \hat{z} + \varepsilon\eta$, $z_x = z_x|_{\hat{z}} + \varepsilon\eta_x$ and $z_y = z_y|_{\hat{z}} + \varepsilon\eta_y$. For $\varepsilon = 0$, the optimal surface is obtained. Thus, the derivative of Eq. (5.28) with respect to ε at $\varepsilon = 0$ needs to be equal to zero. Accordingly, the Euler equation is

$$\Delta z - \tau \cdot \left(f_{\mathrm{lp}}(z) - f_{\mathrm{lp}}(z_{\mathrm{DEM}}) \right) \cdot \frac{\partial}{\partial z} f_{\mathrm{lp}}(z) = p_x + q_y \qquad (5.30)$$

and the corresponding boundary conditions are

$$\mathbf{n}_\Omega^T \cdot \begin{bmatrix} \frac{\partial z}{\partial x} \\ \frac{\partial z}{\partial y} \end{bmatrix} = \mathbf{n}_\Omega^T \cdot \begin{bmatrix} p \\ q \end{bmatrix} \qquad (5.31)$$

where $\mathbf{n}_\Omega$ is the vector normal to the region boundary Ω. Thus, the boundary conditions are identical to those derived by Horn (1990).

Eq. (5.30) requires the derivative of the convolution with respect to z. For the computation of the derivative the chain rule is applied to obtain

$$\begin{aligned} \frac{\partial}{\partial x} f_{\mathrm{lp}}(z) &= \frac{\partial}{\partial z} f_{\mathrm{lp}}(z) \cdot \frac{\partial z}{\partial x}, \qquad (5.32) \\ \frac{\partial}{\partial y} f_{\mathrm{lp}}(z) &= \frac{\partial}{\partial z} f_{\mathrm{lp}}(z) \cdot \frac{\partial z}{\partial y} \qquad (5.33) \end{aligned}$$

which is solved in a least-squares sense to obtain

$$\frac{\partial}{\partial z} f_{\mathrm{lp}}(z) = \frac{z_x \cdot \frac{\partial}{\partial x} f_{\mathrm{lp}}(z) + z_y \cdot \frac{\partial}{\partial y} f_{\mathrm{lp}}(z)}{z_x^2 + z_y^2} \tag{5.34}$$

which holds if either $\frac{\partial z}{\partial x}$ or $\frac{\partial z}{\partial y}$ is nonzero and accounts for the error inherent in the finite difference approximation of the partial derivatives.

5.3.2 Depth from gradient field

The basic idea of an iterative relaxation approach is to update the unknowns one at a time while assuming the values of the solution as known. Thus, an update equation for a centre pixel z_c is derived as a function of the surrounding, known, neighbourhood by applying finite difference discretisations. To emphasise the discrete variables a different coordinate system, where u corresponds to the discrete x–axis and v represents the discrete y–axis, is used. The low-pass function $f_{\mathrm{lp}}(z)$ is interpreted as a discrete convolution with a filter matrix $\mathbf{F}$. Since the filter is placed in a different coordinate system, whose origin lies at the centre pixel, u_{f} denotes the discrete filter x–axis and v_{f} denotes the discrete filter y–axis. Prior to discussing the derivation of the update equation, several symbols are introduced to increase the readability.

The depth value at the pixel of interest (u, v) is denoted by z_{c}. The edge-adjacent pixels are denoted z_{l}, $z_{2\mathrm{l}}$, z_{r}, $z_{2\mathrm{r}}$, z_{u}, $z_{2\mathrm{u}}$, z_{d} and $z_{2\mathrm{d}}$ as shown in Fig. 5.2(a). Accordingly h_{cx} and h_{cy} denote the pixel extent at (u, v) in x– and y–direction, respectively. The pixel extent in x–direction of the horizontally adjacent pixels are denoted h_{l} and h_{r} while the pixel extent in y–direction of the vertically adjacent pixels are denoted by h_{u} and h_{d} as presented in Fig. 5.2(b) and Fig. 5.2(c). The filter coefficient at its origin is denoted by F_0 and the edge-adjacent filter coefficients are denoted by F_{l}, F_{r}, F_{u} and F_{d} (cf. Fig. 5.2(d)).

Eq. (5.30) is composed of three terms containing z, namely

$$t_1 = \Delta z, \tag{5.35}$$

$$t_2 = (f_{\mathrm{lp}}(z) - f_{\mathrm{lp}}(z_{\mathrm{DEM}})) \text{ and} \tag{5.36}$$

$$t_3 = \frac{\partial}{\partial z} f_{\mathrm{lp}}(z) = \frac{z_x \cdot f_{\mathrm{lp}}(z_x) + z_y \cdot f_{\mathrm{lp}}(z_y)}{z_x^2 + z_y^2}, \tag{5.37}$$

on the left hand side and a constant on the right hand side. These terms are examined one by one and z_{c} is separated from the surrounding pixels of z to find an expression for z_{c}. The singularity of t_3 for $z_x = 0$ and $z_y = 0$ is regarded after the update equation is derived.

Figure 5.2: Explanation of the introduced symbols. (a) Location of symbols within the depth image z. (b) – (c) Location of symbols within the horizontal and vertical extents matrices h^x and h^y,respectively. (d) Location of symbols within the discrete filter matrix $\mathbf{F}$.

The Laplacian of z can be rewritten, using finite differences, to

$$\begin{aligned} t_1 = \Delta z &= \frac{z_\mathrm{l} - 2z_\mathrm{c} + z_\mathrm{r}}{h_\mathrm{cx}^2} + \frac{z_\mathrm{u} - 2z_\mathrm{c} + z_\mathrm{d}}{h_\mathrm{cy}^2} \\ &= -z_\mathrm{c}\frac{2\left(h_\mathrm{cx}^2 + h_\mathrm{cy}^2\right)}{h_\mathrm{cx}^2 h_\mathrm{cy}^2} + \frac{h_\mathrm{cy}^2 z_\mathrm{h} + h_\mathrm{cx}^2 z_\mathrm{v}}{h_\mathrm{cx}^2 h_\mathrm{cy}^2} \end{aligned} \tag{5.38}$$

where $z_\mathrm{h} = z_\mathrm{l} + z_\mathrm{r}$ and $z_\mathrm{v} = z_\mathrm{u} + z_\mathrm{d}$ are the sums of the neighbouring depth values in horizontal and vertical direction, respectively.

Since the discrete convolution can be interpreted as a sum of depth values weighted by the corresponding filter coefficients, the second term can be rewritten as

$$\begin{aligned} t_2 &= \left(f_\mathrm{lp}(z) - f_\mathrm{lp}(z_\mathrm{DEM})\right) \\ &= \left(F_0 z_\mathrm{c} + f_{-0}(z) - f_\mathrm{lp}(z_\mathrm{DEM})\right) \\ &= \left(F_0 z_\mathrm{c} + \mathbf{F}_{-0} * z - \mathbf{F} * z_\mathrm{DEM}\right) \end{aligned} \tag{5.39}$$

where $f_{-0}(z)$ is the convolution with a filter matrix $\mathbf{F}_{-0}$ that is obtained by setting the element of $\mathbf{F}$ at the origin to zero:

$$\mathbf{F}_{-0}(u_\mathrm{f}, v_\mathrm{f}) = \begin{cases} \mathbf{F}(u_\mathrm{f}, v_\mathrm{f}) & u_\mathrm{f} \neq 0 \vee v_\mathrm{f} \neq 0 \\ 0 & u_\mathrm{f} = 0 \wedge v_\mathrm{f} = 0 \end{cases}. \tag{5.40}$$

Thus $f_{-0}(z)$ does not depend on z_c.

Due to the non-linearity in t_3, the denominator and the numerator are examined separately. The denominator of Eq. (5.37)

$$t_\mathrm{3den} = z_x^2\big|_{u,v} + z_y^2\big|_{u,v} \tag{5.41}$$

contains partial derivatives of z. The central differences discretisation yields

$$z_x\big|_{u,v} = \frac{z_\mathrm{r} - z_\mathrm{l}}{2h_\mathrm{cx}}, \tag{5.42}$$

$$z_y\big|_{u,v} = \frac{z_\mathrm{u} - z_\mathrm{d}}{2h_\mathrm{cy}}. \tag{5.43}$$

Accordingly, the partial derivatives of z at the position (u, v) do not depend on z_c. For brevity, the notations z_x and z_y are kept instead of using the finite difference equivalents of $z_x|_{u,v}$ and $z_x|_{u,v}$, respectively.

Following the above reasoning, the partial derivatives of z appearing in the numerator of Eq. (5.37)

$$t_\mathrm{3num} = z_x\big|_{u,v} \cdot f_\mathrm{lp}(z_x)\big|_{u,v} + z_y\big|_{u,v} \cdot f_\mathrm{lp}(z_y)\big|_{u,v} \tag{5.44}$$

do not need further treatment. In contrast, $f_{\mathrm{lp}}(z_x)|_{u,v}$ and $f_{\mathrm{lp}}(z_y)|_{u,v}$ do contain all partial derivatives within the neighbourhood defined by the filter mask $\mathbf{F}$. After applying central differences, four partial derivatives are obtained that actually contain z_{c}:

$$z_x|_{u-1,v} = \frac{z_{\mathrm{c}} - z_{2\mathrm{l}}}{2h_{\mathrm{l}}}, \tag{5.45}$$

$$z_x|_{u+1,v} = \frac{z_{2\mathrm{r}} - z_{\mathrm{c}}}{2h_{\mathrm{r}}}, \tag{5.46}$$

$$z_y|_{u,v-1} = \frac{z_{\mathrm{c}} - z_{2\mathrm{d}}}{2h_{\mathrm{d}}}, \tag{5.47}$$

$$z_x|_{u,v+1} = \frac{z_{2\mathrm{u}} - z_{\mathrm{c}}}{2h_{\mathrm{u}}}. \tag{5.48}$$

Similar to the treatment of t_2, these are removed from the filter operations by setting the corresponding filter coefficients to zero and manually adding the eliminated terms. Defining the filter operations $f_{-\mathrm{h}}$ using the filter matrix

$$\mathbf{F}_{-\mathrm{h}}(u_{\mathrm{f}}, v_{\mathrm{f}}) = \begin{cases} \mathbf{F}(u_{\mathrm{f}}, v_{\mathrm{f}}) & (u_{\mathrm{f}} \neq -1 \wedge u_{\mathrm{f}} \neq 1) \vee v_{\mathrm{f}} \neq 0 \\ 0 & (u_{\mathrm{f}} = -1 \vee u_{\mathrm{f}} = 1) \wedge v_{\mathrm{f}} = 0 \end{cases} \tag{5.49}$$

and $f_{-\mathrm{v}}$ using the filter matrix

$$\mathbf{F}_{-\mathrm{v}}(u_{\mathrm{f}}, v_{\mathrm{f}}) = \begin{cases} \mathbf{F}(u_{\mathrm{f}}, v_{\mathrm{f}}) & u_{\mathrm{f}} \neq 0 \vee (v_{\mathrm{f}} \neq -1 \wedge v_{\mathrm{f}} \neq 1) \\ 0 & u_{\mathrm{f}} = 0 \wedge (v_{\mathrm{f}} = -1 \vee v_{\mathrm{f}} = 1) \end{cases}, \tag{5.50}$$

the numerator is rewritten as

$$\begin{aligned} t_{3\mathrm{num}} =& z_x \cdot \left(F_{\mathrm{l}} \frac{z_{2\mathrm{r}} - z_{\mathrm{c}}}{2h_{\mathrm{r}}} + F_{\mathrm{r}} \frac{z_{\mathrm{c}} - z_{2\mathrm{l}}}{2h_{\mathrm{l}}} + f_{-\mathrm{h}}(z_x) \right) \\ &+ z_y \cdot \left(F_{\mathrm{d}} \frac{z_{2\mathrm{u}} - z_{\mathrm{c}}}{2h_{\mathrm{u}}} + F_{\mathrm{u}} \frac{z_{\mathrm{c}} - z_{2\mathrm{d}}}{2h_{\mathrm{d}}} + f_{-\mathrm{v}}(z_y) \right). \end{aligned} \tag{5.51}$$

Combining $t_{3\mathrm{den}}$ and $t_{3\mathrm{num}}$ and collecting z_{c}, t_3 is reformulated to

$$\begin{aligned} t_3 = z_{\mathrm{c}} & \frac{z_x \left(\frac{F_{\mathrm{r}}}{2h_{\mathrm{l}}} - \frac{F_{\mathrm{l}}}{2h_{\mathrm{r}}} \right) + z_y \left(\frac{F_{\mathrm{u}}}{2h_{\mathrm{d}}} - \frac{F_{\mathrm{d}}}{2h_{\mathrm{u}}} \right)}{z_x^2 + z_y^2} \\ + & \frac{z_x \left(\frac{F_{\mathrm{l}}}{2h_{\mathrm{r}}} z_{2\mathrm{r}} - \frac{F_{\mathrm{r}}}{2h_{\mathrm{l}}} z_{2\mathrm{l}} + f_{-\mathrm{h}}(z_x) \right) + z_y \left(\frac{F_{\mathrm{d}}}{2h_{\mathrm{u}}} z_{2\mathrm{u}} - \frac{F_{\mathrm{u}}}{2h_{\mathrm{d}}} z_{2\mathrm{d}} + f_{-\mathrm{v}}(z_y) \right)}{z_x^2 + z_y^2}. \end{aligned} \tag{5.52}$$

Notably, due to the 180 ° rotation of the filter which is inherent in the convolution, the left filter coefficient is combined with the right neighbouring image cell and vice versa.

Finally, by inserting Eq. (5.38), Eq. (5.39) and Eq. (5.52) into Eq. (5.30) and collecting powers of z_c, the quadratic equation

$$c_{\mathrm{absDepth}_2} z_\mathrm{c}^2 + c_{\mathrm{absDepth}_1} z_\mathrm{c} + c_{\mathrm{absDepth}_0} = 0 \tag{5.53}$$

is obtained where

$$c_{\mathrm{absDepth}_2} = -\tau F_\mathrm{c} \frac{z_x \left(\frac{F_\mathrm{r}}{2h_\mathrm{l}} - \frac{F_\mathrm{l}}{2h_\mathrm{r}}\right) + z_y \left(\frac{F_\mathrm{u}}{2h_\mathrm{d}} - \frac{F_\mathrm{d}}{2h_\mathrm{u}}\right)}{z_x^2 + z_y^2}, \tag{5.54}$$

$$\begin{aligned} c_{\mathrm{absDepth}_1} = {} & -\tau \left(f_{-0}(z) - f_\mathrm{lp}(z_\mathrm{DEM})\right) \frac{z_x \left(\frac{F_\mathrm{r}}{2h_\mathrm{l}} - \frac{F_\mathrm{l}}{2h_\mathrm{r}}\right) + z_y \left(\frac{F_\mathrm{u}}{2h_\mathrm{d}} - \frac{F_\mathrm{d}}{2h_\mathrm{u}}\right)}{z_x^2 + z_y^2} \\ & - \tau F_\mathrm{c} \frac{z_x \left(\frac{F_\mathrm{l}}{2h_\mathrm{r}} z_{2\mathrm{r}} - \frac{F_\mathrm{r}}{2h_\mathrm{l}} z_{2\mathrm{l}} + f_{-\mathrm{h}}(z_x)\right) + z_y \left(\frac{F_\mathrm{d}}{2h_\mathrm{u}} z_{2\mathrm{u}} - \frac{F_\mathrm{u}}{2h_\mathrm{d}} z_{2\mathrm{d}} + f_{-\mathrm{v}}(z_y)\right)}{z_x^2 + z_y^2} \\ & - \frac{2\left(h_{\mathrm{cx}}^2 + h_{\mathrm{cy}}^2\right)}{h_{\mathrm{cx}}^2 h_{\mathrm{cy}}^2} \end{aligned} \tag{5.55}$$

$$\begin{aligned} c_{\mathrm{absDepth}_0} = {} & -\tau (f_{-0}(z) - f_\mathrm{lp}(z_\mathrm{DEM})) \cdot \\ & \frac{z_x \left(\frac{F_\mathrm{l}}{2h_\mathrm{r}} z_{2\mathrm{r}} - \frac{F_\mathrm{r}}{2h_\mathrm{l}} z_{2\mathrm{l}} + f_{-\mathrm{h}}(z_x)\right) + z_y \left(\frac{F_\mathrm{d}}{2h_\mathrm{u}} z_{2\mathrm{u}} - \frac{F_\mathrm{u}}{2h_\mathrm{d}} z_{2\mathrm{d}} + f_{-\mathrm{v}}(z_y)\right)}{z_x^2 + z_y^2} \\ & + \frac{h_{\mathrm{cy}}^2 z_\mathrm{h} + h_{\mathrm{cx}}^2 z_\mathrm{v}}{h_{\mathrm{cx}}^2 h_{\mathrm{cy}}^2} - (p_x + q_y). \end{aligned} \tag{5.56}$$

In case of a rotationally symmetric filter and different but constant pixel extents in x– and y–direction, respectively, c_{absDepth_2} vanishes and the algorithm has a unique solution. Although this is a special case, it is quite common since low-pass filters usually are rotationally symmetric and the pixel extents in images often are different but constant in x– and y–direction, respectively. The cylindrical projection which is commonly used in planetary science, yields pixel extents in x–direction that change with the value of the y–coordinate. However, they are constant along one row and thus match the special case.

The general case yields two possible solutions of z_c, but the experiments showed that one solution is close to the value of the last solution while the other solution is very far off. Since it is assumed that a DEM of lower lateral resolution is already known, the solution that is closest to the value of z_c obtained in the previous iteration is selected.

A singularity exists in case of a zero-valued gradient, i.e. $z_x = 0$ and $z_y = 0$. Due to the fact that the method aims at the recovery of high-frequent depth changes, it is assumed that only a minority of surface pixels has a zero valued gradient. This can always be achieved by rotating the coordinate system by a small angle. This way even a plane that is perpendicular to the z-axis in the old coordinate system will have a non zero valued

gradient in the new coordinate system. Furthermore, most surfaces of interest show a texture and only small planar areas. Since the intensity-based estimates of the surface gradients will be noisy and thus, even for small noise, the surface gradient is not zero valued. Thus a possible strategy is removing zero valued surface gradients by adding a small random value. Due to this random behaviour, convergence problems might be the consequence. Another approach is to ignore the known DEM for the corresponding pixels and update the pixels using the Poisson solver. During the evaluation a different technique is applied. The remaining pixels are updated and the new depth values of singular pixels are determined by interpolating the updated pixels. For simplicity, all depth values within a radius of one pixel are averaged. If no valid pixels are in the specified range the range is increased by one pixel until at least one updated pixel is in the range.

5.3.3 Stopping criteria

An important aspect of iterative methods is a suitable stopping and/or convergence criterion. The general answer to the question when to stop iterating is: stop after the algorithm converged to the optimal solution. This statement, however, rises two important issues. First, the convergence to the optimal solution needs to be tracked, and second, the possibility of divergence has to be taken into account.

A common approach to measure the convergence is the decrease of the overall error or the individual residuals. Convergence in a strict sense requires a monotonous decrease of the overall error after each subsequent iteration and thus leads to a diminishing "gain" in optimality. Hence, convergence is achieved if the decrease of the overall error is less than a threshold and divergence leads to an increasing overall error. Following this reasoning, a time optimality constraint may be added by limiting the number of iterations which yields the best estimate that may be obtained in a given runtime.

These criteria, however, are too simplistic as discussed based on the following observations:

1. If the algorithm diverges it does so very fast and the value of the error functional approaches infinity after a few steps.

2. Large changes of the solution estimate are observed in the early steps while the later steps "polish" small details.

3. The algorithm may oscillate like many iterative methods, e.g. gradient descent, and may oscillate close to the optimum. In other words: One step decreases the absolute depth error while increasing the integrability error and vice versa. Often, the value of the overall error functional then increases slightly.

Notably, the term step is used instead of iteration when referring to a single update of the solution estimate. The term iteration is reserved for steps that decrease the overall

error functional. This small but important detail is necessary to describe the approach to terminate the algorithm without stopping at the first oscillation.

From observation 1 follows that divergence can be measured by a strongly increased overall error value. Since the algorithm diverges fast, a large increase is not quantitatively measured but a threshold E_{div} on the value of the error function is set. The algorithm stops if the overall error equals or exceeds E_{div}.

According to observation 2, the norm of the change of the solution estimate decreases if the algorithm proceeds. Thus, the number of iterations is limited by introducing an iteration counter n_{iter} that is increased after each step that successfully decreases the overall error. Consequently, a step that decreases the overall error value is termed an iteration. If the maximum number of iterations N_{iter} is reached the algorithm stops.

Since a monotonous decrease of the overall error value is not assured as described in observation 3, the overall error is allowed to increase. The number of steps since the last successful iteration is termed n_{step}. Consequently, n_{step} is increased after each update step and set to zero after each iteration. If n_{step} reaches the maximum number of steps N_{step} the algorithm is stopped. Hence, the algorithm stops even if oscillating near the optimum.

A step as defined in the previous stopping criteria may be interpreted as a try to further minimise the overall error. Due to this possibly increasing error, the current solution estimate is saved after each iteration as the best solution estimate z^*. After termination of the algorithm, z^* is returned.

The overall iteration cycle is shown in Fig. 5.3. Notably, i is a counter of total updates which is neither the iteration nor the step counter and is bounded by $N_{\text{iter}} \cdot N_{\text{step}}$. The algorithm stops if one of the three stopping criteria is met.

5.3.4 Further extended SfS method

Including the absolute depth constraint into the SfS problem is rather straight forward. The SfS problem is solved by an alternating update of the photometric gradient estimates p and q and the estimated surface z. Since the additional error term does not include the photometric gradient estimates p and q, the update equation for p and q is adopted from Eq. (5.24). Furthermore, the update equation for z may be replaced by the update equation Eq. (5.53) as derived in Section 5.3.2 due to the absence of p and q in the error functional. The integrability error, however, is weighted with γ in the shape from shading algorithm. The weight τ thus needs to be replaced by

$$\tau \leftarrow \frac{\tau}{\gamma}. \tag{5.57}$$

The alternating update of the photometric gradient estimates and the surface shows the same oscillating behaviour as the gradient integration method and thus the iteration

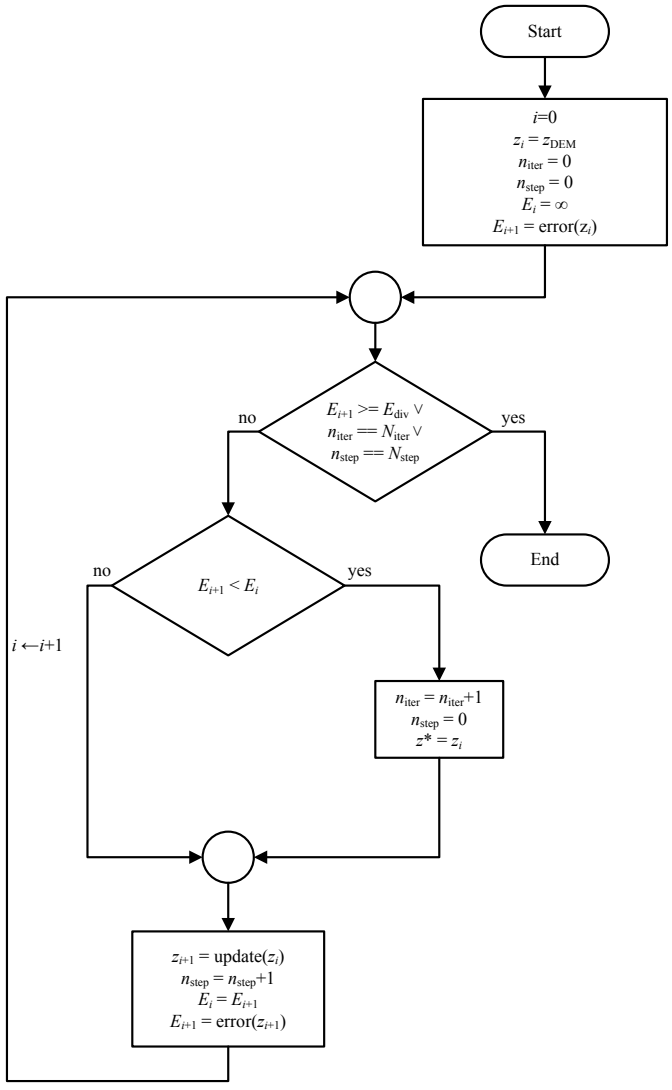

Figure 5.3: Flowchart of the proposed depth recovery from a gradient field estimate.

strategy is adopted from Section 5.3.3, i.e. only a successful reduction of the overall error is accepted as an iteration and a temporary increase in the overall error is tolerated.

5.4 The reconstruction algorithm

The proposed methods allow for two different reconstruction approaches. First, the gradient field may be estimated using the extended PHCL algorithm (cf. Section 5.2.2) and the surface is then recovered from the possibly noise gradient field using the integration method introduced in Section 5.3.2. Second, the further extended SfS method discussed in Section 5.3.4 may be applied to directly derive the surface and the gradient field. The former method will be referred to as the two-step method.

In Section 5.5.2, it is shown that the two-step method produces seemingly less blurred results. It, however, shows significant artefacts in regions where the overlap of the radiance images changes. This may be related to an imperfect radiance calibration and indicates that the two-step method is more sensitive to the radiance information. The further extended SfS methods shows no such artefacts which indicates a certain level of robustness. Consequently, it may be more appropriate to select the two-step method if the radiance calibration is of high quality while the further extended SfS method may be more appropriate to images of unknown or reduced calibration quality.

Both methods, however, require the reflectance model and thus the albedo map of the surface area. The proposed approach is similar to the method proposed by Danzl and Scherer (2002). It uses the fact that an optimization in a high-dimensional space is often infeasible while a one-dimensional line search along a pre-defined direction requires significantly less efford. The well known line search method by Powell (1964) optimizes the problem by alternating between search directions that form a basis of the search space. Similar to the one-dimensional line search, the search space may be partitioned into subspaces. As proposed by Danzl and Scherer (2002) the optimization alternates between the estimation of the surface reflectance properties while the surface model is kept constant and the optimzation of the surface model while the surface reflectance properties are kept constant. They propose to reduced the image resolution until it matches the resolution of their stereo analysis based DEM. The DEM is then refined using the downscaled images and a smoothness constaint. By increasing the resolution and decreasing the weight of the smoothness constraint over multiple cycles, they obtain a final surface estimate. Notably, the low-pass filter introduced in Section 4.2.1 covers the different resolution of the surface model and the image. By subsequently decreasing the width of the low-pass filter, the surface model will be refined to image resolution. Since the smoothness constaint is replaced with the relative depth constaint and/or the absolute depth constraint, it is omitted.

5.5 Results

The relative depth constraint results in a less complex problem and thus the ability to reduce large-scale errors by suppressing systematic errors in the gradient estimation step are discussed in Section 5.5.1. It is shown, that the overall reconstruction accuracy does not decrease compared to synthetic ground truth and laser altimeter measurements while the lateral resolution is greatly improved. In case of imperfect radiance calibrations, the methods fail to suppress the systematic error since it is inherent to the radiance data. The resulting DEM show a large-scale drift which is successfully supressed by the absolute depth constraint. The corresponding results are given in Section 5.5.2.

5.5.1 Relative depth constraint

The evaluation of the effect of the relative depth constraint on the extended PHCL algorithm and the extended SfS algorithm consists of two distinct experiments. At first, the reconstruction accuracy of the algorithms is evaluated based on synthetic imaged and independent laser altimeter measurements. Since the reflectance model is crucial for all photometric methods, the influence of the reflectance model is examined afterwards.

Reconstruction accuracy

To measure the reconstruction accuracy of the extended PHCL algorithm and the extended SfS algorithm, two different techniques are applied. At first, a synthetic image is created from a "ground-truth" surface. The "ground-truth" surface is then compared to the reconstructed DEM. This technique corresponds to perfectly matching reflectance modelling and no sensor noise. Afterwards, a more realistic scenario is considered. The single measurement footprints of the Lunar Orbiter Laser Altimeter (LOLA) are set to be the ground truth dataset. These footprints provide an independent dataset and are accurate to 1 m (Zuber et al., 2010).

Synthetic images: Initially, the region of the lunar crater Bullialdus (longitude 336.5 °E –337.85 °E, Latitude 20 °S–22 °S) was reconstructed from M3G20090207T083836, a single M^3 image, (cf. Fig. 5.4(a)) based on the gridded LOLA DEM (cf. Fig. 5.4(c)). The output of the extended photoclinometry algorithm with $\delta_{\mathrm{PHCL}} = 2.5 \cdot 10^{-5}$, $\sigma_{\mathrm{refl}_{\mathrm{PHCL}}} = 16$ pixels, and $\sigma_{\mathrm{grad}_{\mathrm{PHCL}}} = 7$ pixels was used as an input by the shape from shading algorithm. The corresponding parameters for the shape from shading algorithm were $\gamma_{\mathrm{SfS}} = 9 \cdot 10^{-4}$, $\delta_{\mathrm{SfS}} = 2.5 \cdot 10^{-5}$, $\sigma_{\mathrm{grad}_{\mathrm{SfS}}} = 7$ and $\sigma_{\mathrm{refl}_{\mathrm{SfS}}} = \{11, 10, 9, 8, 7\}$. The Gaussian filter kernel width is due to the high data density of the LOLA DEM within the region of interest. In order to allow a maximum amount of surface structure, the parameter γ_{SfS} was chosen as small as possible. We allowed $N_{\mathrm{pyr}_{\mathrm{PHCL}}} = N_{\mathrm{pyr}_{\mathrm{SfS}}} = 4$ pyramid levels during each reconstruction. The chosen reflectance model is the Hapke IMSA model with the phase

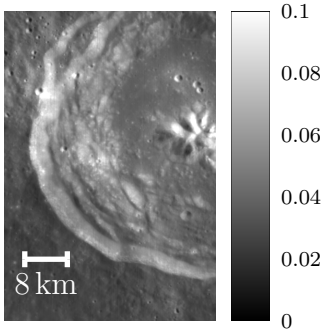

(a) M^3 radiance image at 1579 nm.

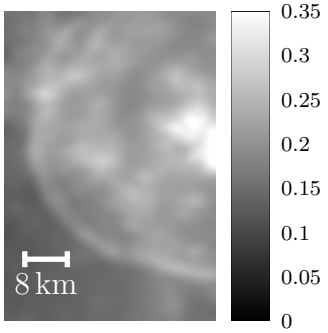

(b) Single-scattering albedo at 750 nm.

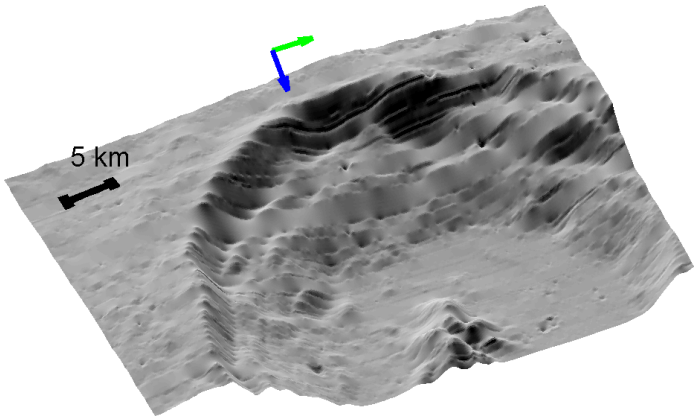

(c) LOLA gridded DEM.

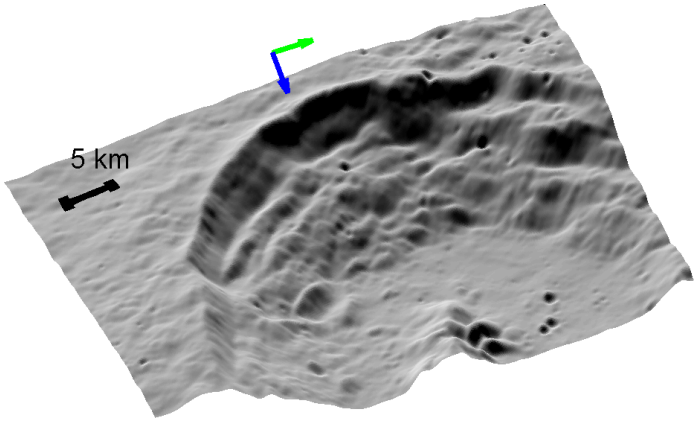

(d) Refined DEM.

Figure 5.4: Reconstruction of the crater Bullialdus (longitude 336.5 °E–337.85 °E, latitude 20 °S–22 °S, diameter: 63 km). (a) M^3 radiance image. Image credit: NASA/JPL-Caltech. (b) Estimated single-scattering albedo. (c) LOLA gridded DEM. (d) Result of the shape from shading algorithm. The elevation axis of both DEM is scaled by a factor of three.

function $f_{\mathrm{DHG}}(\alpha)$. The resulting DEM (cf. Fig. 5.4(d)) and single-scattering albedo (cf. Fig. 5.4(b)) were selected to render an artificial image using the Hapke IMSA model with $f_{\mathrm{DHG}}(\alpha)$ and the illumination geometry of the original M^3 image. A first look at the shaded photometric DEM yields the impression that the visual appearance is much less blurred than the shaded LOLA DEM. However, this is a purely qualitative statement.

The photometrically obtained DEM and albedo are considered as ground truth for a new reconstruction based on the synthetic image. If the extended photoclinometry or the shape from shading scheme with the aforementioned parameters are applied to the synthetic data on their own, the result is unsatisfying as the RMSE amount to 45 m and

50 m, respectively. However, if the shape from shading algorithm is initialised with the result of the extended photoclinometry scheme, the RMSE decreases to 9 m while the RMSE of the albedo map amounts to 0.003. The latter value corresponds to less than 1% of the mean albedo of the channel centred at 1579 nm which, amounts to 0.390. Both photometric methods rely on the integration of a gradient field. Hence, the surface is only defined up to a constant. To account for this missing constant, the surfaces are centred on their means before computation of the RMSE. The subsequent application of extended photoclinometry and shape from shading yields a large increase in accuracy. Hence, for the remainder of this section the DEM obtained from the extended photoclinometry scheme and is used as an initial DEM for the shape from shading algorithm.

Ground truth evaluation: In order to estimate the absolute error of the constructed DEM, a "ground truth" of sufficiently high lateral resolution is required. However, none of the currently available DEM has the same effective lateral resolution as the M^3 images (cf. Section 2.1.2) and the refined DEM cannot be compared as a whole. The LOLA single-point measurements, nevertheless, have a high vertical accuracy of about 1 m (Zuber et al., 2010). These measurements are grouped into batches of continuous measurements during one orbit. This segmentation is based on the temporal difference between two subsequent measurements, where the threshold is set to one hour. These batches of measurements are called "single tracks". The single tracks are then compared to cross-sections of the constructed DEM.

However, the measurements of the single tracks do not coincide with the image grid and the coordinate systems are slightly different, presumably due to pointing errors of the M^3 images. To account for the different grid resolution and coordinate systems, a binning technique and a subsequent registration of the single track onto the constructed DEM are applied. All measurements that fall into one image pixel are averaged to compute a depth value for that pixel. Afterwards, a registration is achieved by minimising the RMSE between the SfS-based DEM and the single track. This is done by shifting all pixels of the track by Δx and Δy along the x- and the$y$-axis, respectively, and performing an exhaustive search on the intervals $\Delta x \in [-15, 15]$ pixels and $\Delta y \in [-15, 15]$ pixels. Notably, all tracks and cross-sections are centred on their mean depth to account for the missing constant during integration. The same technique is applied to the GLD100. In most cases, the misalignments were found to be less than five pixels. However, the algorithm tends to push single tracks close to the image boundaries out of the image to decrease the RMSE between the remaining small number of pixels. To avoid this behaviour, every single track with a norm of the estimated translation that is larger than 5 pixels is ignored for the computation of the RMSE. A comparison to the gridded LOLA DEM shows that it is accurate to 10 m which is mainly due to interpolation artefacts, e.g. smoothing.

Table 5.1: Evaluated Regions: Parameters of the PHCL algorithm.

Region Name	Location Longitude [°]	Latitude [°]	PHCL δ_{PHCL}	$\sigma_{\text{grad}_{\text{PHCL}}}$	$\sigma_{\text{refl}_{\text{PHCL}}}$	$N_{\text{pyr}_{\text{PHCL}}}$
Aristarchus	312 °E – 314 °E	22 °N – 26 °N	$1.0 \cdot 10^{-4}$	7	11	2
Aristillus	0 °E – 2.5 °E	32 °N – 36 °N	$1.0 \cdot 10^{-4}$	15	21	2
Bhabha	194 °E – 196 °E	58 °S – 52 °S	$1.0 \cdot 10^{-4}$	15	21	2
Mairan	311 °E – 313 °E	40 °N – 43 °N	$2.5 \cdot 10^{-3}$	15	21	2
Tycho	348 °E – 350 °E	45 °S – 41 °S	$2.5 \cdot 10^{-4}$	11	21	2

Table 5.2: Evaluated Regions: Parameters of the SfS algorithm. The SfS algorithm is executed multiple times. For each iteration, $\sigma_{\text{refl}_{\text{SfS}}}$ is reduced by 1 pixel, such that the start and end value of $\sigma_{\text{refl}_{\text{SfS}}}$ is given.

Region Name	Location Longitude [°]	Latitude [°]	SFS γ_{SfS}	δ_{SfS}	$\sigma_{\text{grad}_{\text{SfS}}}$	$\sigma_{\text{refl}_{\text{SfS}}}$	$N_{\text{pyr}_{\text{SfS}}}$
Aristarchus	312 °E – 314 °E	22 °N – 26 °N	$6.0 \cdot 10^{-4}$	$2.5 \cdot 10^{-4}$	11	$\{21, \ldots, 7\}$	0
Aristillus	0 °E – 2.5 °E	32 °N – 36 °N	$6.0 \cdot 10^{-4}$	$2.5 \cdot 10^{-4}$	15	$\{21, \ldots, 7\}$	0
Bhabha	194 °E – 196 °E	58 °S – 52 °S	$6.0 \cdot 10^{-4}$	$2.5 \cdot 10^{-4}$	15	$\{21, \ldots, 7\}$	0
Mairan	311 °E – 313 °E	40 °N – 43 °N	$6.0 \cdot 10^{-3}$	$2.5 \cdot 10^{-3}$	15	$\{21, \ldots, 7\}$	0
Tycho	348 °E – 350 °E	45 °S – 41 °S	$2.0 \cdot 10^{-3}$	$2.5 \cdot 10^{-4}$	11	$\{21, \ldots, 7\}$	0

Table 5.3: Evaluated Regions: Filenames of the examined M^3 images.

Region Name	Location Longitude [°]	Location Latitude [°]	M^3 image Filename
Aristarchus	312 °E – 314 °E	22 °N – 26 °N	M3G20090209T054031 M3G20090209T072710 M3G20090418T132620 M3G20090612T060502
Aristillus	0 °E – 2.5 °E	32 °N – 36 °N	M3G20090205T131953 M3G20090205T150614 M3G20090205T171614 M3G20090608T125102
Bhabha	194 °E – 196 °E	58 °S – 52 °S	M3G20090621T065503
Mairan	47.00 °W – 49.00 °W	40.00 °N – 43.00 °N	M3G20090209T072710 M3G20090418T151350 M3G20090612T060502
Tycho	10.00 °W – 12.00 °W	45.00 °S – 41.00 °S	M3G20090206T105850 M3G20090415T202222 M3G20090609T095022

Table 5.4: Evaluated Regions: Absolute accuracy (RMSE). The RMSE is computed from cross-sections of the DEM and the corresponding LOLA single tracks. For comparison, the absolute accuracy of the GLD100 is presented as well.

Region Name	Location Longitude [°]	Location Latitude [°]	RMSE Δz [m] Refined DEM	RMSE Δz [m] GLD100
Aristarchus	312 °E – 314 °E	22 °N – 26 °N	27.3	21.5
Aristillus	0 °E – 2.5 °E	32 °N – 36 °N	45.8	20.0
Bhabha	194 °E – 196 °E	58 °S – 52 °S	32.0	21.5
Mairan	311 °E – 313 °E	40 °N – 43 °N	18.0	14.1
Tycho	348 °E – 350 °E	45 °S – 41 °S	35.2	29.1

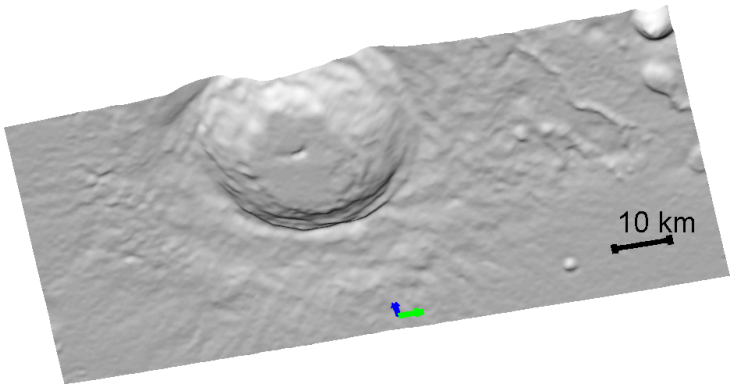

(a) GLD100.

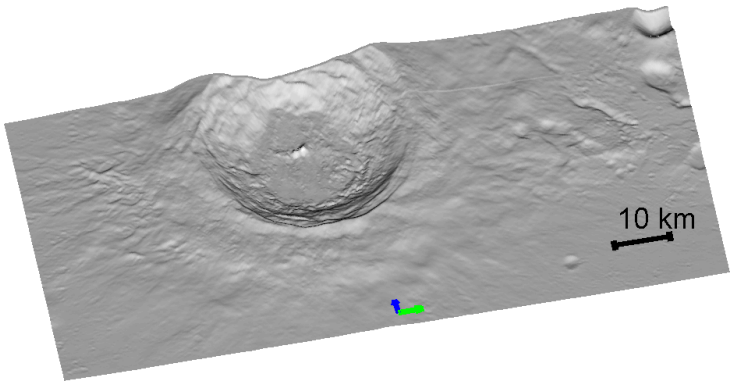

(b) Refined DEM.

Figure 5.5: Rendered DEM of crater Aristarchus (312 °E–314 °E, 22 °S–26 °S, diameter: 41 km). The elevation axis of both DEM is scaled by a factor of three. The lighting direction is indicated by the blue arrow and the green arrow points towards the north.

Table 5.1 – Table 5.4 summarise the M^3 image names, the algorithm parameters and the RMSE for the SfS-based DEM and the GLD100 for several examined regions of the lunar surface. The overall impression is that the RMSE slightly increases in comparison to the GLD100. Most of these additional discrepancies, however, appear to be due to the behaviour of the solution on large spatial scales. Approaches like the integration of the gradient field with an absolute depth data constraint (cf. Section 5.3) or the interpolation surface technique (Horovitz and Kiryati, 2004) may be helpful to compensate this effect. Nevertheless, the rather small loss in absolute accuracy is accompanied by a significant gain in lateral resolution, which follows from a qualitative analysis of Fig. 5.5, Fig. 5.6, and Fig. 5.7. Noteworthy, the textures in these figures are the shaded DEM and no other image data are overlaid. While the GLD100 appears to be slightly blurred, the DEM constructed based on shape from shading appears to be of higher resolution.

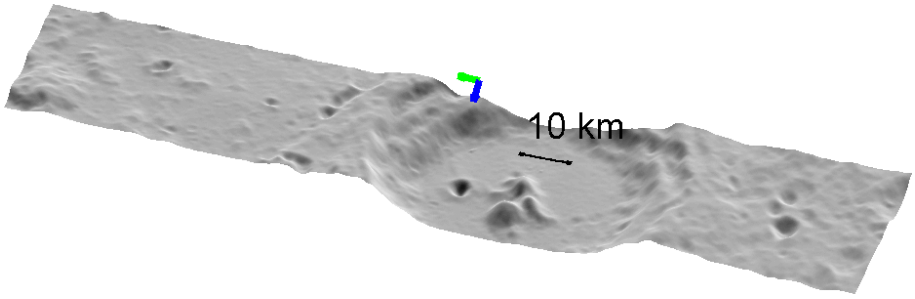

(a) GLD100.

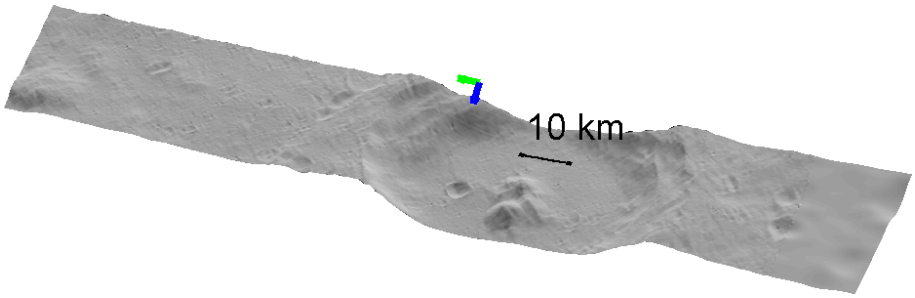

(b) Refined DEM.

Figure 5.6: Rendered DEM of crater Bhabha (194 °E–196 °E, 58 °S–52 °S, diameter: 64 km). The elevation axis of both DEM is scaled by a factor of three. The lighting direction is indicated by the blue arrow and the green arrow points towards the north.

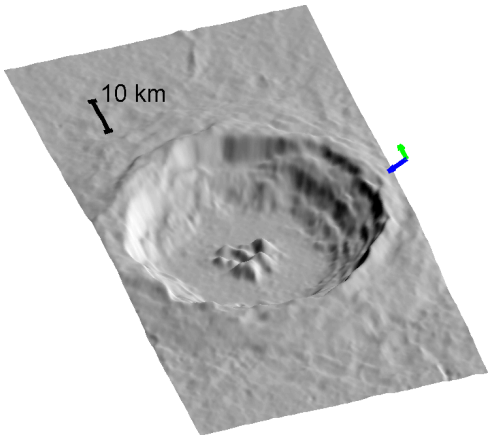

(a) GLD100.

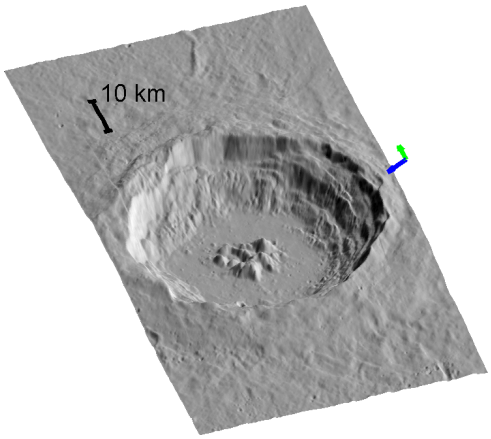

(b) Refined DEM.

Figure 5.7: Rendered DEM of crater Aristillus (0 °E–2.5 °E, 32 °N–36 °S, diameter: 56 km). The elevation axis of both DEM is scaled by a factor of three. The lighting direction is indicated by the blue arrow and the green arrow points towards the north.

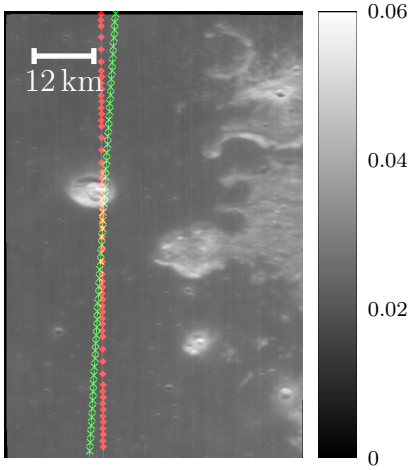

(a) M^3 reflectance image.

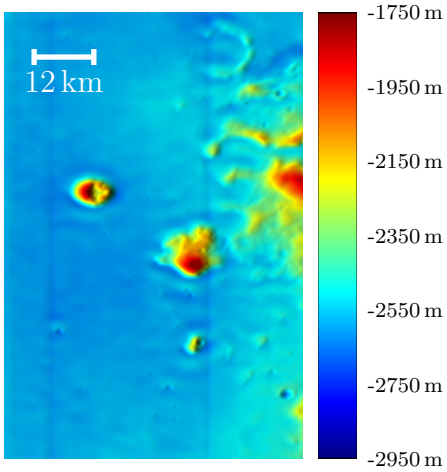

(b) Colour coded DEM.

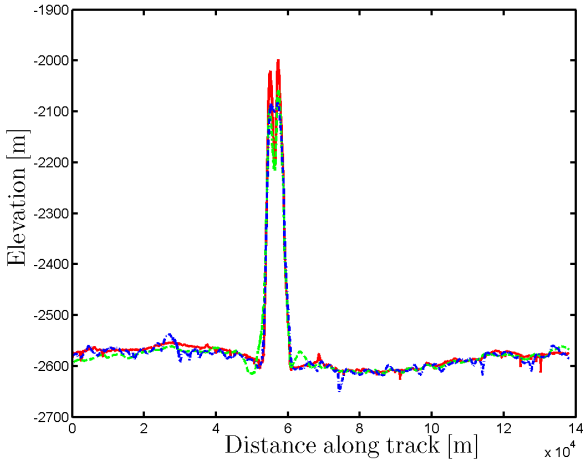

(c) Comparison to LOLA single track (green).

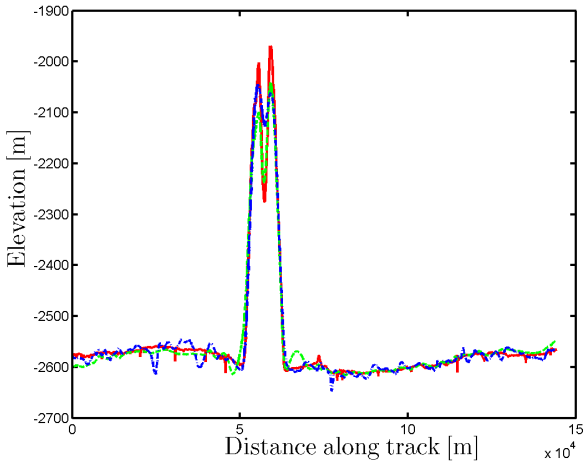

(d) Comparison LOLA single track (red).

Figure 5.8: Comparison between LOLA single tracks and the refined DEM of the Mairan region (longitude 311 °E–313 °E, latitude 40 °N–43 °N). The westernmost dome Mairan T is of nearly circular shape with a diameter of about 6.5 km. (a) M^3 reflectance image. Image credit: NASA/JPL-Caltech. (b) Color coded DEM. The depth value determines the color and a Lambertian shading is overlayed on the intensity channel of the image to visualise the topographic details. (c)–(d) Cross-sections of the DEM marked in (a) as green line by x-marks and as red line by diamonds, respectively. Red: LOLA single track. Blue: GLD100. Green: Refined DEM.

A more detailed analysis (cf. Fig. 5.8) can be performed by regarding cross-sections through the DEM in comparison with LOLA single tracks (Fig. 5.8(c) and Fig. 5.8(d)). Small craters that are clearly visible within the LOLA single track and in the SfS-based DEM are not visible in the GLD100 and cannot be distinguished from the noise level. Specifically, the volcanic vent of Mairan T only appears allusively in the GLD100 but is nearly as pronounced in the refined DEM as in the LOLA single track (cf. Fig. 5.8). As a general result, a comparison of the refined DEM to the LOLA single tracks shows that most of the absolute error is not due to missing craters and overestimated or underestimated heights but mainly a result low spatial frequency bias, where small gradient estimation errors add up during the integration. This bias might be further compensated by methods such as the interpolation surface proposed by Horovitz and Kiryati (2004) or an integration of the gradient field with an absolute depth constraint rather than its gradients as described in Section 5.3. The DEM (cf. Fig. 5.8(b)) was obtained using the Hapke IMSA model with the phase function $f_{\mathrm{DHG}}(\alpha)$. Notably, the apparent vertical lines correspond to image borders. This behaviour may be caused by imperfect radiance calibrations influencing the estimation of the surface gradient field. Since there is no absolute depth constraint involved in the gradient integration step, the effect is reflected in the estimated DEM. A further examination on this effect follows in Section 5.5.2.

Influence of the reflectance model

The synthetic evaluation technique is also applied to the lunar crater Tycho (longitude 348 °E–350 °E, latitude 45 °S–41 °S). Three suitable M^3 images are available (cf. Fig. 5.9(a)–Fig. 5.9(c)), which allow the estimation of both the albedo w and the parameter ξ of the single-particle scattering function $f_{\mathrm{CS}}(\alpha)$ at an increased spatial resolution. Hence, this region is appropriate for a further evaluation. The region is reconstructed using the Hapke IMSA model with the phase function $f_{\mathrm{DHG}}(\alpha)$. The weight parameters are $\delta_{\mathrm{PCHL}} = 2.5 \cdot 10^{-4}$, $\sigma_{\mathrm{grad}_{\mathrm{PHCL}}} = 15$, $\sigma_{\mathrm{refl}_{\mathrm{PHCL}}} = 21$ for the extended photoclinometry scheme, and $\gamma_{\mathrm{SfS}} = 5 \cdot 10^{-3}$, $\delta_{\mathrm{SfS}} = 2.5 \cdot 10^{-3}$, $\sigma_{\mathrm{grad}_{\mathrm{SfS}}} = 15$, $\sigma_{\mathrm{refl}_{\mathrm{SfS}}} = \{21, 15, 11, 7, 5\}$ for the shape from shading algorithm. The initial and constraining DEM is the GLD100 (cf. Fig. 5.9(e)). Based on the resulting DEM (cf. Fig. 5.9(f)), the reflectance parameters are estimated, setting $\sigma_{\mathrm{refl}_{\mathrm{synth}}} = 5$ for the Hapke IMSA and AMSA model in combination with $f_{\mathrm{DHG}}(\alpha)$ and $f_{\mathrm{CS}}(\alpha)$, respectively. Finally, three images were rendered using the estimated parameters and the light source and viewing directions of the original images. For each set of images, a reconstruction is computed using the aforementioned parameters, i.e. the Hapke IMSA model with $f_{\mathrm{DHG}}(\alpha)$. This experiment simulates a known reflectance model (rendering: Hapke IMSA with $f_{\mathrm{DHG}}(\alpha)$), a reflectance model with unknown multiple scattering approximation (rendering: Hapke AMSA with $f_{\mathrm{DHG}}(\alpha)$), an unknown single-particle scattering function (rendering: Hapke IMSA and $f_{\mathrm{CS}}(\alpha)$), and a mixture of both unknowns (rendering: Hapke AMSA and $f_{\mathrm{CS}}(\alpha)$). Table 5.5 summarises the result. Again, the DEM are vertically centred before the RMSE is computed.

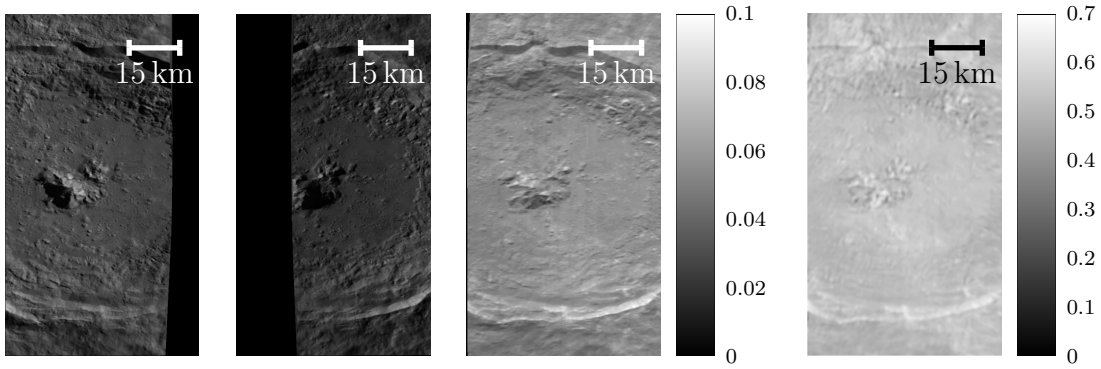

(a) M^3 reflectance image 1. (b) M^3 reflectance image 2. (c) M^3 reflectance image 3. (d) Single-scattering albedo.

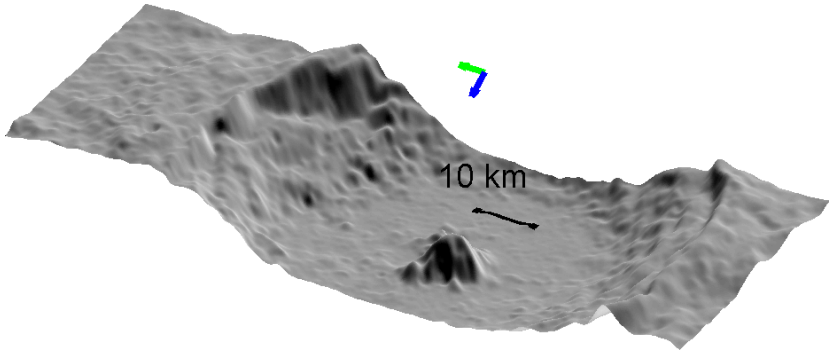

(e) GLD100.

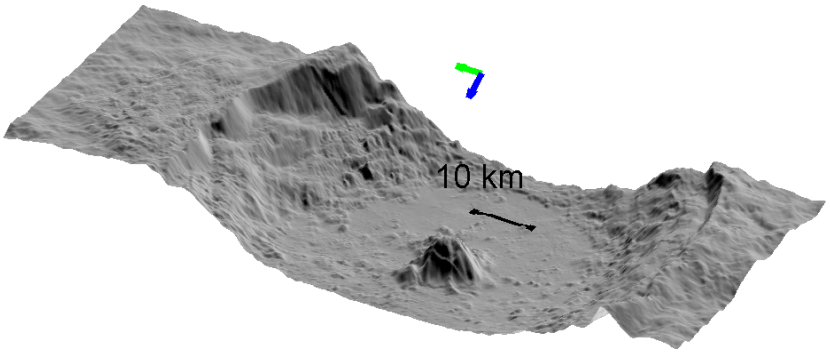

(f) Refined DEM.

Figure 5.9: Reconstruction of the crater Tycho (348 °E–350 °E, 41 °S–45 °S, diameter: 88 km). (a)–(c) M^3 reflectance images at 1579 nm. Image credit: NASA/JPL-Caltech. (d) Estimated single-scattering albedo at 1579 nm. (e) GLD100. (f) Result of the shape from shading algorithm. The elevation axis of both DEM is scaled by a factor of three. The lighting direction is indicated by the blue arrow and the green arrow points towards the north.

Table 5.5: Comparison of constructed DEM to synthetic image "ground truth". Different multiple scattering approximations and single-particle scattering functions are used to create synthetic images from a "ground truth" DEM. The RMSE of depth Δz and albedo Δw are presented alongside the mean albedo $\bar{w}$. The DEM were all constructed based on the Hapke IMSA model combined with the single-particle scattering function $f_{\mathrm{DHG}}(\alpha)$.

Multiple Scattering Approximation	**Single-Particle Scattering Function**	**RMSE** Δz [m]	Δw	$\bar{w}$
IMSA	$f_{\mathrm{DHG}}(\alpha)$	18.6	0.007	0.526
IMSA	$f_{\mathrm{CS}}(\alpha)$	19.0	0.046	0.560
AMSA	$f_{\mathrm{DHG}}(\alpha)$	53.7	0.012	0.530
AMSA	$f_{\mathrm{CS}}(\alpha)$	70.5	0.055	0.560

In the case of a matching reflectance model, the single-scattering albedo w is reconstructed to 1.3% of the mean albedo, which corresponds to 0.5255. This result is in good agreement with the single image reconstruction experiment. However, the depth error is about twice as high as in the first case. This may be related to the larger spatial variations of the albedo (cf. Fig. 5.9(d)), which is not as homogeneous as in the previous case. The overestimated or underestimated albedo pixels influence the estimated gradients, such that the slopes of the corresponding surface pixels are underestimated or overestimated, respectively. The resulting slope error is accumulated during the integration of the surface gradient field.

If the single-particle phase function is inaccurately known, the effect on the surface is insignificant as the RMSE increases by merely 0.3 m. The albedo estimation error might appear quite large but is understandable as the estimated albedo has to absorb the discrepancy between the reflectance model used for rendering and the one used for reconstruction. This behaviour is due to the fact that the range of phase angles under which the utilised images were acquired is rather small (typically between 20 ° and 60 °). Effectively, it is not possible to estimate the full single-particle scattering function but only its mean slope across the available phase angle interval.

If the multiple scattering within the surface is non-isotropic (e.g. for the Hapke AMSA model), the effect is completely different. The large albedo estimation error indicates that the algorithm tries to absorb these effects into the albedo. Since the anisotropic multiple scattering approximation highly depends on the surface slope and therefore the effect shows pixel-wise variations, the albedo is not fully able to absorb the resulting distortion, which results in an increase of the depth error.

The result of unknown multiple scattering approximation and unknown single-particle scattering function shows a similar behaviour since the estimation error of both, depth

and albedo, further increases. The rather large increase is due to the fact that the single-particle scattering function is of essential importance for the multiple scattering approximation and thus cannot be absorbed by the albedo alone. This stresses the importance of estimating the reflectance model along with the surface reconstruction. However, as it has been demonstrated in the case of unknown single-particle scattering function with isotropic multiple scattering, the parameters of the model cannot be separated if the phase angles do not cover a broad range. Hence, for accurate spectral normalisation it would be beneficial to abandon the nadir viewing direction and take further images at different viewing directions.

5.5.2 Absolute depth constraint

The absolute depth constraint influences only the gradient integration step of the photometric methods. The evaluation thus is based on the integration method (cf. Section 5.3.2). At first, the details of the conducted experiments are described. To compare the algorithm to the reference methods (cf. Section 3.3), the influence of its parameters is then evaluated over a broad range of parameter values. Afterwards, the reconstruction accuracy and a direct comparison to the method without absolute depth constraint and the influence of the reflectance model are detailed. Finally, the two step surface reconstruction method, i.e. the extended PHCL algorithm followed by a gradient field integration, is compared to the further extended SfS scheme.

Experiments

Since the presented algorithm recovers depth from a *gradient* field, the extended PHCL scheme (cf. Section 5.2.2) is applied to obtain photometric surface gradient estimates from M^3 images.

The reflectance of the surface R is modelled by the Hapke model including the macroscopic roughness extension (cf. Section 2.3.3). The model uses an isotropic multiple scattering approximation and is thus termed IMSA. The parameters, with the exception of the single-scattering albedo w, are adopted from Warell (2004). The single-scattering albedo, however, is estimated pixel-wise as described in Section 4.2. This approach implies an uncertainty of the albedo due to the lower lateral resolution of the surface normals derived from the known DEM and suppresses albedo artefacts due to shading at the cost of a blurred albedo estimate.

The IMSA model provides a convenient trade-off between model complexity and model accuracy. In some cases, the reflectance is not described sufficiently well due to multiple scattering effects and the estimated surface gradients are exaggerated. This leads to spikes in the gradient field at the affected pixels. In those cases, the Hapke model based on a more complex anisotropic multiple scattering approximation (AMSA) introduced by Hapke (2002) is applied (cf. Section 2.3.3). The AMSA model depends on the same

parameters as the IMSA model and the single-scattering albedo is estimated using the same aforementioned approach. To avoid computational complexity, the IMSA model is used for all experiments. If errors are detected, the experiment is repeated using the AMSA model. Due to the dependence of the spikes on local surface and scene properties and the large impact of those effects, they are easy to identify. An example is presented in the remainder of this section.

In order to estimate the absolute accuracy of the reconstruction, the LOLA single track measurements within the regions of interest are mapped onto the DEM by using the coordinates supplied alongside the M^3 reflectance data and the LOLA depth data and the approach described in Section 5.5.1. A minor modification is introduced: The translation is considered optimal if the normalised cross-correlation between the DEM and the single track measurements reaches a maximum. The procedure is applied to each DEM separately. After registering all single tracks on the DEM, the total RMSE of the absolute height difference is computed by averaging the squared error over all LOLA measurement points that fall onto the DEM. Since the absolute depth is important in this case, the mean of the tracks and the DEM cross-sections is not removed prior to the computation of the RMSE.

The proposed algorithm is tested on a small region around the Mairan T dome (48.20 °W – 48.60 °W, 41.67 °N – 41.93 °N) (Glotch et al., 2011) by initialising the algorithm with the known DEM. Furthermore, the algorithm is evaluated on three larger regions, namely the region around the Mairan domes (47.00 °W – 49.00 °W, 40.00 °N – 43.00 °N), a fault system near the lunar Lansberg crater (26.00 °W – 27.00 °W, 2.00 °S – 3.00 °S) recently examined by Wood (2013), and the lunar crater Tycho (10.00 °W – 12.00 °W, 45.00 °S – 41.00 °S). Table 5.6 lists the PHCL parameters we used to create the presented results. If multiple images are available the images are registered using the method proposed in Section 6.3. The M^3 image names are listed in Table 5.7.

The low-pass filter function $f_{\text{lp}}(z)$ of the algorithm is defined as a Gaussian function of width σ_{absDepth}. The optimal values for the parameters τ and σ_{absDepth} are computed using a grid search technique. To evaluate a broad range of values for τ, an exponential scale is used, i.e. $\tau = 10^{n_\tau}$ with $n_\tau \in \{-5, -4, -3, -2, -1, 0, 1, 2, 3, 4, 5, 6, 7\}$. The width of the Gaussian filter is varied between 1 pixel and 15 pixels using a step size of 2 pixels, i.e. $\sigma_{\text{absDepth}} \in \{1, 3, 5, 7, 9, 11, 13, 15\}$ pixels. An optimal parameter set is determined for each region separately. Additionally, the methods of Shao et al. (1991) and the Poisson solver by Horn (1990) (cf. Section 3.3) are applied. These methods correspond to the special cases $\sigma_{\text{absDepth}} = 0$ pixels and $\tau = 0$, respectively. According to Scholten et al. (2012) objects with sizes below 1.5 km are not fully resolved by the GLD100. In the setting at hand, this size corresponds to 15 pixels, such that the Gaussian filter width σ_{absDepth} should correspond to at least 7 pixels.

The maximum number of allowed iterations is set to $N_{\text{iter}} = 10^5$ and the maximum number of steps between iterations was set to $N_{\text{step}} = 5 \cdot 10^2$. These large values are chosen to ensure that the algorithm does not stop early. Divergence is assumed if E_{div} exceeds the

Table 5.6: Evaluated Regions: Parameters of the PHCL scheme.

Region Name	Location		Parameters			
	Longitude [°]	Latitude [°]	δ_{PHCL}	$\sigma_{\mathrm{grad}_{\mathrm{PHCL}}}$ [px]	σ_{refl} [px]	Model
Mairan T	48.20 °W – 48.60 °W	41.67 °N – 41.93 °N	$1 \cdot 10^{-4}$	15	21	AMSA
Mairan Domes	47.00 °W – 49.00 °W	40.00 °N – 43.00 °N	$1 \cdot 10^{-4}$	15	21	AMSA
Tycho	10.00 °W – 12.00 °W	45.00 °S – 41.00 °S	$1 \cdot 10^{-4}$	15	21	IMSA
Lansberg Fault	26.00 °W – 27.00 °W	2.00 °S – 3.00 °S	$1 \cdot 10^{-4}$	15	21	IMSA

Table 5.7: Evaluated Regions: Filenames of the examined M^3 images.

Region Name	Location		M^3 image filename
	Longitude [°]	Latitude [°]	
Mairan T	48.20 °W – 48.60 °W	41.67 °N – 41.93 °N	M3G20090209T072710 M3G20090418T151350 M3G20090612T060502
Mairan Domes	47.00 °W – 49.00 °W	40.00 °N – 43.00 °N	M3G20090209T072710 M3G20090418T151350 M3G20090612T060502
Tycho	10.00 °W – 12.00 °W	45.00 °S – 41.00 °S	M3G20090206T105850 M3G20090415T202222 M3G20090609T095022
Lansberg Fault	26.00 °W – 27.00 °W	2.00 °S – 3.00 °S	M3G20090416T235340

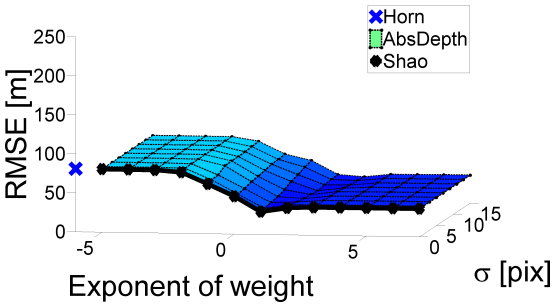

(a) Region: Mairan T dome

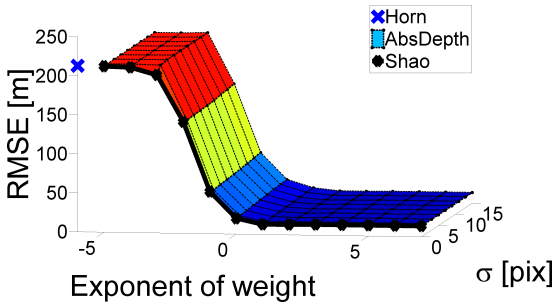

(b) Region: Mairan domes

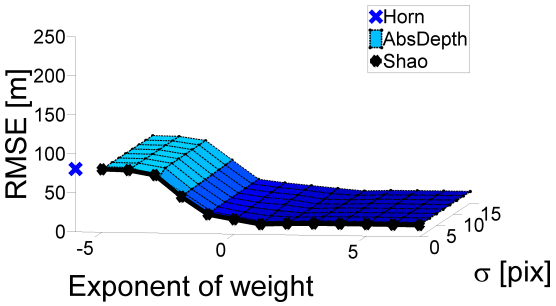

(c) Region: Fault near Lansberg crater

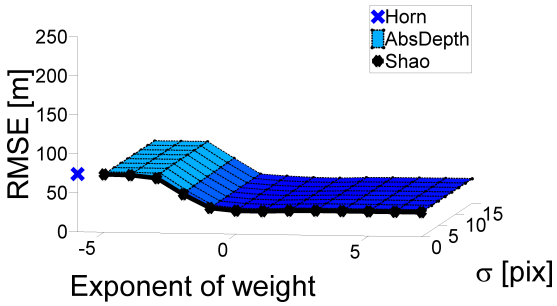

(d) Region: Crater Tycho

Figure 5.10: Computed RMSE for the various regions. The algorithms have been initialised and restricted using the GLD100. The surface area corresponds to the proposed algorithm while the black line with diamonds marks the case $\sigma_{\text{absDepth}} = 0$ and corresponds to the method by Shao et al. (1991). For reference, the output of the method by Horn (1990) that does not use a restricting DEM has been marked by a blue "x".

data type range. The proposed method, however, converges after a few hundred iterations while the Poisson solver needs several thousand iterations.

Influence of the parameters τ and σ_{absDepth}

In order to evaluate the influence of the weight τ and the low-pass filter width σ_{absDepth}, a series of DEM is computed for all aforementioned combinations. The evaluation is carried out for different sets of DEM and compared to the methods of Horn (1990) and Shao et al. (1991).

Fig. 5.10 shows the computed RMSE values. Decreasing the value of τ, i.e. $\tau \to 0$, yields the solution of the Poisson solver by Horn (1990) as marked by the blue "x" on the left side of the graph. The other side, i.e. large values of τ, corresponds to the GLD100, i.e. the a-priori known DEM. All regions show an optimal value of $\tau \in [1 \ldots 1000]$. Interestingly, the optimal value of τ increases with the value of σ_{absDepth}. Since larger values

of σ_{absDepth} eliminate more high-frequency information from the DEM, the error E_{absDepth} tends to decrease with increasing value of σ_{absDepth}. To maintain a stronger "pull" towards the low-frequency component of the DEM without increasing the high-frequency difference. The value of τ needs to increase accordingly. All RMSE values, however, are close to each other and no significant difference occurs for the medium-sized and large regions. In the case of the single Mairan T dome (cf. Fig. 5.10(a)), the reflectance-based reconstructions show a significant advantage over the restricting DEM. All RMSE values, with the aforementioned exception of the Poisson solver, are very close to each other and thus show no significant difference, given that the LOLA data have a vertical accuracy of ± 1 m and a different footprint size.

While the medium scale DEM of all examined surface reconstruction algorithms look similar (cf. Fig. 5.11), the small-scale properties show strong differences. The optimal values of τ were adopted from the previously described experiment. The large RMSE of the Poisson solver is due to a large scale drift which is discussed in detail later on. The results of the proposed method and the method by Shao et al. (1991), corresponding to $\sigma_{\text{absDepth}} = 0$, do not show this systematic large scale error. The resulting DEM, however, look very similar. To visualize the different properties of the methods, the difference between the DEM obtained using $\sigma_{\text{absDepth}} = 0$ and $\sigma_{\text{absDepth}} = 15$ is shown in Fig. 5.13. The difference map (cf. Fig. 5.13(a)) shows rapidly changing deviations. To further illustrate these small-scale differences, Fig. 5.13(b) shows a LOLA track that passes through two domes within the area and thus can be accurately registered onto the DEM. In the centre of the track between these two domes, there is a small crater with a diameter of about 1 km that is not visible in the GLD100 data. Fig. 5.13(c) to Fig. 5.13(e) show the resulting DEM for different values of τ. It can be seen that a larger value of τ yields more symmetric craters. The depth of the crater, however, decreases as it is not contained in the DEM. An increase of σ_{absDepth}, in contrast, increases the estimated crater depth and thus effectively increases the degree of freedom of the DEM estimation. While the result for $\sigma_{\text{absDepth}} = 0$ (Shao et al., 1991) uses τ as a trade-off factor between the Poisson solver by Horn (1990) and the DEM, the proposed method additionally allows for variations of high spatial frequency. This is shown in Fig. 5.13(e) where the GLD100 and the method by Shao et al. (1991) coincide. While it is tempting to assume that further increasing σ_{absDepth} may yield even deeper crater estimates, an increase of σ_{absDepth} also increases the low-pass effect and thus allows more low-frequent variations to appear in the DEM. If σ_{absDepth} is increased too much, i.e. $\sigma_{\text{absDepth}} \to \infty$, only the mean of the DEM is constrained.

Since the gridded LOLA DEM shows interpolation artefacts that are distinct from the stereo noise of the GLD100, also the reconstructions using the gridded LOLA DEM both for initialization and as the constraining DEM of the algorithm are computed. The corresponding RMSE are summarized in Fig. 5.12. Due to the origin of the gridded LOLA DEM being based on single LOLA point measurements, the RMSE should not be interpreted as a meaningful accuracy measure. Accordingly, the RMSE obtains its

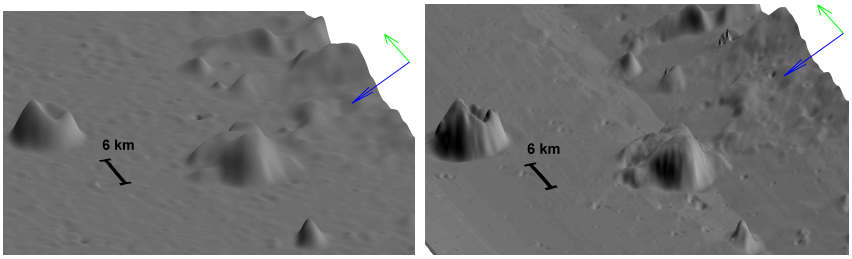

(a) GLD100 (b) Poisson solver

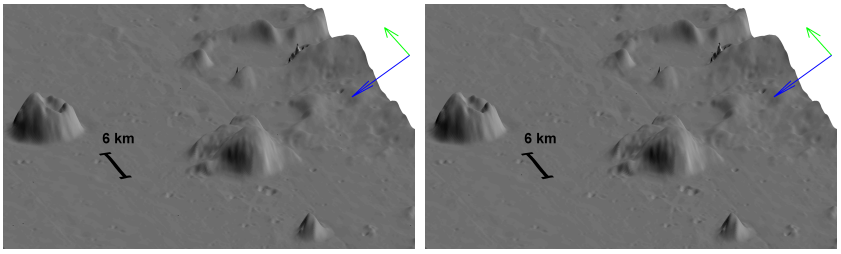

(c) Shao et al. (1991)($\tau = 10^2$) (d) Proposed Method ($\sigma_{\text{absDepth}} = 1\,\text{px}$, $\tau = 10^1$)

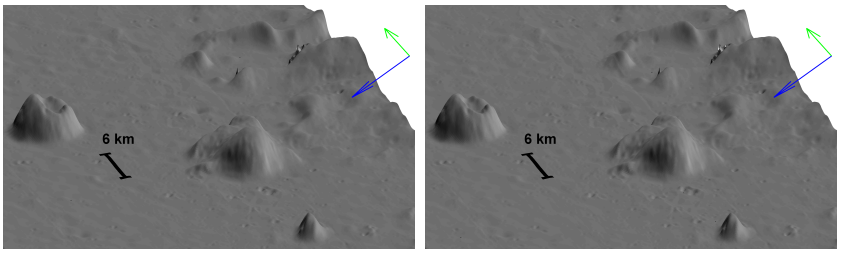

(e) Proposed Method ($\sigma_{\text{absDepth}} = 3\,\text{px}$, $\tau = 10^2$) (f) Proposed Method ($\sigma_{\text{absDepth}} = 5\,\text{px}$, $\tau = 10^2$)

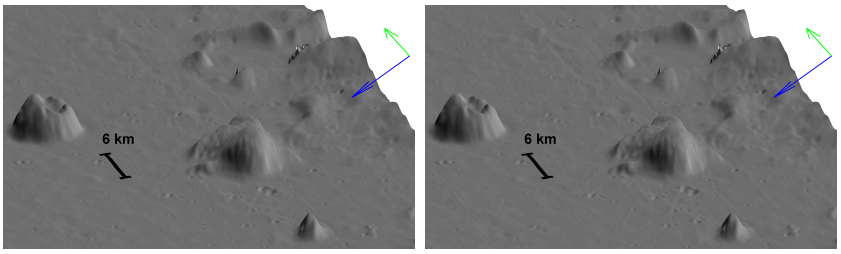

(g) Proposed Method ($\sigma_{\text{absDepth}} = 7\,\text{px}$, $\tau = 10^2$) (h) Proposed Method ($\sigma_{\text{absDepth}} = 9\,\text{px}$, $\tau = 10^3$)

Figure 5.11: Closeup of the Mairan T dome (47.00 °W – 49.00 °W, 40.00 °N – 43.00 °N). (a) The initial and restricting DEM. (b) The result of the Possion solver. (c) The result of the method by Shao et al. (1991). (d) – (h) The results of the proposed method for different values of σ_{absDepth}.

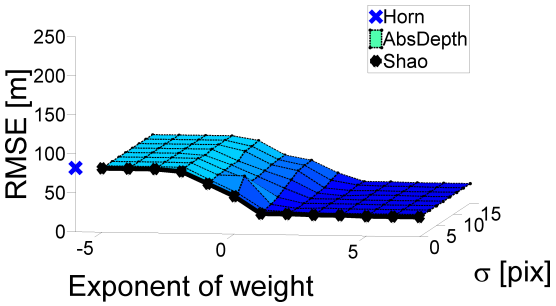

(a) Region: Mairan T dome

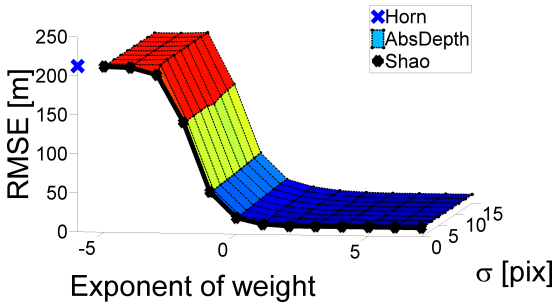

(b) Region: Mairan domes

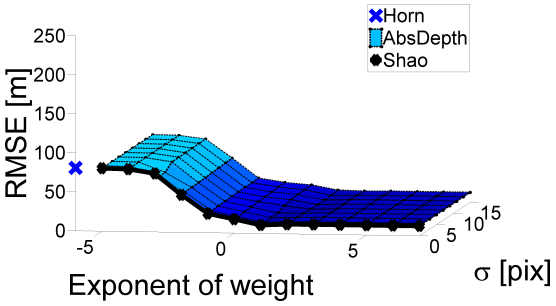

(c) Region: Fault near Lansberg crater

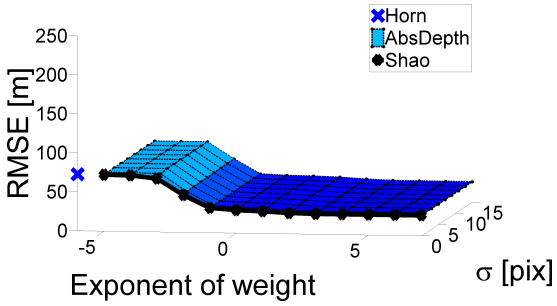

(d) Region: Crater Tycho

Figure 5.12: Computed RMSE for the various regions. The algorithms have been initialized and restricted using the gridded LOLA DEM. The surface area corresponds to the proposed algorithm while the black line with diamonds marks the case $\sigma_{\text{absDepth}} = 0$ and corresponds to the method by Shao et al. (1991). For reference, the output of the method by Horn (1990) that does not use a restricting DEM has been marked by a blue "x".

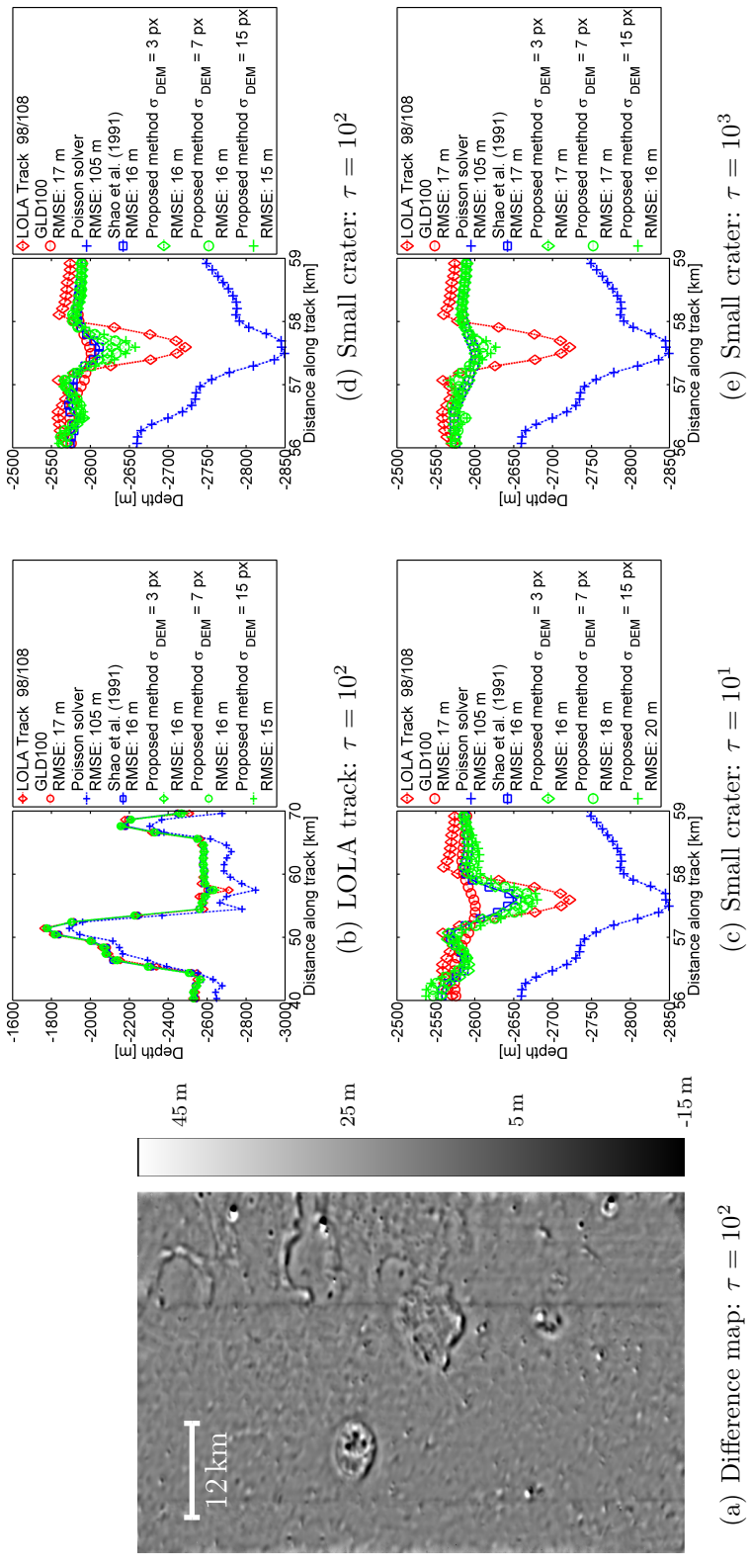

(a) Difference map: $\tau = 10^2$ (b) LOLA track: $\tau = 10^2$ (c) Small crater: $\tau = 10^1$ (d) Small crater: $\tau = 10^2$ (e) Small crater: $\tau = 10^3$

Figure 5.13: Influence of the parameters σ_{absDepth} and τ. (a) Difference between the DEM obtained using $\sigma_{\text{absDepth}} = 0$ pixels and $\sigma_{\text{absDepth}} = 15$ pixels. The small craters show asymmetric differences corresponding to the direction of the incident light rays, i.e. sunlit crater rims are overestimated. (b) Registered LOLA track and DEM profiles. (c) – (e) close up of the small crater shown in (b). Notably, for $\tau = 10^3$ the GLD100 and the method by Shao et al. (1991) coincide.

minimum for very large values of τ which yields DEM very close to the gridded LOLA DEM. The behaviour of the RMSE, however, is similar to the case in which the GLD100 is used. If the value of τ is kept constant, the RMSE changes for larger values of σ_{absDepth}, increasing the algorithm's degree of freedom.

In the following, only the GLD100 is used to estimate a meaningful RMSE of the reconstructed DEM, i.e. a DEM that is not independent of the LOLA single tracks. According to Fig. 5.13, the values $\tau = 100$ and $\sigma_{\text{absDepth}} = 15$ pixels have been found to represent an optimal trade-off between small-scale properties and similarity to the LOLA track. Furthermore, the choice $\sigma_{\text{absDepth}} = 15$ pixels corresponds to the size of objects that are not contained in the GLD100 (Scholten et al., 2012).

Reconstruction accuracy

The small-scale properties are examined based on the Mairan T dome. Afterwards, the medium scale properties are discussed based on the Mairan domes area and the Fault near lunar crater Lansberg. The large-scale properties are shown on example of the Lunar crater Tycho.

Small-scale properties (Mairan T): The Mairan T dome is of almost circular shape with a diameter of about 6.5 km. The albedo of the dome itself is very high and shows a sharp borderline to the surrounding mare basalt. Hence, it is a very challenging object for intensity-based surface reconstruction. The M^3 image of the volcano is shown in Fig. 5.14(a). On top of the dome, an endogenous crater is visible (Glotch et al., 2011). Thus, the dome with a barely visible crater on top as shown in the GLD100 Fig. 5.14(b) looks like an overly smooth version of the rough volcano dome. Both reconstructions, the Poisson solver and the proposed method, show these small-scale features: The roughness of the dome walls is increased and the endogenous crater prominently resides on top of the dome as illustrated in Fig. 5.14(c) and Fig. 5.14(d), respectively. Thus, the lateral resolution of the resulting DEM seems to be increased in comparison to the GLD100 while no significant difference between both integration methods is visible.

Comparing the DEM to the LOLA single tracks, however, yields a RMSE of 34 m for the proposed method and a RMSE of 80 m for the Poisson solver. The RMSE of the GLD100 amounts to 33 m and is thus slightly lower than the RMSE of the proposed method. Hence, the lateral accuracy is increased while the absolute depth error is of the same order. This is illustrated by the track marked in Fig. 5.14(a) which is presented in Fig. 5.15. Both intensity-based reconstructions yield better estimates of the crater and the dome itself but show larger deviations at the bottom of the dome. This behaviour might be partly due to the integration of noise and partly due to inaccurate albedo estimates. On the illuminated southern side of the dome a small rift is created, which possibly results from the blurred albedo estimate that does not match the sharp albedo boundary. This effect, however, is limited to the width of the Gaussian low-pass in the albedo estimation

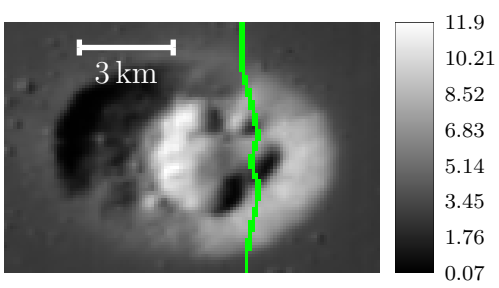

(a) M^3 radiance image.

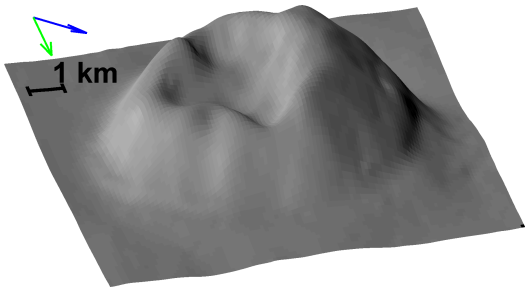

(c) Poisson solver

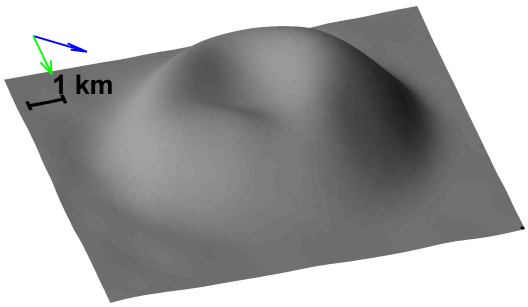

(b) GLD100

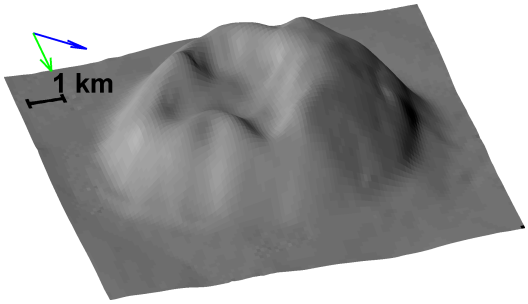

(d) Proposed method

Figure 5.14: Results for the Mairan T dome (48.20 °W – 48.60 °W, 41.67 °N – 41.93 °N). (a) M^3 radiance image at 1579 nm. Image credit: NASA/JPL-Caltech. The green line marks the LOLA track presented in Fig. 5.15. (b)-(d) Shaded DEM. The lighting direction is indicated by the blue arrow and the green arrow points towards the north. All heights are three times exaggerated.

step and is thus of high spatial frequency and not covered by the DEM error term which itself uses a similar low-pass. In contrast, on the shaded northern side, the Poisson solver shows an increasing deviation towards the northern image boundary. This effect seems to be due to the accumulation of small gradient estimation errors during the integration since it it extends over a large area and slightly increases. Whether this is due to an inaccurate albedo estimate or noisy data within the shaded reason is not clear. Since it is a low frequency error, it is greatly reduced by the DEM error term within the proposed method.

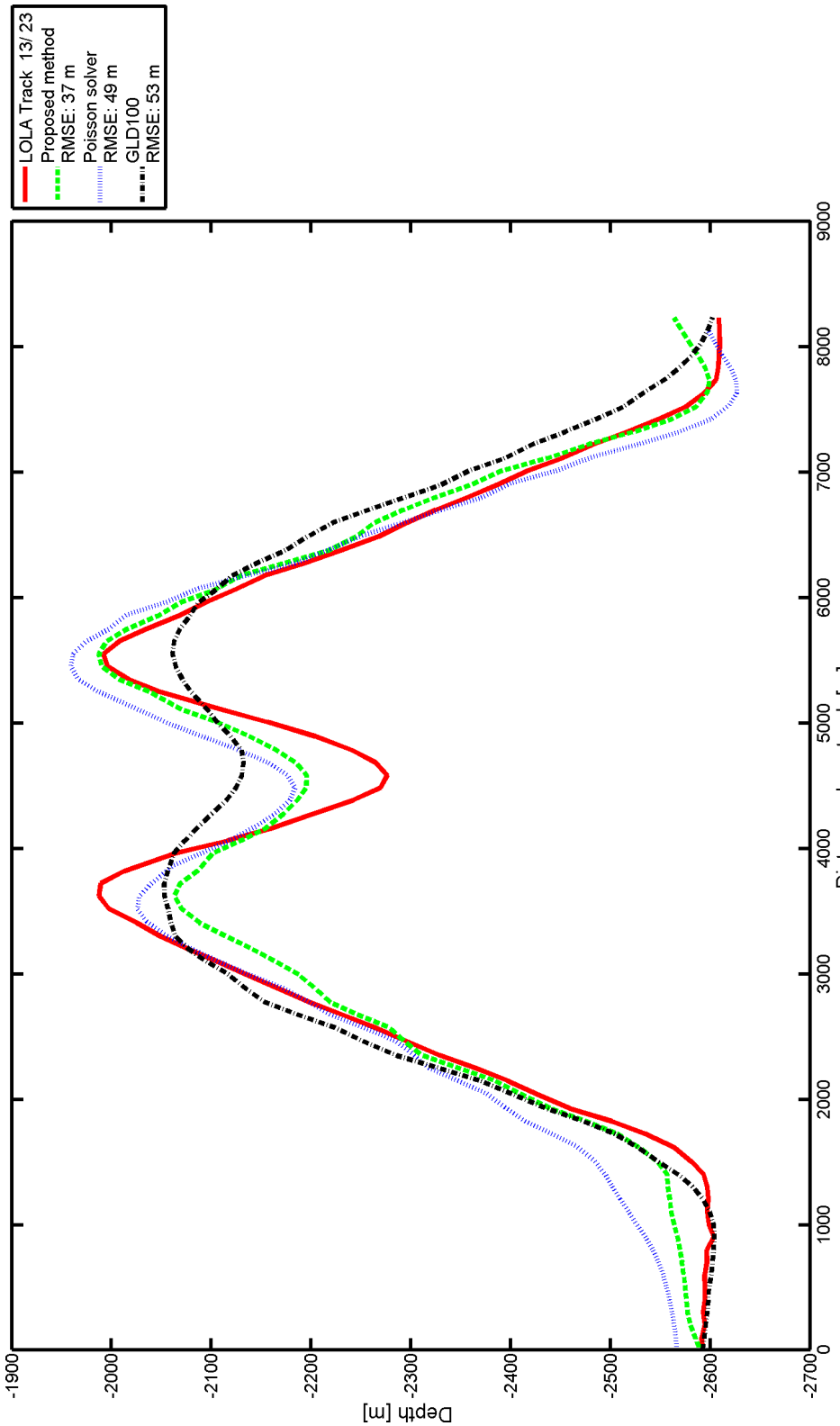

Figure 5.15: Comparison of all DEM with respect to the LOLA track marked in Fig. 5.14(a). The track starts at the northern image boundary.

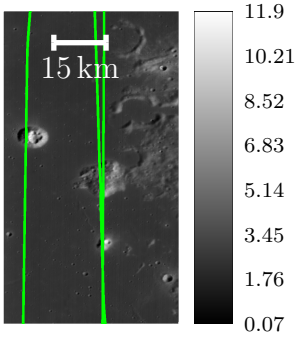

(a) M^3 radiance image.

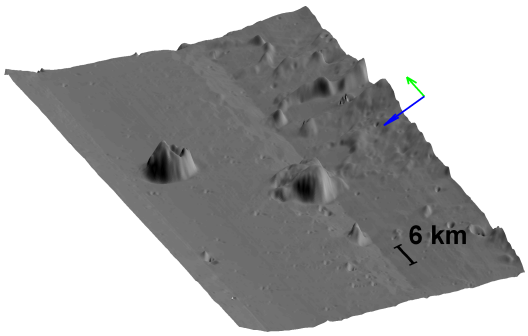

(c) Poisson solver

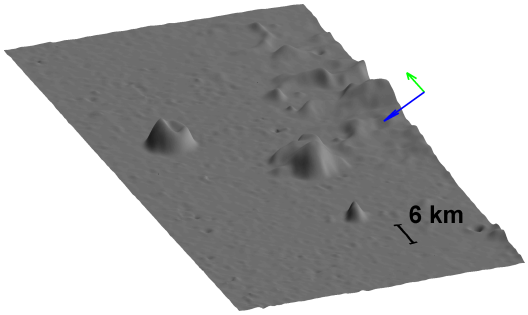

(b) GLD100

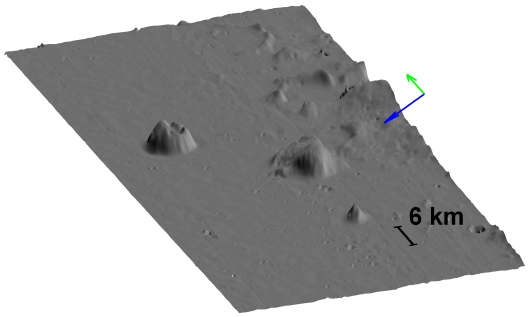

(d) Proposed method

Figure 5.16: Results for the Mairan domes (47.00 °W – 49.00 °W, 40.00 °N – 43.00 °N). (a) M^3 radiance image at 1579 nm. Image credit: NASA/JPL-Caltech. The green lines mark the LOLA tracks presented in Fig. 5.17. (b)-(d) Shaded DEM. The lighting direction is indicated by the blue arrow and the green arrow points towards the north. All heights are five times exaggerated.

Medium scale properties (Mairan domes): The same effects, although even more pronounced, are observed for the whole region containing domes named Mairan T, Mairan "middle" and Mairan "south" (Wilson and Head, 2003) as shown in Fig. 5.16. The GLD100 (cf. Fig. 5.16(b)), again, appears overly smooth and shows high frequency noise on the more or less planar mare basalt. The RMSE for the GLD100, the Poisson solver and the proposed method are 13 m, 212 m and 13 m, respectively. The high RMSE of the Poisson solver (cf. Fig. 5.16(c)) results from a large integration error on both the eastern and the western side of the area. The whole DEM shows a mean slope at the sides which may result from an imperfect radiance calibration as it occurs in regions where only two out of the three images overlap. This error is eliminated by the proposed method (cf. Fig. 5.16(d)).

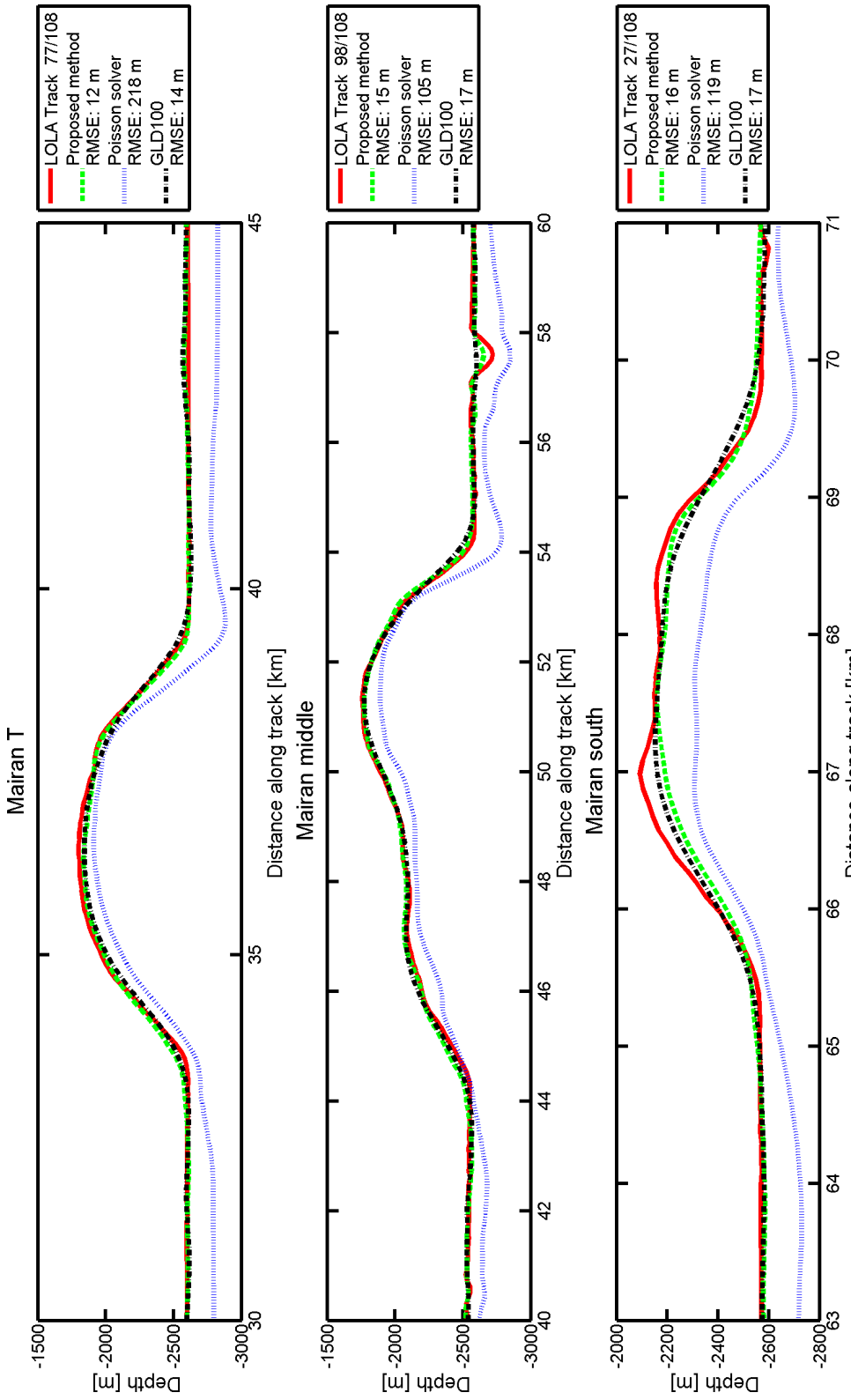

Figure 5.17: Comparison of all DEM with respect to the LOLA track marked in Fig. 5.16(a). The track starts at the northern image boundary.

In order to measure the height of the three domes, the maximum heights from all LOLA tracks that pass the highest measured point of the domes are selected. Although this is not guaranteed to be the highest point of the domes it is the most accurate height estimate possible. Accordingly, the height of Mairan T, Mairan "middle" and Mairan "south" amount to 813 m, 822 m and 480 m, respectively. Thus, the Mairan T dome is about 50 m higher than derived from the GLD100 by Glotch et al. (2011). The corresponding three tracks are shown in Fig. 5.17. Again, the aforementioned effects of the reconstructed surfaces are visible. The albedo artefacts and long term drift are especially pronounced for the Mairan "middle" dome where the Poisson solver drifts further away towards the southern region. Notably, the crater at about 57.5 km is a real surface feature that is covered by the LOLA single-track and missing in the GLD100 which confirms the increase in lateral resolution.

Medium scale properties (Lansberg Fault): Recently, Wood (2013) discussed the topic of the linear feature near Lansberg being a fault or a rille (cf. radiance image in Fig. 5.18(a)). Wood (2013) found the structure to be a fault containing a 200 m wide rille in the mid-section of a 3 km wide, 80 m high rise by analysing a cross-section of the GLD100. The DEM for the region around the fault system near the Lansberg crater are presented in Fig. 5.18(b)–Fig. 5.18(d). The whole fault system is barely visible in the GLD100 due to its small width. Both photometric reconstructions, however, show a 109 m high rise which is steeper than the previously derived 3 km wide rise. Comparing the cross-sections of the DEM (cf. Fig. 5.18(e)), the rise is found to be 542 m wide while the rille is about 349 m wide and 10 m deep. Besides the real fault system, the photometrically estimated DEM shows two small "fault" zones near the eastern boundary. These, however, correspond to the two vertical lines that are visible within the radiance image (cf. Fig. 5.18(a)) and thus are artefacts possibly originating from incorrect radiance measurements and emphasising the importance of correct radiance data. The Poisson solver, again, shows a large-scale drift that is barely visible within the 3D visualisation but clearly stands out as a translation in Fig. 5.18(e) where the fault system has been lowered by 23 m. The RMSE values derived from the LOLA tracks amount to 14 m, 80 m and 17 m for the GLD100, the Poisson solver and the proposed method, respectively. The proposed method, again, shows an RMSE that is comparable to the GLD100 while the lateral resolution is strongly increased.

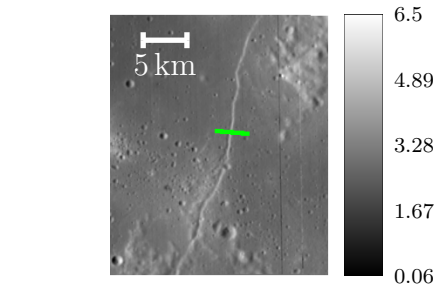

(a) M^3 radiance image

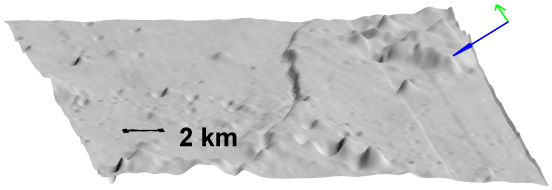

(c) Poisson solver

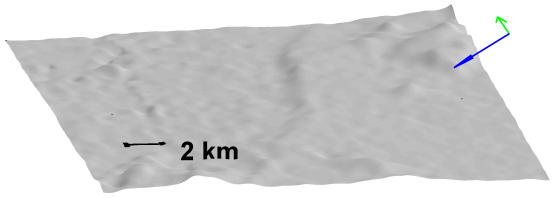

(b) GLD100

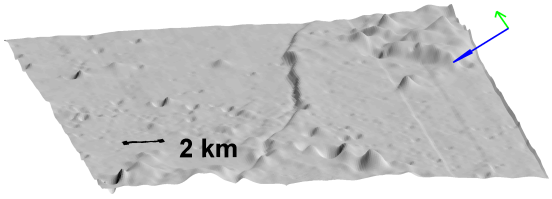

(d) Proposed method

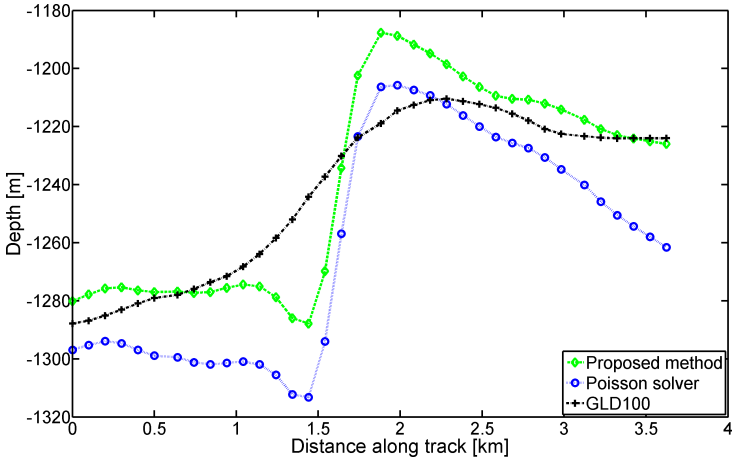

(e) Cross-sections of the fault system

Figure 5.18: Results for the fault system near Lansberg (26.00 °W – 27.00 °W, 2.00 °S – 3.00 °S). (a) M^3 radiance image at 1579 nm. Image credit: NASA/JPL-Caltech. The green line marks the cross-section of the fault presented in (e). (b)-(d) Shaded DEM. The lighting direction is indicated by the blue arrow and the green arrow points towards the north. All heights are six times exaggerated. (e) Comparison of all DEM with respect to the LOLA track marked in (a). The track starts at the western point of the marked path.

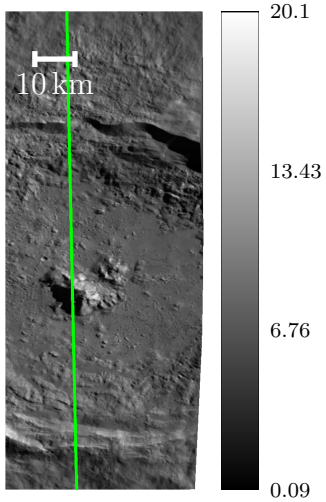

(a) M^3 radiance image.

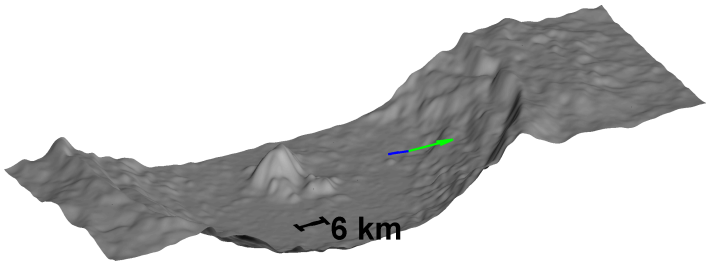

(b) GLD100

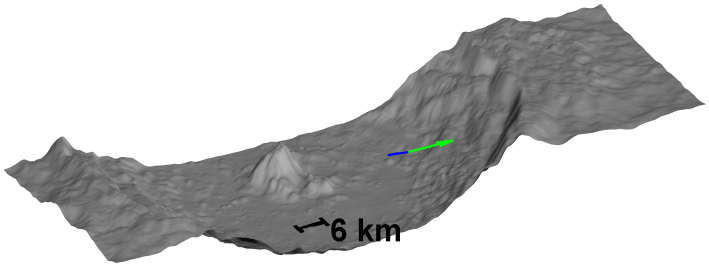

(c) Poisson solver

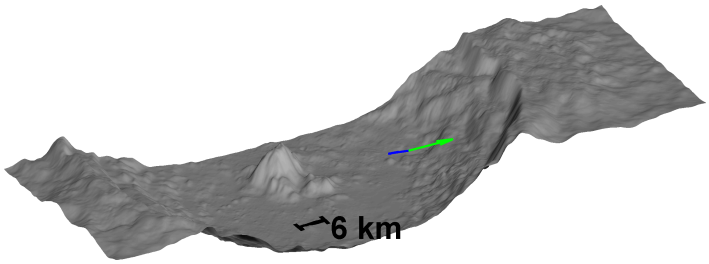

(d) Proposed method

Figure 5.19: Results for the lunar crater Tycho (10.00 °W – 12.00 °W, 45.00 °S – 41.00 °S). (a) M^3 radiance image at 1579 nm. Image credit: NASA/JPL-Caltech. The green line marks the LOLA track presented in Fig. 5.20. (b)-(d) Shaded DEM. The lighting direction is indicated by the blue arrow and the green arrow points towards the north. All heights are three times exaggerated.

Large scale properties (Crater Tycho): To further evaluate the large scale properties of the proposed method, a region containing the large impact crater Tycho is examined. The region extents 2 ° in the east-west direction and 4 ° in the north-south direction. The corresponding radiance image is shown in Fig. 5.19(a). At print resolution, only subtle differences between the GLD100 and the photometrically estimated DEM are visible. The roughness of the central peak and the crater rims seem increased, and the crater floor appears to be less noisy than the one shown by the GLD100 (cf. Fig. 5.19(b)–Fig. 5.19(d)). These observations are in good agreement with the previously discussed results.

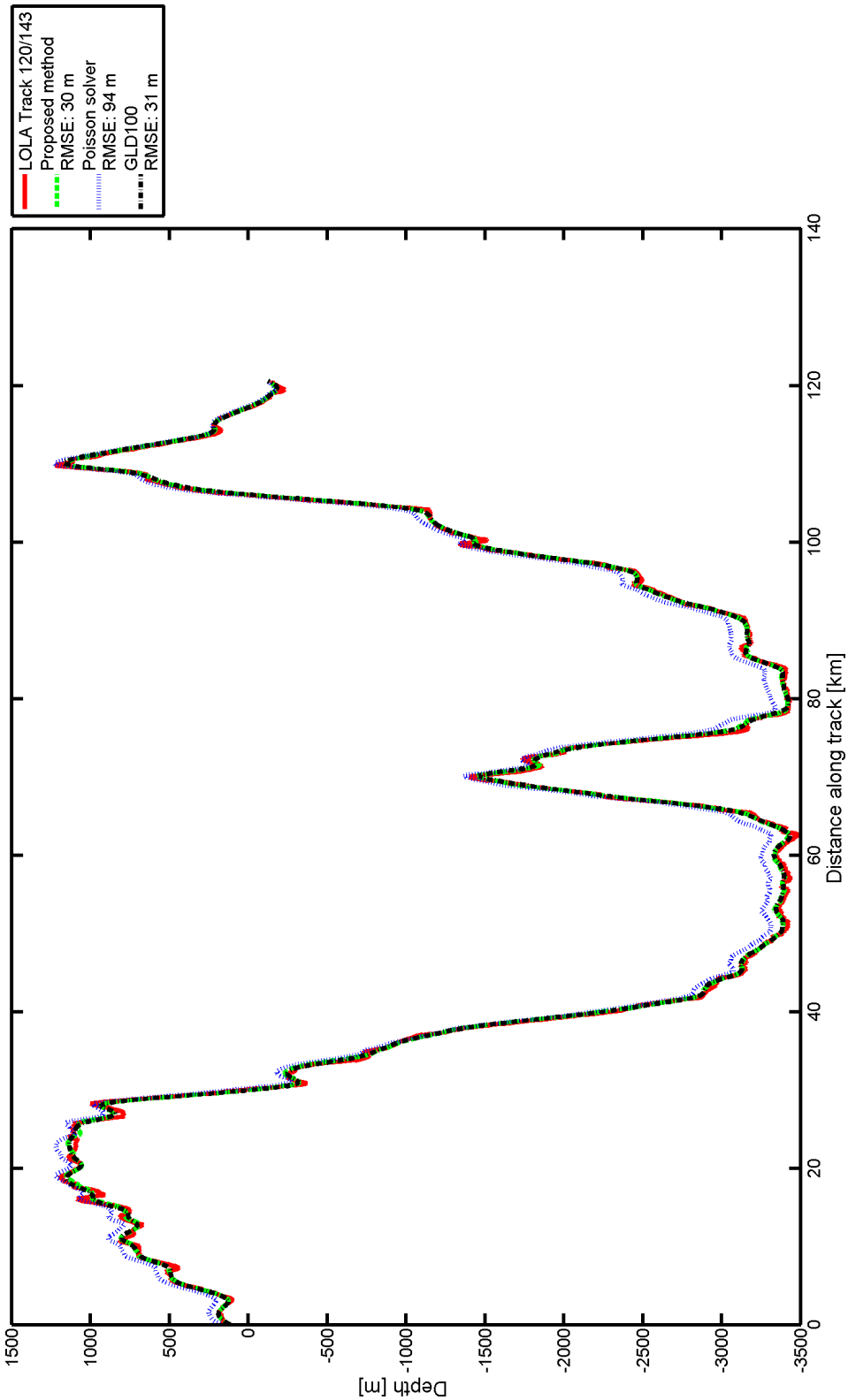

Figure 5.20: Comparison of all DEM with respect to the LOLA track marked in Fig. 5.19(a). The track starts at the northern image boundary.

Regarding the RMSE values, the Poisson solver yields a high RMSE of 74 m. In contrast, the GLD100 and the proposed method yield RMSE values of 30 m and 30 m, respectively. The previous observations indicate an accumulation of small errors that is confirmed by the LOLA single-track presented in Fig. 5.20. The Poisson solver shows a drift towards the northern image boundary and the depth of the crater floor is underestimated by 80–100 m The latter indicates an accumulation of small surface gradient errors along the crater rims while the former might result from the boundary. Thus, the proposed method effectively removes the large scale errors.

Influence of the reflectance model

Fig. 5.21 illustrates the result of the proposed method for the two different reflectance models. The DEM derived using the IMSA model shows steeper, possibly overestimated, slopes than the one derived using the AMSA model. Also, occasionally occuring "spikes" are visible (cf. Fig. 5.21(a)). In contrast, Fig. 5.21(b) shows the DEM derived using the AMSA model. Here, the area looks less ragged and there are no "spikes". Beside these apparent effects on the DEM, the estimated albedo is increased in value for the AMSA model (cf. Fig. 5.21(c) and Fig. 5.21(d)). This is especially the case in the eastern region where two images of strongly varying illumination conditions exist.

While the large scale drift dominates the RMSE value of the Poisson solver (81 m for IMSA and 76 m for AMSA), the possibly overestimated slopes of the IMSA model result in an increased RMSE of about 19 m for the proposed method. The RMSE of the proposed method drops to 13 m if the AMSA model is used for the reconstruction. If the weight τ is decreased to $\tau = 10^1$, this effect is even stronger. The RMSE of the IMSA-based reconstruction amounts to 39 m and decreases to 17 m if the reconstruction is based on the AMSA model. Thus, it seems that the directional multiple scattering approximation increases the influence of the single-scattering albedo such that the strongly varying shading can be explained by an increased albedo rather than extreme surface slopes.

The small craters, however, appear to be more apparent in the IMSA-based reconstructions. Thus, the hypothesis that the IMSA-derived craters are more correct is tested. To evaluate the accuracy for small-scale craters, a crater RMSE is defined by computing the LOLA single-track RMSE only within the craters marked in Fig. 5.22. Every measurement that lies within a circle whose radius is 1.5 times the crater radius is included in the crater RMSE. The corresponding values are 24 m and 25 m for the IMSA- and the AMSA-based reconstructions, respectively. Thus, at a weight $\tau = 10^2$ the difference between the reflectance models is absorbed by the DEM constraint. In case of the lower value $\tau = 10^1$, the RMSE values correspond to 42 m and 27 m, respectively. Hence, the AMSA model provides a much more accurate solution at a weaker constraint and is thus preferable if the DEM is not well known beforehand. The IMSA model, however, reduces the computation time and yields accurate solutions for the other regions.

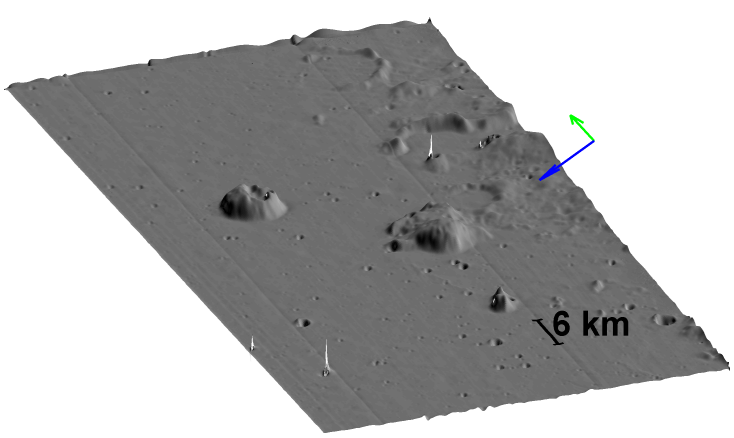

(a) Reconstruction (IMSA)

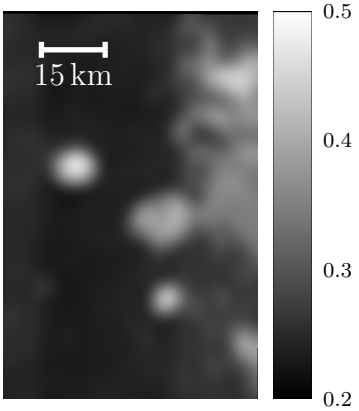

(c) Estimated albedo w (IMSA)

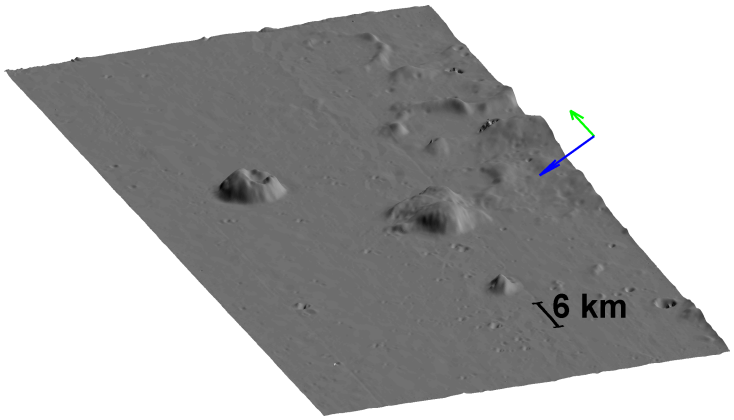

(b) Reconstruction (AMSA)

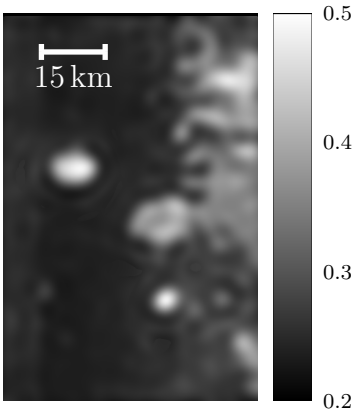

(d) Estimated albedo w (AMSA)

Figure 5.21: Comparison of the reflectance models. (a)-(b) Shaded DEM. The lighting direction is indicated by the blue arrow and the green arrow points towards the north. All heights are three times exaggerated. (c)-(d) Estimated single-particle scattering albedo w.

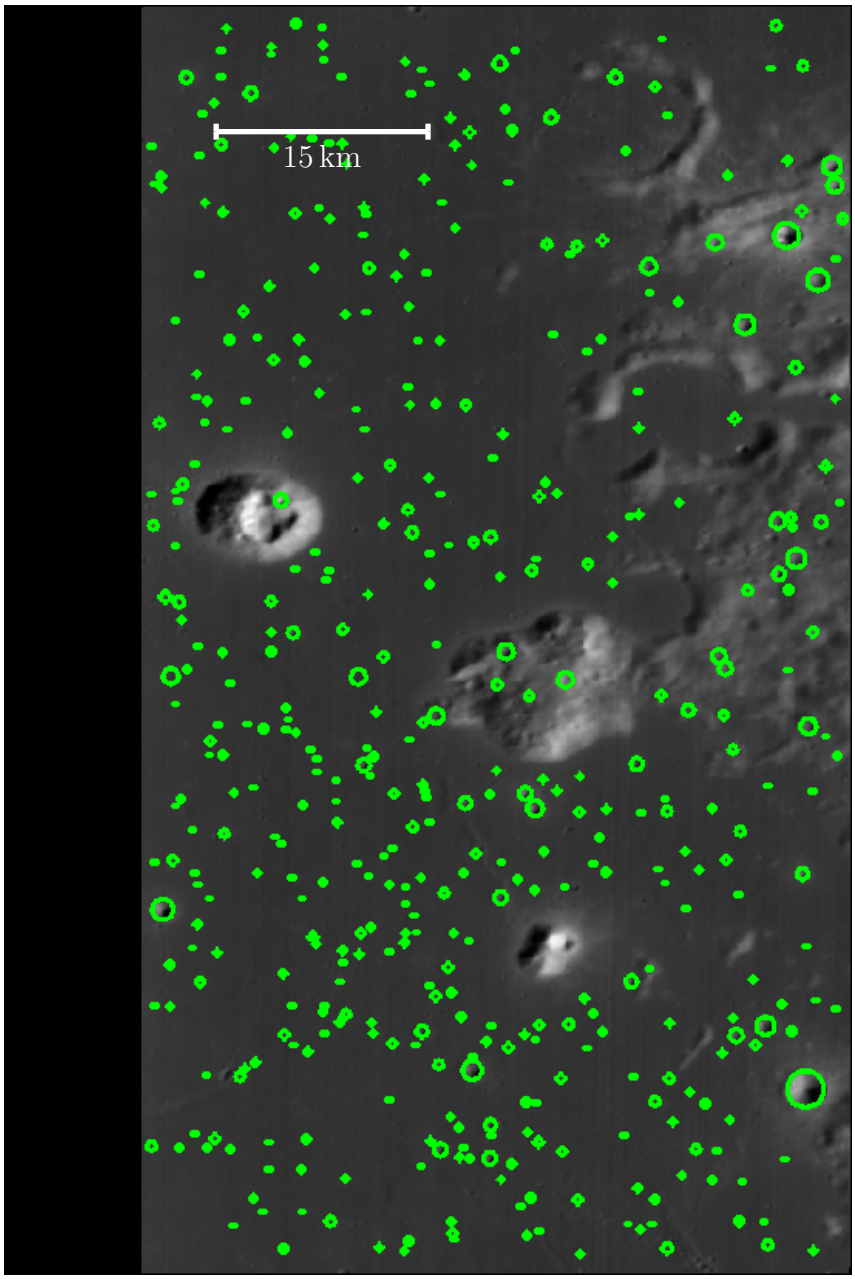

Figure 5.22: Craters that define the crater RMSE. All LOLA single-track measurements residing within the marked craters were used to compute the RMSE for small craters.

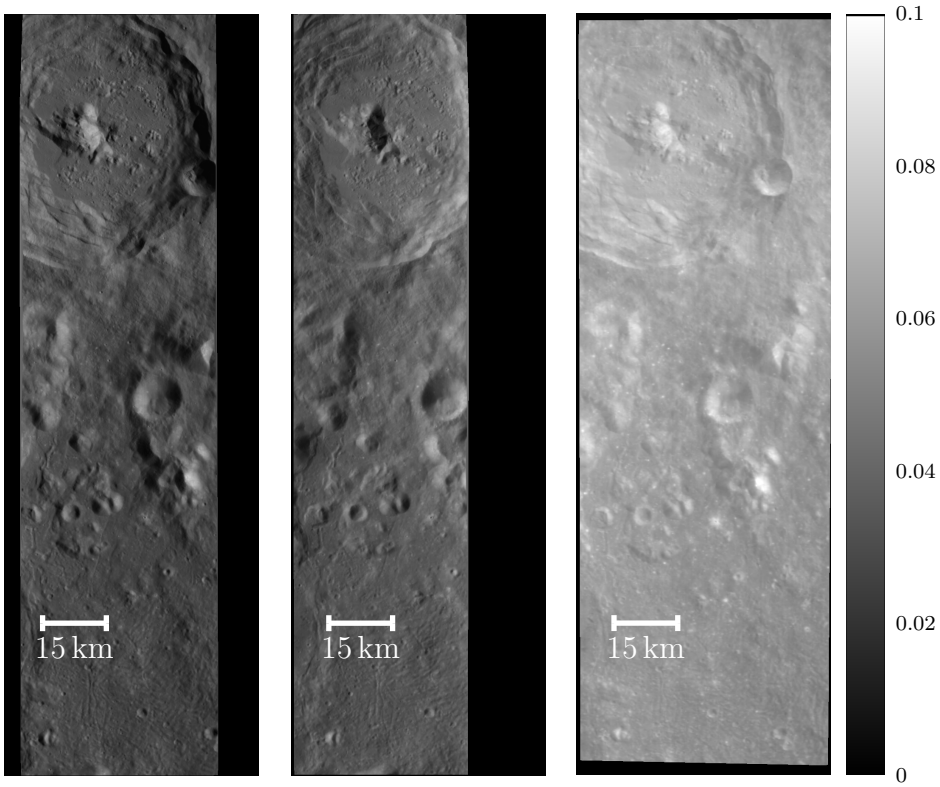

(a) M3 reflectance image 1.

(b) M3 reflectance image 2.

(c) M3 reflectance image 3.

Figure 5.23: Reflectance near lunar crater Lowell (102.00 °W – 104.00 °W, 12.00 °S – 18.00 °S). (a)–(c) M^3 reflectance images image at 1579 nm. Image credit: NASA/JPL-Caltech. The corresponding phase angles are 59.9 °, 54.3 ° and 31.6 °, respectively.

Further extended SfS scheme

The effect of the further extended SfS scheme is shown by a refinement of the GLD100 in the area near the lunar crater Lowell covered by the M^3 images M3G20090213T115953, M3G20090422T193000 and M3G20090713T192732 acquired at the phase angles 59.9 °, 54.3 ° and 31.6 °, respectively. The images span a comparable large range of phase angles and overlap partly. Consequently, the effects of different co-registered images forming a mosaic are visible in the refined DEM.

Fig. 5.23 shows the reflectance images at 1579 nm. The GLD100 and the results of the two step method, i.e. an estimation of the surface gradient field using the extended PHCL algorithm followed by a recovery of the surface applying the absolute depth constraint, and the result of the further extended SfS scheme are shown in Fig. 5.24. The parameters

for the extended PHCL algorithm and the surface recovery is $\delta = 0.001$. The optimal value of $\tau = 100$ for the recovery of the surface from the estimated gradient field has been adopted from the previous evaluation. The parameters of the further extended SfS algorithm are $\delta = 0.001$, $\gamma = 0.001$ and $\tau = 100\gamma$.

Again, the GLD100 appears blurred and does not show large parts of the topography that are clearly visible in the reflectance images. Both photometric DEM refinement methods provide a greater detail of topography, which is barely visible on the large scale observation but stands out at the close-up of the central peak of crater Lowell (cf. Fig. 5.24(d)–Fig. 5.24(f)). The result of the two-step method appears to be more sharp than the other methods. It, however, shows a distorted surface area in the Eastern part of the image where the co-registered images change. This effect is limited to a rather small subregion of the image. The further extended SfS method, in contrast, appears slightly blurred but does not show the artefacts. A possible explanation is an imperfect radiance calibration of the images, e.g. the sensor temperature (Lundeen et al., 2011), and lack of surface details in the initial DEM which causes systematic errors in the estimated surface gradient field. The distorted radiance field is then integrated in the two step method while the further extended SfS scheme iteratively re-estimates the gradient field after updating the surface. This update of the gradient field based on the current surface estimate and less influenced by the initially larger systematic errors. Following the previous evaluations, the residual error based on the LOLA tracks is computed. The corresponding RMSE values are 30 m, 35 m and 29 m for the GLD100, the two-step method and the further extended SfS method, respectively. The increased RMSE of the two-step method may originate from the artefacts caused by changing co-registered images. The further extended SfS scheme thus seems to be more robust and thus preferable. Nevertheless, both methods provide highly detailed topographic models that match the absolute depth accuracy of the GLD100.

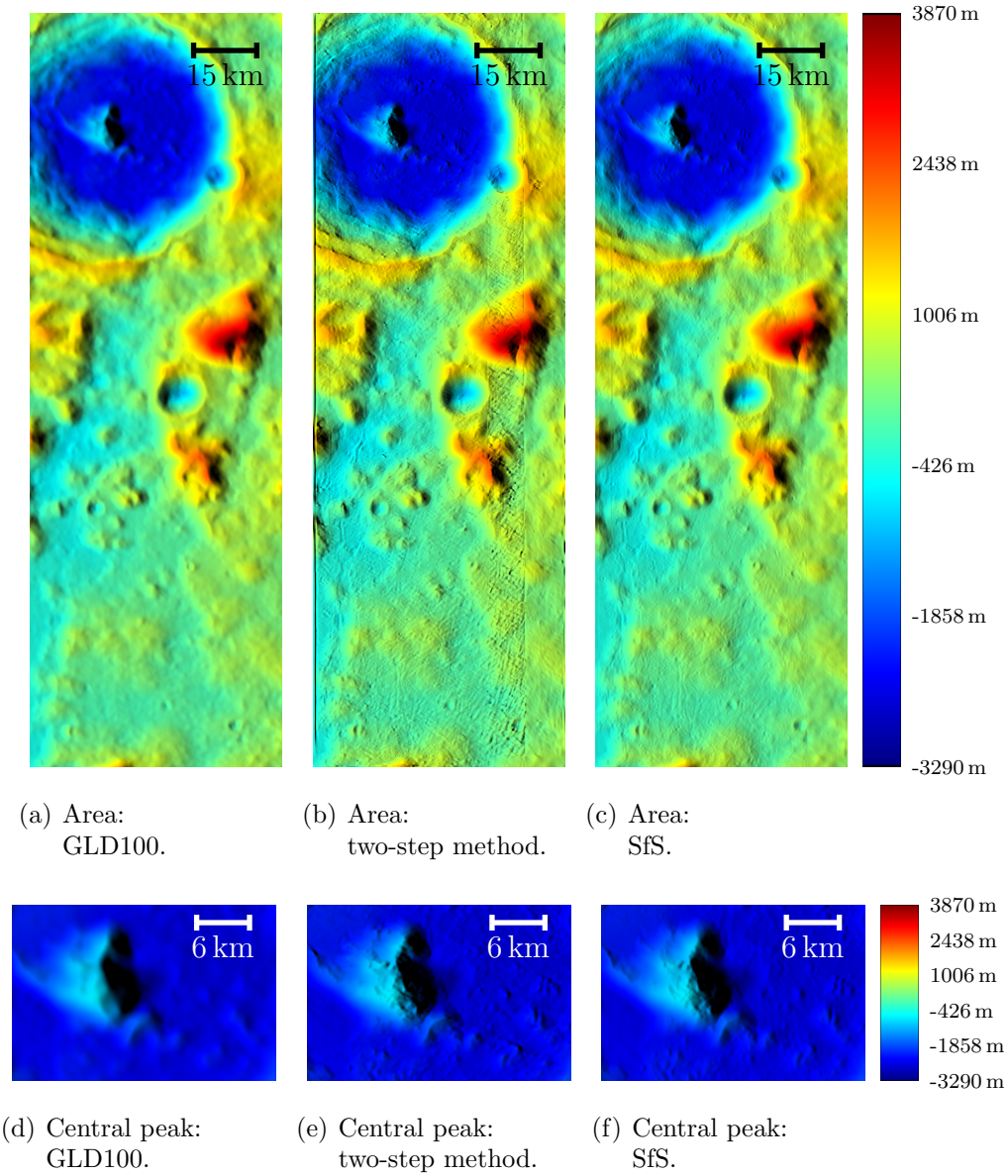

(a) Area: GLD100. (b) Area: two-step method. (c) Area: SfS.

(d) Central peak: GLD100. (e) Central peak: two-step method. (f) Central peak: SfS.

Figure 5.24: Topography near lunar crater Lowell (102.00 °W – 104.00 °W, 12.00 °S – 18.00 °S). (a)–(c) The topography of the area near lunar crater Lowell for the GLD100, the two-step method consisting of the extended PHCL algorithm followed by a recovery of the surface applying the absolute depth constraint and the further extended SfS method, respectively. (d)–(f) Close-up of the central peak of lunar crater Lowell for the GLD100, the two-step method consisting of the extended PHCL algorithm followed by a recovery of the surface applying the absolute depth constraint and the further extended SfS method, respectively.

6

Application scenarios

The reflectance normalisation and photometric DEM refinement techniques presented in Chapter 4 and Chapter 5 enable various applications. At first, a near-global reflectance mosaic is constructed which is corrected for local topography. This mosaic is presented in Section 6.1. Global elemental abundance maps are then derived from the near-global photometrically corrected mosaic as detailed in Section 6.2. An illumination-independent image registration technique is presented in Section 6.3 using the fact that the photometric DEM refinement techniques provide co-registered DEM at image resolution. Finally, in Section 6.4 the application of the photometric surface refinement methods is applied to the LROC NAC images to derive DEM at the highest possible resolution.

This chapter has been adapted and/or adopted from: (Grumpe et al., 2014a; Wöhler et al., 2014; Grumpe et al., 2012b; Grumpe and Wöhler, 2011a)

6.1 Photometrically corrected near-global mosaic

To construct a nearly global mosaic the M^3 hyperspectral image data, all images available at the Planetary Data System (PDS)[1] are remapped using a cylindrical projection of the spherical body which spans a rectangular grid, i.e. the selenographic longitude is the first unit vector and the selenographic latitude is the second unit vector, and rescaled to 20 pixels per degree. Since the signal to noise ratio decreases towards the poles, the mosaic is limited to $\pm 60\,^\circ$ latitude. The same rescaling procedure has been applied to the GLD100 DEM. At a scale of 20 pixels per degree, i.e. spatial extents of about 1.5 km per pixel, the GLD100 is regarded as accurate (Scholten et al., 2012) and the remaining misalignment of the M^3 data, which is less then a few km, is neglected.

To compensate the thermal emission of the surface, the superposition of a reference spectrum and a black body emission spectrum are estimated from the radiance data (cf.

[1] Available at http://pds-imaging.jpl.nasa.gov/volumes/m3.html

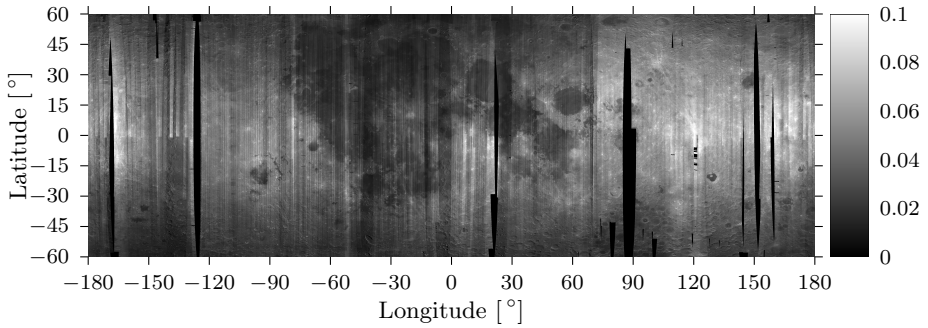

(a) Average reflectance at 1579 nm.

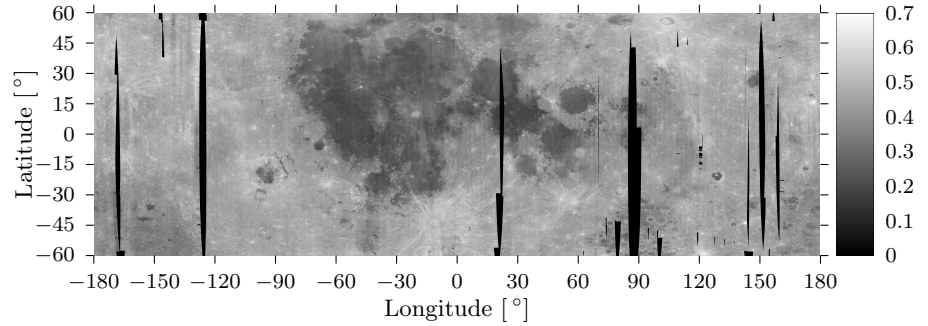

(b) Estimated single-scattering albedo at 1579 nm.

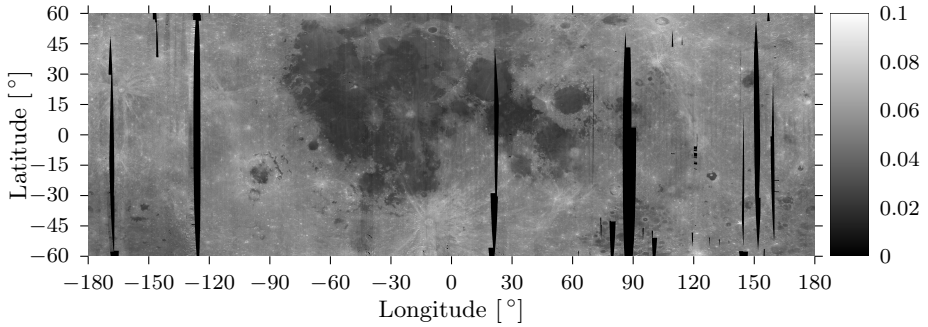

(c) Normalised reflectance at 1579 nm.

Figure 6.1: Near-global M^3 mosaic: Results. (a) Average reflectance map. The reflectance without photometric corrections shows illumination dependent artefacts, i.e. bright strips corresponding to images acquired at low incidence angles and a darkening towards the poles resulting from increased incidence angles. (b) Single-scattering albedo map. The single-scattering of the albedo is estimated during the normalisation process. (c) Normalised reflectance map. The result of the photometric correction shows no darkening towards the poles and largely reduced artefacts.

Section 4.1). The black body emission spectrum is then subtracted from the radiance data. Afterwards, the radiance is converted to reflectance by dividing the radiance by the solar irradiance spectrum. The surface gradients derived from the GLD100 and the observation conditions supplied with the M^3 data, i.e. the solar position and the sensor position with respect to a spherical body, are then used to estimate a pixel-wise single-scattering albedo of the full Hapke AMSA model that best matches all co-registered images (cf. Section 4.2). The single-scattering albedo is regarded as the most important parameter since a mixture of different minerals results in a linear mixture of single-scattering albedos (Mustard et al., 1998). The remaining model parameters are adopted from (Warell, 2004). Finally, the estimated single-scattering albedo and a standard viewing geometry of 30 ° incidence angle, 0 ° emission angle and 30 ° phase angle (Pieters, 1999) are inserted into the Hapke model to derive a normalised reflectance for each pixel, respectively.

Fig. 6.1 shows the near-global mosaic. The average reflectance without photometric correction (cf. Fig. 6.1(a)) exhibits the characteristic influences of local topography. The average reflectance decreases towards the lunar poles. This is caused by increasing incidence angles. Additionally, the co-registered images are acquired at different illumination geometries leading to clearly apparent intensity changes, i.e. vertical lines. The normalised reflectance map (cf. Fig. 6.1(c)) shows that the influence of the increasing incidence angles towards the lunar poles is effectively corrected. Furthermore, there are almost no visible borders between adjacent M^3 images. The pixel-wise estimated single-scattering albedo (cf. Fig. 6.1(b)) is in good agreement with the well known reflectance behaviour of the lunar surface. The highland materials appear bright in the albedo map while the basaltic mare regions show a significantly decreased single-scattering albedo. This two region model is widely accepted and used to derive different photometric functions (e.g. Hillier et al., 1999; Hicks et al., 2011) for each region, respectively. Furthermore, there are two clearly distinct brightness values visible within the mare regions representing the Titanium (Ti) content of the surface minerals. The brighter mare region corresponds to the well known low-Ti basalt of north-west Oceanus Procellarum, Mare Imbrium, Mare Serenitatis (Lucey et al., 1998) while the darker mare region corresponds to the mare basalts of increased Ti content, e.g. Mare Tranquilitatis and western Oceanus Procellarum (e.g. Lucey et al., 1998, 2000).

For comparison, the photometrically normalised Clementine mosaic[2] at 750 nm is presented next to the normalised M^3 reflectance at 750 nm in Fig. 6.2. The Clementine mosaic was made publicly available by Eliason et al. (1999). Later, Hare et al. (2008) improved the spatial locations and registered the mosaic to the Unified Lunar Control Network 2005. A comparison shows that both results are in good agreement. The Clementine mosaic, however, appears significantly brighter. This is a known effect. Hillier et al. (1999) quantified that a factor of 0.536 is required to map the reflectance measured by

[2]Available at http://astrogeology.usgs.gov/search/details/Moon/Clementine/UVVIS/UVVIS_Warp_Mosaic_5Bands_200m/cub

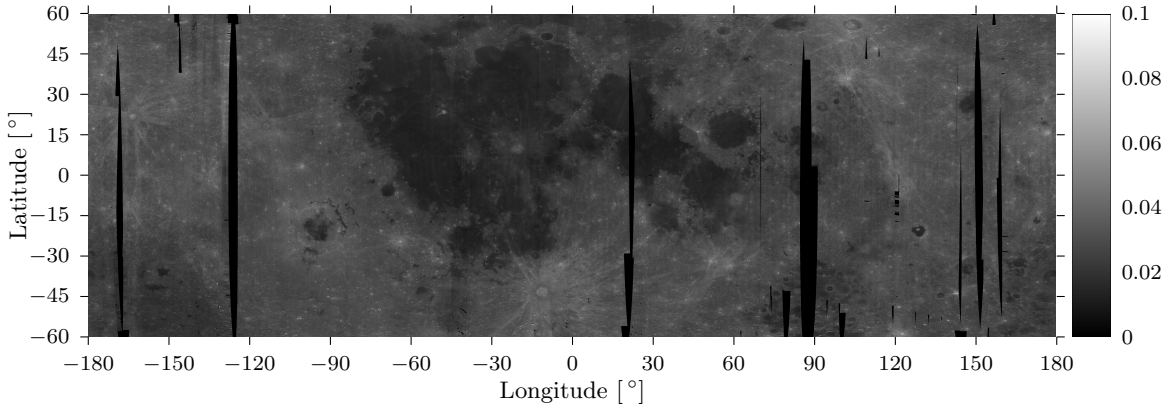

(a) Moon Mineralogy Mapper.

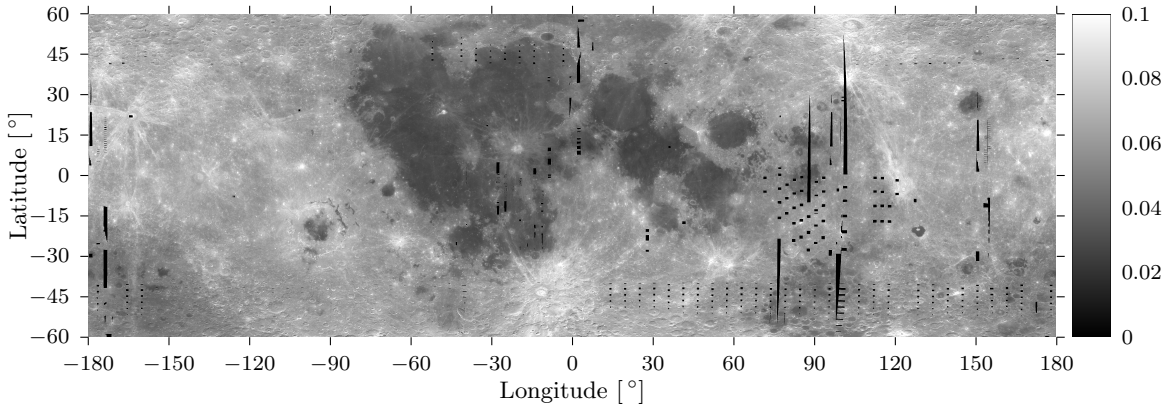

(b) Clementine.

Figure 6.2: Near-global M^3 mosaic: Comparison to Clementine. (a) The normalised reflectance at 750 nm derived from the M^3 measurements. (b) The normalised reflectance at 750 nm of the Clementine mosaic by Eliason et al. (1999) and Hare et al. (2008). The Clementine mosaic appears about twice as bright as the M^3 mosaic. This is in good agreement with the results of Hillier et al. (1999).

Clementine onto the reflectance expected from the earth based measurements by Shorthill et al. (1969). Accordingly, the Clementine data is about twice as bright as expected. The mean ratio of the M^3 data divided by the Clementine data amounts to 0.45 in case of the 750 nm channel which agrees with the aforementioned results. Furthermore, the Clementine mosaic was normalised with respect to a spherical model of the lunar surface, i.e. neglecting local topography. Consequently, the lunar craters are more apparent at higher degrees of latitude, i.e. towards the polar regions. This effect is not apparent in the M^3 dataset.

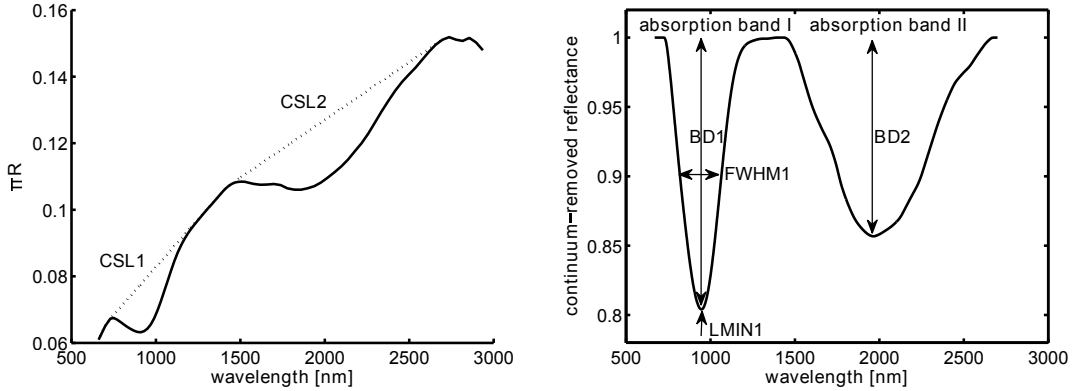

(a) Normalised reflectance spectrum. (b) Continuum-removed spectrum.

Figure 6.3: Extraction of spectral parameters. (a) Reflectance spectrum normalised to standard geometry (solid curve) and the corresponding convex hull (dotted curve). The continuum slopes CSL1 and CSL2 are inferred from the convex hull. (b) Continuum-removed spectrum. The inferred spectral parameters BD1, BD2, FWHM1 and LMIN1 are indicated.

6.2 Mapping elemental abundances

The estimation of elemental abundances based on the hyperspectral imagery has become a standard technique. Lucey et al. (2000) used the absolute reflectance at 750 nm in combination with the colour ratios 950 nm/750 nm and 750 nm/450 nm of the Clementine dataset to predict the elements Fe and Ti, respectively. Later, Ajith Kumar and Kumar (2014) recalibrated the approach for the M^3 dataset. Shkuratov et al. (2005b), in contrast, use a regression approach to map the Clementine data onto the Lunar Prospector Gamma-Ray Spectrometer data. Similarly, Wöhler et al. (2011) used different parameters, here referred to as spectral parameters, derived from the Clementine multispectral dataset to compute a regression and map the spectral parameters onto elemental abundance maps measured by the Lunar Prospector Gamma-Ray Spectrometer. Here, the approach by Wöhler et al. (2011) is adapted. Section 6.2.1 defines the spectral parameters derived from the M^3 dataset used in this thesis. The construction of elemental abundance maps is then detailed in Section 6.2.2. Finally, the construction of petrographic maps is discussed in Section 6.2.3.

6.2.1 Spectral parameters

The parameters of the Hapke AMSA model are estimated using the techniques described in Section 4.2. Based on these inferred parameters, the reflectance spectrum is computed

for the standard geometry given by 30 ° incidence angle, 0 ° emission angle and 30 ° phase angle (Pieters, 1999). These normalised spectra are smoothed in the spectral direction by adapting a polygonal line, i.e. a smoothing spline (Marsland, 2009, pp. 113ff). The smoothing spline is based on a simultaneous minimisation of the mean squared deviation from the normalised reflectance values and the mean squared second derivative, representing a measure for the curvature. The smoothed spectrum is then interpolated to integer wavelength values in nm using the method by Akima (1970). To emphasize the absorption bands of the reflectance spectra, the continuum is removed, i.e. the convex hull of the smoothed spectrum is computed and the smoothed interpolated spectrum is divided by the convex hull yielding the continuum-removed (CR) spectrum (Fu et al., 2007). An example is shown in Fig. 6.3.

According to Heiken et al. (1991), the lunar surface consists mainly of minerals. These are silicates, such as pyroxene, olivine and plagioclase feldspar. Important oxide minerals are ilmenite, spinels and armalcolite. Typical continuum-removed lunar reflectance spectra are thus characterised by two absorption bands centred around 1000 nm and 2000 nm, termed "1 μm band" and "2 μm band", respectively. The 1 μm band results from iron oxide (FeO) contained in lunar minerals such as pyroxene and olivine (Burns et al., 1972; Burns, 1989; Hazen et al., 1978; Matsunaga et al., 2008; Smrekar and Pieters, 1985) or agglutinated glass (Farr et al., 1980; Tompkins and Pieters, 2010). The 2 μm band is caused by electron transitions in the minerals pyroxene (Burns et al., 1972; Burns, 1989; Hazen et al., 1978), spinel (Cloutis et al., 2004) or in agglutinated glass (Farr et al., 1980; Tompkins and Pieters, 2010). Since the position, depth and width vary with the elemental composition of the minerals (e.g. Hazen et al., 1978), these spectral parameters are related to the elemental composition of the surface material. In some lunar regions, a weak absorption band around 1300 nm can be observed, which is attributed to the mineral plagioclase (Adams and Goullaud, 1978; Cheek et al., 2009) but neglected here and no parameters are defined. An absorption trough around 2800 nm due to water molecules and hydroxyl ions is described by Clark et al. (2010) but not regarded here.

As spectral parameters, the wavelength of the absorption minimum (LMIN1), the relative band depth (BD1) and the full width at half maximum (FWHM1) of the 1 μm band are inferred from the continuum-removed spectrum (Fig. 6.3(b)), while the slope of the continuum (CSL1) is obtained from the convex hull (Fig. 6.3(a)). Similarly, the band depth (BD2) and continuum slope (CSL2) of the 2 μm band are computed. Due to the noise level of the M^3 spectra around 2000 nm wavelength, a reliable determination of the wavelength absorption minimum of the 2 μm band is not possible. For similar reasons, the likewise strongly noise-affected value of the the 2 μm band absorption width is neglected. An important spectral parameter is the logarithm of the ratio between the depths of the 1 μm band and the 2 μm band:

$$\mathrm{LBD} = \log_{10} \frac{\mathrm{BD1}}{\mathrm{BD2}}. \tag{6.1}$$

The parameter measures the ratio between the two absorption depths. The ratio itself, however, is not symmetric around one, i.e. it changes if numerator and denominator are interchanged. In order to obtain a "symmetric" measure of the band depth ratio, the logarithm is introduced.

6.2.2 Construction of elemental abundance maps

In order to map the spectral parameters to elemental abundances, a polynomial regression is applied (Wöhler et al., 2011). The Lunar Prospector Gamma-Ray Spectrometer (LP GRS)[3] (e.g. Lawrence et al., 1998) measurements are the target values, i.e. the dependent variables, while the extracted spectral parameters are the independent variables of the regression. A linear regression approach relying on LP GRS elemental abundance data of the elements Calcium (Ca), Aluminium (Al), Iron (Fe), Magnesium (Mg), Titanium (Ti) and Oxygen (O) using a different set of independent variables extracted from Clementine UVVIS reflectance data has also been earlier proposed by Shkuratov et al. (2005a). Notably, the element O does not have a characteristic spectral absorption. Its abundance, however is highly correlated to the elements Fe and Ti (Shkuratov et al., 2011).

The lateral resolution of the LP GRS data is about 150 km per pixel which corresponds to 0.2 pixels per degree in the cylindrical coordinate system. The available data is thus mapped to the chosen cylindrical coordinate system with a grid spacing of 0.2 pixels per degree. The near-global M^3 mosaic (cf. Section 6.1) is computed in the cylindrical coordinate system of the near-global mosaic with a grid spacing of 20 pixels per degree and thus downscaled to 0.2 pixels per degree prior to the extraction of the spectral parameters. All measurements are in percentage of weight (%wt).

The estimation of the abundances of the elements Ca, Al, Fe, Mg and O is based on the absorption wavelength (LMIN1), depth (BD1), width (FWHM1) and continuum slope (CSL1) of the 1 μm band and the depth (BD2) and continuum slope (CSL2) of the 2 μm band, where a linear regression model is applied. A second-order regression model leads to extrapolation artefacts especially in regions of low optical maturity, which are not encountered on the large spatial scales of 0.2 degrees per pixel used for calibration of the regression function. For the element Ti a quadratic regression model based on the CSL1 and the logarithm of the ratio between the BD1 and BD2 absorption depths was determined. Additionally, the confidence bands of the regression polynomials are computed according to Kardaun (2005, pp. 194ff).

The calibrated regression functions may be applied to construct elemental abundance maps at the full resolution of the M^3 images. This technique, however, has to be carefully judged due to the so-called optical maturity of the surface (Lucey et al., 2000). The space-weathering induces an aging process of the surface, i.e. the absorption depth is lowered and the spectra are reddened (e.g. Noble et al., 2001). Some events, e.g. impacts

[3]Available at http://www.mapaplanet.org/explorer/moon.html

and crater formation, seismic activity and volcanoes may break the weathered surface layer and exhibit fresh material showing significantly deeper absorptions. Corresponding data is missing at the spatial scale of the regression and thus maps produced at the full resolution may be erroneous.

The result of the iron estimation method by Lucey et al. (2000) and the proposed method are shown in Fig. 6.4 alongside the abundance map derived from LP GRS measurements. Since the method by Lucey et al. (2000) has been calibrated with respect to the Clementine dataset, and the Clementine dataset measured about twice the expected reflectance (Hillier et al., 1999), the method by Lucey et al. (2000) is applied to the global Clementine mosaic[4] made publicly available by Eliason et al. (1999) and registered to the Unified Lunar Control Network 2005 by Hare et al. (2008). The global Clementine mosaic at about 200 m per pixel resolution is cropped to $\pm 60\,^\circ$ latitude and rescaled to the resolution of the near-global M^3 mosaic (cf. Section 6.1). According to Lucey et al. (2000), the Iron oxide (FeO) content is computed according to

$$\theta_{\mathrm{FeO}} = \tan^{-1}\left(\frac{\frac{R_{950}}{R_{750}} - y_{\mathrm{FeO}}}{\pi R_{750} - x_{\mathrm{FeO}}}\right) \tag{6.2}$$

$$\mathrm{FeO}[\%wt] = 17.427\theta_{\mathrm{FeO}} - 7.565. \tag{6.3}$$

The space-weathering moves the reflectance on straight lines in the coordinate system defined by the normalised reflectance at 750 nm R_{750} and the ratio of the normalised reflectance at 950 nm R_{950} and R_{750}. All lines representing different FeO content intersect in the optimised origin $x_{\mathrm{FeO}} = 0.08$ and $y_{\mathrm{FeO}} = 1.19$. The FeO content thus depends only on the angle θ_{FeO}. The inverse tangent $\tan^{-1}$ needs to cover the whole angular range $\pm\pi$. The proposed regression approach is directly applied to the near-global mosaic. Since the result of the regression method and the LP GRS measurements represent the Fe content rather than the FeO content, it is converted using the atomic masses $u_{\mathrm{Fe}} = 56\,\mathrm{u}$ and $u_{\mathrm{O}} = 16\,\mathrm{u}$ of Fe and O, respectively, by applying

$$\mathrm{FeO}[\%wt] = \frac{u_{\mathrm{Fe}} + u_{\mathrm{O}}}{u_{\mathrm{Fe}}}\mathrm{Fe}[\%wt]. \tag{6.4}$$

Both methods are in very good agreement with the FeO abundance distribution derived from LP GRS data. On a global scale, most of the lunar surface consists of mature material, i.e. material darkened by space weathering, while only small portions of fresh immature minerals are uncovered, e.g. by impact events or quakes. The immature material thus only exists on local scales and is not covered by the LP GRS dataset. This effect causes the proposed method to overestimate the FeO content, which is reflected by bright spots in the FeO abundance map produced by the proposed method. The proposed

[4]Available at http://astrogeology.usgs.gov/search/details/Moon/Clementine/UVVIS/UVVIS_Warp_Mosaic_5Bands_200m/cub

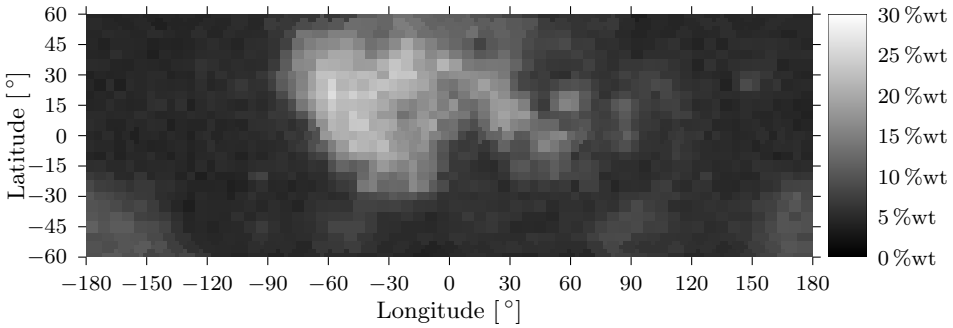

(a) LP GRS derived map

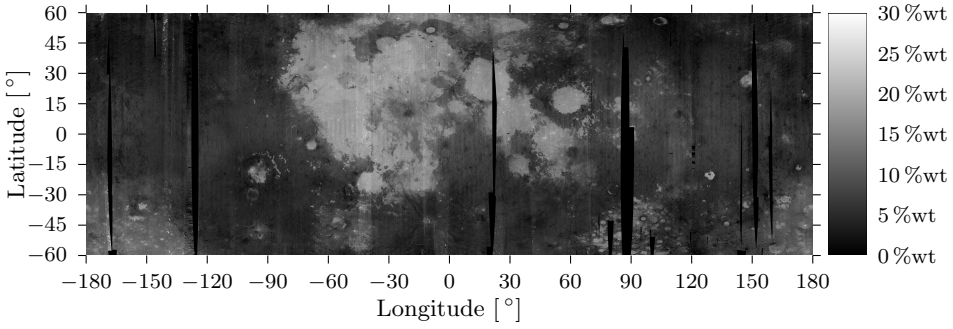

(b) Proposed method

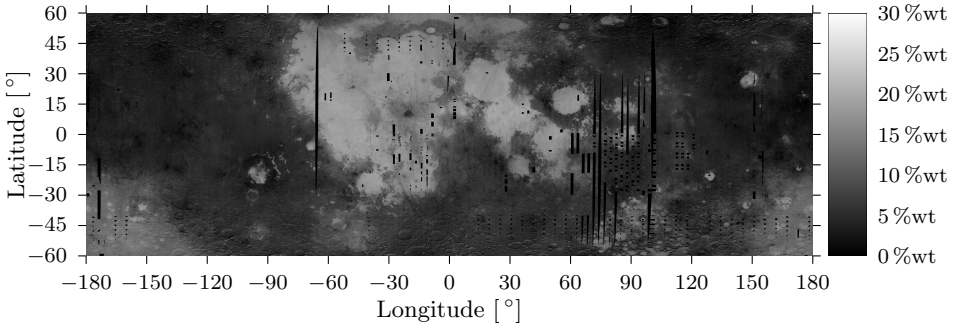

(c) (Lucey et al., 2000)

Figure 6.4: Iron oxide (FeO) content map: Comparison to Lucey et al. (2000). (a) Map derived from the LP GRS measurements at about 150 km per pixel resolution. (b) Result of the regression algorithm applied to the near-global M^3 mosaic at full resolution of about 1.5 km per pixel. (c) FeO content estimtated by applying the method of Lucey et al. (2000) to the cropped and downscaled global Clementine mosaic of Eliason et al. (1999).

method does not show the artefacts related to topography in the northern and southern regions. This, however, is due to the different normalisation procedure and not related to the FeO abundance estimation method. A direct application of the method by Lucey et al. (2000) to the M^3 data is, however, not possible due to the higher reflectance values measured by the Clementine sensor.

Zhang and Bowles (2013) applied the method by Lucey et al. (1995) to the M^3 data. The only difference between the methods by Lucey et al. (1995) and by Lucey et al. (2000) is the different value of the optimised origin ($x_{\mathrm{FeO}} = 0.01, y_{\mathrm{FeO}} = 1.26$) and the regression coefficients that map the angle onto the FeO content. The model by Lucey et al. (1995) has been adapted to laboratory spectra and is thus applicable to the M^3 data. Lucey et al. (1998), however, note that the laboratory spectra are in units of the directional-hemispherical reflectance. The M^3 instrument measured the bidirectional reflectance which is related to the directional-hemispherical reflectance in a non-linear way (Hapke, 1981, 2002). According to Lucey et al. (1998), the method may provide reasonable estimates for low resolution maps such as the near-global mosaic. Notably, the model by Lucey et al. (1995) estimates Fe rather than FeO. The resulting map is thus converted using Eq. (6.4).

In contrast, Ajith Kumar and Kumar (2014) recalibrated the method by Lucey et al. (2000) with respect to M^3 data. The obtained origin ($x_{\mathrm{FeO}} = 0.08, y_{\mathrm{FeO}} = 1.18$) is very close to the origin given by Lucey et al. (2000) which is unexpected due to the increased R_{750} values of the Clementine sensor. Additionally, the linear mapping of θ_{FeO} onto the FeO abundance was replaced by the power law

$$\mathrm{FeO}[\%wt] = 10.59\theta_{\mathrm{FeO}}^{1.209}. \tag{6.5}$$

The corresponding FeO estimates are shown in Fig. 6.5. The result of the method by Lucey et al. (1995) is in good agreement with the expected FeO abundance map and similar to the previous methods. The model proposed by Ajith Kumar and Kumar (2014) provides significantly increased FeO abundance values on the global scale. The unrealistic high FeO abundance estimates of the Mare regions (¿ 30 %wt) suggests that the coefficients obtained by Ajith Kumar and Kumar (2014) may work well for the small regions used in the optimisation but lack generalisation capability, since the band depth shows a saturation effect for FeO contents above 20 %wt (Lucey et al., 1998). The results show the high sensitivity of the parameters. Lucey et al. (1998) noted that there are many equally good origins with respect to the FeO abundance estimation. They, however, stated that the influence of the optical maturity of the surface depends on the choice of the origin and thus included a visual inspection of multiple FeO estimation maps with respect to the effect of optical maturity into the optimisation. This is the strength of the regression approach which maps the spectral absorption parameters onto the LP GRS dataset and thus uses data of the whole lunar surface instead of a few laboratory measurements. The effect of optical maturity, however, is not completely compensated due to the lack of immature surface material in the LP GRS training set.

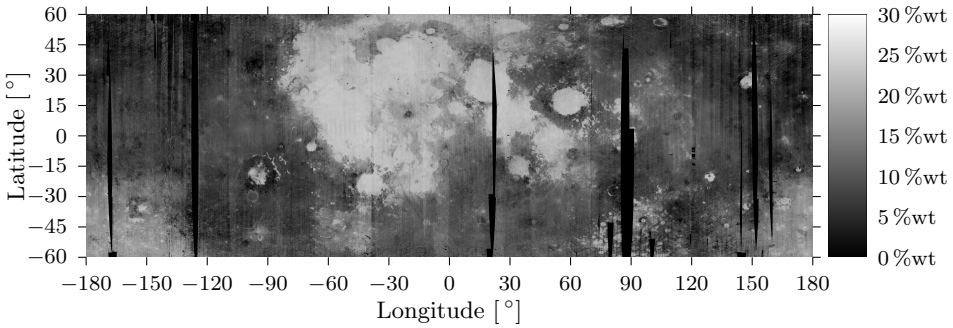

(a) (Zhang and Bowles, 2013; Lucey et al., 1995)

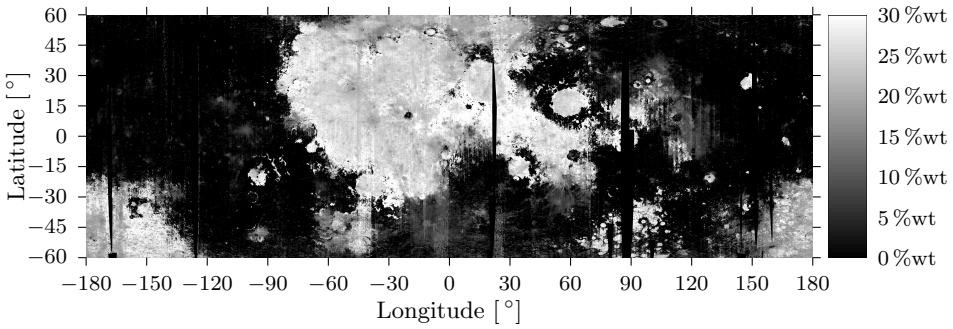

(b) (Ajith Kumar and Kumar, 2014)

Figure 6.5: Iron oxide (FeO) content map: M^3 based reference methods. (a) The results of the method by Lucey et al. (1995) as proposed by Zhang and Bowles (2013). According to Lucey et al. (1998), the method was calibrated on directional-hemispherical measurements and is thus non-linearly related to the bidirectional reflectance measured by the M^3 instrument. It may, however, produce accurate results on large scales (Lucey et al., 1998). (b) Result of the method by Lucey et al. (2000) recalibrated to the M^3 measurements by Ajith Kumar and Kumar (2014). The estimated FeO abundances exceed 30 %wt which is physically unreasonable due to saturation effects of the absorption band for abundance values above 20 %wt (Lucey et al., 1998).

The results of the Titanium dioxide (TiO_2) estimation are shown in Fig. 6.6. The method by Lucey et al. (2000) estimates the TiO_2 content according to

$$\theta_{TiO_2} = \tan^{-1}\left(\frac{\frac{R_{415}}{R_{750}} - 0.42}{\pi R_{750} - 0.00}\right) \tag{6.6}$$

$$TiO_2[\%wt] = 3.708\theta_{TiO_2}^{5.979} \tag{6.7}$$

where R_{415} is the normalised reflectance at 415 nm wavelength. The conversion of the LP GRS data and the result of the regression algorithm is computed according to

$$TiO_2[\%wt] = \frac{u_{Ti} + 2u_O}{u_{Ti}} Ti[\%wt] \tag{6.8}$$

where the atomic mass of Ti amounts to $u_{Ti} = 48$ u.

Comparing the TiO_2 maps produced by both methods, again, shows a good agreement with the LP GRS derived map. The proposed method, however, does not fully capture the increased TiO_2 content of Mare Tranquillitatis while the method by Lucey et al. (2000) strongly overestimates the TiO_2 content of Mare Tranquillitatis and western Oceanus Procellarum. For other areas, e.g. Mare Orientale, both methods show an increased TiO_2 content that is not visible in the LP GRS derived map due to its low lateral resolution. Bussey and Spudis (1997) classified the mare region within Mare Orientale as low-Ti mare basalt, i.e. the TiO_2 concentration is increased compared to the highland spectrum but less than the TiO_2 concentration of high-Ti mare areas, which is covered by both methods.

Fig. 6.7 summarises the elemental composition of the lunar surface for the elements Ca, Al, Mg and O, respectively. Comparing the LP GRS derived abundance maps and the predicted abundances resulting from the proposed method, the global distribution is in good agreement. The Ca content, however, is underestimated for the far side highland areas. The proposed method, however, captures the known inverse correlations between Ca and Fe (Elphic et al., 1998) and Al and Fe (Fischer and Pieters, 1995), respectively.

6.2.3 Construction of petrographic maps

It is found by Berezhnoy et al. (2005) based on an analysis of LP GRS abundance data of the elements Al, Fe and Mg that the corresponding LP GRS measurements can be described at high accuracy by a plane in the three-dimensional (Al, Fe, Mg) abundance space. This finding is confirmed by applying the M^3-based regression approach on global scales at 20 pixels per degree resolution. The deviations of the estimated Al, Fe and Mg abundances from a plane are always well below 1 %wt.

Hence, the abundances of Fe and Mg alone are sufficient to describe a lunar soil in terms of the petrographic model suggested by Berezhnoy et al. (2012), which is defined by the endmembers mare basalt (or pyroxene), Mg-rich rock (including e.g. norite), and

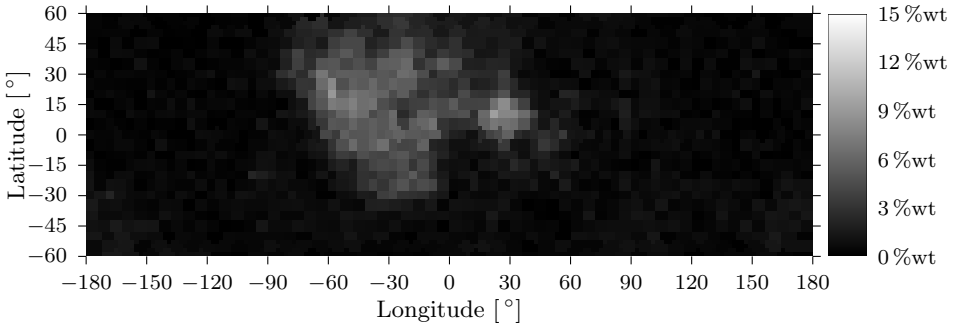

(a) LP GRS derived map

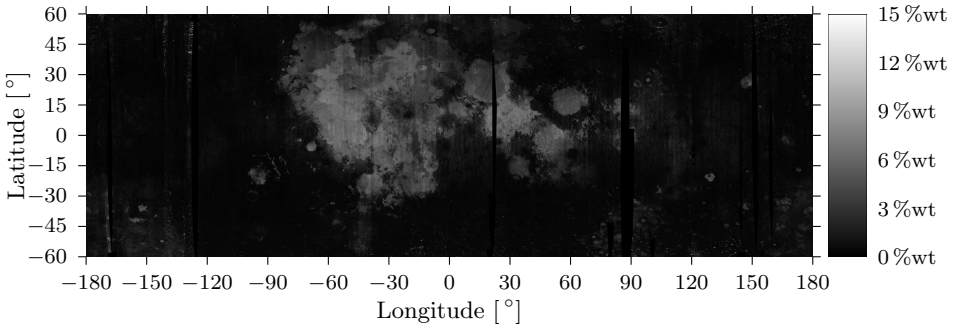

(b) Proposed method

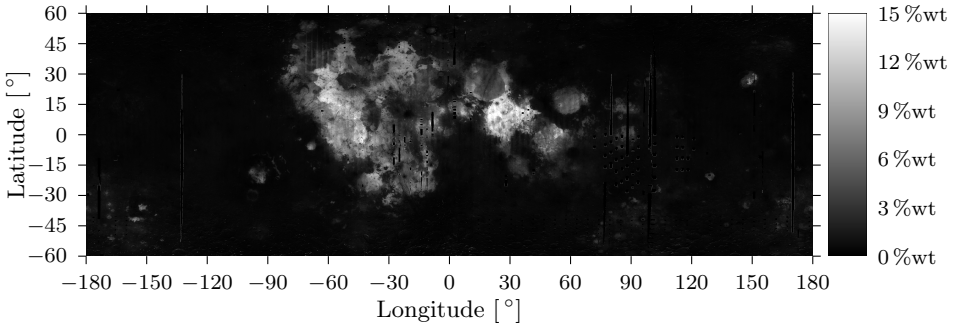

(c) (Lucey et al., 2000)

Figure 6.6: Titanium dioxide (TiO_2) content map. (a) Map derived from the LP GRS measurements at about 150 km per pixel resolution. (b) Result of the regression algorithm applied to the near-global M^3 mosaic at full resolution of about 1.5 km per pixel. (c) FeO content estimtated by applying the method of Lucey et al. (2000) to the cropped and downscaled global Clementine mosaic of Eliason et al. (1999).

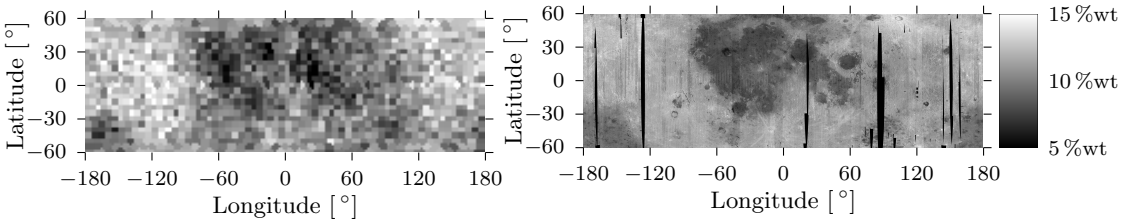

(a) Ca: LP GRS derived map

(e) Ca: Proposed method

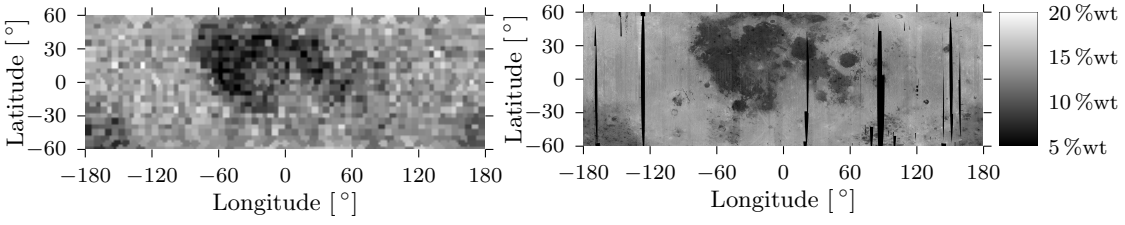

(b) Al: LP GRS derived map

(f) Al: Proposed method

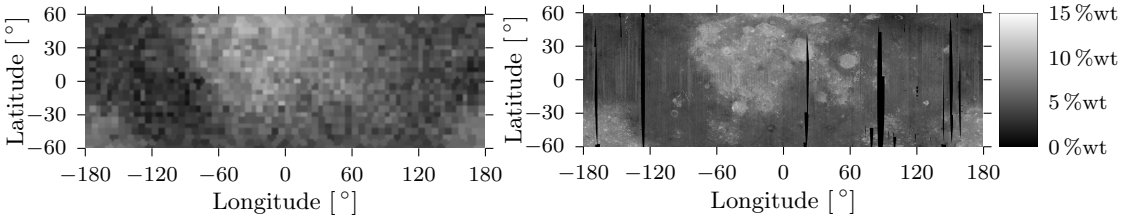

(c) Mg: LP GRS derived map

(g) Mg: Proposed method

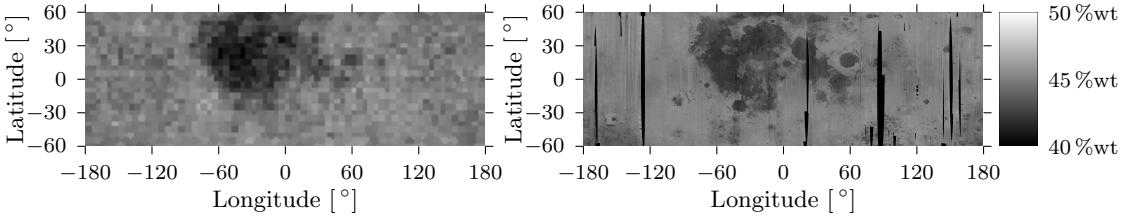

(d) O: LP GRS derived map

(h) O: Proposed method

Figure 6.7: Elemental abundance maps of Ca, Al, Mg and O. (a)–(d) Elemental abundance maps derived from the LP GRS dataset showing the content of Ca, Al, Mg and O in %wt, respectively. (e)–(h) The predicted content in %wt of Ca, Al, Mg and O, respectively, as computed by the proposed regression method.

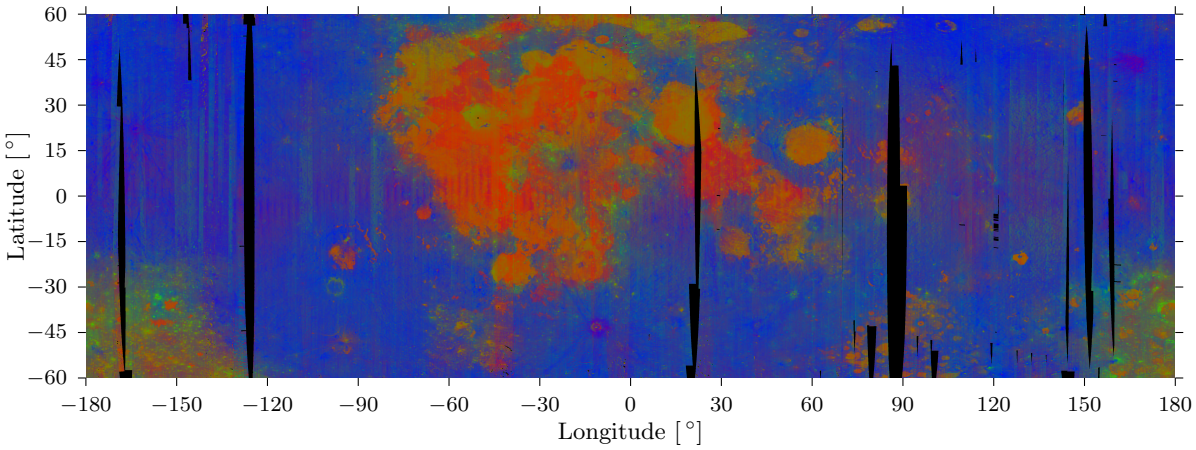

Figure 6.8: Near-global petrographic map of the Moon using the M^3 data set, covering the latitude range from 60 °S to 60 °N. The resolution corresponds to 20 pixels per degree. Red channel: mare basalt/pyroxene. Green channel: Mg-rich rock. Blue channel: feldspathic material.

feldspathic rock (ferroan anorthosite, FAN). The relative fractions of the three endmembers are read from a ternary diagram in the Fe-Mg space and visualised in the form of a RGB image, where the red channel is assigned to the mare basalt fraction, the green channel to the Mg-rich rock fraction, and the blue channel to the FAN fraction. For illustration, a near-global petrographic map ranging from 60 °S to 60 °N of 20 pixels per degree resolution is shown in Fig. 6.8, where the highlands appear in deep blue colour and are characterised by high reflectance with weak band I and II absorptions. Mare regions appear red to orange or greenish depending on their content of Mg-rich rock (e.g. olivine-rich material or norite rich in orthopyroxene). They are characterised by low reflectance with distinct pyroxene-related band I and II absorptions whose absorption wavelengths, within the limitations outlined in Section 6.2.2, indicate the presence of low-Ca orthopyroxene vs. high-Ca clinopyroxene (Matsunaga et al., 2008). Small localised areas of high Mg-rich rock content appear in bright green colour. They are characterised by deep band I absorptions with short wavelengths. Based on this relatively simple model it is possible to obtain an overview of the general petrography of a lunar region and, in particular, to detect mineralogical anomalies easily.

6.3 Illumination independent image registration

Unfortunately, Chandrayaan-1 lost both of its star sensors during the mission, which led to the lack of pointing data and thus loss of position and orientation information. Although the first sensor failed before the first M^3 image was acquired, Boardman et al.

(2011) registered all images to the LOLA DEM grid with an RMSE of 200 m between adjacent images. However, for some regions misalignments between overlapping images of up to a few kilometres may appear, including minor rotations and projective distortions. Since co-registered images are required for the mapping of reflectance parameters and the photometric surface reconstruction algorithms, the lateral displacements have to be less than one pixel which, in case of the M^3 sensor, corresponds to 100 m. Hence, a robust image registration method is necessary.

Registering images from multiple orbits, i.e. different illumination conditions, requires illumination independent descriptors. The proposed photometric methods, however, compute a surface model that corresponds to the shading information and thus is illumination independent. Two images are aligned by registering the two recovered surfaces. Here, the registration procedure is limited to two images that overlap at least partly. Section 6.3.1 gives an overview over the proposed method and Section 6.3.2 then gives details about the matching criteria that are used to determine the alignment of two images. The transformation between both images are described in Section 6.3.3. Finally, Section 6.3.4 gives a detailed evaluation of the residual misalignment.

6.3.1 Overview

Generally, "image registration is the first step towards using remote sensed images for any purpose" (Dawn et al., 2010). Especially if sub-pixel accuracy is required, e.g. for the evaluation of spectral data and mapping of reflectance parameters, or data sets originating from different spacecraft are fused, a robust image registration is inevitable. As an example, to match the coordinate systems of the Mars Reconnaissance Orbiter and the Mars Express spacecraft, Albertz et al. (2005) include the Mars Orbiter Laser Altimeter single point measurements into the bundle adjustment that is used to determine the exterior orientation of the Mars Express spacecraft. In the proposed normalisation framework, the pixel-wise reflectance parameter mapping might fail due to varying information of the different images acquired under different illumination conditions if the lateral offset between two images is one pixel or larger. The situation is further complicated due to the missing pointing data.

The multi-modal registration of images and DEM has been of interest for a long time (Horn and Bachman, 1978; Jankó and Chetverikov, 2004; Jankó et al., 2007). Horn and Bachman (1978) proposes to use artificial images by illuminating an existing DEM under conditions identical with the illumination geometry of the image. Soderblom and Kirk (2003) use this approach to reduce the alignment inaccuracy between the gridded Mars Orbiter Laser Altimeter dataset and the Mars Orbiter Narrow Angle Camera from $<$ 200 m to $<$ 50 m. The DEM itself as well as its gradients can be considered an illumination-invariant representation of the image (a related idea is mentioned by Horn (1975, 1977) but regarded therein as computationally too expensive). However, the lateral resolution of the available DEM (LOLA, GLD100) is several times lower than the resolution of the

M^3 images and thus the inferred artificial images do not match the image data very well. Since images of the same surface were acquired during different orbits, the illumination and the corresponding surface appearance vary strongly over different images. Most intensity-based image registration algorithms are bound to fail because of the changing illumination. However, the surface itself is supposed to be illumination-independent and thus, instead of tackling the problem heads-on, the extended photoclinometry algorithm is applied to each image separately. The resulting surface gradient estimates are assumed illumination-independent and co-registered with the M^3 images. Thus, by registering the gradient fields the M^3 images are registered as well. Due to the residual error in the gradient estimates, the results might be improved by recovering the actual surface, e.g. by applying the technique described in Section 5.3.2. The gradient field, however, is sufficient in most cases and this computationally expensive step is omitted. Notably, all surface properties, e.g. the reflectance parameters, the gradient fields or derived values like surface slopes may be used instead.

Each image is registered on a reference image that has been defined in advance by the user. Thus, the problem is limited to the pair wise registration of images. In order to register the gradient images, two different methods alignment measures are proposed. The first method is based on control points (CP), while the second method maximises the mutual information (MI), which has been studied extensively as a measure for image registration (e.g. Maes et al. (1997)).

6.3.2 Alignment measures

A standard procedure of measuring the alignment of two images is the comparison of control points (CP). Control points are assumed to be characteristic features of an image and two images are well aligned if the position of corresponding CP in both images coincides. The correspondence between CP from different images is established by comparing the image intensities in a neighbourhood around the CP. To extract possible CP, the Harris corner detector (Harris and Stephens, 1988) is applied to each gradient field separately and an identical number of CP candidates are extracted from all gradient fields. The number $\tilde{n}_{\mathrm{CP}}$ of CP candidates is chosen as three times the number of CP desired for determining the transformation between the images (n_{CP}). The resulting points are matched at sub-pixel accuracy using either normalised cross-correlation or the SSIM measure (Wang et al., 2004) and an adaptive threshold value. The adaptive threshold value is chosen such that the number of CP matches is $2 \cdot n_{\mathrm{CP}}$. The transformation between the images usually mainly consists of a translation. Perspective distortions are also important, while the influence of rotations tends to be minor. It can thus be assumed that pairs of corresponding CP have connecting lines of similar length and direction. The CP pair candidates with the largest deviations from the mean length and direction value of the connecting line, respectively, are potential outliers and are thus removed from the set of CP candidates. The two sets of removed CP candidates may overlap, such that

the process is repeated until n_{CP} CP candidates remain. In the proposed system, the extracted CP pairs are presented to the user before the transform is computed, where the user may add or discard CP pairs. The process of registration using CP is shown in Fig. 6.9. At first, the surface gradients are computed from the reflectance. Afterwards, CP are matched and the transformation is determined. Finally, the radiance images are registered using the obtained transformations.

The MI is a measure of similarity between two random processes. Each image acquisition is assumed to be a random process and the measured intensity is regarded as the random variable. The MI is computed from probability distributions using the Shannon entropy formulation (Shannon, 2001):

$$\begin{aligned} \mathrm{MI} = & - \int_{I_1} p_{I_1}(\chi_1) \log(p_{I_1}(\chi_1)) d\chi_1 - \int_{I_2} p_{I_2}(\chi_2) \log(p_{I_2}(\chi_2)) d\chi_2 \\ & + \int_{I_1} \int_{I_2} p_{I_1,I_2}(\chi_1, \chi_2) \log(p_{I_1,I_2}(\chi_1, \chi_2)) d\chi_1 d\chi_2 \end{aligned} \tag{6.9}$$

where $p_{I_1}(\chi_1)$ is the probability of encountering the intensity χ_1 in the image I_1, $p_{I_2}(\chi_2)$ is the probability of encountering the intensity χ_2 in the image I_2, and $p_{I_1,I_2}(\chi_1, \chi_2)$ is the joint probability of encountering the intensities χ_1 in image I_1 and χ_2 in image I_2.

The joint and marginal probability distributions $p_{I_1}(\chi_1)$, $p_{I_2}(\chi_2)$, and $p_{I_1,I_2}(\chi_1, \chi_2)$ are estimated using either a joint histogram, Parzen windowing or the IsoContour method proposed by Rajwade et al. (2009). The joint histogram and the Parzen windowing methods assume the measured intensity to be random and neglect the position within the image. Furthermore, the kernel estimators are known to converge to the real probability density if the number of samples approaches infinity which is rarely met in practice. The joint histogram is computed by binning the measured intensities within both images. If the number of bins is chosen too small, information is lost, and if the number of bins is chosen too large, the probability is not smooth and results in a non-smooth behaviour of the MI around the optimum. The Parzen windowing method uses a kernel estimator to estimate the probability distributions (Parzen, 1962; Wells III et al., 1996). The IsoContour method deals with the image as a continuous entity and avoids the so-called binning problem of discrete probability estimators such as histograms (Rajwade et al., 2009). This is achieved by a transformation of the random variable. Rajwade et al. (2009) assume the location within the image to be random and the intensity as a function of the location. This relates the probability distributions directly to the intensity and intensity gradients. Using an interpolation routine the image is assumed to be continuous and the probability density function can be computed without setting further parameters (Rajwade et al., 2009).

Since in most cases the MI of sharp images is not smooth around the global optimum, a multi-level search for the optimal transformation parameters is applied. Initially, the images are blurred using a Gaussian of width σ_{MI}, and the obtained parameters are used

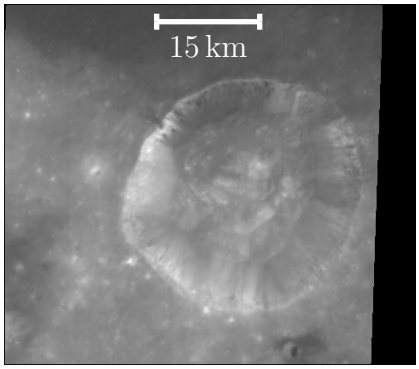

(a) Floating image. Image credit: NASA/JPL-Caltech.

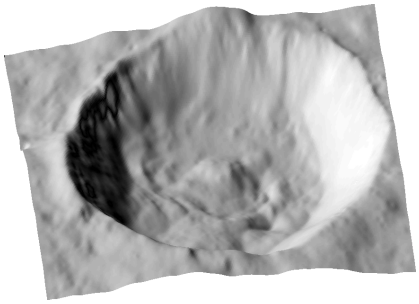

(b) Estimated DEM. The elevation axis is scaled by a factor of three.

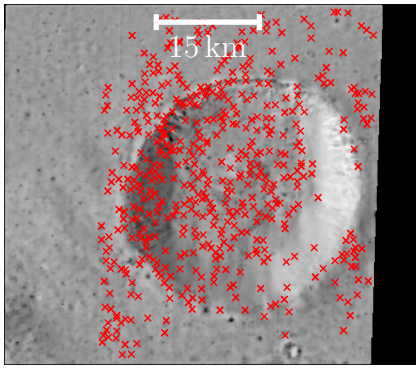

(c) Photometric surface gradient estimate p with control points, floating image.

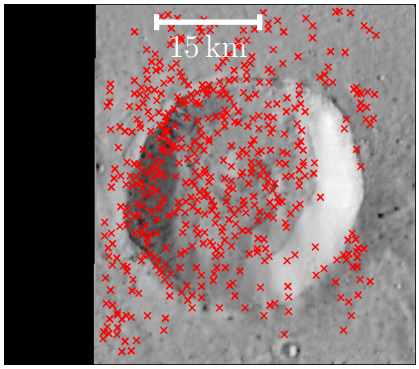

(d) Photometric surface gradient estimate p with control points, reference image.

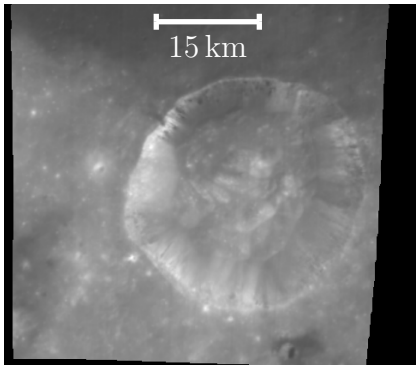

(e) Transformed floating image.

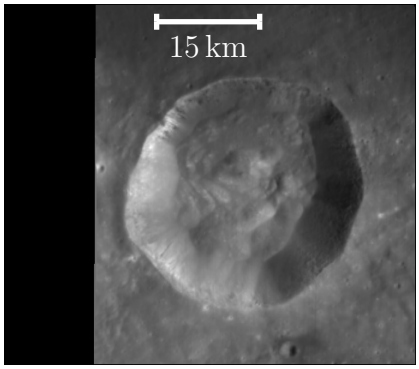

(f) Reference image. Image credit: NASA/JPL-Caltech.

Figure 6.9: Image registration based on control points, regarding the example of the lunar crater Menelaus (coordinates of crater centre: 16.0 °N, 16.3 °E, diameter: 27 km).

as initial values for the search at a lower value of σ_{MI}. The algorithm starts at $\sigma_{\mathrm{MI}} = 5$ and reduces σ_{MI} to $\sigma_{\mathrm{MI}} = 3$ and $\sigma_{\mathrm{MI}} = 1$. A Simplex algorithm according to Nelder and Mead (1965) is applied to maximise the MI. After the algorithm terminates at $\sigma_{\mathrm{MI}} = 1$, Powell's direction search (Powell, 1964) is used on the original images to obtain the final value of the transformation parameters.

6.3.3 Transformations

The images are distorted due to changing 3D perspective. Image matching thus cannot be obtained based on affine or projective transformations alone. Therefore a polynomial transformation or a 3D rigid transformation can be chosen as a distortion model.

Initially, a fourth-order polynomial was used to transform the images. However, the amount of parameters and therefore the degree of freedom is large and a large number of CP are necessary. In case of the MI, the solvers fail to find suitable solutions for the required number of parameters. Therefore, the degree and thus the parameters are reduced to a second-order polynomial transformation. For comparison, a simple 2D rigid transformation with two translations in the horizontal and vertical direction, respectively, and one rotation is applied. However, due to the presence of perspective distortions, the simple rigid transformation is not sufficient. To include perspective effects, the depth data of the DEM is included by assuming a virtual pinhole camera (Jähne, 2004, p. 126ff) with nadir viewing direction at 100 km altitude over the centre of the DEM. Then the projection of the surface into the virtual camera is computed. Since the DEM and the surface gradient maps are co-registered, the resulting image is the projection of the surface gradients as seen by the virtual camera. Thus, the surface gradient texture is overlaid onto the DEM and projected into the camera. Fig. 6.10 depicts this process. Due to the usage of a texture, the lateral resolution of the DEM is not as important as it is in the case of matching artificially illuminated DEM. The transformation parameters are the Cartesian coordinates of the camera in 3D space as well as its orientation. The camera constant is set to $b_{\mathrm{MI}} = 1000$, which corresponds to 100 m per pixel at a distance of 100 km.

6.3.4 Evaluation

The CP-based image registration method is evaluated using a cross-validation strategy. The region of interest is the lunar crater Menelaus (longitude 15 °E–16.6 °E, latitude 15.6 °N–17 °N, M^3 images: M3G20090108T044645 and M3G20090204T113444). Using the Harris corner detector (Harris and Stephens, 1988), 500 CP candidates are determined in each image and matched using normalised cross-correlation. Since the main part of the transformation between the images usually consists of a translation while perspective distortions and rotations show minor influence, the length and orientation of the connecting lines is computed. Outliers in both sets are removed until the target amount of CP is reached. Using this approach, 250 corresponding CP are matched automatically

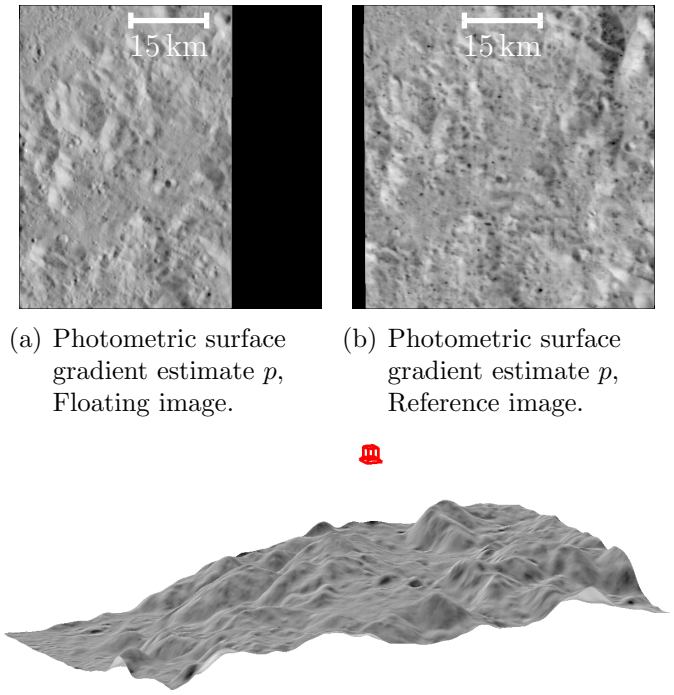

(a) Photometric surface gradient estimate p, Floating image.

(b) Photometric surface gradient estimate p, Reference image.

(c) Camera observing the surface. The surface gradients are overlaid as texture.

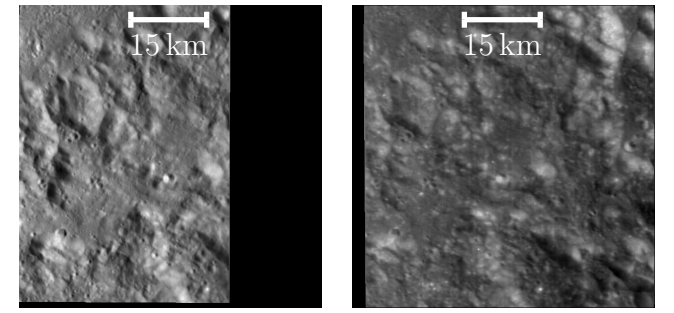

(d) Transformed floating image.

(e) Reference image.

Figure 6.10: Image registration process using a pinhole camera projection. (a) and (b) The reflectance images are transformed to surface gradients using the extended photoclinometry approach. (c) The estimated gradients resulting from the floating image are overlaid on the DEM, i.e. the depth data determines the 3D mesh and the surface gradient determines the texture, and projected into a pinhole camera. (d) and (e) The obtained position and orientation of the camera are used to project the floating image and obtain a co-registered pair of reflectance images. Image credit (d) and (e): NASA/JPL-Caltech.

and the CP pairs are then randomly divided into ten disjoint subsets. While leaving out one of the subsets, a transformation was determined based on the remaining CP, and the RMSE of the left-out CP was determined for each of the ten subsets, respectively. Furthermore, the partitioning of the subset was repeated 1000 times to account for the random position of outliers in the subsets. The overall RMSE amounts to 0.444 pixels and the standard deviation to 0.296 pixels. Sub-pixel accuracy can therefore be assumed at least for image areas close to the extracted CP.

However, due to the absence of CP pairs this method is not applicable to the MI based registration. To measure the residual misalignment, a single-image reconstruction of each registered image is computed. The residual misalignment is then estimated by computing the misalignment between the DEM using the iterative closest point (ICP) algorithm as proposed by Zhang (1994). According to the evaluation (cf. Section 5.5), the reconstruction accuracy is of the order 10 m due to integration bias. Hence, the z component of each surface is scaled by 0.1 before applying the ICP algorithm. The transformation consists of a 3D translation vector $\mathbf{t}_{\mathrm{ICP}} = [t_x, t_y, t_z]^{\mathrm{T}}$ and a Rodrigues vector $\mathbf{r}_{\mathrm{ICP}}$ denoting a 3D rotation. The Rodrigues vector points parallel to the axis of rotation and its norm represents the rotation angle. Table 6.1 and Table 6.2 show the partial norm of both $\|\mathbf{t}_{\mathrm{ICP}}\|_{\mathrm{part}} = \sqrt{t_x^2 + t_y^2}$ and and the norm of $\mathbf{r}_{\mathrm{ICP}}$. The images are planar and thus only in the translation along x and y direction is of interest, such that the translation norm is computed from the components t_x in x direction and t_y in y-direction only.

The region examined for evaluation is located east of the crater Lewis (longitude 253 °E–255 °E, latitude 19 °S–17 °S). Four images of the region are available. Hence, three floating images are transformed onto the reference image. The angle of rotation is of the order 10^{-4} rad and thus comparable to the round-off error. Furthermore, nearly all methods achieve a residual translation of sub-pixel accuracy if the transformation model is adequate. As previously assumed, the simple 2D rigid transformation fails to achieve sub-pixel accuracy for all MI estimators. The second-order polynomial as well as the pinhole camera model (3D rigid transformation) achieve sub-pixel accuracy for all images. A subsequent application of the pinhole camera model and a second-order polynomial transform does not yield a further increase of the registration accuracy. In contrast, the accuracy appears to decrease, which may be due to the high model complexity. The IsoContour MI estimation technique proposed by Rajwade et al. (2009) outperforms the simpler histogram-based method. Regarding the Parzen windowing technique, a few properties should be discussed. Although this method achieves results that are comparable to the two other methods, the randomness of the method reduces its reliability, and different outputs are obtained each time it is applied. On the other hand, the IsoContour method as well as the histogram-based approach are fully deterministic. The results in Table 6.1 and Table 6.2 are the best accuracies achieved during two runs of Parzen windowing for each floating image, respectively.

Table 6.1: Evaluation of the MI-based methods: 2D rigid and polynomial transformation. Based on single-image DEM constructed based on the registered images, the translation $\|\mathbf{t}_{\mathrm{ICP}}\|_{\mathrm{part}}$ in the image plane and the absolute rotation angle $\|\mathbf{r}_{\mathrm{ICP}}\|$ are estimated for different combinations of MI estimation methods and transformations.

		Rigid transform		**2nd order polynomial**	
Method	**FloatNo.**	$\|\mathbf{t}_{\mathrm{ICP}}\|_{\mathrm{part}}$	$\|\mathbf{r}_{\mathrm{ICP}}\|$	$\|\mathbf{t}_{\mathrm{ICP}}\|_{\mathrm{part}}$	$\|\mathbf{r}_{\mathrm{ICP}}\|$
Joint Histogram	1	1.66	3.29	0.47	3.42
	2	0.31	2.16	0.63	2.62
	3	0.88	7.31	0.26	3.38
Parzen Windowing	1	1.66	3.42	0.05	2.86
	2	0.56	1.80	0.18	3.11
	3	0.53	6.09	0.22	3.39
IsoContour	1	1.67	3.31	0.10	3.20
	2	0.57	1.78	0.17	3.11
	3	0.40	6.05	0.13	3.41

$\|\mathbf{t}\|_{\mathrm{part}}$: absolute translation in pixels; $\|\mathbf{r}\|$: absolute rotation in 10^{-4} rad.

Table 6.2: Evaluation of the MI-based methods: Pinhole camera based transformations. Based on single-image DEM constructed based on the registered images, the translation $\|\mathbf{t}_{\mathrm{ICP}}\|_{\mathrm{part}}$ in the image plane and the absolute rotation angle $\|\mathbf{r}_{\mathrm{ICP}}\|$ are estimated for different combinations of MI estimation methods and transformations.

		Pinhole camera model		**Pinhole camera model and subsequent 2nd order polynomial**	
Method	**FloatNo.**	$\|\mathbf{t}_{\mathrm{ICP}}\|_{\mathrm{part}}$	$\|\mathbf{r}_{\mathrm{ICP}}\|$	$\|\mathbf{t}_{\mathrm{ICP}}\|_{\mathrm{part}}$	$\|\mathbf{r}_{\mathrm{ICP}}\|$
Joint Histogram	1	0.15	2.01	0.33	3.64
	2	0.48	2.68	0.60	2.68
	3	0.23	3.30	0.05	3.42
Parzen Windowing	1	0.82	1.97	1.41	3.39
	2	0.60	2.87	0.14	3.12
	3	0.21	3.27	0.05	3.42
IsoContour	1	0.06	1.97	0.38	3.55
	2	0.47	2.72	0.43	2.74
	3	0.17	3.35	0.28	3.39

$\|\mathbf{t}_{\mathrm{ICP}}\|_{\mathrm{part}}$: absolute translation in pixels, $\|\mathbf{r}_{\mathrm{ICP}}\|$: absolute rotation in 10^{-4} rad.

6.4 Narrow-Angle Camera (NAC) derived DEM of highest resolution

The Narrow-Angle Camera (NAC) is a subsystem of the Lunar Reconnaissance Orbiter Camera. It provides photometric measurements of the lunar surface at a resolution of up to 0.5 m per pixel which is the highest resolution available. There are two different but parallel cameras, the left NAC and the right NAC, which cover a surface width of about 5 km per line in total. The distributed calibrated data records contain the so-called "intensity over flux" (IoF) which is the measured and calibrated intensity divided by the solar flux, i.e. the estimated reflectance of the surface. The NAC images are thus suitable for the photometric surface refinement methods given in Chapter 5. The IoF data is accompanied by the selenographic coordinates of the image centre and the image corners. Additionally, the sun position is known. The selenographic coordinate of each pixel is determined by bilinear interpolation and the vector pointing towards the sun is computed. According to the low emission angle of the selected image M145664820R[5], the emission angle is estimated by the nadir view, i.e. zero emission angle.

In order to initialise the surface refinement methods, the GLD100 is selected. Its nominal resolution, however, is only 100 m per pixel and the effective lateral resolution is about 1.5 km per pixel (Scholten et al., 2012). To bridge the gap in resolution, a pyramidal approach is applied by downscaling the image by a factor of two until the resolution is less than the resolution of the GLD100, i.e. the NAC image is downscaled $n_{\text{pyr}} = 8$ times by a factor of two which yields an image at a resolution of about 128 m per pixel. The resulting image is then input into the two-step surface reconstruction method consisting of a consecutive execution of the extended PHCL method (cf. Section 5.2.2) with $\delta = 0.001$ and the recovery of depth from a gradient field using an absolute depth constraint $\tau = 100$ (cf. Section 5.3.2). Additionally, the surface is retrieved by the further extended SfS method (cf. Section 5.3.4) with $\delta = 0.001$, $\gamma = 0.001$ and $\tau = 100\gamma$. Finally, the resulting DEM is upscaled by a factor of two and input to another surface refinement at a higher pyramid level $n_{\text{pyr}} \leftarrow n_{\text{pyr}} - 1$, i.e. refined by an image of increased resolution. The sequence is repeated until the full resolution of the NAC image is reached. Notably, the GLD100 is used only in the pyramid level of lowest lateral resolution. Afterwards, the refined DEM of the previous pyramid level is used as initial and restricting DEM which allows to keep the low-pass filters $\sigma_{\text{grad}} = 7$ pixels and $\sigma_{\text{absDepth}} = 7$ pixels constant while maintaining a pull towards the inherited low-frequency components. The low-pass width of the albedo computation algorithm was set to $\sigma_{\text{refl}} = 21$ pixels.

Both methods, the two-step extended PHCL and subsequent recovery of depth from the estimated gradient field and the further extended SfS produce very similar results. Consequently, only the result of the further extended SfS algorithm is presented here. A

[5]Available at http://wms.lroc.asu.edu/lroc/view_lroc/LRO-L-LROC-2-EDR-V1.0/M145664820RE

quantitative assessment of the reconstruction accuracy is not possible at a resolution this high since the footprints cover a 5 m diameter circular area (Smith et al., 2010). There exists, however, a stereo analysis based DEM (NAC_DTM_IMPACTMELT2_E010N2010[6]) of the area covered by the NAC image. The stereo analysis of the NAC images includes an orthorectification step, which corrects perspective distortions, and a mapping to the cylindrical coordinate system. Both steps were neglected during the photometric surface refinement. Due to the low emission angle, the perspective distortions are rather small and the image was acquired almost parallel to latitude axes of the cylindrical grid. Both effects are thus assumed to be negligible.

Fig. 6.11 shows the southern half of the NAC image M145664820R. The image shows the melt flow at the floor of the lunar crater Korolev X (159.0 °W, 0.6 °N). Detailed close-ups of two regions of interest (ROI) on the melt flow illustrating the high resolution of the NAC images are shown in Fig. 6.11(b) and Fig. 6.11(c). At print resolution, the full image does not display the fractures, which are clearly visible in the close-up images, within the total image. Consequently, the DEM do not show any significant difference if the whole region is regarded and the discussion is restricted to both ROI.

Fig. 6.12 shows the high resolution DEM of the northern ROI (cf. Fig. 6.11(b)). To differentiate between large-scale inaccuracies and small-scale inaccuracies, the local median of each DEM was subtracted. The result of the further extended SfS algorithm (cf. Fig. 6.12(a)) captures the high frequent details visible in Fig. 6.11(b). In contrast, the stereo DEM (cf. Fig. 6.12(b)) appears rather blurred and shows only larger details. There is, however, a difference of a few meters between both DEM at the northern boundary. This small difference is below the vertical resolution of the GLD100, which has a standard deviation of about 20 m (Scholten et al., 2012). This also holds for the absolute difference between the local median values, which amounts to 25.1 m. Thus it is not clear whether the differences are due to the initialisation or whether it was caused by the surface recovery.

The different lateral resolution is even more pronounced within the southern ROI (cf. Fig. 6.11(c)). While the large crater near the centre of the area is visible in both DEM, the fractures in the solidified melt surrounding the crater vaguely appear in the stereo based DEM (cf. Fig. 6.13(b)). Furthermore, the stereo analysis tends to broaden the narrow fractures. This may be caused by the low-pass inherent to the point matching in stereo analysis. All fractures and small-scale features are clearly visible in the result of the extended SfS (cf. Fig. 6.13(a)). The absolute difference between the local median values amounts to 18.4 m and is thus comparable to the northern ROI.

[6]Available at http://lroc.sese.asu.edu/data/LRO-L-LROC-5-RDR-V1.0/LROLRC_2001/DATA/SDP/NAC_DTM/IMPACTMELT2/NAC_DTM_IMPACTMELT2_E010N2010.IMG

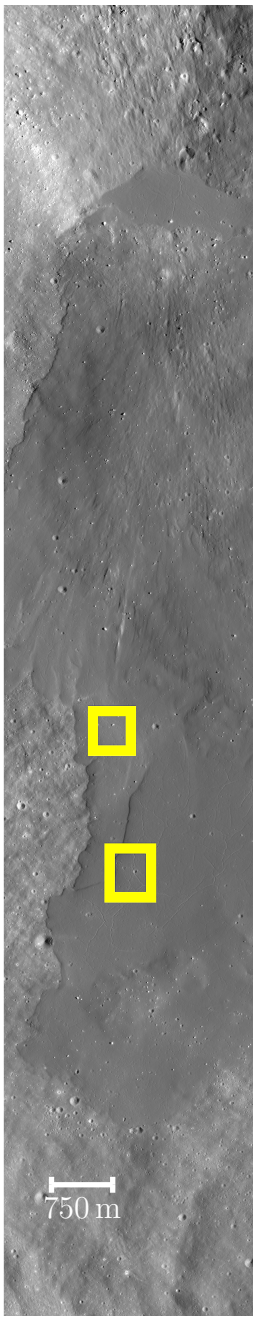

(a) NAC Image

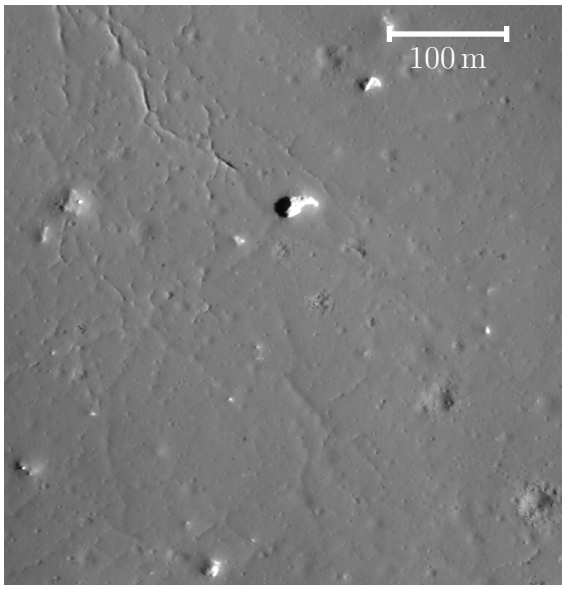

(b) Northern ROI (ROI 1)

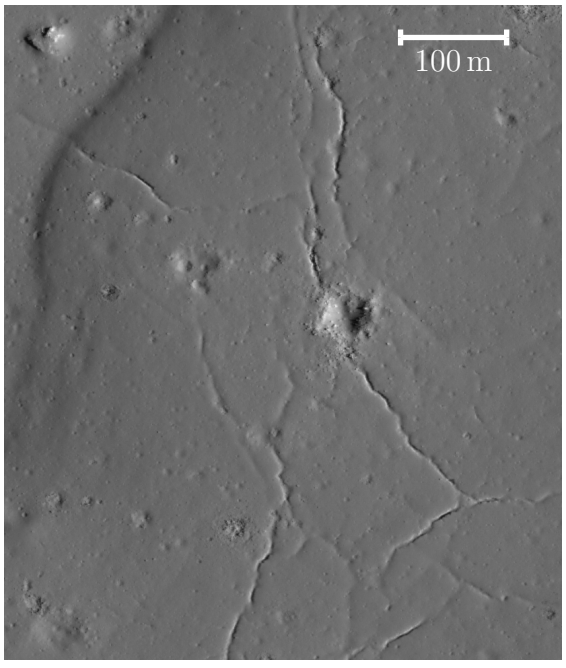

(c) Southern ROI (ROI 2)

Figure 6.11: Surface recovery from NAC image M145664820R: Image overview. (a) The southern half of the NAC image M145664820R. The regions of interest (ROI) are marked by the yellow rectangles. (b)–(c) Close-up images of northern ROI 1 and southern ROI 2, respectively.

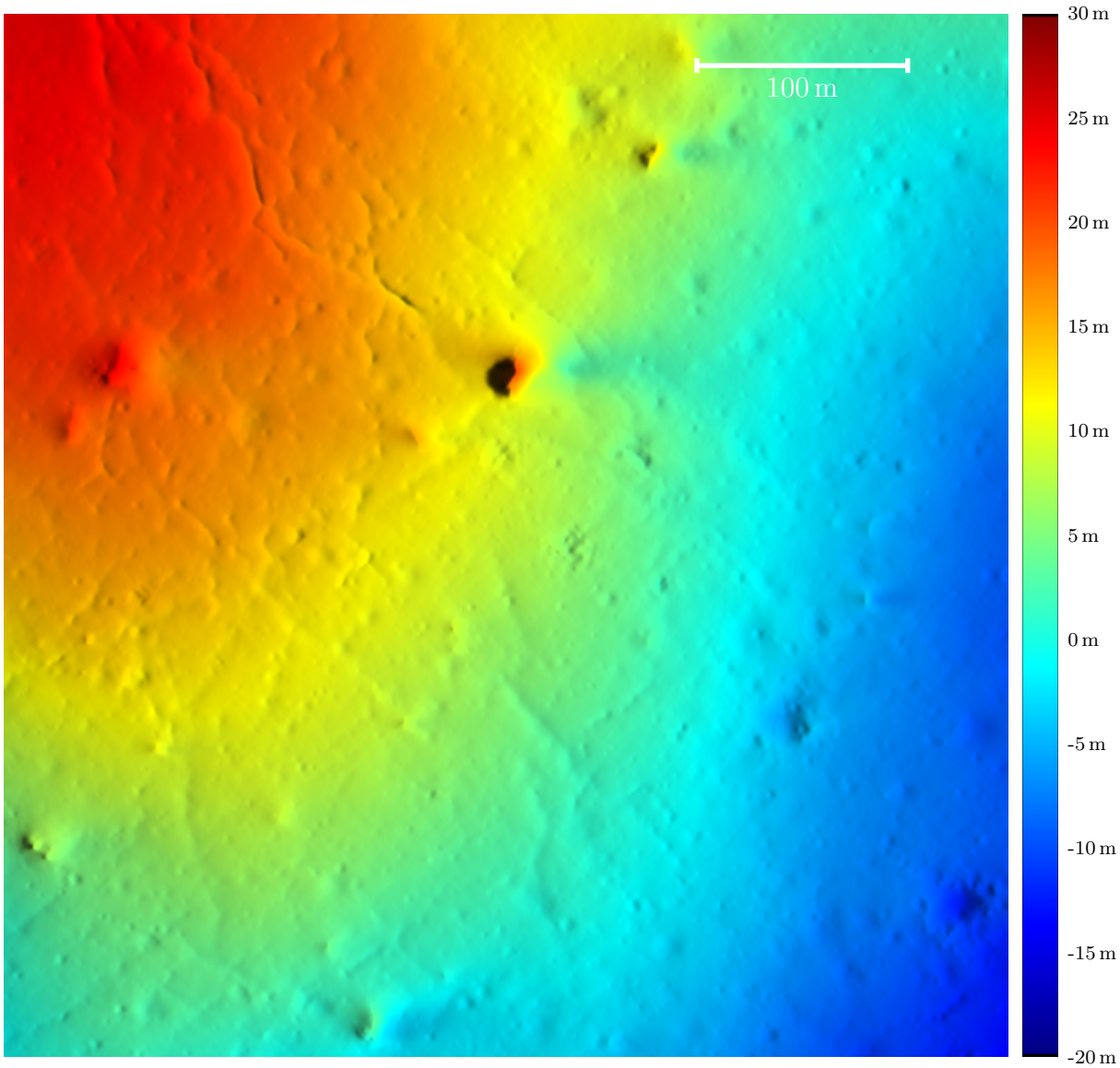

(a) Further extended SfS

Figure 6.12: Surface recovery from NAC image M145664820R: ROI 1. (a) The result of the further extended SfS method. (b) The stereo DEM. The nominal resolution of the stereo DEM is two meter per pixel.

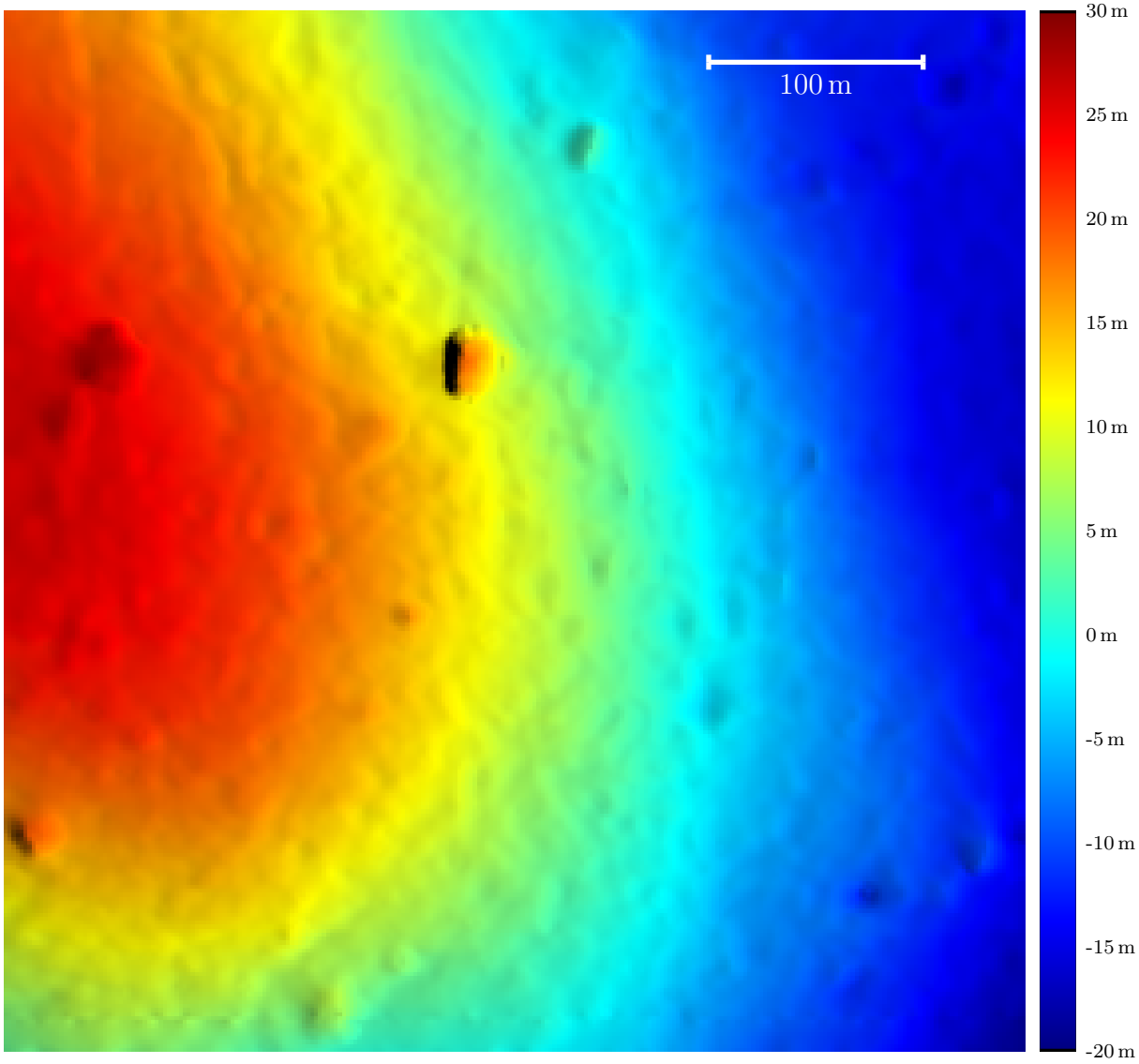

(b) Stereo DEM

Figure 6.12: (continued)

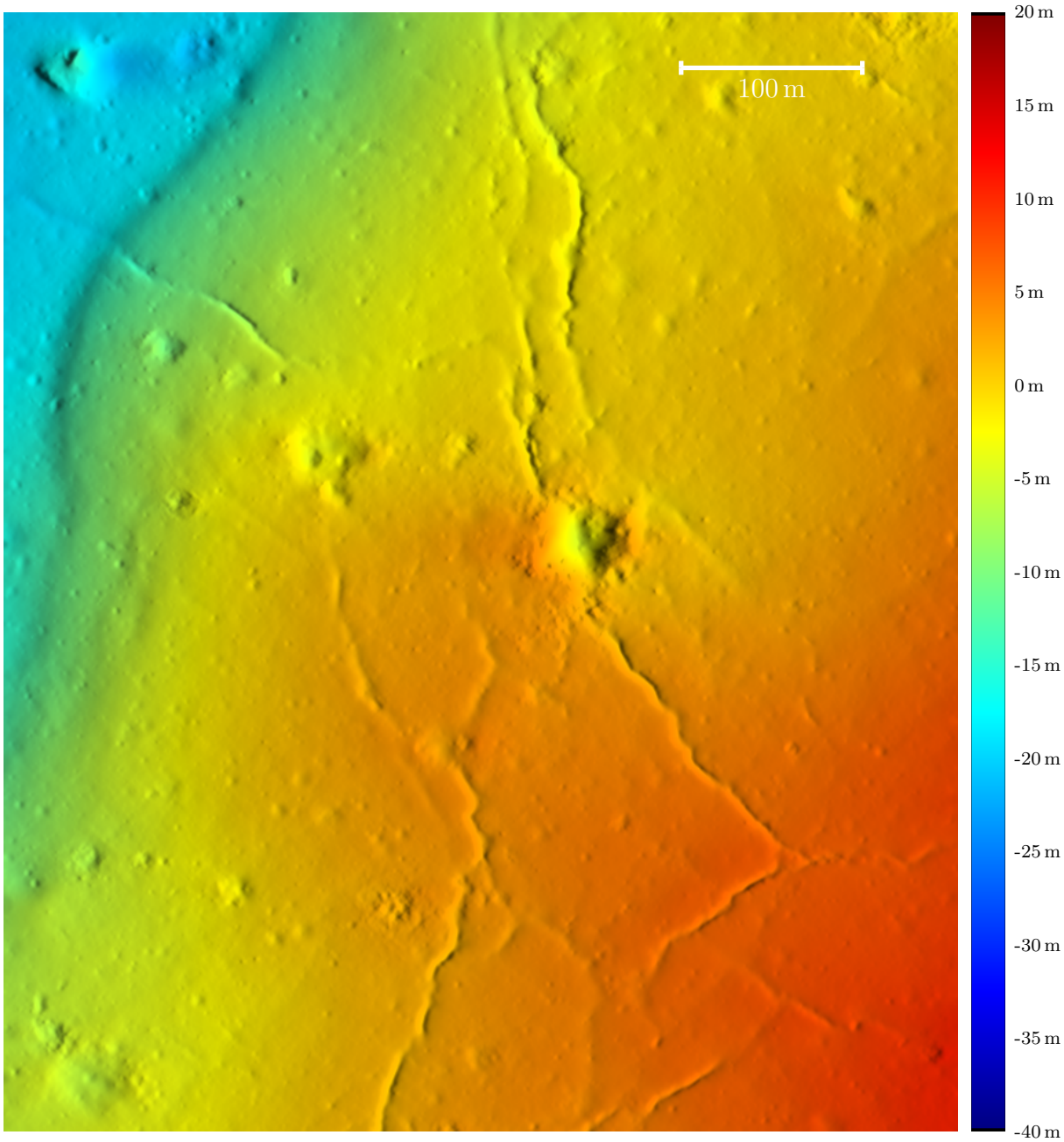

(a) Further extended SfS

Figure 6.13: Surface recovery from NAC image M145664820R: ROI 2. (a) The result of the further extended SfS method. (b) The stereo DEM. The nominal resolution of the stereo DEM is two meter per pixel.

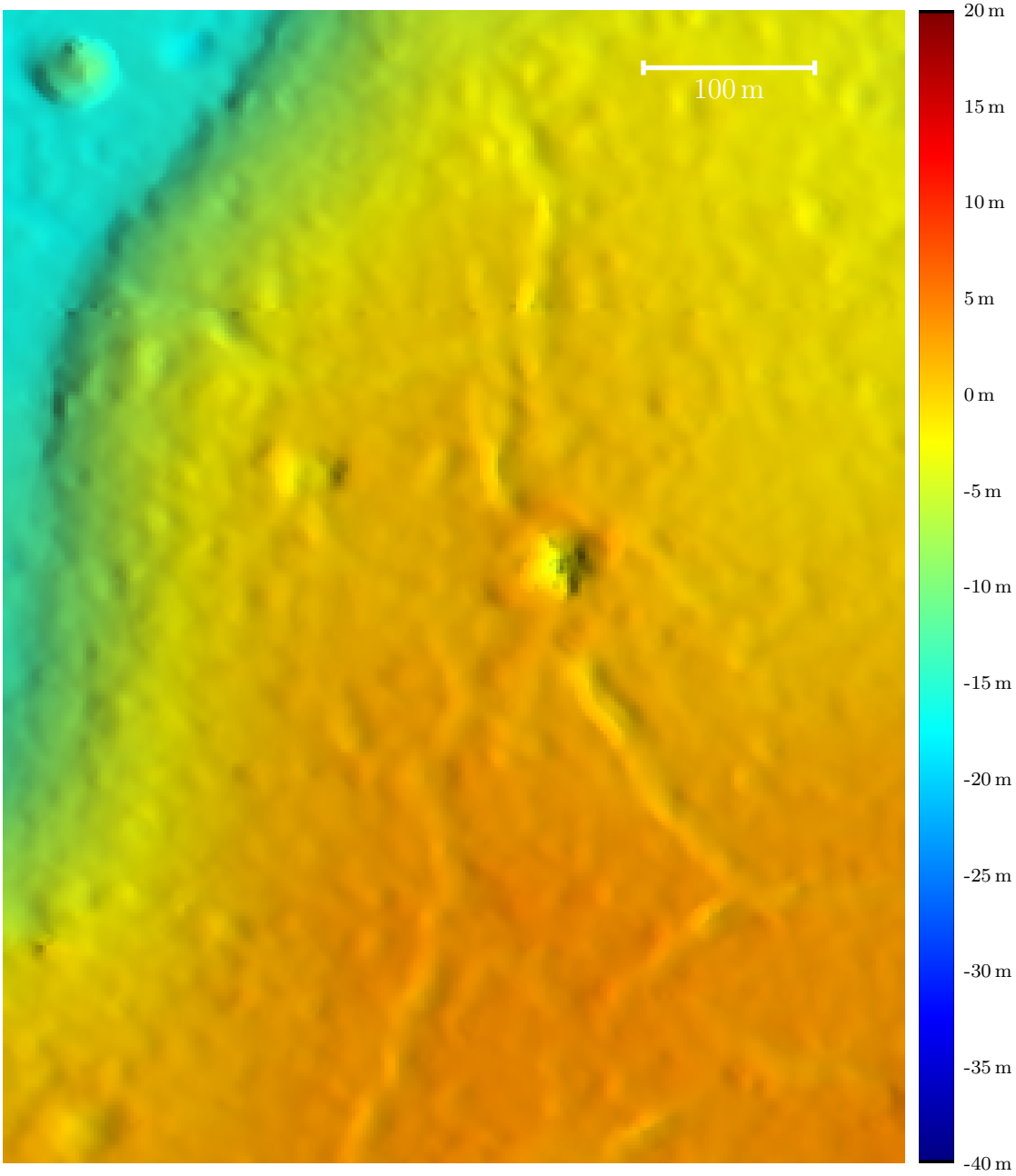

(b) Stereo DEM

Figure 6.13: (continued)

7

Outlook

The physically based photometric models require the estimation of multiple parameters. Shkuratov et al. (2005b), however, have shown by ray-tracing simulations that the change in one parameter may be compensated by a variation of a different parameter if the range of available incidence and emission angles is small, e.g. the effect of the unresolved surface roughness may be compensated by an albedo variation for small phase angle ranges (Shkuratov et al., 2005b). Typically, cameras installed at orbiters are set to be in nadir view, i.e. a zero degree emission angle, and thus the range of phase angles is limited. This leaves two important questions unanswered: Which parameters may be estimated reliably, and which observation geometry is required to estimate the important parameters? In particular, the single-scattering albedo is extremely important because it directly influences the normalised reflectance while the phase function may be assumed constant within a small range of phase angles (Bertsatos and Makris, 2010) and it carries direct information about the surface composition, as a mixture of different minerals leads to a mixture of different single-scattering albedos (Mustard and Pieters, 1989; Mustard et al., 1998). Global parameter estimates may suffer from the so-called selection problem (Hillier et al., 1999), i.e. larger phase angles commonly appear at higher degrees of selenographic latitude which might combine surface points of completely different mineralogical composition.

Using ray-tracing experiments, i.e. an ideal model, measurements of arbitrary incidence angles and emission angles covering the whole range of phase angles, i.e. zero to 180 degrees, may be simulated. Simulating sensor noise, the Monte Carlo method allows the computation of confidence bands for the estimated parameters. It is thus possible to determine the reliability of the estimated parameters for different sets of observation angles. This, however, produces results for an idealised world. In order to verify these results, measurements of well defined lunar analogue minerals, e.g. ilmenite, different pyroxenes, olivine and plagioclase feldspar of known composition and grain size, covering the whole range of phase angles need to be evaluated. The experiments will provide detailed insights about the required sets of observation angles to estimate all parameters

of the reflectance model. Furthermore, they may be used to derive constraints and/or assumptions that allow for the reliable determination of a partial set of parameters and the corresponding error propagation with respect to the estimated parameters. In addition, the effect of different phase functions and its influence on the normalised reflectance may be examined in detail based on these experiments and the physical interpretation of the parameters may be verified. Furthermore, different physically based reflectance models, e.g. the models by Hapke (2002) and Shkuratov et al. (1999a), may be evaluated and compared to pure empiric models with respect to the accuracy of the normalised reflectance.

The results of the previously mentioned experiments may be combined with the methods presented in this thesis to derive high resolution maps of normalised reflectance values and parameters of the reflectance models. Applying the photometric surface refinement methods additionally provides a near-global digital elevation model at image resolution. Since the photometric methods may be computed based on wavelengths below 2000 nm, the refinement topographic model is not influenced by the surface temperature and thus enables the accurate determination of incidence angles at image resolution and thus simulation based estimations of the surface temperature, e.g. using the thermal equilibrium assumption (Shkuratov et al., 2011), providing more reliable temperature estimates than the purely data driven approach presented in this thesis.

8

Summary and conclusion

Following the goal of a combined recovery of topographic and reflectance data from hyperspectral imagery, this thesis presented methods that allow for the complete normalisation of previously calibrated, i.e. converted to radiance, hyperspectral data, here the M^3 data. The proposed normalisation procedure covers the estimation of the surface temperature from the spectral data, the estimation of the parameters of the reflectance model and the normalisation to a reference geometry. Additionally, a method to correct the spectral data for residual effects was introduced. Since it is known that the M^3 sensor calibration was imperfect due to changing sensor temperatures, it is not clear whether these residual effects were caused by the sensor temperature or not. The correction may thus not be applicable in the general case.

The normalisation procedure computes spatially varying maps of reflectance parameters using the available information from one or more co-registered images. The mapping thus avoids the selection problem of Hillier et al. (1999). There are, however, parameters which are interchangeable with each other (Shkuratov et al., 2005b) and thus the quality of the map highly depends on the available spectral information. This influence requires further assessment. Experiments with synthetic data show that the presented algorithms are capable of estimating the albedo with in accuracy of about one percent of its mean value.

The estimation of the thermal emission component produces reasonable results for temperatures above 300 K that are comparable to the reference method by Clark et al. (2011). The method, however, does not suffer from the 2000 nm pyroxene absorption that influences the extrapolated reflectance by Clark et al. (2011). The empirical compensation for the observed residual phase angle based effects produces more homogeneous continuum-removed spectra and less variation in the spectral parameters, i.e. depth, position and width of the spectral absorption features, and thus significantly improves the quality of the normalised data.

The presented normalisation procedure requires the precise knowledge of the local

topography, which is successfully recovered from the spectral images by the presented surface refinement methods. The surface refinement methods require knowledge of the surface's reflectance behaviour. The computation of the reflectance parameters, however, is part of the normalisation procedure. Consequently, an integrated recovery of a DEM at image resolution and computation of reflectance parameters maps is achieved by alternating between the estimation of the reflectance parameters with respect to the spatial resolution of the DEM and refinement of the DEM.

Using both, a relative depth restriction for the photometric surface gradient estimation step and an absolute depth for the recovery of the DEM from the estimated gradient field, robust methods were presented that use an a-priori known DEM of lower lateral resolution and high resolution images to compute a refined DEM of higher lateral resolution.

If only the relative depth restriction is applied then the two-step method consisting of a subsequent application of the extended PHCL method and a recovery of the DEM from the estimated gradient field showed to be complementary to the extended SfS algorithm, and, consequently, the accuracy increased if the result of the two-step method was used as an initialisation to the extended SfS method. The absolute accuracy slightly increased, in comparison to the GLD100 DEM, while the lateral resolution was greatly increased. The method, however, produces unreasonable results if the high resolution images are subject to an imperfect calibration. Although the absolute depth restriction exhibited a higher vertical accuracy, the computational complexity of the relative depth restriction is much lower than the computational complexity of an added absolute depth restriction.

Using both the relative depth restriction and the absolute depth restriction, the vertical accuracy of the resulting DEM was nearly identical to the vertical accuracy of the initial DEM while the lateral resolution, again, was increased to image resolution. These methods obtained better results for imperfectly calibrated high resolution images. A two-step surface refinement did not show any complementary properties to the further extended SfS method. In contrast, the further extended SfS method provided better results, i.e.so visible artefacts due to imperfect image calibrations, in the examined region.

The normalisation and surface refinement methods were applied to a variety of scenarios. The normalisation method was applied to derive a near-global normalised reflectance map of the lunar surface and a computation of elemental abundance maps from the normalised reflectance. Furthermore, an illumination independent image registration method based on the photometric DEM refinement method was developed and evaluated. In all examined cases, sub-pixel accuracy could be achieved. Finally, the photometric surface refinement including both the relative depth and the absolute depth restrictions was applied to very high resolution images, thus increasing the lateral resolution of the initial DEM by a factor of 200. A pyramidal approach using the DEM of the next lower resolution level as restriction was used to derive a high resolution DEM that does not show any low-frequent drift.

Overall, the presented methods provide the required tools to compute both, the reflectance behaviour of the object and its DEM from the hyperspectral imagery. The

estimation of the reflectance behaviour, however, was restricted to a few parameters of the reflectance model due to the interchangeability of the parameters. Defining optimal measurement scenarios to compute all parameters or computing the uniqueness of the found solution is still an open question. The presented surface refinement methods, however, produced good results on real data and thus proved to be robust against these uncertainties.

Bibliography

J. B. Adams. Visible and near-infrared diffuse reflectance spectra of pyroxenes as applied to remote sensing of solid objects in the solar system. *Journal of Geophysical Research*, 79(32):4829–4836, 1974. ISSN 2156–2202. doi: 10.1029/JB079i032p04829.

J. B. Adams and L. H. Goullaud. Plagioclase feldspars: Visible and near infrared diffuse reflectance spectra as applied to remote sensing. *Proc. Lunar and Planetary Science Conference IX*, pages 1–2, 1978.

J. B. Adams and T. B. McCord. Optical properties of minerals separates, glass and anorthositic fragments from Apollo mare samples. In *Lunar and Planetary Science Conference Proceedings*, volume 2 of *Lunar and Planetary Science Conference Proceedings*, pages 2183–2195, 1971.

A. Agrawal, R. Raskar, and R. Chellapa. What is the Range of Surface Reconstructions from a Gradient Field? *European Conference on Computer Vision (ECCV)*, 2006.

P. Ajith Kumar and S. Kumar. Estimation of optical maturity parameter for lunar soil characterization using Moon Mineralogy Mapper (M3). *Advances in Space Research*, page In Press, 2014. doi: 10.1016/j.asr.2014.01.009.

H. Akima. A new method of interpolation and smooth curve fitting based on local procedures. *Journal of the Association for Computing Machinery*, 17(4):589–602, 1970.

L. A. Akimov. Light reflection by the moon. *Kinematika i Fizika Nebesnykh Tel*, 4:3–10, 1988. in Russian language.

L. A. Akimov, Y. I. Velikodskiy, and V. V. Korokhin. Dependence of latitude brightness distribution over the lunar disk on albedo and relief. *Kinematika i Fizika Nebesnykh Tel*, 16:181–187, 2000. in Russian language.

J. Albertz, M. Attwenger, J. Barrett, S. Casley, P. Dorninger, E. Dorrer, H. Ebner, S. Gehrke, B. Giese, K. Gwinner, C. Heipke, E. Howington-Kraus, R. L. Kirk, H. Lehmann, H. Mayer, J.-P. Muller, J. Oberst, A. Ostrovskiy, J. Renter, S. Reznik, R. Schmidt, F. Scholten, M. Spiegel, M. Wählisch, G. Neukum, and the HRSC CoI Team. HRSC on Mars Express - Photogrammetric and Cartographic Research. *Photogrammetric Engineering and Remote Sensing*, 71(10):1153–1160, 2005.

M. S. Andresen, B. S. Dissing, and H. Løje. Quality assessment of butter cookies applying multispectral imaging. *Food Science & Nutrition*, 1(4):315–323, 2013. doi: 10.1002/fsn3.46.

H. Araki, S. Tazawa, H. Noda, Y. Ishihara, S. Goossens, S. Sasaki, N. Kawano, I. Kamiya, H. Otake, J. Oberst, and C. Shum. Lunar Global Shape and Polar Topography Derived from Kaguya-LALT Laser Altimetry. *Science*, 323(5916):897–900, 2009. doi: 10.1126/science.1164146.

J. T. Barron and J. Malik. High-frequency shape and albedo from shading using natural image statistics. In *The 24th IEEE Conference on Computer Vision and Pattern Recognition, CVPR 2011, 20-25 June 2011*, pages 2521–2528, Colorado Springs, CO, USA, 2011. IEEE. doi: http://dx.doi.org/10.1109/CVPR.2011.5995392.

J. T. Barron and J. Malik. Shape, Albedo, and Illumination from a Single Image of an Unknown Object. In *The 25th IEEE Conference on Computer Vision and Pattern Recognition, CVPR 2012, 16-21 June 2012*, pages 2521–2528, Providence, RI, USA, 2012. IEEE. doi: http://dx.doi.org/10.1109/CVPR.2011.5995392.

A. A. Berezhnoy, N. Hasebe, M. Kobayashi, G. G. Michael, O. Okudaira, and N. Yamashita. A three end-member model for petrologic analysis of lunar prospector gamma-ray spectrometer data. *Planetary and Space Science*, 53:1097–1108, 2005.

A. A. Berezhnoy, E. A. Kozlova, M. P. Sinitsyn, A. A. Shangaraev, and V. V. Shevchenko. Origin and stability of lunar polar volatiles. *Advances in Space Research*, 50:1638–1646, 2012.

I. Bertsatos and C. Makris. Statistical biases and errors inherent in photoclinometric surface slope estimation with natural light. *Icarus*, 208:798–810, 2010.

S. Besse, J. Sunshine, M. Staid, J. Boardman, C. Pieters, P. Guasqui, E. Malaret, S. McLaughlin, Y. Yokota, and J.-Y. Li. A visible and near-infrared photometric correction for Moon Mineralogy Mapper M^3. *Icarus*, 222:229–242, 2013a.

S. Besse, Y. Yokota, J. Boardman, R. Green, J. Haruyama, P. Isaacson, U. Mall, T. Matsunaga, M. Ohtake, C. Pieters, M. Staid, J. Sunshine, and S. Yamamoto. One Moon, many measurements 2: Photometric corrections. *Icarus*, 226:127–139, 2013b.

J. W. Boardman, C. M. Pieters, R. O. Green, S. R. Lundeen, P. Varanasi, J. Nettles, N. Petro, P. Isaacson, S. Besse, and L. A. Taylor. Measuring moonlight: An overview of the spatial properties, lunar coverage, selenolocation, and related level 1B products of the Moon Mineralogy Mapper. *Journal of Geophysical Research*, 116:E00G14, 2011. doi: 10.1029/2010JE003730.

R. G. Burns. Spectral mineralogy of terrestrial planets: scanning their surfaces remotely. *Mineralogical Magazine*, 53:135–151, 1989.

R. G. Burns. *Mineralogical Applications of Crystal Field Theory.* Cambridge University Press, 2 edition, 1993. ISBN 0–521–43077–1.

R. G. Burns, R. M. Abu-Eid, and F. E. Huggins. Crystal field spectra of lunar pyroxenes. *Proc. Lunar Science Conference*, 2:533–543, 1972.

D. B. J. Bussey and P. D. Spudis. Compositional analysis of the Orientale basin using full resolution Clementine data: Some preliminary results. *Geophysical Research Letters*, 24(4):445–448, 1997.

S. Chandrasekhar. *Radiative Transfer.* Dover Publications, Inc., New York, 1960. ISBN 0-486-60590-6.

M. P. Charette, T. B. McCord, C. Pieters, and J. B. Adams. Application of remote spectral reflectance measurements to lunar geology classification and determination of titanium content of lunar soils. *Journal of Geophysical Research*, 79(11):1605–1613, 1974. ISSN 2156–2202. doi: 10.1029/JB079i011p01605.

L. C. Cheek, C. M. Pieters, M. D. Dyar, and K. A. Milam. Revisiting plagioclase optical properties for lunar exploration. *Proc. Lunar and Planetary Science Conference XXXX*, page #1928, 2009.

R. Clark, C. M. Pieters, R. O. Green, J. Boardman, B. J. Buratti, J. W. Head, P. J. Isaacson, K. E. Livo, T. B. McCord, J. W. Nettles, N. E. Petro, J. M. Sunshine, and L. A. Taylor. Water and Hydroxyl on the Moon as Seen by the Moon Mineralogy Mapper (M3). *Lunar and Planetary Science Conference XXXXI*, page #1533, 2010.

R. N. Clark, C. M. Pieters, R. O. Green, J. W. Boardman, and N. E. Petro. Thermal removal from near-infrared imaging spectroscopy data of the moon. *Journal of Geophysical Research*, 116:E00G16, 2011. doi: 10.1029/2010JE003751.

E. A. Cloutis and M. J. Gaffey. Lunar Regolith Analogues: Spectral Reflectance Properties of Compositional Variations. *Icarus*, 102(2):203–224, 1993. ISSN 0019–1035. doi: 10.1006/icar.1993.1044.

E. A. Cloutis, J. M. Sunshine, and R. V. Morris. Spectral reflectance compositional properties of spinels and chromites: Implications for planetary remote sensing and geothermometry. *Meteoritics and Planetary Science*, 39(4):545–565, 2004.

W. M. Cornette and J. G. Shanks. Physically reasonable analytic expression for the single-scattering phase function. *Applied Optics*, 31:3152–3160, 1992. doi: 10.1364/AO.31.003152.

R. Danzl and S. Scherer. Integrating Shape form Shading and Shape from Stereo for Variable Reflectance Surface Reconstruction from SEM images. In *Proceedings of 26th Workshop of the Austrian Association for Pattern Recognition (OAGM/AAPR)*, pages 281–288, 2002.

P. A. Davis and L. A. Soderblom. Modeling crater topography and Albedo from monoscopic viking orbiter images 1. Methodology. *Journal of Geophysical Research*, 89(B11): 9449–9457, 1984.

S. Dawn, V. Saxena, and B. Sharma. Remote Sensing Image Registration Techniques: A Survey. In A. Elmoataz, O. Lezoray, F. Nouboud, D. Mammass, and J. Meunier, editors, *Image and Signal Processing*, volume 6134 of *Lecture Notes in Computer Science*, pages 103–112. Springer Berlin Heidelberg, 2010. ISBN 978-3-642-13680-1. doi: 10.1007/978-3-642-13681-8-13.

A. Dollfus. Lunar Surface Imaging Polarimetry: I. Roughness and Grain Size. *Icarus*, 136:69–103, 1998.

E. Dorrer, H. Mayer, A. Ostrovskiy, S. Reznik, and G. Neukum. De- and Re-shading of Mars Express HRSC Image Data for Homogenization of Map Relief Shading. *ISPRS Archives*, XXXV(B4):1299–1303, 2004.

N. D. Efford. Sources of Error in the Photoclinometric Determination of Planetary Topography: a Reappraisal. *Earth, Moon, and Planets*, 54:19–58, 1991.

E. Eliason, C. Isbell, E. Lee, T. Becker, L. Gaddis, A. McEwen, and M. Robinson. Mission to Moon: the Clementine UVVIS gobal mosaic. PDS Volumes USA_NASA_PDS_CL4001 – USA_NASA_PDS_CL4078, U.S. Geological Survey, 1999.

E. M. Eliason, A. S. McEwen, M. Robinson, P. G. Lucey, T. Duxbury, E. Malaret, C. Pieters, T. Becker, C. Isbell, and E. Lee. Multispectral Mapping of the Moon by Clementine. In B. L. Jolliff and G. Ryder, editors, *New Views of the Moon: Integrated Remotely Sensed, Geophysical, and Sample Datasets*, page 26, January 1998.

R. C. Elphic, D. J. Lawrence, W. C. Feldman, B. L. Barraclough, S. Maurice, A. B. Binder, and P. G. Lucey. Lunar Fe and Ti Abundances: Comparison of Lunar Prospector and Clementine Data. *Science*, 281:1493–1496, 1998. doi: 10.1126/science.281.5382.1493.

T. G. Farr, B. A. Bates, R. L. Ralph, and J. B. Adams. Effects of overlapping optical absorption bands of pyroxene and glass on the reflectance spectra of lunar soils. In S. A. Bedini, editor, *Lunar and Planetary Science Conference Proceedings*, volume 11 of *Lunar and Planetary Science Conference Proceedings*, pages 719–729, 1980.

H. Fassold, R. Danzl, K. Schindler, and H. Bischof. Reconstruction of Archaeological Finds Using Shape from Stereo and Shape from Shading. In *9th Computer Vision Winter Workshop (CVWW), February, Piran*, pages 21–30, 2004.

Q. Feng, X. Jinzhong, K. Jincheng, Y. Lianjie, K. Lingde, W. Guanghua, L. Xiongjun, Y. Lili, L. Cong, and J. Rongbin. Dark conductivity and photoconductivity of amorphous $Hg_{0.78}Cd_{0.22}Te$ thin films. *Journal of Semiconductors*, 32(3):033004–1 – 033005–5, 2011.

E. M. Fischer and C. M. Pieters. Lunar surface aluminum and iron concentration from Galileo solid state imaging data, and the mixing of mare and highland materials. *Journal of Geophysical Research*, 100(E11):23279–23290, 1995.

R. T. Frankot and R. Chellappa. A method for enforcing integrability in shape from shading algorithms. *IEEE Transactions on Pattern Analysis and Machine Intelligence*, 10:439–451, 1988.

R. T. Frankot and R. Chellappa. Estimation of surface topography from SAR imagery using shape from shading techniques. *Artificial Intelligence*, 43(2):271–310, 1990.

Z. Fu, A. Robles-Kelly, T. Caelli, and R. Tan. On Automatic Absorption Detection for Imaging Spectroscopy: A Comparative Study. *IEEE Transactions on Geoscience and Remote Sensing*, 45(11):3827–3844, 2007.

R. W. Gaskell, O. S. Barnouin-Jha, D. J. Scheeres, A. S. Konopliv, T. Mukai, S. Abe, J. Saito, M. Ishiguro, T. Kubota, T. Hashimoto, J. Kawaguchi, M. Yoshikawa, K. Shirakawa, T. Kominato, N. Hirata, and H. Demura. Characterizing and navigating small bodies with imaging data. *Meteoritics and Planetary Science*, 43:1049–1061, 2008. doi: 10.1111/j.1945-5100.2008.tb00692.x.

S. Gehrke. Geometric and Radiometric modeling of the Martian Surface based on Object Space Matching and Photoclinometry. *ISPRS Archives*, XXXVI(B4), 2006.

P. E. Gill, W. Murray, and M. H. Wright. *Practical optimization*. Academic Press, 1981. ISBN 978-0-12-283952-8.

T. D. Glotch, J. J. Hagerty, P. G. Lucey, B. R. Hawke, T. A. Giguere, J. A. Arnold, J.-P. Williams, B. L. Jolliff, and D. A. Paige. The Mairan domes: Silicic volcanic constructs on the Moon. *Geophysical Research Letters*, 38(21):DOI: 10.1029/2011GL049548, 2011. ISSN 1944–8007.

R. O. Green, C. Pieters, P. Mouroulis, M. Eastwood, J. Boardman, T. Glavich, P. Isaacson, M. Annadurai, S. Besse, D. Barr, B. Buratti, D. Cate, A. Chatterjee, R. Clark, L. Cheek, J. Combe, D. Dhingra, V. Essandoh, S. Geier, J. N. Goswami, R. Green, V. Haemmerle, J. Head, L. Hovland, S. Hyman, R. Klima, T. Koch, G. Kramer, A. S. K. Kumar, K. Lee, S. Lundeen, E. Malaret, T. McCord, S. McLaughlin, J. Mustard, J. Nettles, N. Petro, K. Plourde, C. Racho, J. Rodriquez, C. Runyon, G. Sellar, C. Smith, H. Sobel, M. Staid, J. Sunshine, L. Taylor, K. Thaisen, S. Tompkins, H. Tseng, G. Vane, P. Varanasi, M. White, and D. Wilson. The Moon Mineralogy Mapper (M^3) imaging spectrometer for lunar science: Instrument description, calibration, on-orbit measurements, science data calibration and on-orbit validation. *Journal of Geophysical Research*, 116:E00G19, 2011. doi: 10.1029/2011JE003797.

B. T. Greenhagen and D. A. Paige. Mapping lunar surface petrology using mid-infrared emissivity maximum with the LRO diviner radiometer. In *Lunar and Planetary Institute Science Conference Abstracts*, volume 37 of *Lunar and Planetary Inst. Technical Report*, page #2406, 2006.

A. Grumpe and C. Wöhler. DEM construction and calibration of hyperspectral image data using pairs of radiance images. In *7th International Symposium on Image and Signal Processing and Analysis (ISPA)*, pages 609–614. IEEE, 2011a.

A. Grumpe and C. Wöhler. A Photometric Approach to the Construction of Lunar Digital Elevation Maps Using Chandrayaan-1 M3 Imagery in Combination with Laser Altimetry Data. In *Lunar and Planetary Science Conference*, volume 42 of *Lunar and Planetary Inst. Technical Report*, page #1478, 2011b.

A. Grumpe and C. Wöhler. Image-Based Construction of Lunar Digital Elevation Models of very High Lateral Resolution. In *Lunar and Planetary Science Conference*, volume 43 of *Lunar and Planetary Inst. Technical Report*, page #2597, 2012.

A. Grumpe and C. Wöhler. Recovery of elevation from estimated gradient fields constrained by digital elevation maps of lower lateral resolution. *ISPRS Journal of Photogrammetry and Remote Sensing*, 94:37–54, 2014. doi: 10.1016/j.isprsjprs.2014.04.011.

A. Grumpe, F. Brinkmeier, and C. Wöhler. Analysis of Topographic Effects Observed in Spectral Features Extracted from Chandrayaan-1 M3 Imagery. In *Lunar and Planetary Science Conference*, volume 42 of *Lunar and Planetary Inst. Technical Report*, page #1484, 2011a.

A. Grumpe, S. Herbort, and C. Wöhler. 3D Reconstruction of Non-Lambertian Surfaces with Non-Uniform Reflectance Parameters by Fusion of Photometrically Estimated Surface Normal Data with Active Range Scanner Data. In T. Luhman and C. Müller, editors, *Photogrammetrie - Laserscanning - Optische 3D-Messtechnik. Beiträge der Oldenburger 3D-Tage*, pages 54–61. Wichmann, 2011b.

A. Grumpe, F. Belkhir, V. Zirin, and C. Wöhler. Normalisation of hyperspectral data with respect to illumination and local topography. *Geophysical Research Abstracts*, 14: EGU2012–11034, 2012a.

A. Grumpe, C. Wöhler, and A. Berezhnoy. Full Topographic Correction of M3 Data for Lunar Elemental Abundance Estimation. In *Proc. 3th Moscow Solar System Symposium*, volume 3, Moscow, Russia, 2012b.

A. Grumpe, V. Zirin, F. Belkhir, and C. Wöhler. Normalisation of Continuum-removed Lunar Spectra. In *Proc. 1st European Lunar Symposium*, Berlin, Germany, 2012c.

A. Grumpe, M. P. Felder, C. Wöhler, and U. Mall. SIR-2 data normalization and integration with M^3 data. In *European Planetary Science Congress abstracts*, volume 8, pages EPSC2013–683, 2013.

A. Grumpe, F. Belkhir, and C. Wöhler. Construction of lunar DEMs based on reflectance modelling. *Advances in Space Research*, 53(12):1735–1767, 2014a. doi: 10.1016/j.asr.2013.09.036.

A. Grumpe, V. Zirin, and C. Wöhler. Phase Angle Based Correction of the Moon Mineralogy Mapper Radiance Measurements. In *Lunar and Planetary Science Conference*, volume 45 of *Lunar and Planetary Inst. Technical Report*, page #2562, 2014b.

B. Hapke. Bidirectional reflectance spectroscopy. 1. Theory. *Journal of Geophysical Research*, 86(B4):3039–3054, 1981. doi: 10.1029/JB086iB04p03039.

B. Hapke. Bidirectional reflectance spectroscopy: 3. Correction for macroscopic roughness. *Icarus*, 59(1):41–59, 1984. doi: 10.1016/0019-1035(84)90054-X.

B. Hapke. Bidirectional reflectance spectroscopy: 4. The extinction coefficient and the opposition effect. *Icarus*, 67(2):264–280, 1986. doi: 10.1016/0019-1035(86)90108-9.

B. Hapke. *Theory of reflectance and emittance spectroscopy*. Cambridge University Press, 1993.

B. Hapke. Bidirectional reflectance spectroscopy: 5. The Coherent Backscatter Opposition Effect and Anisotropic Scattering. *Icarus*, 157(2):523–534, 2002. doi: 10.1006/icar.2002.6853.

T. M. Hare, B. A. Archinal, T. L. Becker, L. R. Gaddis, E. M. Lee, B. L. Redding, and M. R. Rosiek. Clementine Mosaics Warped to ULCN2005 Network. In *Lunar and Planetary Science Conference Proceedings*, volume 39 of *Lunar and Planetary Science Conference Proceedings*, page #2337, 2008.

C. Harris and M. Stephens. A Combined Corner and Edge Detector. *Proceedings of The Fourth Alvey Vision Conference (1988)*, pages 147–151, 1988.

R. M. Hazen, P. M. Bell, and H. K. Mao. Effects of compositional variation on absorption spectra of lunar pyroxenes. In *Lunar and Planetary Science Conference Proceedings*, volume 9 of *Lunar and Planetary Science Conference Proceedings*, pages 2919–2943, 1978.

J. W. Head and T. B. McCord. Imbrian-age highland volcanism on the moon – The Gruithuisen and Mairan domes. *Science*, 199:1433–1436, 1978.

G. H. Heiken, D. T. Vaniman, and B. M. French, editors. *Lunar sourcebook - A user's guide to the moon*. Cambridge University Press, 1991. ISBN 0-521-33444-6.

S. Herbort, A. Grumpe, and C. Wöhler. Reconstruction of non-Lambertian surfaces by fusion of Shape from Shading and active range scanning. In *Proc. 18th International Conference on Image Processing (ICIP), Invited contribution*, pages 17–20, Brussels, Belgium, 2011. IEEE. doi: 10.1109/ICIP.2011.6115812.

M. D. Hicks, B. J. Buratti, J. Nettles, M. Staid, J. Sunshine, C. M. Pieters, S. Besse, and J. Boardman. A photometric function for analysis of lunar images in the visual and infrared based on Moon Mineralogy Mapper observations. *J. Geophys. Res.*, 116: E00G15, 2011. doi: 10.1029/2010JE003733.

J. K. Hillier, B. J. Buratti, and K. Hill. Multispectral Photometry of the Moon and Absolute Calibration of the Clementine UV/Vis Camera. *Icarus*, 141(2):205–225, 1999. ISSN 0019-1035. doi: 10.1006/icar.1999.6184.

B. K. P. Horn. *Shape from Shading: A Method for Obtaining the Shape of a Smooth Opaque Object from One View*. Ph.d. thesis, Department of Electrical Engineering, MIT, MIT, Cambridge, MA, USA, 1970.

B. K. P. Horn. Obtaining shape from shading information. In P. H. Winston, editor, *The psychology of computer vision*, chapter 4, pages 115–155. McGraw-Hill, New York, 1975.

B. K. P. Horn. Understanding Image Intensities. *Artificial Intelligence*, 11(2):201–231, 1977.

B. K. P. Horn. *Robot Vision*. MIT Press, 1st edition, 1986. ISBN 0070303495.

B. K. P. Horn. Height and Gradient from Shading. *International Journal of Computer Vision*, 5(1):37–75, 1990.

B. K. P. Horn and B. L. Bachman. Using Synthetic Images to Register Real Images with Surface Models, 1978.

I. Horovitz and N. Kiryati. Depth from gradient fields and control points: bias correction in photometric stereo. *Image and Vision Computing*, 22(9):681–694, 2004. doi: http://dx.doi.org/10.1016/j.imavis.2004.01.005.

B. Jähne. *Practical Handbook on Image Processing for Scientific Applications*. CRC Press, 2nd edition, 2004. ISBN 978-0849319006.

Z. Jankó and D. Chetverikov. Registration of an Uncalibrated Image Pair to a 3D Surface Model. *Pattern Recognition, International Conference on*, 2:208–211, 2004. ISSN 1051-4651. doi: http://doi.ieeecomputersociety.org/10.1109/ICPR.2004.1334097.

Z. Jankó, D. Chetverikov, and A. Ekárt. Using genetic algorithms is computer vision: registering images to 3D surface model. *Acta Cybern.*, 18:193–212, February 2007. ISSN 0324-721X.

O. J. W. F. Kardaun. *Classical Methods of Statistics*. Springer Verlag, Berlin, Heidelberg, New York, 2005. ISBN 978-3-540-21115-0.

H. H. Kieffer and T. C. Stone. The Spectral Irradiance of the Moon. *The Astronomical Journal*, 129(6):2887–2901, 2005.

R. L. Kirk. *III A fast finite element algorithm for two-dimensional photoclinometry.* Ph.D. Thesis (unpubl.), California Intstitute of Technology, Pasadena, 1987. URL `http://resolver.caltech.edu/CaltechETD:etd-11142006-131417`.

R. L. Kirk, J. M. Barrett, and L. A. Soderblom. Photoclinometry Made Simple...? In *ISPRS Working Group IV/9 Workshop "Advances in Planetary Mapping"*, 2003a.

R. L. Kirk, E. Howington-Kraus, B. Redding, D. Galuszka, T. M. Hare, B. A. Archinal, L. A. Soderblom, and J. M. Barrett. High-resolution topomapping of candidate MER landing sites with Mars Orbiter Camera narrow-angle images. *Journal of Geophysical Research*, 108(E12):DOI: 10.1029/2003JE002131, 2003b.

R. L. Kirk, E. Howington-Kraus, D. Galuszka, B. Redding, and T. M. Hare. Topomapping of Mars with HRSC Images, ISIS, and a Commercial Stereo Workstation. *ISPRS Archives*, XXXVI(B4), 2006.

S. Kodama, M. Ohtake, Y. Yokota, A. Iwasaki, J. Haruyama, T. Matsunaga, R. Nakamura, H. Demura, N. Hirata, T. Sugihara, and Y. Yamamoto. Characterization of Multiband Imager Aboard SELENE. *Space Science Reviews*, 154(1–4):79–102, 2010. doi: 10.1007/s11214-010-9661-z.

V. V. Korokhin, Yu. I. Velikodsky, Yu. G. Shkuratov, and U. Mall. The phase dependence of brightness and color of the lunar surface: a study based on integral photometric data. *Solar System Research*, 41(1):19–27, 2007. ISSN 0038-0946. doi: 10.1134/S0038094607010029.

V. V. Korokhin, Y. I. Velikodsky, E. V. Shalygin, Y. G. Shkuratov, V. G. Kaydash, and G. Videen. Retrieving lunar topography from multispectral LROC images. *Planetary and Space Science*, 92(0):65–76, 2014. ISSN 0032-0633. doi: 10.1016/j.pss.2014.01.008.

D. J. Lawrence, W. C. Feldman, B. L. Barraclough, A. B. Binder, R. C. Elphic, S. Maurice, and D. R. Thomsen. Global Elemental Maps of the Moon: The Lunar Prospector Gamma-Ray Spectrometer. *Science*, 281(5382):1484–1489, 1998.

L. P. Lebedev, M. J. Cloud, and V. A. Eremeyev. *Advanced Engineering Analysis. The Calculus of Variations and Functional Analysis with Applications in Mechanics*. World Scientific Publishing Co. Pte. Ltd., Singapore, 2012. ISBN 10981–4390–47–X.

V. Lohse, C. Heipke, and R. L. Kirk. Derivation of planetary topography using multi-image shape-from-shading. *Planetary and Space Science*, 54(7):661–674, 2006.

P. G. Lucey, G. J. Taylor, and E. Malaret. Abundance and Distribution of Iron on the Moon. *Science*, 268:1150–1153, 1995. doi: 10.1126/science.268.5214.1150.

P. G. Lucey, D. T. Blewett, and B. R. Hawke. Mapping the FeO and TiO_2 content of the lunar surface with multispectral imagery. *Journal of Geophysical Research: Planets*, 103(E2):3679–3699, 1998. ISSN 2156-2202. doi: 10.1029/97JE03019.

P. G. Lucey, D. T. Blewett, and B. L. Jolliff. Lunar iron and titanium abundance algorithms based on final processing of Clementine ultraviolet-visible images. *Journal of Geophysical Research*, 105(E8):20297–20306, 2000.

S. Lundeen, S. McLaughlin, and R. Alanis. Moon Mineralogy Mapper Data Product Software Interface Specification. PDS document Version 9.10 JPL D-39032, Jet Propulsion Laboratory, Pasadena, CA, 2011.

F. Maes, A. Collignon, D. Vandermeulen, G. Marchal, and P. Suetens. Multimodality image registration by maximization of mutual information. *IEEE Transactions on Medical Imaging.*, 16(2):187–198, 1997.

U. Mall, M. Banaszkiewiez, K. Brønstad, S. McKenn-Lawlor, A. Nathues, F. Søraas, E. Vilenius, and K. Ullaland. Near Infrared Spectrometer SIR-2 on Chandrayaan-1. *Current Science*, 96:506–511, 2009.

U. Mall, V. Korokhin, Yu. Shkuratov, and the SIR-2 collaboration. Photometric investigations using the SIR-2 data of the Chandrayaan-1 mission. In *Lunar and Planetary Institute Science Conference Abstracts*, volume 41 of *Lunar and Planetary Inst. Technical Report*, page #1616, 2010.

S. Marsland. *Machine Learning: An Algorithmic Perspective*. CRC Press, New Jersey, USA, 2009. ISBN 978-1420067187.

T. Matsunaga, M. Ohtake, J. Haruyama, Y. Ogawa, R. Nakamura, Y. Yokota, T. Morota, C. Honda, M. Torii, M. Abe, T. Nimura, T. Hiroi, T. Arai, K. Saiki, H. Takeda, N. Hirata, S. Kodama, T. Sugihara, H. Demura, N. Asada, J. Terazono, and H. Otake. Discoveries on the lithology of lunar crater central peaks by SELENE Spectral Profiler. *Geophysical Research Letters*, 35(23):L23201, 2008. doi: 10.1029/2008GL035868.

T. B. McCord, M. P. Charette, T. V. Johnson, L. A. Lebofsky, C. Pieters, and J. B. Adams. Lunar spectral types. *Journal of Geophysical Research*, 77(8):1349–1359, 1972. ISSN 2156-2202. doi: 10.1029/JB077i008p01349.

A. McEwen, E. Eliason, P. Lucey, E. Malaret, C. Pieters, M. Robinson, and T. Sucharski. Summary of Radiometric Calibration and Photometric Normalization Steps for the Clementine UVVIS Images. In *Lunar and Planetary Institute Science Conference Abstracts*, volume 29 of *Lunar and Planetary Inst. Technical Report*, page #1466, 1998.

A. S. McEwen. Photometric functions for photoclinometry and other applications. *Icarus*, 92(2):298–311, 1991. ISSN 0019-1035.

A. S McEwen. A Precise Lunar Photometric Function. In *Lunar and Planetary Institute Science Conference Abstracts*, volume 27 of *Lunar and Planetary Inst. Technical Report*, pages 841–842, 1996.

J. C. McGlone, E. M. Mikhail, and J. S. Bethel, editors. *Manual of photogrammetry*. American Society for Photogrammetry and Remote Sensing, fifth edition edition, 2004. ISBN 1-570-83071-1.

A. F. McGuire and B. W. Hapke. An Experimental Study of Light Scattering by Large, Irregular Particles. *Icarus*, 113(1):134–155, 1995. doi: 10.1006/icar.1995.1012.

D. E. Melendrez, J. R. Johnson, S. M. Larson, and R. B. Singer. Remote sensing of potential lunar resources: 2. High spatial resolution mapping of spectral reflectance ratios and implications for nearside mare TiO2 content. *Journal of Geophysical Research: Planets*, 99(E3):5601–5619, 1994. ISSN 2156–2202. doi: 10.1029/93JE03430. URL `http://dx.doi.org/10.1029/93JE03430`.

J. F. Mustard and C. M. Pieters. Photometric Phase Functions of Common Geologic Minerals and Applications to Quantitative Analysis of Mineral Mixture Reflectance Spectra. *Journal of Geophysical Research*, 94(B10):13619–13634, 1989.

J. F. Mustard, L. Li, and G. He. Nonlinear spectral mixture modeling of lunar multispectral data: Implications for lateral transport. *Journal of Geophysical Research*, 103 (E8):19419–19425, 1998.

D. Nehab, S. Rusinkiewicz, J. Davis, and R. Ramamoorthi. Efficiently Combining Positions and Normals for Precise 3D Geometry. *ACM Transactions on Graphics (SIGGRAPH 2005)*, 24(3), 2005.

J. A. Nelder and R. Mead. A simplex method for function minimization. *The computer journal*, 7(4):308–313, 1965.

G. A. Neumann. 2009 Lunar Orbiter Laser Altimeter, LRO-L-LOLA-4-GDR-V1.0. NASA Planetary Data System, 2010. URL `http://pds-geosciences.wustl.edu/missions/lro/lola.htm`. accessed November 01, 2011.

H.-S. Ng, T. Wu, and C.-K. Tang. Surface-from-Gradients without Discrete Integrability Enforcement: A Gaussian Kernel Approach. *IEEE Transactions on Pattern Analysis and Machine Intelligence*, 32(11):2085–2099, 2010.

S. K. Noble, C. M. Pieters, L. A. Taylor, R. V. Morris, C. C. Allen, D. S. McKay, and L. P. Keller. The optical properties of the finest fraction of lunar soil: Implications for space weathering. *Meteoritics & Planetery Science*, 36:31–42, 2001.

J. Nocedal and S. J. Wright. *Numerical Optimization*. Springer Series in Operations Research. Springer, 1999. ISBN 0-387-98793-2.

S. Nozette, P. Rustan, L. P. Pleasance, D. M. Horan, P. Regeon, E. M. Shoemaker, P. D. Spudis, C. H. Acton, D. N. Baker, J. E. Blamont, B. J. Buratti, M. P. Corson, M. E. Davies, T. C. Duxbury, E. M. Eliason, B. M. Jakosky, J. F. Kordas, I. T. Lewis, C. L. Lichtenberg, P. G. Lucey, E. Malaret, M. A. Massie, J. H. Resnick, C. J. Rollins, H. S. Park, A. S. McEwen, R. E. Priest, C. M. Pieters, R. A. Reisse, M. S. Robinson, R. A. Simpson, D. E. Smith, T. C. Sorenson, R. W. Vorder Breugge, and M. T. Zuber. The Clementine Mission to the Moon: Scientific Overview. *Science*, 266:1835–1839, 1994. doi: 10.1126/science.266.5192.1835.

M. Ohtake, J. Haruyama, T. Matsunaga, Y. Yokota, T. Morota, C. Honda, and the LISM team. Performance and scientific objectives of the SELENE (KAGUYA) Multiband Imager. *Earth Planets Space*, 60(4):257–264, 2008.

M. Ohtake, T. Matsunaga, Y. Yokota, S. Yamamoto, Y. Ogawa, T. Morota, C. Honda, J. Haruyama, K. Kitazato, H. Takeda, A. Iwasaki, R. Nakamura, T. Hiroi, S. Kodama, and H. Otake. Deriving the Absolute Reflectance of Lunar Surface Using SELENE (Kaguya) Multiband Imager Data. *Space Science Reviews*, 154(1-4):57–77, 2010. ISSN 0038-6308. doi: 10.1007/s11214-010-9689-0.

M. Ohtake, C. M. Pieters, P. Isaacson, S. Besse, Y. Yokota, T. Matsunaga, J. Boardman, S. Yamamoto, J. Haruyama, M. Staid, U. Mall, and R. O. Green. One Moon, Many measurements 3: Spectral reflectance. *Icarus*, 226:364–374, 2013.

E. Parzen. On estimation of a probability density function and mode. *The annals of mathematical statistics*, 33(3):1065–1076, 1962.

C. M. Pieters. The Moon as a Spectral Calibration Standard Enabled by Lunar Samples: The Clementine Example. In *Workshop on New Views of the Moon II: Understanding the Moon Through the Integration of Diverse Datasets*, page #8025, Flagstaff, Arizona, 1999.

C. M. Pieters, J. Boardman, B. Buratti, A. Chatterjee, R. Clark, T. Glavich, R. Green, J. Head III, P. Isaacson, E. Malaret, T. McCord, J. Mustard, N. Petro, C. Runyon, M. Staid, J. Sunshine, L. Taylor, S. Tompkins, P. Varanasi, and M. White. The Moon Mineralogy Mapper (M^3) on Chandrayaan-1. *Current Science*, 96(4):500–505, 2009a.

C. M. Pieters, J. N. Goswami, R. N. Clark, M. Annadurai, J. Boardman, B. Buratti, J.-P. Combe, M. D. Dyar, R. Green, J. W. Head, C. Hibbitts, M. Hicks, P. Isaacson, R. Klima, G. Kramer, S. Kumar, E. Livo, S. Lundeen, E. Malaret, T. McCord, J. Mustard, J. Nettles, N. Petro, C. Runyon, M. Staid, J. Sunshine, L. A. Taylor, S. Tompkins, and P. Varanasi. Character and Spatial Distribution of OH/H2O on the Surface of the Moon Seen by M3 on Chandrayaan-1. *Science*, 326(5952):568–572, 2009b. doi: 10.1126/science.1178658.

C. M. Pieters, J. W. Boardman, M. Ohtake, T. Matsunaga, J. Haruyama, R. O. Green, U. Mall, M. I. Staid, P. J. Isaacson, Y. Yokota, S. Yamamoto, S. Besse, and J. M. Sunshine. One Moon, many measurements 1: Radiance values. *Icarus*, 226:951–963, 2013.

F. Poulet, J. N. Cuzzi, D. P. Cruikshank, T. Roush, and C. M. Dalle Ore. Comparison between the Shkuratov and Hapke Scattering Theories for Solid Planetary Surfaces: Application to the Surface Composition of Two Centaurs. *Icarus*, 160(2):313–324, 2002. ISSN 0019-1035.

M. J. D. Powell. An efficient method for finding the minimum of a function of several variables without calculating derivatives. *The Computer Journal*, 7(2):155–162, 1964.

A. Rajwade, A. Banerjee, and A. Rangarajan. Probability density estimation using isocontours and isosurfaces: applications to information-theoretic image registration. *IEEE Transactions on Pattern Analysis and Machine Intelligence.*, 31(3):475–491, 2009.

H. Riris, J. F. Cavanaugh, X. Sun, L. Ramos-Izquierdo, P. Liiva, M. Rodriguez, S. Schmidt, J. McGarry, C. Peters, G. B. Jackson, and D. E. Smith. The Lunar Orbiter Laser Altimeter (LOLA) on NASA's Lunar Reconnaissance Orbiter (LRO) Mission. *Conference on Lasers and Electro-Optics and Conference on Quantum electronics and Laser Science CLEO/QELS 2009*, pages 114–115, 2009.

M. S. Robinson and B. L. Jolliff. Apollo 17 landing site: Topography, photometric corrections, and heterogeneity of the surrounding highland massifs. *Journal of Geophysical Research: Planets*, 107(E11):20–1–20–30, 2002. ISSN 2156-2202. doi: 10.1029/2001JE001614. URL `http://dx.doi.org/10.1029/2001JE001614`.

M. S. Robinson, S. M. Brylow, M. Tschimmel, D. Humm, S. J. Lawrence, P. C. Thomas, B. W. Denevi, E. Bowman-Cisneros, J. Zerr, M. A. Ravine, M. A. Caplinger, F. T. Ghaemi, J. A. Schaffner, M. C. Malin, P. Mahanti, A. Bartels, J. Anderson, T. N. Tran, E. M. Eliason, A. S. McEwen, E. Turtle, B. L. Jolliff, and H. Hiesinger. Lunar Reconnaissance Orbiter Camera (LROC) Instrument Overview. *Space Science Reviews*, 150(1–4):81–124, 2010. doi: 10.1007/s11214-010-9634-2.

P. M. Schenk. Thickness Constraints on the Icy Shells of the Galilean Satellites from a Comparison of Crater Shapes. *Nature*, 417:419–421, 2002. doi: 10.1038/417419a.

P. M. Schenk. Cartographic and Topographic Mapping of the Icy Satellites of the Outer Solar System. *ISPRS Archives*, XXXVII(B4):967–972, 2008.

F. Schmidt, M. Legendre, and S. Le Mouëlic. Minerals detection for hyperspectral images using adapted linear unmixing: LinMin. *Icarus*, 237:61–74, 2014. doi: 10.1016/j.icarus.2014.03.044.

F. Scholten, J. Oberst, K.-D. Matz, T. Roatsch, M. Wählisch, E. J. Speyerer, and M. S. Robinson. GLD100: The near-global lunar 100 m raster DTM from LROC WAC stereo image data. *Journal of Geophysical Research*, 117:DOI: 10.1029/2011JE003926, 2012.

R. A. Schowengerdt. *Remote Sensing: Models and Methods for Image Processing*. Academic Press, 3rd edition, 2006.

C. E. Shannon. A mathematical theory of communication. *ACM SIGMOBILE Mobile Computing and Communications Review*, 5(1):3–55, 2001.

M. Shao, R. Chellappa, and T. Simchony. Reconstructing a 3-D Depth Map from One or More Images. *CVGIP: Image Understanding*, 53(2):219–226, 1991.

Y. Shkuratov, L. Starukhina, H. Hoffmann, and G. Arnold. A Model of Spectral Albedo of Particulate Surfaces: Implications for Optical Properties of the Moon. *Icarus*, 137 (2):235–246, 1999a. ISSN 0019-1035.

Y. Shkuratov, V. Kaydash, V. Korokhin, Y. Velikodsky, N. Opanasenko, and G. Videen. Optical measurements of the Moon as a tool to study its surface. *Planetary and Space Science*, 59:1326–1371, 2011.

Y. G. Shkuratov, V. G. Kaydash, D. G. Stankevich, L. V. Starukhina, P. C. Pinet, S. D. Chevrel, and Y. H. Daydou. Derivation of elemental abundance maps at intermediate resolution from optical interpolation of lunar prospector gamma-ray spectrometer data. *Planetary and Space Science*, 53(12):1287–1301, 2005a.

Y. G. Shkuratov, D. G. Stankevich, D. V. Petrov, P. C. Pinet, A. M. Cord, and Y. H. Daydou. Interpreting photometry of regolith-like surfaces with different topographies: shadowing and multiple scatter. *Icarus*, 173:3–15, 2005b.

Yu. G. Shkuratov, M. A. Kreslavsky, A. A. Ovcharenko, D. G. Stankevich, E. S. Zubko, C. Pieters, and G. Arnold. Opposition Effect from Clementine Data and Mechanisms of Backscatter. *Icarus*, 141(1):132–155, 1999b. ISSN 0019-1035. doi: 10.1006/icar.1999.6154.

R. W. Shorthill, J. M. Saari, F. E. Baird, and J. R. LeCompte. *Photometric properties of selected lunar features*. Number CR–1429 in NASA Contractor Reports. National Aeronautics and Space Administration; for sale by the Clearinghouse for Federal Scientific and Technical Information, Springfield, VA, 1969.

R. Sibson. A Brief Description of Natural Neighbor Interpolation. In Vic Barnett, editor, *Interpolating multivariate data*, chapter 2, pages 21–36. John Wiley & Sons, New York, 1981.

T. Simchony, R. Chellappa, and M. Shao. Direct analytical methods for solving poisson equations in computer vision problems. *Pattern Analysis and Machine Intelligence, IEEE Transactions on*, 12(5):435–446, 1990. ISSN 0162-8828. doi: 10.1109/34.55103.

D. E. Smith, M. T. Zuber, G. B. Jackson, J. F. Cavanaugh, G. A. Neumann, H. Riris, X. Sun, R. S. Zellar, C. Coltharp, J. Connelly, R. B. Katz, I. Kleyner, P. Liiva, A. Matuszeski, E. M. Mazarico, J. F. McGarry, A.-M. Novo-Gradac, M. N. Ott, C. Peters, L. A. Ramos-Izquierdo, L. Ramsey, D. D. Rowlands, S. Schmidt, V. S. Scott III, G. B. Shaw, J. C. Smith, J.-P. Swinski, M. H. Torrence, G. Unger, A. W. Yu, and T. W. Zagwodzki. The Lunar Orbiter Laser Altimeter Investigation on the Lunar Reconnaissance Orbiter Mission. *Space Science Reviews*, 150:209–241, 2010.

S. Smrekar and C. M. Pieters. Near-infrared spectroscopy of probable impact melt from three large lunar highland craters. *Icarus*, 63:442–452, 1985.

L. A. Soderblom and R. L. Kirk. Meter-Scale 3-D Models of the Martian Surface from Combining MOC and MOLA Data. In *Lunar and Planetary Institute Science Conference Abstracts*, volume 34 of *Lunar and Planetary Inst. Technical Report*, page #1730, 2003.

L. A. Soderblom, R. L. Kirk, and K. E. Herkenhoff. Accurate Fine-Scale Topography for the Martian South Polar Region from Combining MOLA Profiles and MOC NA Images. In *Lunar and Planetary Institute Science Conference Abstracts*, volume 33 of *Lunar and Planetary Inst. Technical Report*, page #1254, 2002.

S. Tompkins and C. M. Pieters. Spectral characteristics of lunar impact melts and inferred mineralogy. *Meteoritics and Planetary Science*, 45(7):1152–1169, 2010.

J. van Diggelen. A Photometric Investigation of the Slopes and the Heights of the Ranges of Hills in the Maria of the Moon. *Bulletin of the Astronomical Institutes of the Netherlands*, XI(423):283–289, 1951.

Y. I. Velikodsky, N. V. Opanasenko, L. A. Akimov, V. V. Korokhin, Y. G. Shkuratov, and V. G. Kaydash. Kharkiv Absolute Photometry of the Moon. In *Lunar and Planetary Institute Science Conference Abstracts*, volume 41 of *Lunar and Planetary Inst. Technical Report*, page #1760, 2010.

Z. Wang, A. C. Bovik, H. R. Sheikh, and E. P. Simoncelli. Image quality assessment: From error visibility to structural similarity. *IEEE Transactions on Image Processing*, 13(4):600–612, 2004.

J. Warell. Properties of the Hermean regolith: IV. Photometric parameters of Mercury and the Moon contrasted with Hapke modelling. *Icarus*, 167(2):271–286, 2004.

M. Weisensee. *Modelle und Algorithmen für das Facetten-Stereosehen*, volume 374 of *DGK-Reihe C*. C.H. Beck Verlag, München, 1992. ISBN 3-7696-9421-X.

W. M. Wells III, P. Viola, H. Atsumi, S. Nakajima, and R. Kikinis. Multi-modal volume registration by maximization of mutual information. *Medical image analysis*, 1(1): 35–51, 1996.

R. L. Wildey. Generalized Photoclinometry for Mariner 9. *Icaurs*, 25:613–626, 1975.

D. E. Wilhelms. A Photometric Technique for Measurement of Lunar Slopes. In *In: Astrogeological Studies Annual Progress Report, Part D: Studies for Space Flight Program. U.S. Geological Survey Open-File Report*, pages 1–12, 1964.

L. Wilson and J. W. Head. Lunar Gruithuisen and Mairan domes: Rheology and mode of emplacement. *Journal of Geophysical Research*, 108(E2):DOI: 10.1029/2002JE001909, 2003. ISSN 2156-2202.

C. Wöhler and A. Grumpe. Correction of Chandrayaan-1 M^3 Lunar Hyperspectral Image Data with Respect to Local Topography. In *Lunar and Planetary Science Conference*, volume 43 of *Lunar and Planetary Inst. Technical Report*, page #1906, 2012.

C. Wöhler and A. Grumpe. Integrated DEM Construction and Calibration of Hyperspectral Imagery: A Remote Sensing Perspective. In Michael Breuß, Alfred Bruckstein, and Petros Maragos, editors, *Innovations for Shape Analysis: Models and Algorithms*, Mathematics and Visualization, pages 467–492, Berlin Heidelberg, 2013. Springer-Verlag.

C. Wöhler, A. Berezhnoy, and R. Evans. Estimation of elemental abundances of the lunar regolith using clementine UVVIS+NIR data. *Planetary and Space Science*, 59:92–110, 2011.

C. Wöhler, A. Grumpe, A. Berezhnoy, M. U. Bhatt, and U. Mall. Integrated topographic and spectral analysis of the lunar surface: Application to impact melt flows and ponds. *Icarus*, 235:86–122, 2014. doi: 10.1016/j.icarus.2014.03.010.

C. Wood. Lunar Photo of the Day, March 8, 2013. Online ressource, 2013. URL `http://lpod.wikispaces.com/March+8,+2013`. accessed March 21, 2013.

C. A. Wood and L. Andersson. New morphometric data for fresh lunar craters. In *Lunar and Planetary Institute Science Conference Abstracts*, volume 9 of *Lunar and Planetary Inst. Technical Report*, pages 3369–3389, 1978.

S. Yamamoto, T. Matsunaga, Y. Ogawa, R. Nakamura, Y. Yokota, M. Ohtake, J. Haruyama, T. Morota, C. Honda, T. Hiroi, and S. Kodama. Preflight and In-Flight Calibration of the Spectral Profiler on Board SELENE (Kaguya). *IEEE Transactions on Geoscience and Remote Sensing*, 49(11):4660–4676, 2011.

Y. Yokota, T. Matsunaga, M. Ohtake, J. Haruyama, R. Nakamura, S. Yamamoto, Y. Ogawa, T. Morota, C. Honda, K. Saiki, K. Nagasawa, K. Kitazato, S. Sasaki, A. Iwasaki, H. Demura, N. Hirata, T. Hiroi, R. Honda, Y. Iijima, and H. Mizutani. Lunar photometric properties at wavelengths 0.5-1.6 μm acquired by SELENE Spectral Profiler and their dependency on local albedo and latitudinal zones. *Icarus*, 215: 639–660, 2011. doi: 10.1016/j.icarus.2011.07.028.

W. Zhang and N. E. Bowles. Mapping Lunar TiO2 and FeO with Chandrayaan-1 M3 Data. In *Lunar and Planetary Science Conference Abstracts*, volume 44 of *Lunar and Planetary Inst. Technical Report*, page #1212, 2013.

Z. Zhang. Iterative point matching for registration of free-form curves and surfaces. *Int. J. Comput. Vision*, 13(2):119–152, 1994. ISSN 0920-5691. doi: 10.1007/BF01427149.

M. T. Zuber, D. E. Smith, R. S. Zellar, G. A. Neumann, X. Sun, R. B. Katz, I. Kleyner, A. Matuszeski, J. F. McGarry, M. N. Ott, L. A. Ramos-Izquierdo, D. D. Rowlands, M. H. Torrence, and T. W. Zagwodzki. The Lunar Reconnaissance Orbiter Laser Ranging Investigation. *Space Science Reviews*, 150:63–80, 2010.

List of Figures

2.1 Global M^3 mosaic at 2 pixels per degree resolution 8
2.2 Comparison of datasets 10
2.3 Illustration of the illumination and observation geometry. 15

4.1 Comparison of apparent and thermally corrected reflectance 34
4.2 Global surface temperature estimates 36
4.3 Local surface temperature estimates 37
4.4 Global coverage of the M^3 dataset 41
4.5 M^3 reflectance images of the lunar crater Lowell (103.4 °W, 13.0 °S) 44
4.6 Topographic models of the lunar crater Lowell (103.4 °W, 13.0 °S) 44
4.7 Influence of the parameter σ_{refl} 45
4.8 Influence of the parameter σ_{refl} 46
4.9 Comparison to the official M^3 reflectance 47
4.10 Surface refinement of the Mairan region (longitude 311 °E–313 °E, latitude 40 °N–43 °N) 49
4.11 Spectral reflectance parameters of the Mairan region (longitude 311 °E–313 °E, latitude 40 °N–43 °N) 51
4.12 Reflectance parameters map of the Mairan region (longitude 311 °E–313 °E, latitude 40 °N–43 °N) 52
4.13 Phase angle dependence of the sensor temperature. 53
4.14 Dataset for the correction of the sensor temperature effect 54
4.15 CR spectra dependence on the phase angle 59
4.16 Result of the CR based correction based on the v1 dataset 66
4.17 Result of the CR based correction based on the v3 dataset 67
4.18 Relative band depth for $\mu_{\text{ident}} = 0$ and $\mu_{\text{ref}} = 0.01$ 69
4.19 Relative band depth for $\mu_{\text{ident}} = 0.1$ and $\mu_{\text{ref}} = 1.0$ 71

5.1 Flow charts of the proposed algorithm . . . 81
5.2 Introduced symbols . . . 86
5.3 Flowchart of the proposed depth recovery from a gradient field estimate. . . . 92
5.4 Reconstruction of the crater Bullialdus . . . 95
5.5 Rendered DEM of crater Aristarchus (312 °E–314 °E, 22 °S–26 °S) . . . 99
5.6 Rendered DEM of crater Bhabha (194 °E–196 °E, 58 °S–52 °S) . . . 100
5.7 Rendered DEM of crater Aristillus (0 °E–2.5 °E, 32 °N–36 °S) . . . 100
5.8 Comparison between LOLA single tracks and the refined DEM of the Mairan region . . . 101
5.9 Reconstruction of the crater Tycho (348 °E–350 °E, 41 °S–45 °S) . . . 103
5.10 Computed RMSE for the various regions (GLD100) . . . 108
5.11 Closeup of the Mairan T dome (47.00 °W – 49.00 °W, 40.00 °N – 43.00 °N) . . 110
5.12 Computed RMSE for the various regions (Gridded LOLA) . . . 111
5.13 Influence of the parameters σ_{absDepth} and τ . . . 112
5.14 Results for the Mairan T dome (48.20 °W – 48.60 °W, 41.67 °N – 41.93 °N) . . 114
5.15 Comparison of all DEM with respect to the LOLA track marked in Fig. 5.14(a) 115
5.16 Results for the Mairan domes (47.00 °W – 49.00 °W, 40.00 °N – 43.00 °N) . . . 116
5.17 Comparison of all DEM with respect to the LOLA track marked in Fig. 5.16(a) 117
5.18 Results for the fault system near Lansberg (26.00 °W – 27.00 °W, 2.00 °S – 3.00 °S) . . . 119
5.19 Results for the lunar crater Tycho (10.00 °W – 12.00 °W, 45.00 °S – 41.00 °S) . 120
5.20 Comparison of all DEM with respect to the LOLA track marked in Fig. 5.19(a) 121
5.21 Comparison of the reflectance models . . . 123
5.22 Craters that define the crater RMSE . . . 124
5.23 Reflectance near lunar crater Lowell (102.00 °W – 104.00 °W, 12.00 °S – 18.00 °S) 125
5.24 Topography near lunar crater Lowell (102.00 °W – 104.00 °W, 12.00 °S – 18.00 °S) 127

6.1 Near-global M^3 mosaic: Results . . . 130
6.2 Near-global M^3 mosaic: Comparison to Clementine . . . 132
6.3 Extraction of spectral parameters . . . 133
6.4 Iron oxide (FeO) content map: Comparison to Lucey et al. (2000). . . . 137
6.5 Iron oxide (FeO) content map: M^3 based reference methods . . . 139
6.6 Titanium dioxide (TiO_2) content map . . . 141
6.7 Elemental abundance maps of Ca, Al, Mg and O . . . 142
6.8 Near-global petrographic map of the Moon using the M^3 data set, covering the latitude range from 60 °S to 60 °N. The resolution corresponds to 20 pixels per degree. Red channel: mare basalt/pyroxene. Green channel: Mg-rich rock. Blue channel: feldspathic material. . . . 143
6.9 Image registration based on control points . . . 147
6.10 Image registration process using a pinhole camera projection . . . 149
6.11 Surface recovery from NAC image M145664820R: Image overview . . . 155

6.12 Surface recovery from NAC image M145664820R: ROI 1 156
6.13 Surface recovery from NAC image M145664820R: ROI 2 158

A.1 Hyperbolic tangent III

List of Tables

4.1 Detailed information on the selected regions 55
4.2 Residual errors of the radiance based approach 68
4.3 Reference errors of the radiance based approach 70

5.1 Evaluated Regions: Parameters of the PHCL algorithm 97
5.2 Evaluated Regions: Parameters of the SfS algorithm 97
5.3 Evaluated Regions: Filenames of the examined M^3 images. 98
5.4 Evaluated Regions: Absolute accuracy (RMSE) 98
5.5 Comparison of constructed DEM to synthetic image "ground truth" 104
5.6 Evaluated Regions: Parameters of the PHCL scheme. 107
5.7 Evaluated Regions: Filenames of the examined M^3 images. 107

6.1 Evaluation of the MI-based methods: 2D rigid and polynomial transformation 151
6.2 Evaluation of the MI-based methods: Pinhole camera based transformations . 152

List of Symbols

Symbol	Unit[1]	Description
$\mathbf{0}_{N_{\text{chan}}}$	–	A vector containing N_{chan} elements of value 0.
$\mathbf{1}_{N_{\text{chan}}}$	–	A vector containing N_{chan} elements of value 1.
α	$[^\circ]$	The phase angle, i.e. the angle between the vectors $\mathbf{s}$ and $\mathbf{v}$.
α_0	$[^\circ]$	The phase angle at the standard illumination geometry.
α_{ext}	–	The ratio of the vertical and the horizontal pixel edge lengths.
$\alpha_{j_{\text{ref}}}$	$[^\circ]$	The reference phase angle of the jth spectrum.
α_{ref}	$[^\circ]$	A phase angle close to α_0 that is used to compute the empirical corrections a_{CR} and b_{CR}.
a_{CR}	–	The empirical correction gain for the continuum-removed reflectance.
$a_{\text{CR},0}$	–	The offset of the linear function a_{CR}.
$a_{\text{CR},1}$	–	The slope of the linear function a_{CR}.
A_{dh}	–	The directional-hemispherical albedo.
$\mathbf{A}_n$	–	The diagonal blocks of $\mathbf{M}$.
$\mathbf{A}_{n,m}$	–	The block in the nth row and the mth column of the matrix $\mathbf{A}_{\text{reduced}}$.

[1]Some quantities, e.g. error functions or polynomial coefficients, have physical units. These units, however, are artificial and/or removed by their weights. For simplicity, these units are ignored.

Symbol	Unit	Description
$\mathbf{A}_{\text{reduced}}$	–	The gram matrix of the columns of $\mathbf{A}_{\text{sensor}}$, which is used to reduce the memory consumption of the optimisation.
$\mathbf{A}_{\text{sensor}}$	–	The coefficient matrix of the linearised sensor temperature based optimisation.
b	–	A parameter of f_{DHG}.
b_{CR}	–	The empirical correction offset for the continuum-removed reflectance.
$b_{\text{CR},0}$	–	The offset of the linear function b_{CR}.
$b_{\text{CR},1}$	–	The slope of the linear function b_{CR}.
$\mathbf{b}_{\text{reduced}}$	–	The transformed right hand side vector of the linearised sensor temperature based optimisation. It is used to reduce the memory consumption of the optimisation.
$\mathbf{b}_{\text{sensor}}$	–	The right hand side vector of the linearised sensor temperature based optimisation.
B	$[\mathrm{W\,m^{-2}\,sr^{-1}}]$	The emission spectrum of a black body.
B_{CB}	–	The function describing the coherent backscatter opposition effect.
B_{CB_0}	–	The parameter describing the height of the coherent backscatter opposition effect.
B_{SH_0}	–	The parameter describing the height of the shadow hiding opposition effect.
$\mathbf{B}_{n,m}$	–	The off-diagonal blocks of $\mathbf{M}$.
BD1	–	The relative band depth of the $1\,\mu$m absorption band.
BD2	–	The relative band depth of the $2\,\mu$m absorption band.
χ_1	–	The random variable which is the intensity of I_1. Since the intensity may represent any physical value, its unit is ignored.
χ_2	–	The random variable which is the intensity of I_2. Since the intensity may represent any physical value, its unit is ignored.
c	–	A parameter of f_{DHG}.
c_{absDepth_2}	–	The second coefficient of the solution to the discrete optimisation of E_{absDepth}.
c_{absDepth_1}	–	The first coefficient of the solution to the discrete optimisation of E_{absDepth}.

Symbol	Unit	Description
c_{absDepth_0}	–	The constant of the solution to the discrete optimisation of E_{absDepth}.
c_d	–	The dth polynomial coefficient of c_{temp}.
c_{norm}	$[\text{m}^2\,\text{sr}^1\,\text{W}^{-1}]$	The photometric normalisation coefficient.
$c_{\text{norm},j}$	$[\text{m}^2\,\text{sr}^1\,\text{W}^{-1}]$	The photometric normalisation coefficient of the jth radiance spectrum.
c_{refl}	–	A wavelength-independent factor that absorbs the photometric normalisation factor and a possible scaling of the reference spectrum.
c_{temp}	–	The sensor temperature based correction offset.
$\mathbf{c}_d$	–	A vector containing the empirical correction offsets c_d of all wavelength.
$\mathbf{c}_{\text{norm},j}$	$[\text{m}^2\,\text{sr}^1\,\text{W}^{-1}]$	A vector containing the photometric normalisation coefficients $c_{\text{norm},j}$ of all wavelength.
C_{sun}	$[\text{W}\,\text{m}^{-2}]$	The solar constant.
CSL1	$[\text{nm}^{-1}]$	The slope of the at the $1\,\mu$m absorption band.
CSL2	$[\text{nm}^{-1}]$	The slope of the continuum at the $2\,\mu$m absorption band.
δ	–	The weight of E_{grad} in composite error terms.
δ_{PHCL}	–	The weight of Egrad in the PHCL algorithm.
δ_{SfS}	–	The weight of Egrad in the SfS algorithm.
$\Delta\alpha$	$[^\circ]$	The difference between the α and α_0.
Δ_{azi}	$[^\circ]$	The azimuth difference, i.e. the angle between the planes of incidence and scattering.
$\Delta\tilde{\mathbf{D}}_{n,j}$	–	An intermediate matrix used for the computation of $\mathbf{A}_{\text{reduced}}$.
$\Delta\mathbf{X}_{\text{norm},j}$	–	The matrix describing the difference between the normalised reflectance of the jth spectrum and its reference spectrum.
d	–	Index of a polynomial coefficient.
d_{gain}	–	The degree of the polynomial modelling the gain of the sensor temperature based correction.
d_{offset}	–	The degree of the polynomial modelling the offset of the sensor temperature based correction.
d_{px}	[m]	The Euclidean distance between two pixels in metric units.

Symbol	Unit	Description
$\mathbf{D}_{d,j}$	–	A diagonal matrix containing weighted powers of $\Delta\alpha$. The unit of $\mathbf{D}_{d,j}$ is variable. Since $\mathbf{D}_{d,j}$ is used as an intermediate variable in the regression, the physical unit is ignored.
$\tilde{\mathbf{D}}_{n,j}$	–	An intermediate matrix used for the computation of $\mathbf{A}_{\text{reduced}}$ and $\mathbf{b}_{\text{reduced}}$.
ε	–	A small perturbation that is used in the calculus of variations.
$\varepsilon_{\text{grad}}$	–	A small perturbation added to the position $\mathbf{x}_\Omega$ in a direction normal to the region boundary of Ω.
ε_{px}	[m]	The edge length of a square pixel.
η	[m]	An arbitrary surface.
η_x	–	The partial derivative of η with respect to x.
η_y	–	The partial derivative of η with respect to y.
E	[W m^{-2}]	The power per unit area incident on a surface illuminated by a light source, i.e. the irradiance.
E_{act}	–	The actual decrease of the error function.
E_{absDepth}	–	The error term measuring the deviation of a low-pass filtered surface estimate from the low-pass filtered a-priori known DEM.
E_{CoV}	–	The error function that is minimised using the calculus of variations.
E_{CR}	–	The error function measuring the distance of two continuum-removed spectra caused by different sensor temperatures.
E_{div}	–	The value of E_{absDepth} that is regarded as a diverged result of the optimisation.
E_{grad}	–	The error term measuring the deviation of a low-pass filtered gradient field estimate from the low-pass filtered gradient field of an a-priori known DEM.
E_{Horn}	–	The error function proposed by Horn (1990).
E_{ident}	–	A constraint that forces the mapping by c_{temp} and g_{temp} to become the identity.
E_{int}	–	The integrability error, i.e. the error measuring the squared Euclidean distance between the surface gradient field and the photometric gradient field estimate.

Symbol	Unit	Description
E_{I}	–	The intensity error, i.e. the error measuring the squared difference between the observed intensity I and the rendered photometric gradient field estimate.
E_{LM}	–	An error function which is sum of squared residuals $r^2_{n_{\mathrm{res}}}$.
E_{norm}	$[\mathrm{W\,m^{-2}}]$	A normalised value of E, i.e. the power of a light source that reaches a point at a reference distance r_{ref}.
E_{phcl}	–	The error term combining E_{I} and E_{grad}.
E_{pred}	–	The predicted decrease of the error function if it was perfectly linear.
E_{ref}	–	A constraint that forces the resulting normalised reflectance values to be close to the normalised reflectance derived from of the corresponding reference spectrum.
E_{refl}	–	The error describing the squared difference between a smooth rendered surface and a low-pass filtered version of the measured reflectance.
E_{sensor}	–	The total error function that is used to determine c_{temp} and g_{temp}.
E_{SfS}	–	The error term combining E_{I}, E_{int} and E_{grad}.
E_{Shao}	–	The error function proposed by Shao et al. (1991).
E_{sun}	$[\mathrm{W\,m^{-2}}]$	The solar irradiance.
E_{temp}	–	The error term describing the squared deviation between the measured radiance and the modelled radiance.
f_{-0}	–	The convolution with $\mathbf{F}_{-0}$.
$f_{-\mathrm{h}}$	–	The convolution with $\mathbf{F}_{-\mathrm{h}}$.
$f_{-\mathrm{v}}$	–	The convolution with $\mathbf{F}_{-\mathrm{v}}$.
f_{CR}	–	The function that computes the continuum-removed reflectance from a reflectance spectrum.
f_{CS}	–	The phase function proposed by Cornette and Shanks (1992).
f_{DHG}	–	The Double Henyey-Greenstein phase function.
f_{lp}	–	A low-pass filter function.

Symbol	Unit	Description
f_{map}	–	A function that maps an unbounded interval to a bounded interval, e.g. the hyperbolic tangent.
f_{norm}	–	The function that computes the normalised reflectance from radiance values.
f_{phase}	–	The function describing the scattering behaviour of an individual particle.
F	–	A function that depends on z and its partial derivatives $\frac{\partial z}{\partial x}$ and $\frac{\partial z}{\partial y}$.
F_0	–	The filter coefficient $\mathbf{F}(0,0)$ at its origin.
F_{d}	–	The lower adjacent filter coefficient $\mathbf{F}(0,-1)$ to its origin.
F_{l}	–	The left adjacent filter coefficient $\mathbf{F}(-1,0)$ to its origin.
F_{r}	–	The right adjacent filter coefficient $\mathbf{F}(1,0)$ to its origin.
F_{u}	–	The upper adjacent filter coefficient $\mathbf{F}(0,1)$ to its origin.
F_z	–	The partial derivative of F with respect to z.
F_{z_x}	–	The partial derivative of F with respect to z_x.
F_{z_y}	–	The partial derivative of F with respect to z_y.
$\mathbf{F}$	–	The filter mask of the low-pass f_{lp}.
$\mathbf{F}_{-0}$	–	A version of $\mathbf{F}$ which is set to zero at its origin.
$\mathbf{F}_{-\text{h}}$	–	A version of $\mathbf{F}$ which is set to zero at the pixels horizontally adjacent to its origin.
$\mathbf{F}_{-\text{v}}$	–	A version of $\mathbf{F}$ which is set to zero at the pixels vertically adjacent to its origin.
FWHM1	[nm]	The width at half maximum of the $1\,\mu$m absorption band.
γ	–	The weight of the E_{int} in composite error terms.
γ_{SfS}	–	The weight of the E_{int} in the SfS algorithm.
g_d	–	The dth polynomial coefficient of g_{temp}.
$g_{\sigma_{\text{absDepth}}}$	–	A Gaussian low pass filter of width σ_{absDepth}.
$g_{\sigma_{\text{grad}}}$	–	A Gaussian low pass filter of width σ_{grad}.
$g_{\sigma_{\text{refl}}}$	–	A Gaussian low pass filter of width σ_{refl}.
g_{temp}	–	The sensor temperature based correction gain.

Symbol	Unit	Description
$\mathbf{g}_d$	–	A vector containing the empirical correction gains g_d of all wavelength.
h_{CB}	–	The parameter describing the width of the coherent backscatter opposition effect.
h_{cx}	[m]	The horizontal pixel extent at the pixel (u, v).
h_{cy}	[m]	The vertical pixel extent at the pixel (u, v).
h_{d}	[m]	The vertical pixel extent at the pixel $(u, v-1)$.
h_{grad}	–	The constant non-zero valued entry of $\mathbf{H}_{\mathrm{grad}}$.
h_{l}	[m]	The horizontal pixel extent at the pixel $(u-1, v)$.
h_{r}	[m]	The horizontal pixel extent at the pixel $(u+1, v)$.
h_{SH}	–	The parameter describing the width of the shadow hiding opposition effect.
h_{u}	[m]	The vertical pixel extent at the pixel $(u, v+1)$.
h_x	[m]	The horizontal edge length of a rectangular pixel.
h_y	[m]	The vertical edge length of a rectangular pixel.
H	–	The Chandrasekhar H-function (Chandrasekhar, 1960, pp. 105ff).
$\mathbf{H}_{\mathrm{grad}}$	–	The Hessian of E_{grad}.
i	–	The image index of the measured spectrum.
I	–	The measured image intensity. Here, it is synonymous for the measured reflectance.
I_i	–	The measured intensity of the ith image.
$\mathbf{I}$	–	The identity matrix.
j_{ref}	–	The number of the jth spectrum's reference spectrum.
$J_{n_{\mathrm{res}},n_{\mathrm{param}}}$	–	The element at row n_{res} and column n_{param} of $\mathbf{J}_{\mathrm{LM}}$.
$\mathbf{J}_{\mathrm{LM}}$	–	The Jacobian of E_{LM}.
$\mathbf{J}_{\mathrm{phcl}}$	–	The Jacobian of E_{phcl}.
$\mathbf{J}_{\mathrm{refl}}$	–	The Jacobian of E_{refl}.
κ	–	The amount of pixels that contribute to $\bar{z}$
k	–	The channel index of the measured spectrum.
λ	[nm]	The wavelength of a (light) wave.
λ_k	[nm]	The centre wavelength of the kth channel.
l	–	The index of the parameter from the reflectance model.

Symbol	Unit	Description
L	$[\mathrm{W\,m^{-2}\,sr^{-1}}]$	The power per unit area and solid angle that is emitted by a surface element.
L_{app}	$[\mathrm{W\,m^{-2}\,sr^{-1}}]$	The power per unit area and solid angle that is emitted by a surface element and observed by a detector.
L_{corr}	$[\mathrm{W\,m^{-2}\,sr^{-1}}]$	The empirically corrected radiance.
$L_{\mathrm{corr},j}$	$[\mathrm{W\,m^{-2}\,sr^{-1}}]$	The jth empirically corrected radiance spectrum.
$L_{\mathrm{corr},j_{\mathrm{ref}}}$	$[\mathrm{W\,m^{-2}\,sr^{-1}}]$	The jth reference radiance spectrum.
L_{meas}	$[\mathrm{W\,m^{-2}\,sr^{-1}}]$	The radiance measured by the instrument.
L_{sensor}	$[\mathrm{W\,m^{-2}\,sr^{-1}}]$	The radiance measured by the sensor.
$L_{\mathrm{sensor},j}$	$[\mathrm{W\,m^{-2}\,sr^{-1}}]$	The jth sensor reading.
$\mathbf{L}_{\mathrm{sensor},j}$	$[\mathrm{W\,m^{-2}\,sr^{-1}}]$	A vector containing the sensor readings $L_{\mathrm{sensor},j}$ of all wavelength.
LBD	–	The logarithm of the ratio between the depths of the 1 μm band and the 2 μm band.
LMIN1	[nm]	The position of the absorption minimum of the 1 μm absorption band.
μ	–	The cosine of the emission angle.
μ_0	–	The cosine of the incidence angle.
μ_{ident}	–	The weight of E_{ident} in E_{sensor}.
μ_{ref}	–	The weight of E_{ref} in E_{sensor}.
m	–	The column index of a matrix.
M	–	The function describing multiple scatterings of the light ray within a layer of particles.
$\mathbf{M}$	–	An intermediate matrix used during the Levenberg-Marquard optimisation of E_{PHCL}.
MI	–	The mutual information of two images.
ν	–	The Levenberg-Marquardt parameter that measures the degree of linearity of the error function.
n	–	The row index of a matrix.
n_{CP}	–	The number of control points after outliers have been removed.
$\tilde{n}_{\mathrm{CP}}$	–	The number of control points which is extracted to align two images.
n_{iter}	–	The iteration counter of the iterative methods.
n_{param}	–	The parameter index of E_{LM}.
n_{res}	–	The residual index of E_{LM}.

Symbol	Unit	Description
n_{step}	–	The step counter.
n_τ	–	The order of magnitude used during the evaluation of the influence of the parameter τ.
n_x	[m]	The x component of $\mathbf{n}$.
n_y	[m]	The y component of $\mathbf{n}$.
n_z	[m]	The z component of $\mathbf{n}$.
$\mathbf{n}$	[m]	The vector that is normal to the surface.
$\tilde{\mathbf{n}}$	[m]	A low-pass filtered version of $\mathbf{n}$.
$\mathbf{n}_\Omega$	[m]	The vector that is normal to the image boundary.
N_{chan}	–	The number of sensor channels used in the optimisation.
N_{coeff}	–	The total number of polynomial coefficients in c_{temp} and g_{temp}.
N_{im}	–	The number of images used for the estimation of the reflectance parameters.
N_{iter}	–	The maximum number of iterations.
N_{MaxPHCL}	–	The maximum number of iterations of the PHCL algorithm.
N_{MaxSfS}	–	The maximum number of iterations of the PHCL algorithm.
N_{param}	–	The number of parameters of E_{LM}.
N_{px}	–	The number of pixels used for the surface refinement.
N_{pyr}	–	The number of pyramid levels during the surface refinement algorithms.
$N_{\text{pyr}_{\text{PHCL}}}$	–	The number of pyramid levels in the PHCL algorithm.
$N_{\text{pyr}_{\text{SfS}}}$	–	The number of pyramid levels in the SfS algorithm.
N_{res}	–	The number of residuals of E_{LM}.
N_{spec}	–	The number of spectra used in the optimisation.
N_{step}	–	The maximum number of steps per iteration.
N_{temp}	–	The number of channels used for the estimation of the surface temperature.
Ω	[m]	The set of coordinates describing the image boundary.

Symbol	Unit	Description
Ω_{refl}	–	A region in the reflectace image that represents the cell spacing of the native resolution of the DEM.
o	–	The pixel index.
ψ	[m]	The intermediate horizontal coordinate of the correlation operator.
Ψ_l	–	The lth parameter of the reflectance model.
$\mathbf{\Psi}$	–	A vector that is created by concatenating all properties of the surface that influence the its reflectance. While these parameters may have individual physical units, the collection is given without a specified unit. Many common parameters are dimensionless.
p	–	The photometric estimate of $\frac{\partial z}{\partial x}$.
p_{I_1}	–	The probability of encountering the intensity χ_1 in the image I_1.
p_{I_2}	–	The probability of encountering the intensity χ_2 in the image I_2.
p_{I_1,I_2}	–	The probability of encountering the intensity χ_1 in the image I_1 and the intensity χ_2 in the image I_2s.
p_x	[m^{-1}]	The partial derivative of p with respect to x.
q	–	The photometric estimate of $\frac{\partial z}{\partial y}$.
q_y	[m^{-1}]	The partial derivative of q with respect to y.
r_i	–	The ith residual of E_{PHCL}.
$r_{n_{\text{res}}}$	–	The n_{res}th residual of E_{LM}.
r_{ref}	[m]	A reference distance between the light source and the surface.
r_s	[m]	The actual distance between the light source and the surface.
r_{sun}	[m]	The distance between a point an the surface and the sun.
$\mathbf{r}_{\text{ICP}}$	[pixels]	The Rodrigues vector returned by the ICP algorithm.
R	–	The bi-directional reflectance of the surface.
R_{415}	–	The spectral reflectance at 415 nm.
R_{750}	–	The spectral reflectance at 750 nm.
R_{950}	–	The spectral reflectance at 950 nm.

Symbol	Unit	Description
R_{62231}	–	The linear approximation of the reflectance spectrum of lunar sample no. 62231 in the wavelength range 2400 nm–2600 nm.
R_{AMSA}	–	The bi-directional reflectance model by Hapke (2002) using an anisotropic multiple scattering approximation.
R_{CR}	–	The continuum-removed reflectance.
$\hat{R}_{\mathrm{CR}}$	–	The empirically corrected continuum-removed reflectance.
R_{dh}	–	The directional-hemispherical reflectance.
R_{Hapke}	–	A function that computes the normalised reflectance from a radiance spectrum using the model proposed by Hapke (2002).
R_{IMSA}	–	The bi-directional reflectance model by Hapke (2002) using an isotropic multiple scattering approximation.
R_{lin}	–	A linear approximation to R_{obs}.
R_{meas}	–	The reflectance measured by the instrument.
R_{model}	–	The reflectance mode used for the estimation of the reflectance parameters.
R_{norm}	–	the photometrically normalised reflectance, i.e. the reflectance normalised to a reference illumination geometry.
R_{normlin}	–	A linear approximation to R_{norm}.
R_{obs}	–	The observed reflectance including the distortion caused by the thermal emission spectrum of the observed surface element.
R_p	–	The partial derivative of R with respect to p.
R_q	–	The partial derivative of R with respect to q.
R_{ref}	–	A reference spectral reflectance.
$\mathbf{R}_{\mathrm{CR},j}$	–	The vector containing the jth spectrum's continuum-removed reflectance values of all wavelengths.
$\mathbf{R}_{\mathrm{norm},j}$	–	The vector containing jth spectrum's normalised reflectance values of all wavelengths.
$\mathbf{R}_{\mathrm{poly},j}$	–	The vector containing the values of a second order polynomial fit to the jth normalised reflectance spectrum of all wavelengths.
$\sigma_{\mathrm{absDepth}}$	[pixels]	The parameter determining the width of the Gaussian low-pass filter $g_{\sigma_{\mathrm{absDepth}}}$.

Symbol	Unit	Description
σ_b	$[\mathrm{W\,m^{-2}\,K^{-4}}]$	The Stefan-Boltzmann coefficient.
σ_grad	[pixels]	The parameter determining the width of the Gaussian low-pass filter g_{σ_grad}.
$\sigma_{\mathrm{grad}_\mathrm{PHCL}}$	[pixels]	The parameter determining the width of the Gaussian low-pass filter g_{σ_grad} in the PHCL algorithm.
$\sigma_{\mathrm{grad}_\mathrm{SfS}}$	[pixels]	The parameter determining the width of the Gaussian low-pass filter g_{σ_grad} in the SfS algorithm.
σ_MI	[pixels]	The width of the low-pass that is applied prior to the estimation of the MI.
σ_refl	[pixels]	The parameter determining the width of the Gaussian low-pass filter g_{σ_refl}.
σ_{refl_n}	[pixels]	The parameter determining the width of the Gaussian low-filter g_{σ_refl} at the nth subsequent execution of the SfS algorithm.
$\sigma_{\mathrm{refl}_\mathrm{PHCL}}$	[pixels]	The parameter determining the width of the Gaussian low-filter g_{σ_refl} in the PHCL algorithm.
$\sigma_{\mathrm{refl}_\mathrm{SfS}}$	[pixels]	The parameter determining the width of the Gaussian low-filter g_{σ_refl} in the SfS algorithm.
$\sigma_{\mathrm{refl}_\mathrm{synth}}$	[pixels]	The parameter determining the width of the Gaussian low-filter g_{σ_refl} which is used to derive synthetic images.
$\mathbf{s}$	[m]	The vector pointing from the surface towards the light source.
$\tilde{\mathbf{s}}$	[m]	A low-pass filtered version of $\mathbf{s}$.
τ	–	The weight of error terms describing the deviation of from z_DEM in composite error terms.
$\hat{\tau}$	–	A version of τ that is normalised with respect to the pixel edge length.
$\bar{\theta}$	$[^\circ]$	The average inclination angle of a surface element that is not resolved by the detector, i.e. on small spatial scales.
θ_FeO	–	A regression paramter used by Lucey et al. (2000) to predict the FeO content.
$\theta_{n_\mathrm{param}}$	–	The n_paramth parameter of E_LM.
θ_max	–	The upper boundary of $\theta_{n_\mathrm{param}}$.
θ_min	–	The lower boundary of $\theta_{n_\mathrm{param}}$.

Symbol	Unit	Description
$\theta_{\mathrm{TiO_2}}$	–	A regression paramter used by Lucey et al. (2000) to predict the TiO_2 content.
$\boldsymbol{\theta}_{\mathrm{LM}}$	–	The vector cotaining all parameters $\theta_{n_{\mathrm{param}}}$.
$\boldsymbol{\theta}_{\mathrm{sensor}}$	–	The vector containing the coefficients of the sensor temperature model.
ϑ_e	[°]	The emission angle, i.e. the angle between the vectors $\mathbf{v}$ and $\mathbf{n}$.
ϑ_i	[°]	The incidence angle, i.e. the angle between the vectors $\mathbf{s}$ and $\mathbf{n}$.
t_1	–	The first term resulting from the optimisation of E_{absDepth}.
t_2	–	The second term resulting from the optimisation of E_{absDepth}.
t_3	–	The third term resulting from the optimisation of E_{absDepth}.
$t_{3\mathrm{den}}$	–	The denominator of t_3.
$t_{3\mathrm{num}}$	–	The numerator of t_3.
t_x	[pixels]	The x component of $\mathbf{t}_{\mathrm{ICP}}$.
t_y	[pixels]	The y component of $\mathbf{t}_{\mathrm{ICP}}$.
t_z	[pixels]	The z component of $\mathbf{t}_{\mathrm{ICP}}$.
$\mathbf{t}_{\mathrm{ICP}}$	[pixels]	The translation vector returned by the ICP algorithm.
T	[K]	The temperature of the observed surface element.
T_0	[K]	The temperature of a surface area where $\beta = 1$ and the solar irradiance falls normally.
T_1	[K]	The first temperature estimate by Clark et al. (2011).
T_2	[K]	The second temperature estimate by Clark et al. (2011).
T_{sensor}	[K]	The temperature of the sensor.
T_{sensor_0}	[K]	The reference temperature of the sensor.
u	–	The horizontal image coordinate in pixels.
u_{f}	[pixels]	The horizontal pixel coordinate of $\mathbf{F}$.
u_{Fe}	[u]	The atomic mass of elemental Fe.
u_{O}	[u]	The atomic mass of elemental O.
u_{Ti}	[u]	The atomic mass of elemental Ti.
v	–	The vertical image coordinate in pixels.
v_{f}	[pixels]	The vertical pixel coordinate of $\mathbf{F}$.

Symbol	Unit	Description
$\mathbf{v}$	[m]	The vector pointing from the surface towards the observer.
$\tilde{\mathbf{v}}$	[m]	A low-pass filtered version of $\mathbf{v}$.
w	–	The single-scattering albedo a single particle.
w_{refl}	–	The low pass filter used for the estimation of the reflectance parameters.
ξ	–	The asymmetry parameter of f_{CS}.
x	[m]	The horizontal image coordinate in metric units.
x_{FeO}	–	A regression paramter used by Lucey et al. (2000) to predict the FeO content.
$\hat{x}$	[m]	The x coordinate where the correlation is evaluated.
$\mathbf{x}$	[m]	The set of x-coordinates describing the image boundary.
$\mathbf{x}_\Omega$	–	A position on boundary of Ω.
$\mathbf{X}_\lambda$	–	The matrix containing powers of the wavelength.
$\mathbf{X}_{\text{norm},j}$	–	The matrix containing a combination of the photometric normalisation coefficient, the radiance and phase angle values of the jth spectrum.
$\mathbf{X}_{\text{poly}}$	–	A generalised inverse of $\mathbf{X}_\lambda$.
$\tilde{\mathbf{X}}_{\text{poly}}$	–	The difference between the identity matrix and $\mathbf{X}_{\text{poly}}$.
$\mathbf{X}_{\text{sensor},j}$	–	The matrix containing a combination of the radiance and phase angle values of the jth spectrum.
y	[m]	The vertical image coordinate in metric units.
$\hat{y}$	[m]	The y coordinate where the correlation is evaluated.
y_{FeO}	–	A regression paramter used by Lucey et al. (2000) to predict the FeO content.
$\mathbf{y}$	[m]	The set of y-coordinates describing the image boundary.
ζ	[m]	The intermediate vertical coordinate of the correlation operator.
$\zeta_{n_{\text{param}}}$	–	An unconstrained variable that is mapped onto $\theta_{n_{\text{param}}}$.

Symbol	Unit	Description
z	[m]	The height of a surface, i.e. the coordinate which is orthogonal to the image plane.
$\bar{z}$	[m]	The average height in a neighbourhood of a centre pixel. The centre value is ignored
$\hat{z}$	[m]	The optimal surface obtained by the calculus of variations.
z^+	[m]	The optimal value of z.
z^*	[m]	The optimal surface estimate which is returned by the optimisation of E_{absDepth}.
z_{c}	[m]	The value of z at the pixel (u, v).
z_{d}	[m]	The value of z at the pixel $(u, v-1)$.
z_{2d}	[m]	The value of z at the pixel $(u, v-2)$.
z_{DEM}	[m]	An a-priori known DEM that constrains the surface refinement.
z_{h}	[m]	The sum of the z_{l} and z_{r}.
z_{l}	[m]	The value of z at the pixel $(u-1, v)$.
z_{2l}	[m]	The value of z at the pixel $(u-2, v)$.
z_{r}	[m]	The value of z at the pixel $(u+1, v)$.
z_{2r}	[m]	The value of z at the pixel $(u+2, v)$.
z_{u}	[m]	The value of z at the pixel $(u, v+1)$.
z_{2u}	[m]	The value of z at the pixel $(u, v+2)$.
z_{v}	[m]	The sum of the z_{u} and z_{d}.
z_x	–	The partial derivative of z with respect to x.
z_y	–	The partial derivative of z with respect to y.

A

Levenberg-Marquardt Optimisation

Details about the Levenberg-Marquardt (LM) algorithm are out of the scope of this thesis and can be found in Gill et al. (1981, pp. 136ff) and Marsland (2009, pp. 252ff). The important implementation details, however, are presented in Section A.1. The original LM algorithm does not provide upper and lower bounds for the variables. To cover bounds of the variables, a transformation of an unbounded variable to a bounded interval is described in Section A.2.

This chapter has been adapted and/or adopted from: (Grumpe et al., 2014a)

A.1 Levenberg-Marquardt optimisation according to (Marsland, 2009)

The Levenberg-Marquardt algorithm is an iterative optimisation method. The goal is the minimisation of a sum E_{LM} of N_{res} squared errors, so-called residuals $r_{n_{\mathrm{res}}}$:

$$E_{\mathrm{LM}} = \sum_{n_{\mathrm{res}}=1}^{N_{\mathrm{res}}} \frac{1}{2} r_{n_{\mathrm{res}}}^2 \tag{A.1}$$

The residuals depend, possibly non-linearly, on the N_{param} parameters $\theta_{n_{\mathrm{param}}}$. Defining the elements

$$J_{n_{\mathrm{res}},n_{\mathrm{param}}} = \frac{\partial r_{n_{\mathrm{res}}}}{\partial \theta_{n_{\mathrm{param}}}} \tag{A.2}$$

of the Jacobian matrix $\mathbf{J}_{\mathrm{LM}}$, the minimisation is carried out using an iterative update scheme

$$\begin{aligned} \boldsymbol{\theta}_{\mathrm{LM}}{}^{(n_{\mathrm{iter}}+1)} &= \boldsymbol{\theta}_{\mathrm{LM}}^{(n_{\mathrm{iter}})} + \Delta\boldsymbol{\theta}_{\mathrm{LM}}^{(n_{\mathrm{iter}})} \text{ with} \\ \Delta\boldsymbol{\theta}_{\mathrm{LM}}^{(n_{\mathrm{iter}})} &= -\left(\mathbf{J}_{\mathrm{LM}}^{\mathrm{T}}\mathbf{J}_{\mathrm{LM}} + \nu\mathbf{I}\right)^{-1} \nabla E_{\mathrm{LM}} \end{aligned} \tag{A.3}$$

where $\Delta\boldsymbol{\theta}_{\mathrm{LM}}^{(n)}$ is the change in the independent variables $\boldsymbol{\theta}_{\mathrm{LM}} = \left[\theta_1, \ldots, \theta_{N_{\mathrm{param}}}\right]^{\mathrm{T}}$ at iteration n_{iter}, $\mathbf{I}$ is the identity matrix and ν is a weighting factor which is adapted to the optimisation problem, i.e. it is adapted to the degree of linearity of the error function. For small values of ν, i.e. linear error functions, the behaviour is similar to the Newton method (Nocedal and Wright, 1999, pp. 135ff) while for large values of ν it is equivalent to a gradient descent (Marsland, 2009, pp. 248ff) with step size $1/\nu$.

The right hand side of Eq. (A.3) is the negative error gradient, which is computed according to

$$\nabla E_{\mathrm{LM}} = \begin{bmatrix} \sum_{n_{\mathrm{res}}=1}^{N_{\mathrm{res}}} \frac{\partial r_{n_{\mathrm{res}}}}{\partial \theta_1} \\ \vdots \\ \sum_{n_{\mathrm{res}}=1}^{N_{\mathrm{res}}} \frac{\partial r_{n_{\mathrm{res}}}}{\partial \theta_{N_{\mathrm{param}}}} \end{bmatrix}. \tag{A.4}$$

The factor ν is computed as proposed by Marsland (2009, p. 254):

$$\nu = \begin{cases} 1.5\nu, & if E_{\mathrm{act}} < 0 \\ 0.2\nu, & if E_{\mathrm{act}} > 0 \wedge \frac{E_{\mathrm{act}}}{E_{\mathrm{pred}}} \geq 0.05 \end{cases} \tag{A.5}$$

where E_{pred} is a linear error prediction given by $\nabla \mathbf{E}_{\mathrm{LM}}{}^{\mathrm{T}} \boldsymbol{\theta}_{\mathrm{LM}}$ and E_{act} is the actual decrease in error. If the error does not decrease, the step is rejected and ν is increased.

A.2 Implicit upper and lower bounds

The described Levenberg-Marquardt algorithm does not apply any constraints on the values of the parameters $\theta_{n_{\mathrm{param}}}$. A common constraint, however, is the application of physically reasonable parameter values, i.e. lower and upper bounds. This type of constraints is easily added by a transformation that maps an unconstrained variable $\zeta_{n_{\mathrm{param}}}$ onto a bounded interval, i.e.

$$\theta_{n_{\mathrm{param}}} = f_{\mathrm{map}}(\zeta_{n_{\mathrm{param}}}), \tag{A.6}$$

and optimising E_{LM} with respect to $\zeta_{n_{\mathrm{param}}}$. According to the chain rule, the partial derivatives of the residuals are

$$\frac{\partial r_{n_{\mathrm{res}}}}{\partial \zeta_{n_{\mathrm{param}}}} = \frac{\partial r_{n_{\mathrm{res}}}}{\partial \theta_{n_{\mathrm{param}}}} \frac{\partial \theta_{n_{\mathrm{param}}}}{\partial \zeta_{n_{\mathrm{param}}}} = \frac{\partial r_{n_{\mathrm{res}}}}{\partial \theta_{n_{\mathrm{param}}}} \frac{\partial}{\partial \zeta_{n_{\mathrm{param}}}} f_{\mathrm{map}}(\zeta_{n_{\mathrm{param}}}). \tag{A.7}$$

Within this thesis, the hyperbolic tangent is chosen, which maps the interval $]-\infty, \infty[$ onto the interval $]-1, 1[$. The derivative of the hyperbolic tangent is easily obtained by

$$\frac{\partial}{\partial \zeta_{n_{\mathrm{param}}}} \tanh(\zeta_{n_{\mathrm{param}}}) = 1 - \tanh^2(\zeta_{n_{\mathrm{param}}}). \tag{A.8}$$

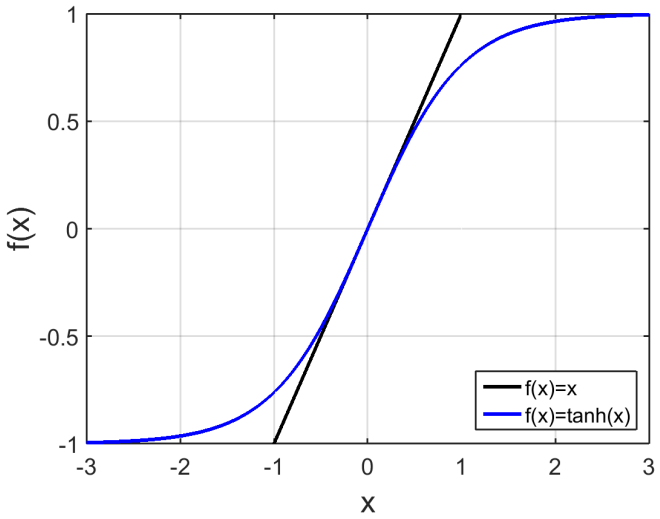

Figure A.1: Hyperbolic tangent (blue line) in the interval $\zeta_{n_{\text{param}}} \in [-3, 3]$. For comparison, the identity (black line) is shown as well. The hyperbolic tangent is almost linear in the interval $\zeta_{n_{\text{param}}} \in [-1, 1]$.

Fig. A.1 shows the values of the hyperbolic tangent in the interval $[-3, 3]$. It is apparent that the hyperbolic tangent is quasi linear in the interval $[1, 1]$ and approaches the upper and lower bound rather fast. Let $\theta_{\max}$ and $\theta_{\min}$ be the upper and the lower bound of the variable $\theta_{n_{\text{param}}}$. The hyperbolic tangent is mapped to the interval $]\theta_{\min}, \theta_{\max}[$ applying a scaling and an offset. Furthermore, a scaling and an offset are applied to $\zeta_{n_{\text{param}}}$ to map the interval $\left[-\frac{\theta_{\max}-\theta_{\min}}{2}, \frac{\theta_{\max}-\theta_{\min}}{2}\right]$ onto the interval $[-1, 1]$, i.e. to ensure a quasi linear behaviour over the whole parameter range:

$$f_{\text{map}}(\zeta_{n_{\text{param}}}) = \frac{\theta_{\max} - \theta_{\min}}{2} \tanh\left(\frac{2}{\theta_{\max} - \theta_{\min}} \zeta_{n_{\text{param}}}\right) + \frac{\theta_{\max} + \theta_{\min}}{2}. \tag{A.9}$$

According to the chain rule, the corresponding derivative is

$$\frac{\partial}{\partial \zeta_{n_{\text{param}}}} f_{\text{map}}(\zeta_{n_{\text{param}}}) = 1 - \tanh^2\left(\frac{2}{\theta_{\max} - \theta_{\min}} \zeta_{n_{\text{param}}}\right). \tag{A.10}$$

Notably, the scaling of the hyperbolic tangent and the unconstrained variable $\zeta_{n_{\text{param}}}$ cancel out.

B

Calculus of Variations

It is well known that the calculus of variations minimises a function with respect to a variable and its partial derivatives. In general, a non-linear partial differential equation defining the solution is obtained. This section summarises the minimisation with respect to the variable z depending on the two independent variables x and y. It presents a short derivation of the partial differential equation, i.e. the Euler equation, and the less well known so-called natural boundary conditions. A detailed derivation and proofs are found in almost any textbook on the calculus of variations, e.g. the book by Lebedev et al. (2012).

This chapter has been adapted and/or adopted from: (Grumpe and Wöhler, 2014; Grumpe et al., 2014a)

Let $F\left(x, y, z(x,y), z_x(x,y), z_y(x,y)\right)$ be a function of two independent variables x and y, a dependent variable $z(x,y)$ and its partial derivatives $z_x(x,y) = \frac{\partial z(x,y)}{\partial x}$ and $z_y(x,y) = \frac{\partial z(x,y)}{\partial y}$ in x-direction and y-direction, respectively. The function F is to be minimised with respect to $z(x,y)$ within an area, i.e.

$$\min_{z(x,y)} \int_{\mathbf{x}} \int_{\mathbf{y}} F\left(x, y, z(x,y), z_x(x,y), z_y(x,y)\right) dxdy. \tag{B.1}$$

The rectangular area of interest $\mathbf{\Omega}$ is defined by the limits $\mathbf{x} = [x_{\min}, x_{\max}]^{\mathrm{T}}$ and $\mathbf{y} = [y_{\min}, y_{\max}]^{\mathrm{T}}$ of the integrals. Non-rectangular areas may be used by introducing a transformation onto the rectangular area defined by $\mathbf{x}$ and $\mathbf{y}$. For clarity, arguments are be omitted where possible.

To determine the optimal value z^+, the dependent variable z is composed of the optimal value and an independent, arbitrary variation η, i.e.

$$z = z^+ + \varepsilon\eta. \tag{B.2}$$

Since the optimal value is obtained at $\varepsilon = 0$, the partial derivative of

$$E_{\mathrm{CoV}} = \int_{\mathbf{x}} \int_{\mathbf{y}} F(x, y, z(x, y, \varepsilon), z_x(x, y, \varepsilon), z_y(x, y, \varepsilon)) dx dy \tag{B.3}$$

with respect to ε needs to equal zero at $\varepsilon = 0$. Thus,

$$0 = \left. \frac{\partial E_{\mathrm{CoV}}}{\partial \varepsilon} \right|_{\varepsilon=0} = \int_{\mathbf{x}} \int_{\mathbf{y}} \left[F_z \eta + F_{z_x} \eta_x + F_{z_y} \eta_y \right]_{\varepsilon=0} dx dy \tag{B.4}$$

where $F_z = \frac{\partial}{\partial z} F$, $F_{z_x} = \frac{\partial}{\partial z_x} F$ and $F_{z_y} = \frac{\partial}{\partial z_y} F$ denote the partial derivatives of F with respect to z, z_x and z_y, respectively. The partial derivatives of η with respect to x and y are denoted by η_x and η_y, respectively. Since η is an arbitrary variation and thus its partial derivatives are unknown, it is not possible to analyse $\frac{\partial E_{\mathrm{CoV}}}{\partial \varepsilon}$ if it depends on η, η_x and η_y. Integration by parts, however, yields

$$\begin{aligned}
\int_{\mathbf{x}} \int_{\mathbf{y}} F_{z_x} \eta_x dx dy &= \int_{\mathbf{y}} \left[F_{z_x} \eta \right]_{\mathbf{x}} dy - \int_{\mathbf{x}} \int_{\mathbf{y}} \frac{\partial}{\partial x} F_{z_x} \eta dx dy \\
\int_{\mathbf{x}} \int_{\mathbf{y}} F_{z_y} \eta_y dx dy &= \int_{\mathbf{x}} \left[F_{z_y} \eta \right]_{\mathbf{y}} dx - \int_{\mathbf{x}} \int_{\mathbf{y}} \frac{\partial}{\partial y} F_{z_y} \eta dx dy
\end{aligned} \tag{B.5}$$

Inserting Eq. (B.5) into Eq. (B.4) yields the Euler equation and the natural boundary conditions of the problem:

$$\begin{aligned}
0 = & \int_{\mathbf{x}} \int_{\mathbf{y}} \underbrace{\left[F_z - \frac{\partial}{\partial x} F_{z_x} - \frac{\partial}{\partial y} F_{z_y} \right]}_{\text{Euler equation}} \eta dx dy \\
& + \underbrace{\int_{\mathbf{x}} \left[F_{z_y} \eta \right]_{\mathbf{y}} dx}_{\substack{\text{upper and lower} \\ \text{boundary}}} + \underbrace{\int_{\mathbf{y}} \left[F_{z_x} \eta \right]_{\mathbf{x}} dy}_{\substack{\text{left and right} \\ \text{boundary}}}
\end{aligned} \tag{B.6}$$

Since η is arbitrary and each integral covers a different part of the area and/or boundary, every integral has to vanish. Thus the first integral covering the whole surface provides a differential equation, i.e. the Euler equation, that determines $z(x, y)$ over the whole area. The other integrals, in contrast, provide the so-called natural boundary conditions at the boundary of the area.

The calculus of variations thus provides boundary conditions that need to be fulfilled in any case. This raises the question how these boundary conditions comply with a-priori

known boundary values of $z(x, y)$ or its partial derivatives. Eq. (B.6) implies, that η has to vanish at the boundary of Ω. If the optimal values $z^+(x, y)$ and thus the values of $z(x, y)$ are known at the boundary , i.e. Dirichlet boundary conditions exist, Eq. (B.2) shows that η has to vanish on the boundary and the natural boundary conditions are always fulfilled. In case of partial derivatives of $z^+(x, y)$, i.e. Neumann boundary conditions, it is not intuitively seen why η should vanish at the boundary. The gradient $\nabla z(x, y) = [z_x, z_y]^{\mathrm{T}}$, however, may be written in vector form as

$$\nabla z(\mathbf{x}_\Omega) = \lim_{\varepsilon_{\mathrm{grad}} \downarrow 0} \frac{1}{\varepsilon_{\mathrm{grad}}} \left(z(\mathbf{x}_\Omega + \varepsilon_{\mathrm{grad}} \mathbf{n}_\Omega) - z(\mathbf{x}_\Omega) \right) \tag{B.7}$$

where $\varepsilon_{\mathrm{grad}}$ is a small value, $\mathbf{x}_\Omega$ is a position on the boundary of Ω and $\mathbf{n}_\Omega$ is a vector that is orthogonal to the boundary and points inside the region. From Eq. (B.7) follows, that $z^+(x, y)$ is implicitly known on the boundary if its gradient and its values inside the region of interest are defined. The former is given by the Neumann boundary conditions and the latter is defined by the Euler equation. This holds for any infinitesimal small value of $\varepsilon_{\mathrm{grad}}$. Literally spoken, the value of $z(x, y)$ on the boundary serves as a variable that adapts to ensure the required partial derivative of $z(x, y)$ based on $z(x, y)$ inside the region. Thus the value of $z(x, y)$ is uniquely determined by the Neumann boundary conditions and no variation η is admissible.